

Surface Chemistry on Oxide-Supported Au Nanoparticle Catalysts and High Surface
Area Oxide Supports

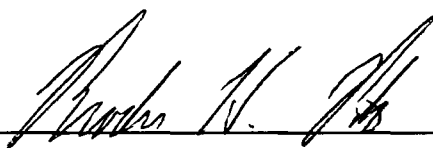
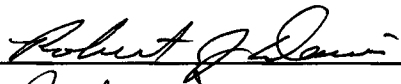


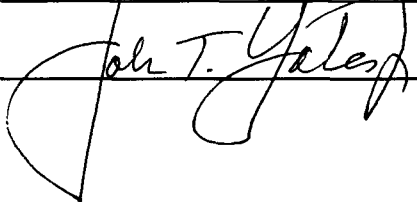
Isabel Xiaoye Green
Beijing, P. R. China

B.S. Chemistry, Peking University, 2007
B.A. Economics, Peking University, 2007

A Dissertation presented to the Graduate Faculty
of the University of Virginia in Candidacy for the Degree of
Doctor of Philosophy

Department of Chemistry

University of Virginia
August, 2012

Abstract

Catalytic reactions are of central importance to today's industrial development and productivity, especially when a metal that is normally unreactive becomes active. Gold nanoparticles supported on TiO₂ powder have been found to be an outstanding catalyst for various reactions, while neither the TiO₂ powder nor the Au nanoparticles by themselves have shown such property. The catalytic activity of a Au/TiO₂ catalyst in oxidation reactions was studied using transmission infrared (IR) spectroscopy in this project. Combining high vacuum-cryogenic temperature experimental techniques and density functional theory (DFT) calculations, a special kind of Au-Ti⁴⁺ dual perimeter site located at the interface of Au and TiO₂ was identified as the key active site for oxygen activation. We demonstrated the working mechanism of this special site via three different reactions with O₂ gas: CO oxidation, H₂ oxidation, and acetic acid partial oxidation. Spectroscopic evidence unambiguously identified the active reaction zone at the Au-Ti⁴⁺ dual perimeter sites.

In addition, the surface properties of high area metal oxide supports were investigated. The adsorption, diffusion, and desorption of pyridine molecules on powdered nano-crystalline TiO₂ and MgO was studied, demonstrating the utility of transmission IR spectroscopy in monitoring such processes. Nano-particle surface crystalline structure, surface acidity, and surface defect sites were found to play important roles in controlling adsorbate diffusivity. The influence of humidity (H₂O) on the surface diffusion/desorption behavior of pyridine was also studied, where a dramatic increase in pyridine surface diffusivity over MgO was observed when modified by H₂O adsorption to produce Brønsted acid sites from Lewis acid sites. A weakly bound IR-active molecular O₂ species was detected on the TiO₂ surface at low temperatures, and its

heat of adsorption was measured to be between -16 and -21 kJ mol^{-1} . It is suspected to be the precursor to “active” O_2 species in various oxidation reactions on the catalyst surface.

Table of Contents

Abstract.....	i
Acknowledgements.....	x
Chapter 1 - Introduction.....	1
I. Using Gold as a Heterogeneous Catalyst.....	1
II. Adsorption, Diffusion, and Desorption Properties of TiO ₂ and MgO.....	6
III. Using Operando FTIR to Monitor Heterogeneous Surface Catalytic Processes.....	8
Chapter 1 References.....	13
Chapter 2 - Instrumentation and Catalyst Preparation.....	17
I. Instrumentation.....	17
II. Gold Catalyst Synthesis.....	20
Chapter 2 References.....	22
Part I. Catalytic Oxidation Activities on Oxide Supported Gold	
Nanoparticles.....	23
Chapter 3 - Spectroscopic Observation of Dual Catalytic Sites during	
Oxidation of CO on a Au/TiO₂ Catalyst.....	24
I. Introduction.....	24
II. Model System and Computation Details.....	27
III. Results and Discussion.....	30
IV. Acknowledgement.....	43

Chapter 3 References.....	43
Chapter 4 - Low Temperature Catalytic H₂ Oxidation over Nanoparticle	
Au/TiO₂ — Dual Perimeter Sites at Work.....	47
I. Introduction.....	47
II. Results and Discussion.....	48
III. Acknowledgement.....	57
Chapter 4 References.....	57
Chapter 5 — Localized Partial Oxidation of Acetic Acid at the Dual	
Perimeter Sites of the Au/TiO₂ Catalyst — Formation of Gold	
Ketenylidene.....	60
I. Introduction.....	60
II. Methodology.....	62
III. Results and Discussion.....	63
IV. Acknowledgement.....	71
Chapter 5 References.....	71
Chapter 6 — Mechanism of the Partial Oxidation of Acetic Acid by O₂ at	
the Dual Perimeter Sites of a Au/TiO₂ Catalyst.....	74
I. Introduction.....	74
II. Methodology.....	76
III. Results and Discussion.....	77
A. FTIR Study of Acetic Acid Adsorption on Different Catalyst Surfaces	77
B. DFT Simulation of Acetate Formation and Most Stable Configuration	
on the Au/TiO ₂ Catalyst.....	79
C. FTIR Study of the Interaction between Adsorbed Acetate and Oxygen	
on Different Catalyst Surfaces.....	81

D. Partial Oxidation of Acetate with $^{18}\text{O}_2$ Isotopic Species on Au/TiO ₂	84
E. Kinetic Studies of the Formation of Ketenylidene.....	85
F. Study of the Deuterium Kinetic Isotope Effect (DKIE) in the Partial Oxidation of Acetate Species.....	86
G. DFT Proposed Mechanism of the Acetate Partial Oxidation.....	89
H. Energy Barriers for Ketenylidene Formation on the TiO ₂ Surface.....	92
IV. Summary of Results.....	94
V. Acknowledgement.....	95
Chapter 6 References.....	95
Chapter 7 - Inhibition at Perimeter Sites of Au/TiO₂ Oxidation Catalyst by Reactant Oxygen..... 98	
I. Introduction.....	98
II. Methodology.....	100
III. Results and Discussion.....	102
IV. Conclusion.....	115
V. Acknowledgement.....	116
Chapter 7 References.....	116
Part II. Adsorption, Diffusion, and Desorption Properties of Metal Oxides.....120	
Chapter 8 - IR Spectroscopic Measurement of Chemisorbed Pyridine Diffusion Kinetics through MgO Nanoparticles – The Involvement of Surface Defect Sites in Slow Diffusion 121	
I. Introduction.....	121

II. Methodology.....	123
A. Experimental.....	123
B. Computational.....	127
III. Results.....	128
A. Spectroscopic Measurements.....	128
B. Diffusion Studies - Compressed MgO.....	130
C. Comparison of Compressed and Uncompressed MgO Powders.....	134
D. Spectroscopic Detection of Defect Site Adsorption.....	135
E. Theoretical Results.....	136
IV. Discussion.....	138
A. Observation of Mobile Precursor Diffusion Kinetics.....	138
B. Crystallographic Issues on MgO Particles. Pyridine Adsorption Sites	140
C. MgO Powder Compression Effects.....	140
D. Observation of the Elementary Surface Diffusion Process by Spectroscopic Measurements.....	141
V. Summary of Results.....	142
VI. Acknowledgement.....	143
Chapter 8 References.....	143
Chapter 9 - Direct Spectroscopic Observation of the Role of Humidity in Surface Diffusion through an Ionic Adsorbent Powder — The Behavior of Adsorbed Pyridine on Nanocrystalline MgO ..	146
I. Introduction.....	146
II. Methodology.....	148
A. Experimental.....	148
B. Computational.....	150
III. Results.....	151

A. Influence of Surface Hydroxylation on Kinetics of Pyridine Diffusion	151
B. Spectroscopic Effects following H ₂ O Introduction to Dehydroxylated MgO.....	155
IV. Discussion.....	157
V. Summary of Results.....	164
VI. Acknowledgement.....	165
Chapter 9 References.....	165
Chapter 10 — IR Spectroscopic Measurement of Diffusion Kinetics of Chemisorbed Pyridine through TiO₂ Particles.....	167
I. Introduction.....	168
II. Methodology.....	170
A. Experimental.....	170
B. Computational.....	175
III. Results and Discussion.....	176
A. Pyridine Chemisorption on TiO ₂ Surfaces.....	176
B. Diffusion/Desorption Studies at Different Temperatures.....	177
C. Spectroscopic Evidence for the Two-Process Diffusion.....	180
D. Computational Results.....	182
E. ESDIAD Study of the Pyridine Adsorption Configuration on the Rutile TiO ₂ (110) Single Crystal Surface.....	189
F. Computational Results for Pyridine Adsorption to Higher Coverages	190
G. Postulate for Fast and Slow Diffusion Sites in the Mobile Precursor Model.....	193
H. Spectroscopic Evidence of Pyridine Adsorption on Rutile and Anatase Surfaces.....	193
IV. Summary.....	198

V. Acknowledgement.....	200
Chapter 10 References.....	200
Chapter 11 - Vibrational Spectroscopic Observation of Weakly-Bound	
Adsorbed Molecular Oxygen on Powdered TiO₂.....	203
I. Introduction.....	204
II. Methodology.....	205
III. Results.....	206
A. ¹⁶ O ₂ Adsorption on TiO ₂	206
B. Isotopic Study of ¹⁸ O ₂ Adsorbed on TiO ₂	209
C. ¹⁶ O ₂ Displacement by CO and CO ₂ on TiO ₂	210
D. Influence of Pre-Adsorbed H ₂ O on ¹⁶ O ₂ Adsorption.....	214
IV. Discussion.....	218
A. Nature of the IR Active O ₂ Species.....	218
B. Confirmation of the Weakly-Bound Oxygen Model Using a Water Modified TiO ₂ Surface.....	221
C. Displacement of Surface-Bound Oxygen and Weakly-Bound Oxygen	222
V. Summary.....	222
VI. Acknowledgement.....	223
Chapter 11 References.....	224
Part III. Appendices.....	227
 Appendix A — Geometry of the Cell — Position of the Sample, Width of the	
IR Beam, and the Calibration and Installation of the Fiber	
Optics.....	228

A.1. The Position of the Sample Center.....	228
A.2. The Width of the IR Beam at the Sample Position and Its Relationship to the Aperture Size.....	230
A.3. Calibration and Installation of the Ultraviolet Fiber Optics.....	233
a. Calibration of the UV Lamp and the Fiber Optics.....	233
b. Installation of the Fiber Optics.....	236
Appendix B - Maintenance of the Parker Purging Gas Generator	238
Appendix C - Gas Line Volume Calibration.....	241
Appendix D - List of Publications.....	244

Acknowledgement

The past five years here at the University of Virginia was truly a leap in my life. I could see my own development because the changes are obvious. The tremendous help and love I receive constantly is the sole reason accounting for what I have become today. It is very clear to me that I absolutely need to express my love and appreciation out loud to those people.

My advisor, John, is a wonderful mentor. He is a great storyteller and holds a project meeting with me almost every week, for five years. Aside from keeping me on the right track, topics during the meeting drift quite often to the history of the field of surface science, to the way scientific knowledge was acquired and developed, to the frontier and the possibilities of the future in science. As a young graduate student parachuted into the field, I have gained extremely lots of nutrients from those mini-lectures, from a thoughtful and experienced professor like John. Knowing that I am interested in pursuing an academic career, he sent me to scientific conferences and introduced me to distinguished researchers from all over the world when possible. He also put effort into assuring I live a happy life outside work, as a foreign student. My appreciation to John cannot fit in a short acknowledgement. I'm truly proud and grateful to be a Yates production. I am lucky.

Many thanks to my collaborators, Professor Matt Neurock, Dr. Corneliu Buda, and Dr. Wenjie Tang. I finished most of my projects with Team Neurock's help on theoretical simulations. We worked so closely that I was asked a couple of times in conferences whether I was jointly trained by Matt and John. It is incredibly nice to have world-class collaborators right next door. I enjoyed being able to run upstairs to Corneliu and Wenjie's office and have a discussion with visual aids on their computers. Thank you for

your patience to my naive questions. Although extremely busy, Matt spends a lot of time on our manuscripts and wouldn't let one flawed sentence slip. This attitude is going to stay with me for a long time. It was a wonderful experience.

I thank all the Yates group members, for setting up such a cozy and caring working environment that encouraged discussion and help-seeking. Special thanks to Dr. Sunhee Kim who trained me very well and gave me a jumpstart, and to Dr. Zhen Zhang who calmly and patiently helped me through my nerve-racks.

I need to thank my dear friend, lab mate, and sister, Lynn Mandeltort. We entered the Yates lab together and supported each other through the years. She has the most wonderful personality and takes great care of people around her. With that said, I believe her sister-like love and help to me was special. Her family embraced me from the beginning. I consider myself adopted by Mom Nancy and Dad Marc in the States. Thank you, Lynn, for giving me a feel of family in the States. I'm not an only child anymore.

My husband Chris is a crucial factor in my accomplishment. Other than making sure I'm happy everyday, he is also my grammar editor. He is the reason behind my "perfect English" from the beginning. (Big secret out!) He started proofreading for me on my very first manuscript, as a favor he did to make his date happy. Then that date became his fiancé and eventually wife. So the "volunteer" scientific editing job never ended. Now, after 5 years of living in the U.S., my writing is finally 90% American-like (judged by Chris), and it's time to give him the credit back.

Last but not the least, I thank my family. My Mom Dr. Ming Cao (W[^]) and Dad Dr. Zhi Wang (1[^]) gave me unlimited support. Knowing that there is somewhere warm and loving that I can always return to is the deepest comfort in my heart. Making you proud is my ever-lasting motivation. My in-laws, the Green family, took me in as their

own the first day they met me. Only when surrounded by loves from my family can I move so steadily forward. Thank you all for loving me.

Chapter 1

Introduction.

I. Using Gold as a Heterogeneous Catalyst.

Gold is the 79th element on the periodic table. It is a group 11 metal with an electron structure of $[\text{Xe}]4f^{14}5d^{10}6s^1$. Bulk gold plays an important role in society as a precious metal used for currency, jewelry, and as a conductor in semiconductor devices, together with two other stable metals, copper and silver, also from group 11. However, until the 1980s, gold was the only coinage metal that had not been demonstrated to be a catalyst.¹

Early attempts at using gold as a catalyst were carried out using gold wire or gauze. The first documented catalytic reaction on gold was from Bone and Wheeler in December 1904, to oxidize H_2 by O_2 on gold gauze.² A small rate of reaction was observed. It was quickly realized that bulk gold is not a good catalyst compared to other transition metals.^{1,3}

In 1970, Cha and Parravano reported that Au nanoparticles supported by MgO could catalyze oxygen exchange between CO and CO_2 above 300°C.⁴ Later in 1973, Bond and Sermon synthesized Au/ SiO_2 and Au/ $\gamma\text{-Al}_2\text{O}_3$ catalysts by impregnation and found them to be active for olefin hydrogenation starting at 100°C.^{5,6} Ozin et al. also demonstrated that single Au atoms condensed in a mixed CO and O_2 matrix could catalyze the formation of CO_2 at 30-40 K.⁷ These studies hinted at the special properties of supported gold nanoparticles as a catalyst and formed the foundation for modern gold catalysis.

The real acceleration of gold catalysis research began circa 1987, following the pioneering work by Haruta *et al.*, in which small gold nanoparticles supported by transition metal oxides were found to catalyze CO oxidation by O_2 at temperatures far

below 0°C.^{8,9} The economic incentive for developing a room temperature CO oxidation catalyst is enormous, since CO removal is beneficial for the environment and for industrial processes producing CO₂ or H₂.⁸ As a result, much effort over the last 25 years has been directed toward understanding the nano-sized gold catalysts to improve performance.

It was later realized that Haruta's success in gold catalyzed CO oxidation lies in the appropriate choice of support and synthesis method: using reducible transition metal oxides such as TiO₂, CeO₂ and Co₃O₄ as the support works better than using conventional non-reducible supports such as SiO₂ and Al₂O₃;¹⁰⁻¹² supported gold nanoparticles made from coprecipitation (COPPT) and deposition-precipitation (DP) are more active than those made by the classical method of impregnation, due to Au's lower melting point and low affinity to oxides (compared to Pd and Pt).¹³⁻¹⁵ As the interest in gold catalysis increases, more reactions catalyzed by Au nanoparticles were developed, such as partial oxidation of olefins,¹⁶ the water-gas-shift reaction ($\text{CO} + \text{H}_2\text{O} \rightarrow \text{CO}_2 + \text{H}_2$),¹⁷ ethyne hydrochlorination,¹⁸ propene epoxidation,¹⁹ and others.²⁰ Interestingly (but maybe unfortunately), it was found that different catalytic reactions are favored by different gold nanoparticle properties, such as nanoparticle size, type of support, and methods of synthesis. For example, the direct synthesis of H₂O₂ from H₂ and O₂ has better yields on SiO₂- and Al₂O₃-supported Au nanoparticles compared to TiO₂- and CeO₂-supported;^{21,22} liquid phase glycerol oxidation is insensitive to the type of support and the Au nanoparticle size (below 180 nm).²³⁻²⁵ As a result, the amount of literature on Au catalysts is overwhelming yet inconclusive in many aspects. CO oxidation remains the most studied reaction on Au catalysts, due to its simplicity and its importance in various applications. As such, the latter part of this section will focus on the landmark

experiments carried out on CO oxidation that revealed the special properties of supported nano-sized Au, with emphasis on TiO₂, as the support.

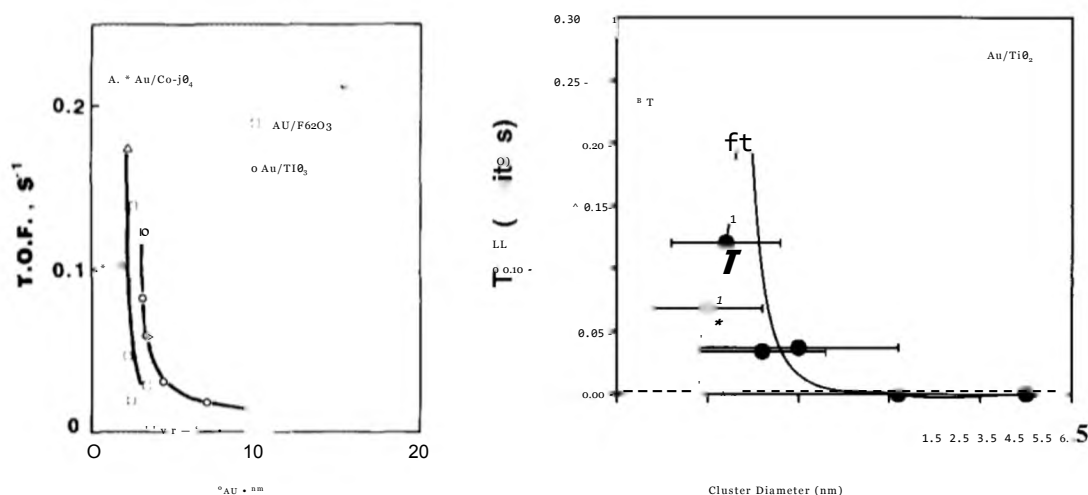


Figure 1.1. Plots of supported Au nanoparticle catalytic activity (turnover frequency, TOF) for CO oxidation as a function of particle size. A is reprinted from ref. 9 with permission; B is reprinted from ref 26 with permission.

It was first thought that the catalytic activity of gold originated from the dimensions (particle size and thickness) of the nanoparticles. Haruta *et al.* first reported,⁹ and Goodman *et al.* later confirmed,²⁶ that the CO oxidation activity on TiO₂ or other oxide supported Au nanoparticles was maximized when the particle size was around 3 nm in Au diameter, as shown in Figure 1.1. Using scanning tunneling microscopy/spectroscopy (STM/STS), the Goodman team reported a quantum effect, where Au clusters smaller than 3 nm showed non-metallic properties, especially when the clusters were below 3-atom-layer-height.^{26,27} The most active catalyst supports, preferably reducible transition metal oxides such as TiO₂, were thought to serve as an oxygen stabilizer or reservoir, since the Au-O₂ interaction is known to be poor.

However, Bollinger and Vannice converted a batch of catalytically inactive Au powder of 10 pm diameter into active catalysts for CO oxidation by depositing TiOx nanoparticles on the inactive Au powder.^{28,29} Rodriguez et al. confirmed this observation by depositing TiOx or CeOx clusters on a Au(rn) single crystal surface and found decent catalytic activity towards the water-gas-shift reaction.³⁰ These results indicate that the quantum size effect of small Au nanoparticles may not be an important factor for gold catalysis, and that the support plays a more important role than previously recognized.

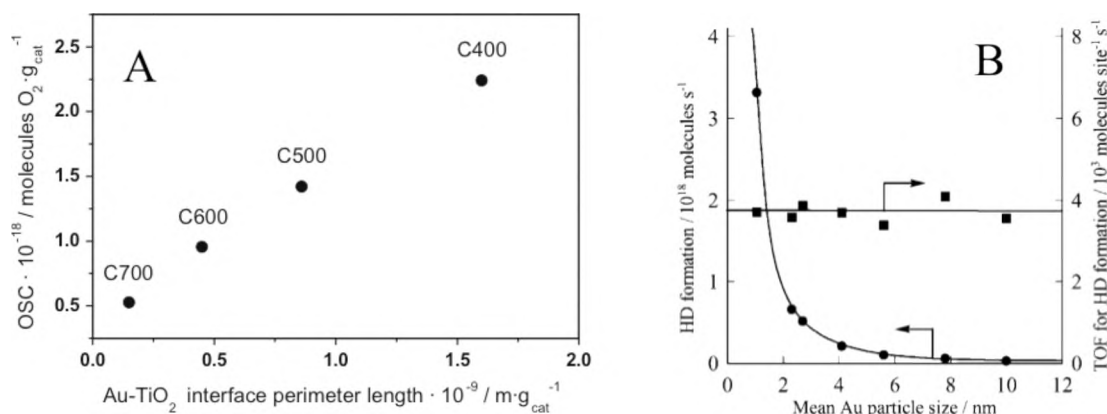


Figure 1.2. Plots showing that the Au/TiO₂ catalytic activity is proportional to the length of the Au-Ti interfacial perimeter. A, for CO oxidation reaction, reprinted from ref. 33 with permission; B, for H₂-D₂ exchange experiment, reprinted from ref. 34 with permission.

Based on the observations that i) Au or support oxide nanoparticles alone do not have catalytic activity for CO oxidation, and ii) Au/TiO₂ and TiOx/Au catalysts both have good performance, Bond and Thompson proposed in 2000 that the activity for CO oxidation probably originates from the interface between the two materials, where Au and the support meet.³¹ They emphasized that the CO oxidation was aided by the hydroxyl groups located on the support, near the periphery of Au nanoparticles. This view was well accepted without experimental proof,^{1,16,32} until Behm *et al.* indirectly linked the

catalytic activity for CO oxidation to the total length of the perimeter of the Au particles at the Au/TiO₂ interface, as shown in Figure 1.2A.³³ Fujitani et al. also demonstrated that for an H-D exchange reaction, the turnover frequency (TOF) is proportional to the total length of the perimeter interface of Au/TiO₂, as shown in Figure 1.2B.³⁴ They also demonstrated that a reverse TiOx/Au catalyst had comparable catalytic activity towards the H-D exchange reaction as the classic Au/TiO₂ catalyst.³⁴ Besides indirect experimental evidences, theory also predicted that the interfacial sites between the Au and TiO₂ support can be the key to activate oxygen.^{35,36}

This project utilizes operando [*operando: study the catalyst in it's working state*] transmission IR spectrometry to provide direct observation of the localized catalytic activity zone at the dual-perimeter region of the Au/TiO₂ catalyst. Part I of this thesis focuses on the mechanistic studies of several oxidation reactions catalyzed by the Au/TiO₂ catalyst.

We first discovered that Au/TiO₂-catalyzed CO oxidation occurred at cryogenic temperatures (~120 K), in which the CO molecules adsorbed on the TiO₂ support were the only mobile species to participate in the reaction (Chapter 3). The fact that the tightly bound CO molecules on the Au nanoparticles were unreactive strongly suggested that the reaction was localized at the perimeter of the Au nanoparticles. Density functional theory (DFT) calculations revealed that the O-O bond scission was activated at the dual perimeter sites where a Au atom and a Ti⁴⁺ ion work together.

Then we show that the special dual-perimeter sites on the Au/TiO₂ catalyst can be used to oxidize hydrogen to form water, where the H-H bond is also activated (Chapter 4). A Ti-OOH intermediate was formed and an early transition state was measured by the deuterium kinetic isotope effect (DKIE), and confirmed by DFT calculations.

Following the recognition of O-O bond scission and H-H bond scission at the dual perimeter sites, we then studied the partial oxidation of acetate/TiO₂ to produce the gold ketenylidene species ($\text{Au}_2=\text{C}=\text{C}=\text{O}$), where C-H bonds in $\text{CH}_3\text{COO}/\text{TiO}_2$ were activated with the help of O atoms formed at the Au-Ti⁴⁺ dual perimeter (Chapters 5 and 6). Besides the novel detection of the surface ketenylidene species by IR, the reactant and product actually switched adsorption sites during the reaction, clearly implicating once again the role of active sites at the localized dual-perimeter sites of the Au/TiO₂ catalyst.

In addition to pinpointing the active sites on the Au/TiO₂ catalyst for oxidation reactions, it was also of interest to identify the charge state of active Au species, since the literature has shown mixed results using different detection techniques.³⁷⁻⁴¹ We have found that extensive pre-oxidation of the Au/TiO₂ sample in O₂ at elevated temperatures generated Au^{s+} sites that can be detected by a distinctive CO/Au^{s+} vibrational frequency (20 cm⁻¹ above the frequency from CO/Au⁰). These Au⁵⁺/TiO₂ sites retarded the 120 K-CO oxidation reaction by 22 fold, indicating an inhibition effect of the positive charge on Au on the catalytic activity (Chapter 7).

II. Adsorption, Diffusion, and Desorption Properties of TiO₂ and MgO.

Metal oxides, especially metal oxide powders, are popular supports for various industrial metal or metal oxide catalysts. Their acidic or basic surface binding sites, plus large surface area, make them good candidates to disperse and stabilize metal or metal oxide nanoparticle catalysts.^{42,43}

The intrinsic surface properties of the oxide support influence the physical and chemical behavior of the metal catalyst of interest, such as gold. For model catalytic studies using metal oxide supported precious metals, the concept of strong metal support interaction (SMSI) was proposed and has been well documented since the late 1970s.^{44,45}

The SMSI effect was also reported for Au catalysts supported by TiO₂,⁴⁶ where the wetting of the TiO₂ surface by Au at 800 K in a reducing environment and the de-wetting of the support and the sintering of the Au in an oxidation environment were observed.²⁶

The surface defect sites on the support were shown to contribute significantly to the interaction between Au nanoparticles and the support. Both experiments and theoretical calculations indicate that the electron rich F-centers on MgO and TiO₂ surfaces are crucial for Au catalytic activity.^{35'40'41'47} Scanning tunneling microscope measurements also observed Au cluster nucleation at the defect sites of TiO₂(110) single crystals⁴⁸, and that Au atoms deposited on a thin MgO film were charged.⁴⁹ The subtle electronic flow between the support and the Au nanoparticles is often suspected to be involved in producing catalytic activity.

In addition to dispersing and stabilizing the Au nanoparticles, the high surface area metal oxide support can also serve as a reservoir/sponge for reactants and products. As a result, understanding the adsorption, diffusion, and desorption properties of the support are valuable to elucidating the molecular details of catalysis. The issue is particularly important because Au is known for its weak adsorption ability, and the reactants need to reach the catalytically active region located at the Au-support interface.

Metal oxide surface adsorption, diffusion, and desorption properties are influenced by many parameters, such as crystal structure, surface defect sites and density, surface acidity, and the presence of surface hydroxyl groups. Part II of this project studied the surface adsorption, diffusion, and desorption properties of two popular metal oxide powders, TiO₂ and MgO, as models for transition (reducible) metal oxides and non-reducible metal oxides. The surface acidity and diffusion/desorption properties of the MgO and TiO₂ powdered material were studied using transmission IR spectroscopy of adsorbed pyridine as a weak-basic probe molecule. The diffusion and desorption of

pyridine from MgO and TiO₂ surfaces were found to occur by means of a mobile precursor model. This model is well known for molecular diffusion/desorption on single crystal surfaces, but was still foreign for diffusion/desorption through powdered materials.^{50,51} The influence of surface defect sites and surface hydroxyl groups on pyridine/MgO diffusion/desorption were studied, where pyridine was found to bind more strongly to the surface defect sites on the MgO surface (Chapter 8), and surface hydroxyl groups (Mg-OH) generated from water vapor were found to dramatically accelerate pyridine diffusion/desorption (Chapter 9).

The differences in pyridine diffusion/desorption on anatase and rutile TiO₂ surfaces were also studied (Chapter 10). It was found that the diffusion activation energy for pyridine/anatase (90 kJ/mol) was more than double the diffusion activation energy for pyridine/rutile (36 kJ/mol). This difference was confirmed by DFT calculations.

Since the TiO₂ support is proposed to be an oxygen reservoir during CO oxidation on a Au/TiO₂ catalyst, the interaction between O₂ and TiO₂ was investigated at cryogenic temperature. A weakly bound surface O₂ species with vibrational frequency at 1550 cm⁻¹, identical to the Raman frequency of O₂(g), was observed by IR (Chapter 11). The adsorption enthalpy of the weakly-bound O₂/TiO₂ species was calculated to be between -16 and -21 kJ/mol. The interaction between the TiO₂ surface and the weakly bound O₂ species was easily disturbed by the co-adsorption of CO, CO₂ and H₂O.

III. Using Operando FTIR to Monitor Heterogeneous Surface Catalytic Processes.

Heterogeneous catalytic processes occur at the surfaces of the catalysts, where adsorbed reactants are activated.^{43,52} Various surface characterization techniques were developed throughout the exploration of the origin of catalytic activities, since the

founding of the field of surface science by Irving Langmuir in the beginning of the 20th century.^{53,54} Infrared spectroscopy was among the first technique developed (~1910 by Coblenz⁵⁵ to study water adsorption on minerals) and then later utilized to characterize catalyst surfaces and the adsorption species on the surfaces (by Terenin *et al.* ~1940 to study adsorbed molecules on oxides).^{52,55-62} The addition of the Fourier transformation technique to IR spectroscopy in the 1960s boosted IR instrumentation to one of the most widely applied spectroscopic techniques.^{57,63}

R. van Santen roughly divided the research in heterogeneous catalysis into three categories:⁶⁴ 1) macroscopic study, which concerns the engineering of the industrial reactor and the bulk quality of the catalyst; 2) mesoscopic study, which explores the kinetics of catalytic reactions and the activation of the catalysts; 3) microscopic study, which reveals the mechanism and atomic-level details of the catalytic system. Surface scientists are most interested in the microscopic portion of catalytic research, where the goal is to understand the structure of the catalyst surface, how reactants adsorb and activate at the surface, and the mechanism of the catalytic reactions. Only with this information, can we manipulate catalysts in a macroscopic manner. Infrared spectroscopy is a technique that provides both microscopic and mesoscopic information, thus linking the fundamental studies to the real catalytic world.

For microscopic studies, IR can be used to probe the catalyst surface properties, and the reactant adsorption configuration.⁶¹⁻⁶³ Figure 1.3 shows IR spectra of the C-O stretching frequencies of gas phase CO, CO adsorption on TiO₂, CO adsorption on Au⁰/TiO₂, and CO adsorption on Au⁵⁺/TiO₂. Clear discrimination between the gas phase and the 3 different adsorption sites of u(CO) are observed. This is because the electronic interaction between CO and the adsorbent during bonding influences the intrinsic

strength and force constant of the C-O bond, causing a shift in $\nu(\text{CO})$. Different adsorbents interact with CO differently, resulting in distinctive $\nu(\text{CO})$ frequencies.

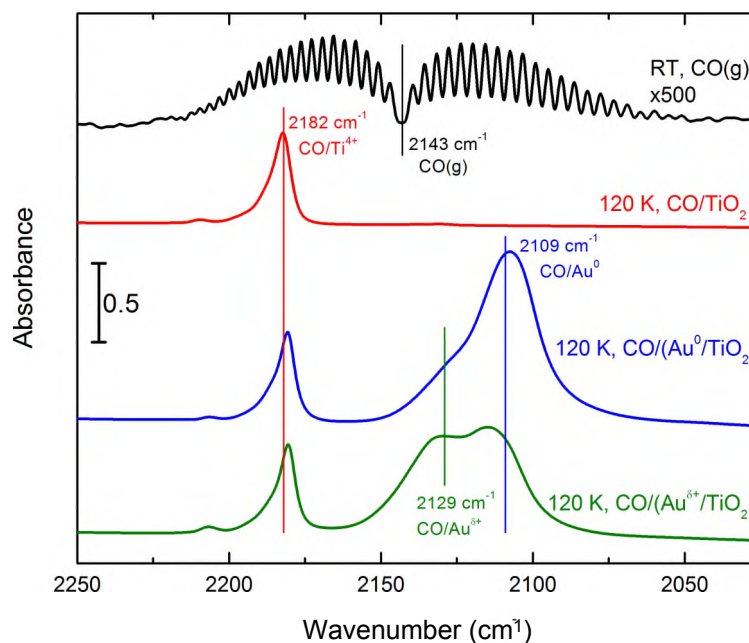


Figure 1.3. IR spectra of room temperature gas phase CO showing the resolved vibration-rotation lines (black), CO adsorbed on TiO_2 at 120 K (red), CO adsorbed on Au^0/TiO_2 at 120 K (blue), and CO adsorbed on $\text{Au}^{5+}/\text{TiO}_2$ at 120 K. The $\text{Au}^{5+}/\text{TiO}_2$ sample is produced by heating the Au^0/TiO_2 in $\text{O}_2(\text{g})$ at 473 K.

IR frequencies of adsorbed molecules can also provide information of bonding configurations. Figure 1.4 shows the pioneering work done by Yates and Garland, of a CO/Ni adsorption configuration assignment.⁶⁵ At room temperature and low CO coverage, only linearly adsorbed CO-Ni species were observed (species C), while at higher CO coverages, less strongly bound bridging CO-Ni₂ species could be seen (species A).⁶⁵ Etching away the Ni by making $\text{Ni}(\text{CO})_4(\text{g})$ showed that the dispersed Ni sites were produced (species E) at the expense of the crystalline Ni sites.⁶⁵

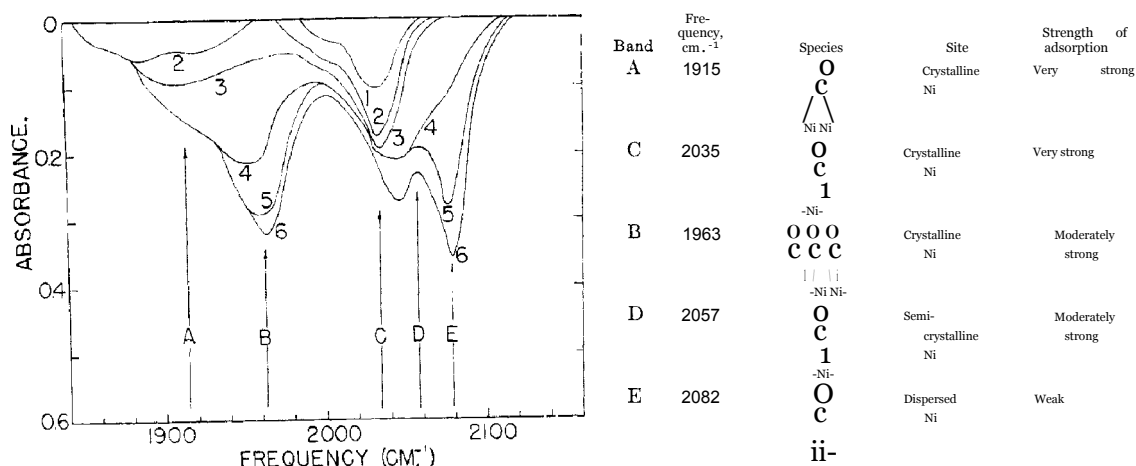


Figure 1.4. IR spectra of room temperature CO adsorption and band assignment on a 25% Ni nanoparticle supported by alumina. Spectrum 1, 1.7×10^{-4} mm. CO pressure; spectrum 2, 2.0×10^{-4} mm.; spectrum 3, 3.5×10^{-4} mm.; spectrum 4, 2.3×10^{-2} mm.; spectrum 5, 1.2 mm; spectrum 6, 1.2 mm. after 12 hours. Reprinted from ref. 65 with permission. Copyright (1961) American Chemical Society.

The mid-IR source employed in IR spectrometry usually covers a photon energy range of 400-4000 cm^{-1} . This radiation can be used to probe molecules in all phases, including gas, liquid, and solid. As a result, IR can be used to monitor catalytic reactions *in situ*, under realistic reaction conditions (compared to other probe sources that only work in vacuum, such as electrons). According to the Lambert-Beer Law, a linear relationship exists between the absorption of the incident light and the concentration of the absorbing species. Thus, the relative concentration of a specific surface-adsorbed species can be deduced from the area of the signature IR absorption band corresponding to one isolated vibrational mode of that species. Using this strategy, IR spectroscopy can be used to gain mesoscopic information of a catalytic system, such as reaction kinetics. Inorganic chemists have used the loss of $\nu(\text{CO})$ band area in transmission-absorption IR measurements to follow the kinetics of ligand exchange reactions such as $\text{M}(\text{CO})_6 + \text{L} \rightarrow \text{M}(\text{CO})_5\text{L} + \text{CO}$ since the mid-1960s,⁶⁶ and the exchange of isotopic CO into a gas-phase metal carbonyl was first investigated in 1961.⁶⁷

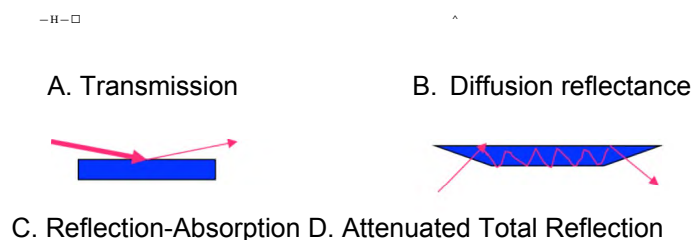


Figure 1.5. Scheme of common IR spectroscopy techniques for studying adsorbed species including A. transmission, B. diffusion reflectance, C. reflection-absorption, and D. attenuated total reflection.

According to the properties of the sample of interest, IR spectroscopy is usually carried out in the following four ways: transmission IR, diffuse reflectance IR, reflection-absorption IR, and attenuated total reflection (ATR) IR, as shown in Figure 1.5. Transmission IR can be used when the bulk of the sample absorbs IR weakly. Samples for transmission IR measurements need to be pressed into self-supported wafers, or supported on an inert mesh or wafer holders. To avoid pressing of the sample, diffuse reflectance IR can be used instead, where the sample can be measured as a loose powder. If the sample does not transmit IR, such as metal single crystals, reflection-absorption IR is employed. Finally, ATR-IR is used to study films or self assembled monolayers (SAMs), where each reflection only penetrates a few micrometers into the sample. The information gained from different IR spectroscopies is similar. Since most of the catalysts used in heterogeneous catalysis are nanoparticles, transmission IR is a convenient choice.

In this project, transmission IR was used to characterize the catalyst surface, as well as to probe the oxide support properties. It was also used to monitor the diffusion/desorption kinetics of reactants through the supports, and the reaction kinetics during *in situ* catalytic reactions.

Chapter 1 References:

1. Haruta, M. *CATTECH* 2002, 6, 102.
2. Bone, W. A.; Wheeler, R. V. *Philosophical Transactions of the Royal Society of London A* 1906, 206, 1.
3. Hammer, B.; Norskov, J. K. *Nature* 1995, 376, 238.
4. Cha, D. Y.; Parravano, G. *Journal of Catalysis* 1970, 18, 200.
5. Bond, G.; Sermon, P. *Gold Bulletin* 1973, 6, 102.
6. Bond, G. C.; Sermon, P. A.; Webb, G.; Buchanan, D. A.; Wells, P. B. *Journal of the Chemical Society, Chemical Communications* 1973, 444b.
7. Huber, H.; McIntosh, D.; Ozin, G. A. *Inorganic Chemistry* 1977, 16, 975.
8. Haruta, M.; Kobayashi, T.; Sano, H.; Yamada, N. *Chemistry Letters* 1987, 2, 405.
9. Haruta, M.; Tsubota, S.; Kobayashi, T.; Kageyama, H.; Genet, M. J.; Delmon, B. *Journal of Catalysis* 1993, 144, 175.
10. Overbury, S. H.; Ortiz-Soto, L.; Zhu, H.; Lee, B.; Amiridis, M.; Dai, S. *Catalysis Letters* 2004, 95, 99.
11. Haruta, M. *Catalysis Today* 1997, 36, 153.
12. Schubert, M. M.; Hackenberg, S.; Veen, A. C. v.; Muhler, M.; Plzak, V.; Behm, R. J. *Journal of Catalysis* 2001, 197, 113.
13. Haruta, M. *Gold Bulletin* 2004, 37, 27.
14. Bamwenda, G. R.; Tsubota, S.; Nakamura, T.; Haruta, M. *Catalysis Letters* 1997, 44, 83.
15. Zanella, R.; Giorgio, S.; Henry, C. R.; Louis, C. *Journal of Physical Chemistry B* 2002, 106, 7634.
16. Hutchings, G. J. *Catalysis Today* 2005, 100, 55.
17. Andreeva, D.; Idakiev, V.; Tabakova, T.; Andreev, A. *Journal of Catalysis* 1996, 158, 354.
18. Hutchings, G. *Gold Bulletin* 1996, 29, 123.
19. Huang, J.; Haruta, M. *Research on Chemical Intermediates* 2012, 38, 1.
20. Bond, G. C.; Louis, C.; Thompson, D. T. *Catalysis by Gold*; Imperial College Press: London, 2006; Vol. 6.
21. Ishihara, T.; Ohura, Y.; Yoshida, S.; Hata, Y.; Nishiguchi, H.; Takita, Y. *Applied Catalysis A: General* 2005, 291, 215.

22. Landon, P.; Collier, P. J.; Carley, A. F.; Chadwick, D.; Papworth, A. J.; Burrows, A.; Kiely, C. J.; Hutchings, G. J. *Physical Chemistry Chemical Physics* 2003, 5, 1917.
23. Zope, B.; Davis, S.; Davis, R. *Topics in Catalysis* 2012, 55, 24.
24. Zope, B.; Davis, R. *Topics in Catalysis* 2009, 52, 269.
25. Zope, B. N.; Hibbitts, D. D.; Neurock, M.; Davis, R. J. *Science* 2010, 330, 74.
26. Valden, M.; Lai, X.; Goodman, D. W. *Science* 1998, 281, 1647.
27. Chen, M. S.; Goodman, D. W. *Science* 2004, 306, 252.
28. Liu, Z. M.; Vannice, M. A. *Catalysis Letters* 1997, 43, 51.
29. Bollinger, M. A.; Vannice, M. A. *Applied Catalysis B: Environmental* 1996, 8, 417.
30. Rodriguez, J. A.; Ma, S.; Liu, P.; Hrbek, J.; Evans, J.; Perez, M. *Science* 2007, 318, 1757.
31. Bond, G.; Thompson, D. *Gold Bulletin* 2000, 33, 41.
32. Meyer, R.; Lemire, C.; Shaikhutdinov, S. K.; Freund, H.-J. *Gold Bulletin* 2004, 37, 72.
33. Kotobuki, M.; Leppelt, R.; Hansgen, D. A.; Widmann, D.; Behm, R. J. *Journal of Catalysis* 2009, 264, 67.
34. Fujitani, T.; Nakamura, I.; Akita, T.; Okumura, M.; Haruta, M. *Angewandte Chemie* 2009, 48, 9515.
35. Wang, J.; Hammer, B. *Topics in Catalysis* 2007, 44, 49.
36. Laursen, S.; Linic, S. *Physical Chemistry Chemical Physics* 2009, 11, 11006.
37. Kung, M. C.; Davis, R. J.; Kung, H. H. *The Journal of Physical Chemistry C* 2007, 111, 11767.
38. Fu, Q.; Saltsburg, H.; Flytzani-Stephanopoulos, M. *Science* 2003, 301, 935.
39. Fierro-Gonzalez, J. C.; Guzman, J.; Gates, B. C. *Topics in Catalysis* 2007, 44, 103.
40. Vijay, A.; Mills, G.; Metiu, H. *Journal of Chemical Physics* 2003, 118, 6536.
41. Yan, Z.; Chinta, S.; Mohamed, A. A.; Fackler, J. P.; Goodman, D. W. *Journal of the American Chemical Society* 2005, 127, 1604.
42. *Metal Oxides: Chemistry and Applications*; Fierro, J. L. G., Ed.; CRC Press: Boca Raton, 2006.
43. van Santen, R. A.; Neurock, M. *Molecular Heterogeneous Catalysis*; Wiley-VCH: Weinheim, 2006.
44. Tauster, S. J.; Fung, S. C.; Garten, R. L. *Journal of the American Chemical Society* 1978, 100, 170.

45. Tauster, S. J.; Fung, S. C. *Journal of Catalysis* 1978, 55, 29.
46. Goodman, D. *Catalysis Letters* 2005, 99, 1.
47. Yang, Z.; Wu, R.; Goodman, D. W. *Physical Review B* 2000, 61, 14066.
48. Matthey, D.; Wang, J. G.; Wendt, S.; Matthiesen, J.; Schaub, R.; Laegsgaard, E.; Hammer, B.; Besenbacher, F. *Science* 2007, 315, 1692.
49. Sterrer, M.; Risse, T.; Martinez Pozzoni, U.; Giordano, L.; Heyde, M.; Rust, H.-P.; Pacchioni, G.; Freund, H.-J. *Physical Review Letters* 2007, 98, 096107.
50. Cassuto, A.; King, D. A. *Surface Science* 1981, 102, 388.
51. Weinberg, W. H. *Kinetics of Interface Reactions*; Springer-Verlag: New York and London, 1986.
52. Niemantsverdriet, J. W. *Spectroscopy in Catalysis: An Introduction*; VCH: Weinheim, New York, 1993.
53. Langmuir, I. *The Collected Works of Irving Langmuir*; Pergamon: Oxford, 1960.
54. Yates Jr, J. T. *Surface Science* 1994, 299-300, 731.
55. Coblenz, W. W. *Journal of the Franklin Institute* 1911, 172, 309.
56. Eischens, R. P. *Science* 1964, 146, 486.
57. Ryczkowski, J. *Catalysis Today* 2001, 68, 263.
58. Yang, C.; Garl, C. W. *The Journal of Physical Chemistry* 1957, 61, 1504.
59. Powell, D. B.; Sheppard, N. *Spectrochimica Acta* 1958, 13, 69.
60. Hair, M. L. *Infrared Spectroscopy in Surface Chemistry*; Marcel Dekker, Inc.: New York, 1967.
61. Sueřaka, W.; J. T. Yates, J. *Surface Infrared and Raman Spectroscopy: Methods and Applications*; Plenum Press: New York and London, 1995.
62. *Vibrational Spectroscopy of Molecules on Surfaces*; John T. Yates, J.; Madey, T. E., Eds.; Plenum Press: New York and London, 1987.
63. *Vibrational Spectroscopies for Adsorbed Species*; Bell, A. T.; Hair, M. L., Eds.; American Chemical Society: Washington, DC, 1980.
64. van Santen, R. A. *Theoretical Heterogeneous Catalysis*; World Scientific: Singapore, 1991.
65. Yates, J. T.; Garland, C. W. *The Journal of Physical Chemistry* 1961, 65, 617.
66. Graham, J. R.; Angelici, R. J. *Inorganic Chemistry* 1967, 6, 2082.

67. McDowell, R. S.; Horrocks, J. W. D.; Yates, J. T. *The Journal of Chemical Physics* 1961, 34, 530.

Chapter 2

Instrumentation and Catalyst Preparation.

I. Instrumentation.

The vacuum transmission IR cell employed in this project was developed on the basis of an earlier cell designed by Yates *et al.*,¹ which is now widely used throughout the field. A top-view scheme of the cell is shown in Figure 2.1. The base pressure of the stainless steel cell after bakeout is 1×10^{-6} Torr, achieved with a 55 L/s (N_2) turbo-molecular pump which can be isolated from the cell by closing a gate valve. The FTIR beam generated from a commercial Bruker TENSOR 27 spectrometer is focused by four external optical mirrors to pass through the center of the IR cell and to reach the external l - N_2 cooled MCT detector. The cell has two differentially pumped KBr windows for IR beam transmission (400-4000 cm^{-1} transparent). A mechanical pump carries out the differential pumping of the space between the two Viton O-ring window seals. The cell pressure is monitored by a MKS I-MAG cold cathode ionization gauge for low pressure readings (10^{-6} - 10^{-3} Torr) and a MKS Baratron capacitance manometer for high pressure readings (0.001-100 Torr). A quadrupole mass spectrometer (QMS) is connected to the cell for gas analysis, and can be isolated from the cell by closing a gate valve.

The IR beam is aligned to focus at the center of the cell, where the samples are mounted. Detailed calibration of the position of the optics and the samples can be found in Appendix A. The samples are held on a l - N_2 cooled reentrant Dewar with Z-direction motion. A closeup view of the sample holder is shown in Figure 2.2. The samples were pressed into 7 mm diameter spots on a piece of tungsten grid by a

hydraulic press, with pressures between 33,500 to 100,000 psi. The 0.051 cm thick tungsten grid has 0.22 mm x 0.22 mm windows (~ 1370 windows/cm²) that are photo-etched in a tungsten foil, each small window holding a portion of the sample.

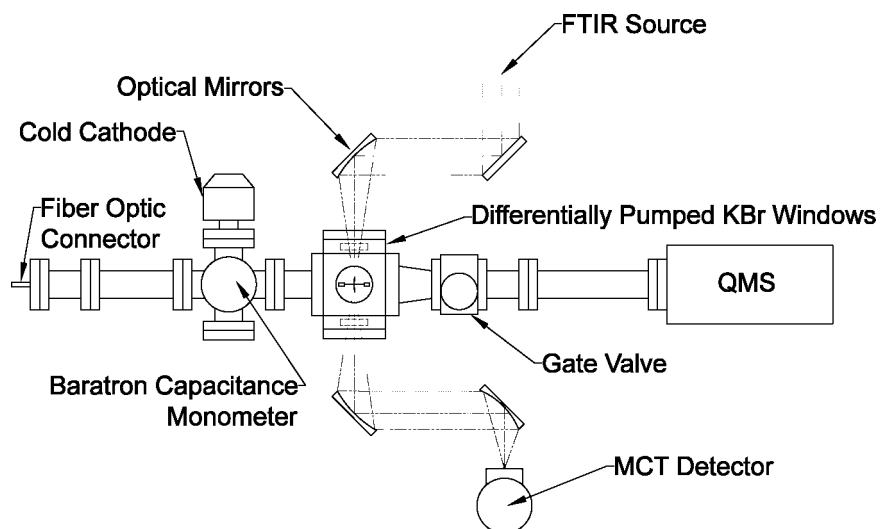


Figure 2.1. Top view scheme of the high vacuum transmission FTIR cell.

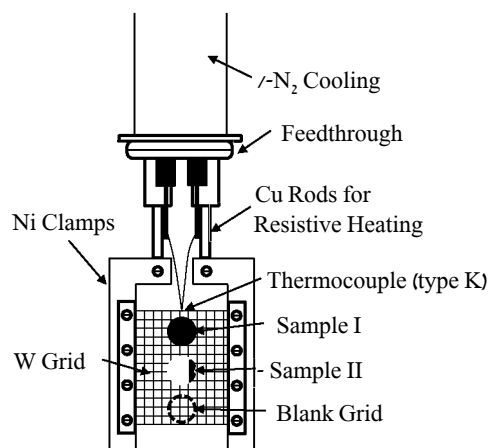


Figure 2.2. A closeup view of the sample holder.

Each sample spot holds approximately 0.005 g of material. The tungsten grid can hold up to two samples at one time as shown in Figure 2.2. As a result, a catalyst and a reference sample can be monitored by IR in the same experiment by moving the manipulator in the Z-direction.

The tungsten grid is mounted between a pair of nickel clamps which are connected to copper rods from the feed-through for efficient electrical heating and cooling. This arrangement generates no vertical temperature gradient upon heating.¹ A type K thermocouple that reads the sample temperatures to 0.1 K resolution is welded on the top of the tungsten grid, directly above the samples. The thermocouple and the electrical power supply for the resistive heating are connected to a National Instruments Data Acquisition (DAQ) card. The DAQ card is controlled by a LabVIEW program, using the proportional-integral-derivative (PID) method to linearly manipulate and program the sample temperature accurately between 85 and 1200 K.

The IR source and the MCT detector together with the entire IR beam pathway are purged constantly by H₂O- and CO₂- free air. Information about the purge air generator can be found in Appendix B. In order to eliminate the influence of the gas phase and the tungsten grid, a reference spectrum taken through the gas phase and the empty tungsten grid was subtracted from every spectrum recorded through the sample under the same conditions.

Although not used in this project, the cell is also equipped with fiber optics, as shown in Figure 2.1. The light source is perpendicular to the IR beam. When the sample is installed diagonally in the cell (45° to the IR and the light source), transmission IR spectroscopy can be used to measure photon-induced activities *in situ*. A detailed description of the fiber optics installation and calibration can be found in Appendix A.

Reactants and probe molecules are introduced into the cell through a gas line manifold. The gas line pressure is measured by a separate capacitance manometer (0.1-1000 Torr). The gas-line is evacuated with the turbo-molecular pump as well. The volumes of the gas-line sections are discussed in Appendix C.

II. Gold Catalyst Synthesis.

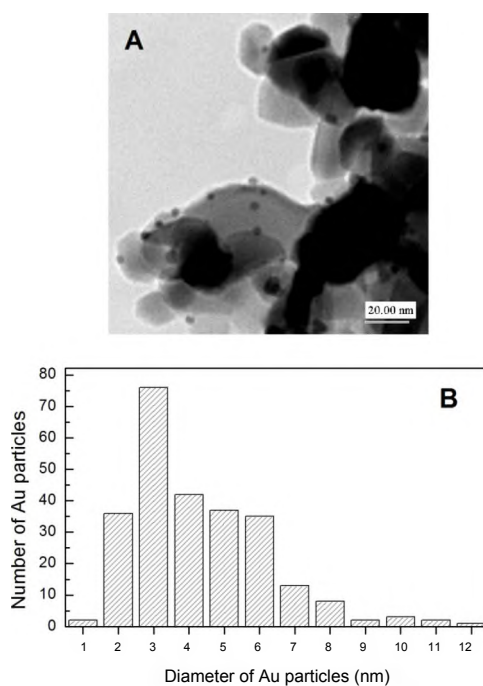


Figure 2.3. A. TEM image of the Au/TiO₂ catalyst *after* pre-treatment in the vacuum cell. B. Plot of the Au particle size distribution.

While most of the oxides and catalysts used in this project were purchased or donated, the Au/TiO₂ catalyst was homemade. As mentioned in Chapter 1, the synthetic method and particle size distribution contribute significantly to the gold catalytic behavior. To avoid complications, the Au/TiO₂ catalyst was synthesized via

deposition-precipitation method with an average nanoparticle diameter of ~ 3 nm, and was used throughout the entire project. The protocol for Au nanoparticle deposition-precipitation with urea on TiO₂ is adopted from Zanella *et al.*³ Figure 2.3 shows a transmission electron microscope (TEM) image of the Au/TiO₂ catalyst used, along with a histogram of measured Au nanoparticle size. TEM data were collected on a JEOL 2000FXII microscope with 200 kV acceleration voltage.

Commercial TiO₂ P25 powder ($49 \text{ m}^2 \text{ g}^{-1}$) is provided by Evonic Industries (previously Degussa). Urea (99.5%) and hydrogen tetrachloroaurate (III) trihydrate (HAuCl₄·3H₂O, Au precursor) were purchased from Acros. Before deposition, the TiO₂ powder was dried and activated at 373 K in a 100 mL/min air flow for at least 24 hours. The rest of the preparation process was carried out in the absence of light, due to the known fact that the gold precursor may decompose under illumination. A gold precursor aqueous solution was made ($4.2 \times 10^{-3} \text{ M}$ HAuCl₄ and 4.2 M urea). One gram of activated TiO₂ powder was mixed with 100 mL of the gold precursor solution and reacted at 353 K with vigorous stirring for 8 hours. The pH of the reaction mixture increased from ~ 2 at the beginning of reaction to ~ 7 at the end. The Au/TiO₂ powder was separated from the suspension by centrifuging at 3800 rpm for 20 min. To wash off the residual Cl⁻ anion, which is suspected to compete with O₂ for active sites during CO oxidation,⁴ the Au/TiO₂ powder was washed by 5 cycles of vigorous stirring in 100 mL double-deionized water at 323 K, followed by centrifugation at 3800 rpm for 20 min. Auger spectra, measured in a separate UHV system, show no Cl⁻ contamination on the samples after washing. The powder was then dried at 373 K for over 24 hours under 100 mL/min air flow. The theoretical Au loading on the catalyst is 8 wt%.

Synthesized Au/TiO₂ catalyst is stored in aluminum foil-covered 1.5 mL Eppendorf tubes in a desiccator at room temperature, before installed in the vacuum IR cell. After the catalyst was installed in the vacuum cell and before initial use, it was heated to 473 K with a temperature ramping rate of 0.2 K/s and was held at 473 K in vacuum for 2.5 hours. Then 20 Torr of O₂ was introduced into the cell at 473 K, remaining for 1 hour. After pumping the cell down to high vacuum, the catalyst was held at 473 K for another 0.5 hour, before it was cooled to desired temperature for experimental use. The goal of the heating in vacuum and in O₂ is to remove most of the hydrocarbon impurities from the catalyst surface. Complete removal of all impurities including hydroxyl groups requires higher treatment temperature, which is known to cause Au particle agglomeration, and thus was not used. The TEM image of the catalyst shown in Figure 2.3 was taken after the initial treatment described above.

An Au/SiO₂ catalyst made by DP method with an average Au particle size of ~3 nm was kindly provided by Dr. Zanella. Detailed description of the synthetic method as well as the characterization of the Au/SiO₂ catalyst can be found elsewhere.⁵

Chapter 2 References:

1. Basu, P.; Ballinger, T. H.; J. T. Yates, Jr. *Review of Scientific Instruments* 1988, 59, 1321.
2. Ryczkowski, J. *Catalysis Today* 2001, 68, 263.
3. Zanella, R.; Giorgio, S.; Henry, C. R.; Louis, C. *Journal of Physical Chemistry B* 2002, 106, 7634.
4. Laursen, S.; Linic, S. *Physical Chemistry Chemical Physics* 2009, 11, 11006.
5. Zanella, R.; Sandoval, A.; Santiago, P.; Basiuk, V. A.; Saniger, J. M. *The Journal of Physical Chemistry B* 2006, 110, 8559.

Part I

Catalytic Oxidation Activities on Oxide Supported Gold Nanoparticles

Chapter 3

Spectroscopic Observation of Dual Catalytic Sites during

Oxidation of CO on a Au/TiO₂ Catalyst.*

[^]Modified with permission from I. X. Green, W. Tang, M. Neurock, and J. T. Yates, Jr., “Spectroscopic Observation of Dual Catalytic Sites During Oxidation of CO on a Au/TiO₂ Catalyst”, *Science*, 333, 736-739 (2011). The theoretical work was performed by Dr. Wenjie Tang and Dr. Matthew Neurock and is included here for completeness.

The prevailing view of CO oxidation on gold-titanium oxide (Au/TiO₂) catalysts is that the reaction occurs on metal sites at the Au/TiO₂ interface. We observed dual catalytic sites at the perimeter of 3 nanometer Au particles supported on TiO₂ during CO oxidation. Infrared-kinetic measurements indicate that O-O bond scission is activated by the formation of a CO-O₂ complex at dual Ti-Au sites at the Au/TiO₂ interface. Density functional theory calculations, which provide the activation barriers for the formation and bond scission of the CO-O₂ complex, confirm this model as well as the measured apparent activation energy of 0.16 electron volts. The observation of sequential delivery and reaction of CO first from TiO₂ sites and then from Au sites indicates that catalytic activity occurs at the perimeter of Au nanoparticles.

I. Introduction.

Determining the atomic and electronic structure of the active site in heterogeneous catalysis is a unifying theme for almost all work in the field.¹⁻⁵ Understanding the cooperative behavior between dual catalytic centers comprised of distinguishable active sites is particularly challenging due to the complexity in resolving the mechanistic role of each site and their interactions under catalytic reaction conditions. Herein, we use *in situ* infrared spectroscopy to follow the dynamic changes at both Au and TiO₂ sites that reside

at the periphery of the Au/TiO₂ interface. We show that the extraordinary catalytic activity of nanometer-sized Au clusters supported on TiO₂ results from dual catalytic sites.

The unique catalytic behavior of Au/TiO₂ contrasts to the inactivity of separate bulk Au and oxide surfaces as was first recognized in the pioneering work of Haruta and coworkers,^{6,7} and in the subsequent applications by others.⁸ While multiple mechanisms have been proposed to explain the high catalytic activity of oxide-supported Au for CO oxidation, there is little consensus on the nature of the active sites or the details of the reaction mechanism. Some have proposed that the novel catalytic activity originates predominantly from nanometer size Au particles, and that the role of the oxide support is to stabilize these particles. Highly dispersed Au clusters thus provide a large fraction of active coordinatively-unsaturated Au surface sites and can also possibly exhibit quantum size effects.⁹⁻¹² Others have proposed that the electronic interaction between the Au nanoparticles and the underlying support is the key feature since cationic Au is thought to be more active for the CO oxidation reaction.^{13,14} Two atom thick Au films, supported on macroscopic-width thin TiO_x films, where no perimeter interface between materials is present, have been reported to show high relative activity supporting the idea of a favorable electronic interaction between Au and TiO₂.¹⁵ Considering the known weak interaction between Au and O₂, it was also proposed that the support may enhance the catalytic reaction by localizing O₂ or O atoms at Au perimeter sites.¹⁶⁻¹⁸ Several experiments carried out with inverse catalysts demonstrated that the oxides might be more important than just supporting the Au or enhancing the reaction on low coordination number (CN) Au sites, by being involved directly in the catalytic reaction: inactive Au single crystals or nano-sized Au powders become active when they come in

contact with particular oxide supports such as TiO_x or CeO_x.¹⁹⁻²¹ The active sites for the catalytic reaction are therefore postulated in this view to be at the Au/oxide interface.

A number of theoretical studies have also been reported which help to elucidate the CO oxidation pathways and mechanisms over the supported Au catalyst,^{22,23} and specifically examine the perimeter sites.²⁴⁻²⁹ Taking the most widely studied Au/TiO₂ system as an example, it was postulated that O₂ is activated at the perimeter sites because of the enhancement of O₂ or O adsorption by the TiO₂ support;²⁴⁻²⁷ others suggest that both the perimeter TiO₂ sites and the Au sites with low CN are important for the CO oxidation.²⁸ In either case, the focus has been on the reaction between O₂ and CO/Au and it was proposed that the bi-molecular mechanism occurs through a postulated CO-O₂ intermediate, exclusively formed on the Au surface.

Although the catalytic importance of the perimeter has been recognized, the role of the support is still generally overlooked. Reactions, and in particular CO oxidation, are thought to occur on Au sites at the perimeter, while the support sites are only thought to be involved in stabilizing O₂ at the interface.^{17,21,24-28,30} The direct reaction of O₂ and CO on TiO₂ sites which are adjacent to Au particles has not been considered, since weak binding of CO occurs on supports such as TiO₂.^{31,32} Although it was reported that CO does not adsorb on smooth Au terrace sites,³³ the CO adsorption on coordinatively unsaturated Au sites is stronger than on TiO₂,^{7,34,35} leading to the view that Au sites deliver CO to active sites for the catalytic process. The experiments and theoretical results reported here require the reconsideration of this fundamentally important issue where just the opposite behavior has been found.

We have carried out CO oxidation over a Au/TiO₂ catalyst at low temperatures, where CO is chemisorbed on both Au and TiO₂ sites and can be separately observed on these sites during reaction. Direct proof of low temperature CO selective oxidation on TiO₂

sites near Au sites is presented here. Based on these experimental findings and the results from density functional theory (DFT) calculations, we propose a new mechanism for the operation of dual Au/TiO₂ catalytic sites at the perimeter of Au nanoparticles.

We studied gold clusters (~2 nm - ~8 nm diameter, with a most probable diameter of 3 nm, as shown in Figure 2.3) supported on high surface area powdered TiO₂ by transmission infrared (IR) spectroscopy. Gold clusters of this size are reported to be the most active for CO oxidation, both in actual supported Au catalysts^{7,9,16} as well as for model catalysts made by vacuum deposition of Au clusters on single crystal films of TiO₂.¹² The temperature range we have worked at (110 to 130 K) for CO oxidation assures that only the low activation energy kinetic steps are being sampled. The observed steps will also occur at the higher temperatures where the full catalytic cycle takes place. For direct comparison, a pure TiO₂ sample and a Au/TiO₂ sample were separately observed in adjacent positions on a W-mesh support in the same high vacuum transmittance IR cell reactor with base pressure of 1×10^{-8} Torr (Figure 2.2).

II. Model System and Computation Details.

To simulate the ~3 nm diameter Au particles supported by TiO₂ system, we used a Au nanorod structure which has a height of 3-atomic layers and is 3-atoms-wide covalently bonded on top of a rutile TiO₂(110) slab, as shown in Figure 3.1A-B. This structure is similar to that used in previously reported DFT calculations.^{24,25} The Au nanorod structure was chosen herein to model the sites on the Au particles supported on TiO₂ due to its computational tractability. It appropriately mimics the terrace and edge sites as well as the Ti sites located at the Au/TiO₂ interface as well as within the local vicinity. The model, however, is an oversimplification of the nm-sized Au clusters on TiO₂ as there are no corner sites. These sites are likely to be somewhat more reactive for CO

oxidation due to their ability adsorb and activate O₂. As such the Au-nanorod structure will somewhat underestimate the actual reactivity.

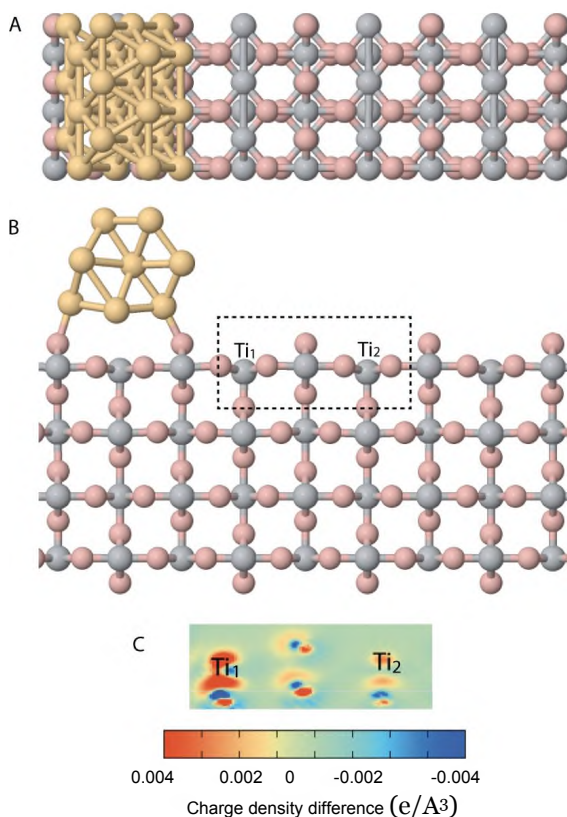


Figure 3.1. A. Top view and B. side view of the 3-atomic-layer Au nanorod on rutile TiO₂ (110) surface model. Au atoms are yellow. Ti atoms are light grey. O atoms in TiO₂ lattice are pink. C. Charge density difference on the Ti_{5c} sites noted by the dotted rectangle in B before and after Au deposition. Red regions exhibit the highest electronic charge.

Two unit cells comprised of four O-Ti-O tri-layers were used to model the rutile TiO₂(110) surface. All of the simulations reported were carried out using a (2x3) unit cell to simulate CO adsorption and diffusion and the larger (4x3) unit cell to model CO oxidation. The atoms in the top two trilayers of the TiO₂ slab were allowed to fully relax while the atoms in the bottom two trilayers of the TiO₂ slab were fixed to their lattice positions for both unit cells. All of the Au atoms were allowed to relax in the Z-direction.

All of the calculations reported herein were carried out using plane wave gradient-corrected DFT calculations as implemented in the Vienna *ab initio* Simulation Package (VASP).^{36,37} The wavefunction was expanded in a plane-wave basis set with energy cutoff of 400 eV. The PW91 gradient approximation (GGA) functional was used to describe the exchange-correlation energy.³⁸ The core-electronic states were described by pseudopotentials constructed with the projector augmented-wave (PAW) method.^{39,40} The DFT+U method was implemented in our calculations to correct on-site Coulomb interactions.⁴¹ The value of U was chosen to be 4.0 eV because it can generate similar electronic structure that was experimentally observed.⁴² Spin-polarization was considered for all calculations and was used when necessary. A vacuum gap of 10 Å was used in the Z-direction between slabs. The (2x3) and (4x3) unit cells were sampled with (2x2x1) and (1x2x1) k-point mesh, respectively.⁴³ Geometries were optimized until the force on each atom was less than 0.03 eV/Å.

The reaction pathway and activation barriers were found by the nudged elastic band (NEB) method with image climbing,^{44,45} combined with the dimer method to isolate transition states.⁴⁶ The NEB method was used to follow the path between the reactant and product states to the point where the perpendicular forces on all of the images along the band were lower than 0.1 eV/Å. The dimer method was subsequently used to isolate the transition state to the point where the force acting on the transition state dimer was lower than 0.03 eV/Å.

The charge density difference, *pdiff*, on the TiO₂ surface before and after Au deposition was calculated following Equation 3.1.

$$P_{diff} = P_{Au/TiO_2} - p_{TiO_2} - p_{Au} \quad (3.1)$$

The electronic charge difference at the perimeter site is plotted in Figure 3.1C, showing that negative charge accumulates on the Ti5c site at the perimeter after Au deposition. This change in charge is responsible for the strong adsorption and activation of O₂ at these sites.^{30,33,47-50}

III. Results and Discussion.

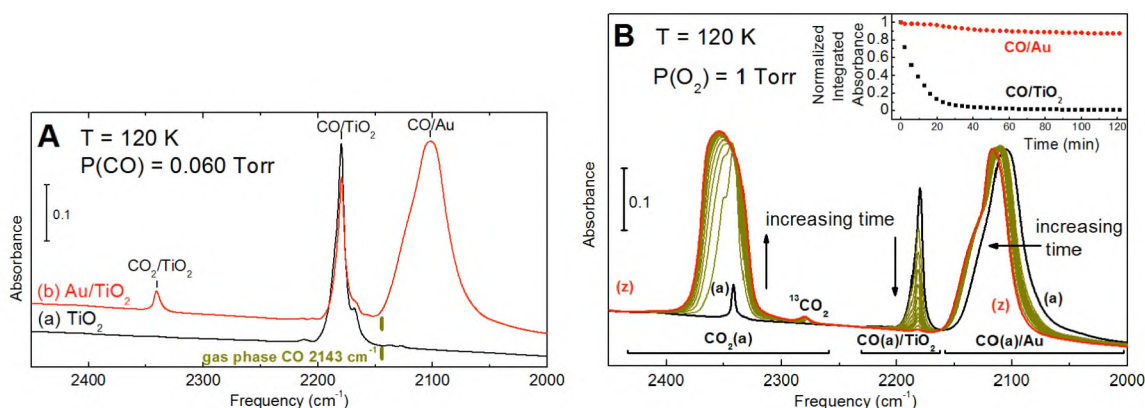


Figure 3.2. A. IR spectra of saturated CO layer: spectrum a, TiO₂; b, Au/TiO₂ under 0.060 Torr of CO pressure at 120 K. B. IR spectral development during the CO oxidation reaction on Au/TiO₂ under 1 Torr of O₂ pressure at 120 K: a, before O₂ introduction; z, after 120 min of reaction. The CO/TiO₂ oxidation was found to continue when the CO coverage was replenished from spectrum z, indicating that the CO₂(a) accumulation did not block the active sites. (Inset) The plot of normalized integrated absorbance of CO/Au (red) and CO/TiO₂ (black) against time during the experiment.

The IR spectra at 0.060 Torr CO pressure at 120 K on both the Au/TiO₂ catalyst and the TiO₂ reference sample are shown at saturation coverage in Figure 3.2A. A feature at 2179 cm⁻¹ with a small shoulder at 2168 cm⁻¹ that appeared on both samples was caused by CO adsorption on TiO₂.⁵¹ The blue shift from the gas phase frequency (2143 cm⁻¹) is generally attributed to CO chemisorbed on a metal cation site such as Ti⁴⁺, while a red shift is observed for adsorption on metallic sites.^{33,51} Two additional features were seen in Figure 3.2A on the Au/TiO₂ sample. We assigned the broad band centered at 2102 cm⁻¹

in spectrum (b) as CO chemisorbed on metallic Au,^{22'32'33} and a small feature at 2341 cm^{-1} to chemisorbed CO_2 on TiO_2 sites on the Au/ TiO_2 catalyst.³² The CO_2 band originated from CO reacting with traces of residual O_2 in the high vacuum cell. CO_2 was only produced on the Au/ TiO_2 catalyst, judging from a comparison of spectra (a) and (b) in Figure 3.2A.

We evacuated the CO-saturated catalyst at 120 K for 1 hour before conducting further experiments. During the evacuation, the small shoulder (2168 cm^{-1}) arising from weakly bound CO/ TiO_2 disappeared from the IR spectrum of the Au/ TiO_2 catalyst (as well as from the pure TiO_2 spectrum) as shown in Figure 3.2B(a) -- none of the more strongly-bound chemisorbed CO or CO_2 molecules desorbed at 120 K. CO oxidation began immediately when the CO-saturated Au/ TiO_2 surface was exposed to 1.0 Torr of $\text{O}_2(\text{g})$ at 120 K, as indicated by the gradual disappearance of the CO absorbance on TiO_2 sites and the growth of the CO_2 feature on TiO_2 sites in the IR spectra shown in Figure 3.2B (green spectra). Surprisingly, the CO/Au feature hardly decreased in absorbance during the oxidation at 120 K under $\text{O}_2(\text{g})$. The integrated IR absorbance of a particular vibrational mode is well-known to be proportional to the number of adsorbed species and can thus be used as a quantitative measure for the reaction progress.⁵² The inset to Figure 3.2B shows the very different kinetics observed for CO removal from TiO_2 sites (fast) and Au sites (slow). The main participant in the reaction is CO/ TiO_2 , which depleted completely. Only about 12% loss in CO/Au coverage occurred in over 120 min. The blue shift ($\sim 14 \text{ cm}^{-1}$) of the CO/Au band after O_2 introduction was likely the result of the coadsorption of O_2 on Au sites in the oxygen-rich environment.^{22'32} Little CO oxidation was detected on the pure TiO_2 reference sample, indicating the critical importance of the Au/ TiO_2 interface.

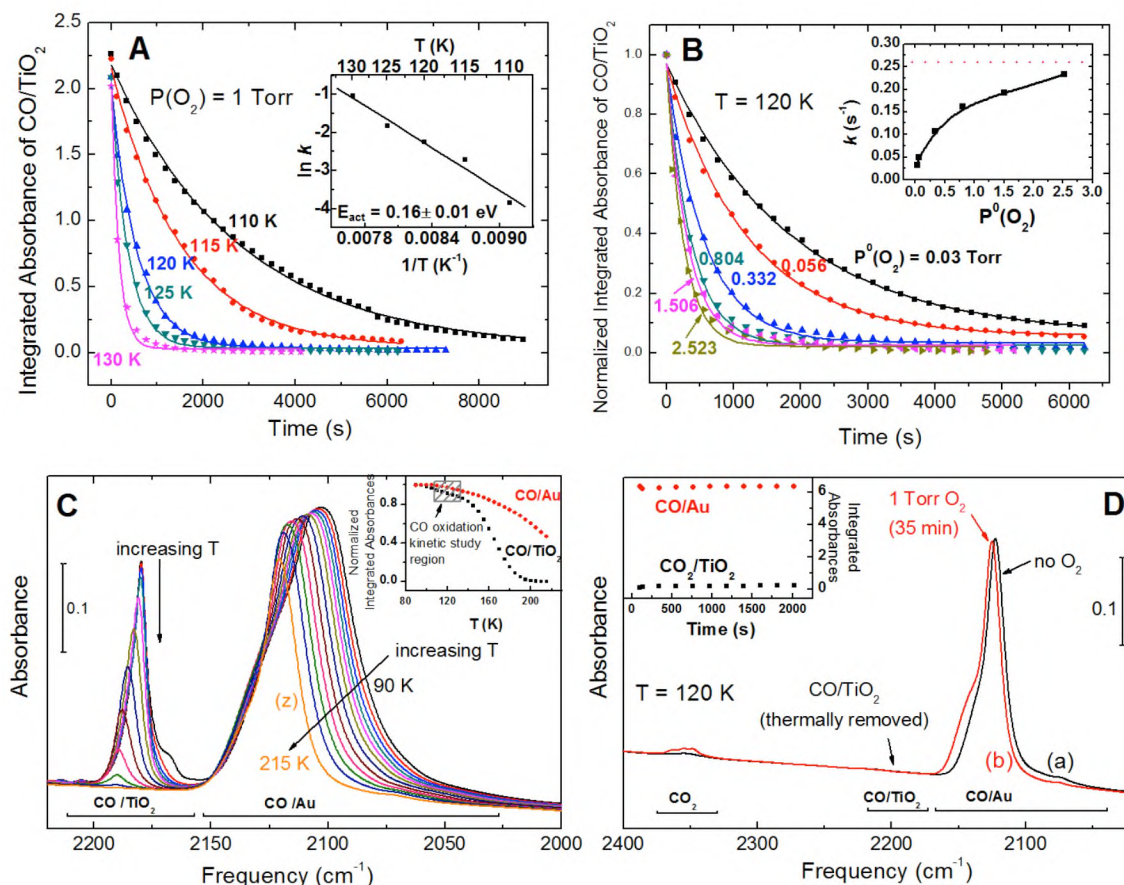


Figure 3.3. A. Plots of the integrated absorbance of CO/TiO₂ against time at various temperatures fitted to first-order kinetics. (Inset) The Arrhenius plot. B. Plots of the normalized integrated absorbance of CO on TiO₂ against time under various O₂ pressures at 120 K. (Inset) The rate of CO consumption approaches a maximum at $P(O_2) \geq 2.5$ Torr. C. IR spectra development during temperature programmed desorption of CO. (Inset) The normalized integrated absorbance of CO/Au (red) and CO/TiO₂ (black) against temperature. D. Spectrum a, IR spectrum of Au/TiO₂ catalyst at 120 K in vacuum after thermally removing the CO/TiO₂ species; b, IR spectrum of the catalyst shown in spectrum a after treatment in 1 Torr of O₂ for 35 min at 120 K. (Inset) The integrated absorbance of CO/Au (red) and CO₂/TiO₂ (black) against time for the process between spectra a and b.

Figure 3.3A shows the results of a kinetics study of the rate of CO/TiO₂ consumption on the Au/TiO₂ catalyst by the reaction in 1.0 Torr O₂(g) at various low temperatures (110–130 K). The solid lines represent the best first-order fits to the data and show that the reaction was accurately first-order in CO/TiO₂ coverage. The inset shows an Arrhenius plot of the data yielding an apparent activation energy of 0.16 ± 0.01 eV for

the overall reaction. This activation energy is confirmed through an Arrhenius analysis of the rate of adsorbed CO₂ formation, yielding also an apparent activation energy of 0.16 ± 0.01 eV. The excellent agreement in the kinetics study between CO/TiO₂ consumption and CO₂/TW₂ generation confirmed that the reaction primarily occurred on the TiO₂ sites and that the contribution from CO/Au oxidation was small at 120 K.

Figure 3.3B shows a plot of the rate of the reaction as a function of the O₂ pressure at 120 K, where higher O₂ pressure caused the reaction rate to increase. A plot of the reaction rate as a function of O₂ pressure (inset of Figure 3.3B) shows that the rate of CO oxidation maximized at an O₂ pressure of ≥ 2.5 Torr at 120 K. This result suggests that the O₂ surface coverage on the Au/TiO₂ catalyst reached a maximum under these conditions, which caused the rate of reaction to remain constant even at higher O₂ pressures.

To further examine the site-specific CO oxidation on Au/TiO₂, we studied the thermal desorption of the CO/TiO₂ species. We gradually heated the CO-saturated Au/TiO₂ catalyst from 90 K to 215 K in vacuum, and selectively removed the CO/TiO₂ species while more than 50% of the CO/Au species remained on the surface (Figure 3.3C). As the CO coverage decreased upon raising the temperature, CO/TiO₂ species desorbed rapidly, while the CO/Au species desorbed more slowly. The inset of Figure 3.3C shows the CO coverage change on Au and TiO₂ plotted separately against temperature. The final spectrum with only CO remaining on Au sites at 215 K is shown in Figure 3.3C(z). This catalyst was then cooled to 120 K in vacuum [Figure 3.3D(a)], and then exposed to 1.0 Torr of O₂. No reaction was detected in 35 min [Figure 3.3D(b) and the inset of Figure 3.3D]. This experiment shows that at 120 K, the most strongly chemisorbed CO/Au species mixed with O₂/Au species are inactive for CO oxidation, indicating that the active site for low temperature CO₂ formation is not a Au site.

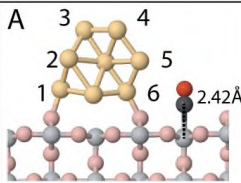

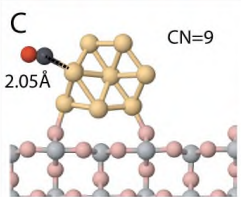
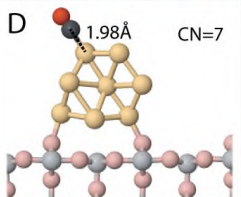

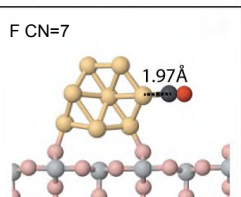
Configuration	Binding Energy	Configuration	Binding Energy
	-0.41 eV		-0.41 eV
	-0.23 eV		-0.89 eV
	-0.80 eV		-0.67 eV

Figure 3.4. CO adsorption energies and configurations on different Au sites or on the Ti_{5c} sites. The distances between the CO and the adsorption site are noted. C atoms are black. O atoms in CO are red.

CO chemisorption on Au and TiO₂ was weak in both cases. It has been reported that at temperatures above 25 K, CO does not chemisorb on Au(rn) terrace sites, neither on single crystal nor on nanoparticles and films.^{103,104} However, CO can chemisorb on coordinately unsaturated Au sites and the binding is stronger than on TiO₂. The heat of adsorption of CO/Au (coordinately unsaturated sites) is reported to be in the range of 0.5-0.8 eV,^{103,104} while the heat of adsorption of CO/TiO₂ is between 0.4 and 0.5 eV.^{79,85} DFT calculations of CO adsorption energies on Au sites and on TiO₂ sites on the Au/TiO₂ model presented herein yielded similar results, with binding energies of 0.7-0.9 eV for CO/Au and 0.4 to 0.5 eV for CO/TiO₂, as shown in Figure 3.4. Diffusion studies of CO/TiO₂ and CO/Au at 140 to 160 K also show that CO diffusion/desorption on TiO₂ is more rapid than on Au at all temperatures (Figure 3.5).

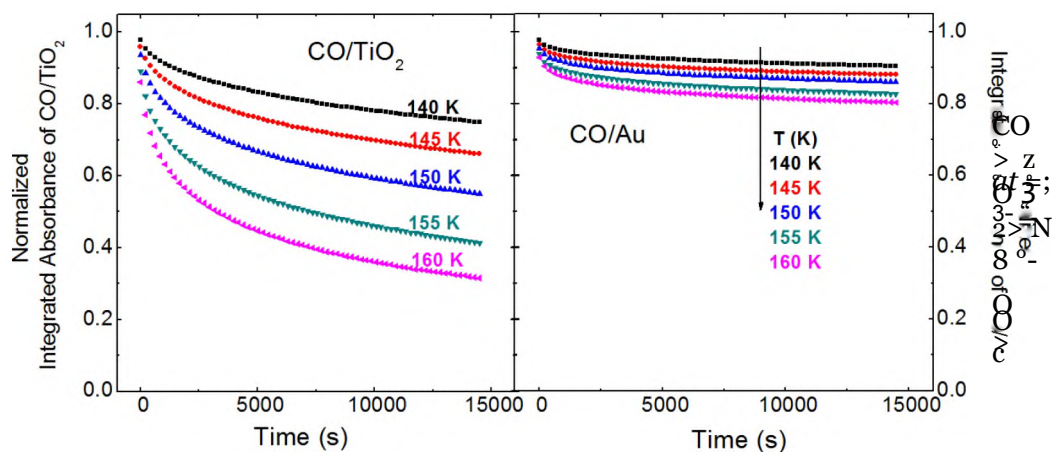


Figure 3.5. Plots of normalized integrated absorbance of CO/TiO₂ (left) and CO/Au (right) against time at various temperatures showing the diffusion/desorption processes of CO from the two surfaces, where CO/TiO₂ diffuses and desorbs more rapidly than CO/Au.

DFT calculations were carried out to help identify the active sites for the low temperature CO oxidation at the Au/TiO₂ interface. In light of the experimental results presented above, the theoretical calculations focused on the reactions that occur at perimeter sites between TiO₂ and Au.

O₂ activation, the critical first step in CO oxidation, has been postulated to occur either through direct O₂ dissociation at the perimeter, or through a bimolecular CO-O₂ reaction.^{24, 27, 28} We have considered both mechanisms at each of the possible sites on the Au nanoparticles, the TiO₂ support, and the Au/TiO₂ perimeter sites. We started by locating the most favorable O₂ adsorption sites on the Au/TiO₂ catalyst. DFT calculations carried out on the adsorption of O₂ on the ideal rutile TiO₂(110) surface revealed that O₂ does not adsorb on these surfaces which is consistent with experimental results.⁵³ This lack of adsorption indicates that it would be very difficult to dissociate O₂ directly over the ideal TiO₂(110) surface, and as such, this was not considered. The adsorption of Au on TiO₂ leads to a significant charge transfer from the Au to the neighboring Ti5c cation as is shown in Figure 3.1C. The charge transfer along with the unique di-o binding of O₂

at the perimeter Ti-Au site significantly enhances its adsorption (Figure 3.6) and promotes the oxidation of CO.^{24,26} A thorough search for the adsorption of O₂ at all of the sites along the Au/TiO₂ perimeter and on the Au nano-rod was carried out to help identify the low barrier O₂ activation sites, as shown in Figure 3.6. The co-adsorption of CO at neighboring sites was found to help facilitate the activation of O₂ either indirectly via through-surface electronic interactions or directly by the formation of a reactive O*-O-C*=O intermediate (where * denotes the atoms bound to the surface), as was recently reported for CO oxidation on CO covered Pt particles.⁵⁴ The results for the coadsorption of CO and O₂ and the activation of O₂ are summarized in Figure 3.7.

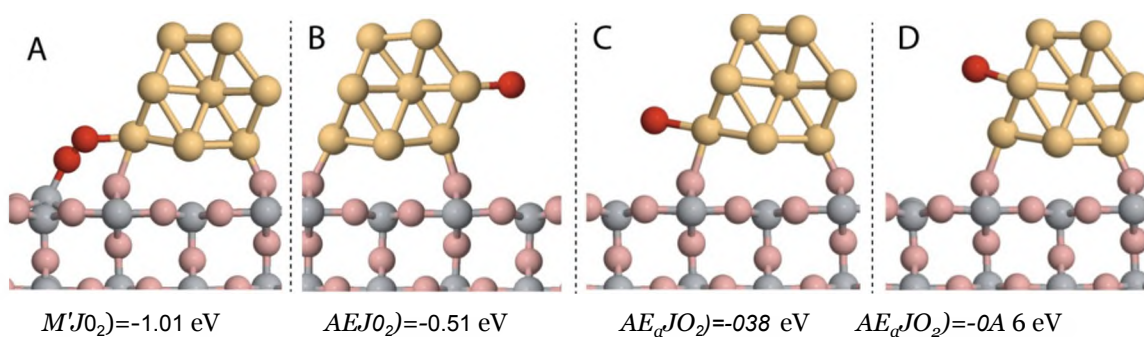


Figure 3.6. O₂ adsorption energy at different Au sites.

The 5 possible sites investigated for O₂ activation are: A) the bridge oxygen O vacancy site on the TiO₂ perimeter; B) the Ti5c sites at the perimeter; C) the Au atoms on the nanorod at the TiO₂ interface; D) the Ti5c-Au perimeter site for the CO-O₂ mechanisms; and E) the Ti5c-Au perimeter site for the direct O₂ dissociation mechanism. The initial, transition (TS), and the final states for O₂ activation, together with the energy required to break the O-O bond are reported for all of the adsorption states in Figure 3.7. The configurations shown in Figures 3.7B-D were found to follow the CO-O₂ bimolecular mechanism, while the remaining configurations involve direct O-O bond scission. The

activation barriers reported for the CO-O₂ bimolecular dissociation steps on the oxide alone (0.65 eV - Figure 3.7B) and the metal alone (0.7 eV - Figure 3.7C) were found to be much higher than the other three paths.

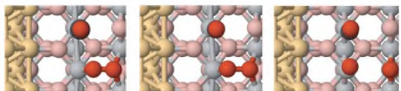
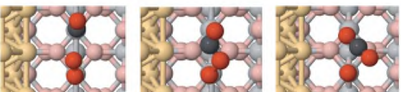
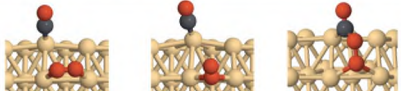
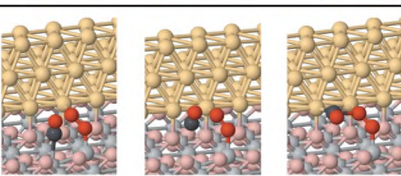

	Initial TS Final	Ea [eV]
A		0.12
B		0.65
C		0.70
D		0.16
E		0.39

Figure 3.7. The initial, transition and final states for the adsorption and activation of O₂ along with the corresponding activation energies for the dissociation of the O-O bond at 5 different sites: A, O-vacancy on the TiO₂ support; B, Ti5c sites at the perimeter; C, two Au atoms on the periphery of the Au nanorod; D, Ti5c-Au perimeter site via CO-O₂ mechanism; E, Ti5c-Au perimeter site via direct O₂ dissociation mechanism. Oxygen atoms in CO and O₂ molecule are red. Hydrogen atoms are cyan.

While the direct activation of O₂ at an O vacancy site adjunct to Ti5c has the lowest barrier (0.12 eV Figure 3.7A), it is very unlikely to be catalytically active, as one of the dissociated O atoms will fill this site eliminating it from the catalytic cycle. The most active sites therefore appear to occur at the Ti5c-Au perimeter sites. The bimolecular CO-O₂ mechanism for the dissociation of O₂ has a barrier of only 0.16 eV (Figure 3.7D) which

is less than half that required for the direct O₂ dissociation (0.39 eV - Figure 3.7E). The results in Figure 3.7 clearly indicate that O₂ activation and CO oxidation proceed at the dual Ti_{5c}-Au perimeter site via a CO-assisted path. This is the only site likely to be able to contribute to the oxidation at temperatures as low as 110 K in the experiments.

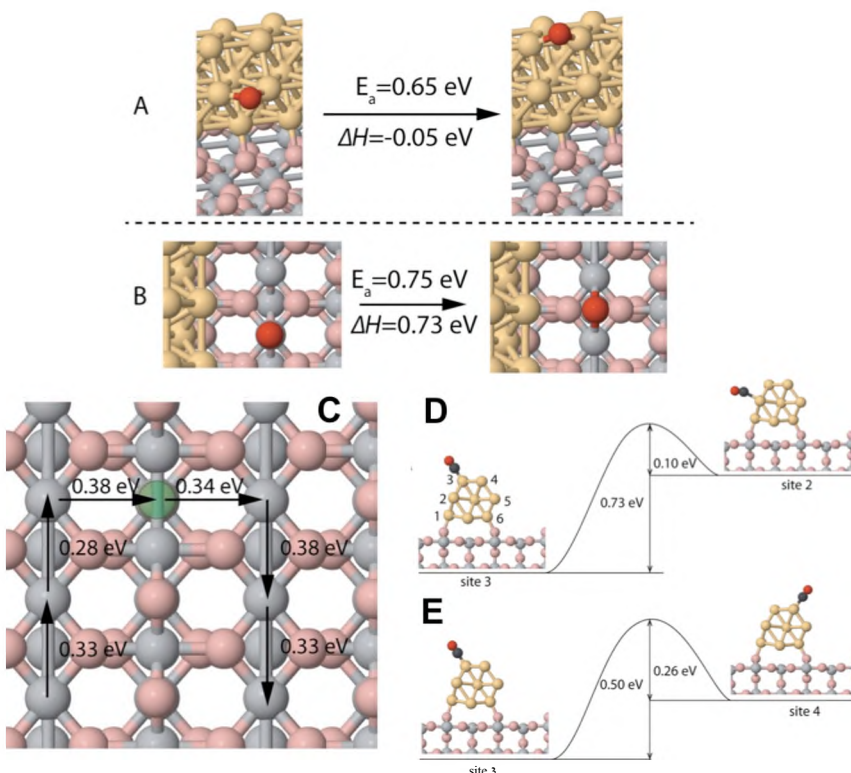


Figure 3.8. A-B, Atomic O diffusion at the Au/TiO₂ interface: A, on Au sites; and B, on Ti_{5c} sites. C-E, CO diffusion barriers on the Au/TiO₂ catalyst: C, on TiO₂, where the position of the O-vacancy under consideration is highlighted by a green circle; D-E, on two different Au adsorption sites.

The oxidation of CO by O₂ subsequently results in the formation of CO₂(g) and an adsorbed oxygen atom which resides either at the Au or Ti_{5c} site. For the next step to proceed, a second CO molecule must diffuse to the adsorbed oxygen atom or the adsorbed oxygen atom must diffuse to a bound CO. The calculations reported in Figure

3.8 provide insights into the mobility of CO and O at the Au/TiO₂ interface and may help to explain the IR observation of the selective oxidation of CO/TiO₂.

Figures 3.8A-B show the calculated barriers for the diffusion of atomic oxygen on Au and TiO₂ to be 0.65 eV and 0.75 eV, respectively. These high diffusion barriers indicate that it is unlikely for the atomic O to diffuse away from either type of adsorption site. Figure 3.8C displays the possible diffusion barriers for CO on TiO₂. CO can diffuse on the TiO₂ surface along paths that connect surface Ti sites. The activation energies for the CO diffusion paths on TiO₂ identified in Figure 3.8C (including a pathway through an O vacancy), were all calculated to be within the range of 0.28-0.38 eV. At O₂-rich conditions there are likely very few O vacancies present and as such the calculated diffusion barrier for CO/TiO₂ should be close to 0.33 eV. This result agrees with the 0.35 eV CO/TiO₂ diffusion energy calculated by Zhao *et al.*⁵⁵ Finally, Figures 3.8D-E show the possible diffusion paths for CO along the Au nano-rod. As was discussed above, CO only chemisorbs on the low CN Au sites. The calculated barriers for CO diffusion indicate that CO can diffuse with barriers of 0.1 eV (from site 1, labeled in Figure 3.8D) and 0.26 eV (from site 2) to the strongest adsorption site (site 3). CO becomes trapped at this site as the barriers to diffuse to the site 1 and 2, were calculated to be 0.73 (Figure 3.8D) and 0.50 eV (Figure 3.8E), respectively. At low temperatures CO is therefore likely localized at these Au sites and can not diffuse to the Au/TiO₂ perimeter sites.

The results from DFT calculations for the reaction energies and activation barriers for all of the steps proposed in the mechanism for CO oxidation at the active Ti_{5c}/Au interface are shown in Figure 3.9. We start with CO on TiO₂ (Figure 3.9A), as indicated by the experimental results. The CO coverage at the TiO₂ perimeter sites is set at 2/3 monolayer (ML), while the rest of the Ti_{5c} sites are all occupied to simulate the saturation coverage of CO used experimentally. This step is followed by the fast coadsorption of O₂

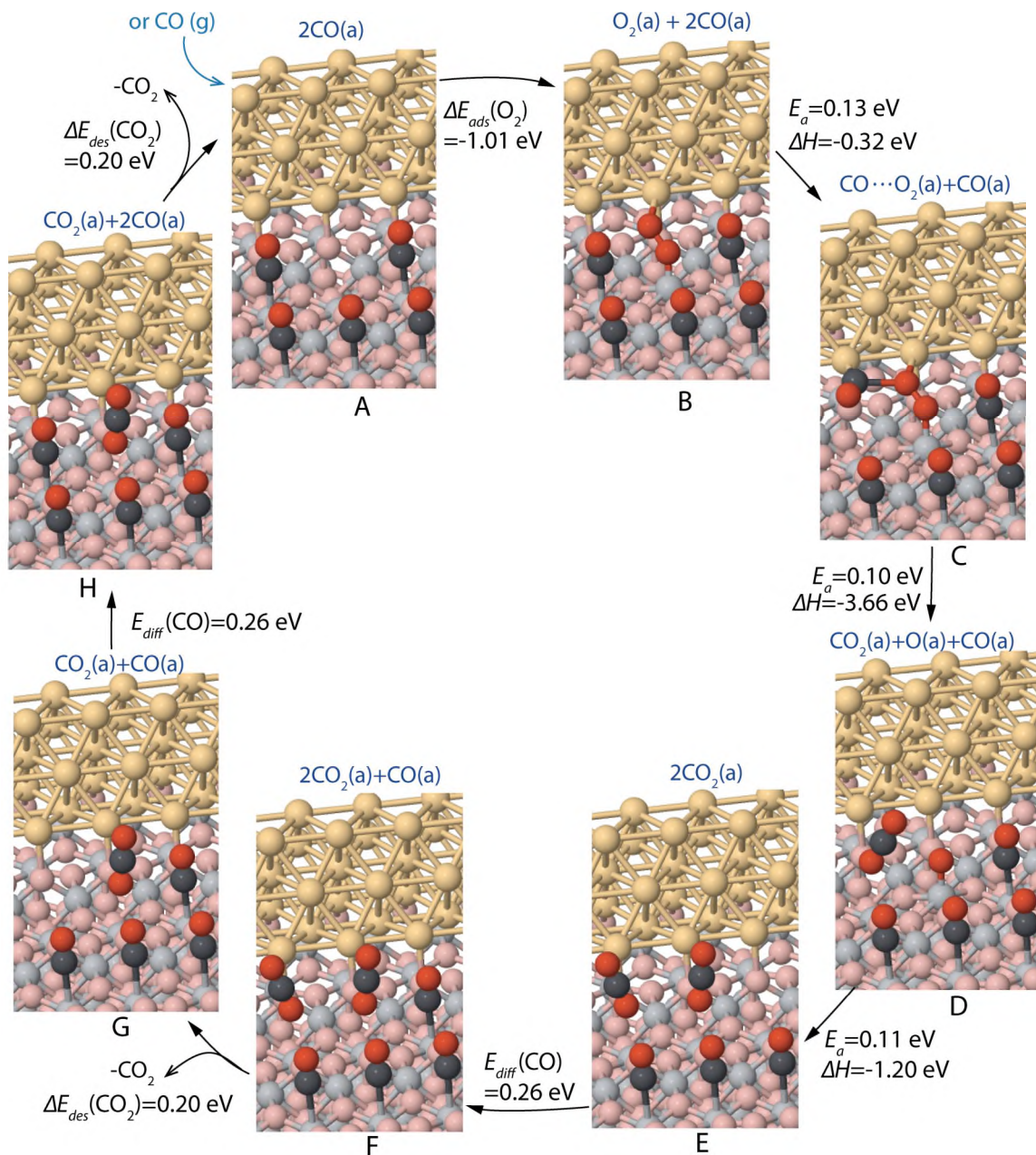


Figure 3.9. CO oxidation cycle proposed from DFT calculation results. The Au atoms and Ti atoms are shown in yellow and grey respectively, whereas the O in TiO₂ lattice, adsorbed O and C atoms are shown in pink, red, and black respectively. E_b , E_a and ΔH refer to the binding energy, activation barrier and reaction enthalpy, respectively. The elementary steps depicted include the adsorption of O₂ (A-B), interaction between O₂ and CO (B-C), reaction of O₂ and CO (C-D), reaction of adsorbed atomic oxygen and CO (D-E), diffusion of CO (E-F and G-H), and desorption of CO₂ (F-G and H-A).

at the dual perimeter site adjacent to the CO/TiO₂ (Figure 3.9B) with a strong binding energy of -1.01 eV. The adsorbed O₂ reacts directly with one CO/TiO₂ to form a CO-O₂ intermediate that is stabilized by its interaction with the Ti5c site and the neighboring Au site at the perimeter (Figure 3.9C); this step has an activation energy of 0.13 eV. The O-O bond is substantially weakened upon its interaction with CO to form an O=C--O₂ intermediate which dissociates with an activation energy of only 0.10 eV and generates CO₂-Ti and O-Ti (Figure 3.9D). The remaining O-Ti, which is trapped as a result of its high diffusion barrier of 0.75 eV (Figure 3.8B), can readily react with a second CO at the active Au/TiO₂ periphery with a barrier of 0.11 eV (Figure 3.9E). The formation of O=C-O and O=C-O-C=O complexes on Ti5c sites on TiO₂(110) has been directly observed at 100-110 K by STM recently.^{56,57} The CO₂ formed can easily diffuse away from the active site or desorb with a barrier of only 0.20 eV (Figure 3.9G). The perimeter sites are then re-occupied by CO which diffuses from neighboring Ti5c sites with a barrier of 0.26 eV (Figure 3.9 F to H). This step returns the catalyst surface to its initial working state. The reaction continues by adsorbing a second O₂(g) at Au perimeter sites and by CO/TiO₂ surface diffusion (Figure 3.9B).

The catalytic cycle shown in Figure 3.9 is consistent with the experimental observation that CO adsorbed on TiO₂ containing Au nanoparticles is consumed by reaction with O₂ at the interface. The activation of O₂ by CO and the reaction to form CO₂ and O proceeds at dual sites along the perimeter involving a Au atom and a Ti5c site. The O/Ti5c species that results readily reacts at low temperature with CO which diffuses from the TiO₂ support to the active Ti5c site. The calculated barrier for this reaction is only 0.11 eV which is consistent with previous results.²⁷ The CO species on Au are much less mobile with diffusion barriers that exceed 0.5 eV because of the strong adsorption of CO (Figure 3.8D-E). The calculated activation barriers for the elementary steps reported

in the oxidation of CO at the Ti5c site (0.10-0.26 eV) are all quite close to the experimentally measured apparent activation energy (0.16 ± 0.01 eV). While it is difficult to distinguish a rate-determining step without full kinetic simulations, the simple analysis of the activation energies in Figure 3.9 suggests that the diffusion of CO from the TiO₂ support to the Ti5c perimeter site has the highest barrier. The apparent activation energy for CO oxidation of 0.16 eV measured herein at low temperatures is in good agreement with previously reported barriers of 0.2-0.3 eV from measurements carried out at much higher temperatures (200-350 K) and pressures on Au/TiO₂ catalysts.^{58,59} The catalytic cycle proposed in Figure 3.9 should likely hold even at high temperature and CO pressure conditions, but requires the addition of CO adsorption from the gas phase (-1.01 eV) and the CO diffusion from Au which can proceed at higher temperatures (0.5 eV) as reflected in Figure 3.9A. Higher temperatures will also likely result in the desorption of CO from the Ti5c sites and increase the oxidation of CO adsorbed at the Au sites.

This Au/TiO₂ interface and the processes that occur here are shown schematically in Figure 3.10. O₂(g) is captured at the perimeter site (process ® in Figure 3.10). CO molecules on TiO₂ sites are initially delivered to the active perimeter sites via diffusion on the TiO₂ surface where they assist O-O bond dissociation and react with oxygen at these perimeter sites (processes @ and ® in Figure 3.10). After most of the CO/TiO₂ is depleted from TiO₂ in the perimeter zone, a small fraction of CO/Au (~12% at 120 K) with weaker binding energies and lower diffusion barriers is oxidized. The remaining tightly bonded CO/Au is kinetically isolated from the CO oxidation at 120 K because these CO/Au surface species cannot approach the active perimeter sites. At higher temperatures, however, the CO on the Au sites become more mobile and can begin to actively participate in catalytic CO₂ production (process @ in Figure 3.10). The

observation of the sequential delivery of the two types of adsorbed CO, present on both sides of the perimeter of the Au nanoparticles, argues persuasively for reactivity to occur within a zone at the perimeter of Au particles surrounded by TiO₂ surface sites which form dual sites for the reaction.

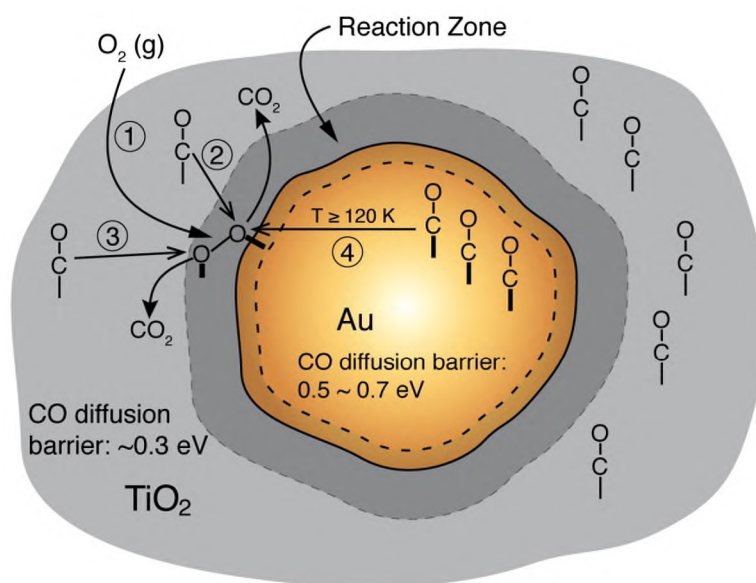


Figure 3.10. Schematic of the mechanism of low temperature CO oxidation over a Au/TiO₂ catalyst at a perimeter zone of reactivity. Experiments directly observing CO/TiO₂ and CO/Au surface species show that processes ② and ③ are fast compared to process ④.

IV. Acknowledgements.

We acknowledge the support of this work by the U.S. Department of Energy-Office of Basic Energy Sciences, Grant Number DE-FG02-09ER16080 as well as the National Science Foundation and the Texas Advanced Computing Center for Teragrid resources.

Chapter 3 References:

1. Somorjai, G. A.; Li, Y. *Introduction to Surface Chemistry and Catalysis*; Second ed.; John Wiley & Sons, Inc.: Hoboken, New Jersey, 2010.

2. van Santen, R. A.; Neurock, M. *Molecular Heterogeneous Catalysis*; Wiley-VCH: Weinheim, 2006.
3. *Model Systems in Catalysis*; Springer: New York, 2010.
4. Yates, J. T., Jr.; Campbell, C. T. *Proceedings of the National Academy of Sciences* **2011**, *108*, 911.
5. Ertl, G. *Reactions at Solid Surfaces*; John Wiley & Sons, Inc.: Hoboken, New Jersey, 2009.
6. Haruta, M.; Kobayashi, T.; Sano, H.; Yamada, N. *Chemistry Letters* **1987**, *2*, 405.
7. Haruta, M.; Tsubota, S.; Kobayashi, T.; Kageyama, H.; Genet, M. J.; Delmon, B. *Journal of Catalysis* **1993**, *144*, 175.
8. Meyer, R.; Lemire, C.; Shaikhutdinov, S. K.; Freund, H.-J. *Gold Bulletin* **2004**, *37*, 72.
9. Lopez, N.; Janssens, T. V. W.; Clausen, B. S.; Xu, Y.; Mavrikakis, M.; Bligaard, T.; Norskov, J. K. *Journal of Catalysis* **2004**, *223*, 232.
10. Diemant, T.; Hartmann, H.; Bansmann, J.; Behm, R. J. *Journal of Catalysis* **2007**, *252*, 171.
11. Overbury, S. H.; Schwartz, V.; Mullins, D. R.; Yan, W.; Dai, S. *Journal of Catalysis* **2006**, *241*, 56.
12. Valden, M.; Lai, X.; Goodman, D. W. *Science* **1998**, *281*, 1647.
13. Guzman, J.; Gates, B. C. *The Journal of Physical Chemistry B* **2002**, *106*, 7659.
14. Fu, Q.; Saltsburg, H.; Flytzani-Stephanopoulos, M. *Science* **2003**, *301*, 935.
15. Chen, M. S.; Goodman, D. W. *Science* **2004**, *306*, 252.
16. Janssens, T.; Clausen, B.; Hvolbæk, B.; Falsig, H.; Christensen, C.; Bligaard, T.; Norskov, J. *Topics in Catalysis* **2007**, *44*, 15.
17. Kotobuki, M.; Leppelt, R.; Hansgen, D. A.; Widmann, D.; Behm, R. J. *Journal of Catalysis* **2009**, *264*, 67.
18. Liu, L. M.; McAllister, B.; Ye, H. Q.; Hu, P. *Journal of the American Chemical Society* **2006**, *128*, 4017.
19. Rodriguez, J. A.; Ma, S.; Liu, P.; Hrbek, J.; Evans, J.; Perez, M. *Science* **2007**, *318*, 1757.
20. Fujitani, T.; Nakamura, I.; Akita, T.; Okumura, M.; Haruta, M. *Angewandte Chemie* **2009**, *48*, 9515.
21. Bollinger, M. A.; Vannice, M. A. *Applied Catalysis B: Environmental* **1996**, *8*, 417.
22. Boronat, M.; Concepcion, P.; Corma, A. *The Journal of Physical Chemistry C* **2009**, *113*, 16772.
23. Mavrikakis, M.; Stoltze, P.; Norskov, J. K. *Catalysis Letters* **2000**, *64*, 101.

24. Molina, L. M.; Rasmussen, M. D.; Hammer, B. *Journal of Chemical Physics* **2004**, *120*, 7673.
25. Laursen, S.; Linic, S. *Physical Chemistry Chemical Physics* **2009**, *11*, 11006.
26. Liu, Z.-P.; Gong, X.-Q.; Kohanoff, J.; Sanchez, C.; aacute; Hu, P. *Physical Review Letters* **2003**, *91*, 266102.
27. Wang, J. G.; Hammer, B. *Physical Review Letters* **2006**, *97*, 136107.
28. Remediakis, I. N.; Lopez, N.; Norskov, J. K. *Angewandte Chemie International Edition* **2005**, *44*, 1824.
29. Pala, R. G. S.; Liu, F. *The Journal of Chemical Physics* **2006**, *125*, 144714.
30. Boccuzzi, F.; Chiorino, A.; Manzoli, M.; Lu, P.; Akita, T.; Ichikawa, S.; Haruta, M. *Journal of Catalysis* **2001**, *202*, 256.
31. Linsebigler, A.; Lu, G.; Yates, J. T., Jr. *Journal of Chemical Physics* **1995**, *103*, 9438.
32. Boccuzzi, F.; Chiorino, A. *Journal of Physical Chemistry B* **2000**, *104*, 5414.
33. Dumas, P.; Tobin, R. G.; Richards, P. L. *Surface Science* **1986**, *171*, 579.
34. Meier, D. C.; Goodman, D. W. *Journal of the American Chemical Society* **2004**, *126*, 1892.
35. Derrouiche, S.; Gravejat, P.; Bianchi, D. *Journal of the American Chemical Society* **2004**, *126*, 13010.
36. Kresse, G. *Physical Review B* **2000**, *62*, 8295.
37. Kresse, G.; Hafner, J. *Surface Science* **2000**, *459*, 287.
38. Perdew, J. P.; Wang, Y. *Physical Review B* **1992**, *45*, 13244.
39. Blöchl, P. E. *Physical Review B* **1994**, *50*, 17953.
40. Kresse, G.; Joubert, D. *Physical Review B* **1999**, *59*, 1758.
41. Dudarev, S. L.; Botton, G. A.; Savrasov, S. Y.; Humphreys, C. J.; Sutton, A. P. *Physical Review B* **1998**, *57*, 1505.
42. Morgan, B. J.; Watson, G. W. *Surface Science* **2007**, *601*, 5034.
43. Monkhorst, H. J.; Pack, J. D. *Physical Review B* **1976**, *13*, 5188.
44. Henkelman, G.; Johansson, H. *The Journal of Chemical Physics* **2000**, *113*, 9978.
45. Henkelman, G.; Uberuaga, B. P.; Jonsson, H. *The Journal of Chemical Physics* **2000**, *113*, 9901.
46. Henkelman, G.; Johansson, H. *The Journal of Chemical Physics* **1999**, *111*, 7010.

- 47- Klimev, H.; Fajerweg, K.; Chakarova, K.; Delannoy, L.; Louis, C.; Hadjiivanov, K. *Journal of Materials Science* 2007, *42*, 3299.
48. Dumas, P.; Tobin, R. G.; Richards, P. L. *Journal of Electron Spectroscopy and Related Phenomena* 1986, *39*, 183.
49. Kim, J.; Samano, E.; Koel, B. E. *The Journal of Physical Chemistry B* 2006, *110*, 17512.
50. Liu, Z. P.; Gong, X. Q.; Kohanoff, J.; Sanchez, C.; Hu, P. *Physical Review Letters* 2003, *91*.
51. Cerrato, G.; Marchese, L.; Morterra, C. *Applied Surface Science* 1993, *70-71*, 200.
52. Green, I. X.; Buda, C.; Zhang, Z.; Neurock, M.; Yates, J. T., Jr. *The Journal of Physical Chemistry C* 2010, *114*, 16649.
53. Pan, J.-M.; Maschhoff, B. L.; Diebold, U.; Madey, T. E. *Journal of Vacuum Science & Technology, A: Vacuum, Surfaces, and Films* 1992, *10*, 2470.
54. Allian, A. D.; Takanabe, K.; Furdala, K. L.; Hao, X.; Truex, T. J.; Cai, J.; Buda, C.; Neurock, M.; Lglesia, E. *Journal of the American Chemical Society* 2011, *133*, 4498.
55. Zhao, Y.; Wang, Z.; Cui, X.; Huang, T.; Wang, B.; Luo, Y.; Yang, J.; Hou, J. *Journal of the American Chemical Society* 2009, *131*, 7958.
56. Wang, Z.; Zhao, Y.; Cui, X.; Tan, S.; Zhao, A.; Wang, B.; Yang, J.; Hou, J. G. *The Journal of Physical Chemistry C* 2010, *114*, 18222.
57. Lee, J.; Zhang, Z.; Deng, X.; Sorescu, D.; Matranga, C.; Yates, J. T., Jr. *The Journal of Physical Chemistry C* 2011, *115*, 4163.
58. Daté, M.; Okumura, M.; Tsubota, S.; Haruta, M. *Angewandte Chemie International Edition* 2004, *43*, 2129.
59. Long, C. G.; Gilbertson, J. D.; Vijayaraghavan, G.; Stevenson, K. J.; Pursell, C. J.; Chandler, B. D. *Journal of the American Chemical Society* 2008, *130*, 10103.

Chapter 4

Low Temperature Catalytic H₂ Oxidation over Nanoparticle

Au/TiO₂ - Dual Perimeter Sites at Work.*

[^]Modified with permission from I. X. Green, W. Tang, M. Neurock, and J. T. Yates, Jr., “*Low-Temperature Catalytic H₂ Oxidation over Au Nanoparticle/TiO₂ Dual Perimeter Sites*”, *Angewandte Chemie International Edition*, 50, 10186-10189 (2011). The theoretical work was performed by Dr. Wenjie Tang and Dr. Matthew Neurock and is included here for completeness.

The catalytic reaction of hydrogen with oxygen was studied by the transmission IR method as well as by density functional theory over 3 nm Au particles supported on TiO₂ powder. The kinetics for the formation of H₂O(a) were investigated at 200-220 K. It was found that dual-perimeter Au-TiO₂ sites adsorb and dissociate molecular O₂ via the formation of a Ti-OOH hydroperoxy intermediate with an activation barrier of 0.16 eV. The Ti-OOH species dissociates at the Au-TiO₂ interface to form O-Au and Ti-OH intermediates. The Ti-OH intermediate is subsequently hydrogenated by H-Au to form water at the peripheral sites on TiO₂. The calculated barrier of 0.25 eV appears to control the initial rate of water formation which is in very good agreement with the experimentally measured apparent activation energy of 0.22 ± 0.02 eV. A deuterium kinetic isotope effect, $kH/kD = 7$, matches the theoretical ratio of 5 indicating that the reaction takes place via an early transition state. By the observation of the changes in the IR background during reaction, where dissolved H in TiO₂ causes the occupancy by electrons of defect sites near the bottom of the conduction band, it was possible to monitor electron transfer effects from H to the defects during the reaction of H₂ and O₂ over the catalyst.

I. Introduction.

The catalytic oxidation of H₂ is of great interest due to its role in H₂O₂ synthesis, catalytic oxidation of hydrocarbons and the selective removal of CO from hydrogen streams¹⁻⁵ as well as for its simplicity which makes it ideal for fundamental bond making and breaking studies. This is especially true for supported Au nanoparticles which were found to show unusually high activity by Haruta, *et al.*⁶ Previous explanations for this activity have invoked quantum size effects for Au particles in the 2 nm range,⁷ electronic effects in thin films of Au,⁸ and enhancement of the fraction of perimeter sites.⁹⁻¹² Recent experiments on inverse TiO₂/Au catalysts have suggested that the enhanced catalytic activity may be due to active sites at the TiO₂/Au interface rather than a quantum size effect.^{10,13}

The presence of H₂ gas in CO + O₂ reaction streams is known to produce enhanced catalytic activity for CO oxidation over Au/TiO₂ catalysts. The promotional effect originates from the addition of H₂ and has been ascribed to H₂'s ability to regenerate the catalyst by reducing the hydrocarbon accumulation^{4,5} or by its reaction with O₂ to form hydroperoxy (OOH*) intermediates which readily oxidize CO.¹⁴⁻¹⁶ Previous theoretical studies have provided unique insights for this reaction, but have only focused on the role of Au.¹⁶⁻²⁰ To our best knowledge, there are no reported theoretical studies on the H₂ + O₂ reaction that have considered the influence or involvement of the TiO₂ perimeter sites at the Au-TiO₂ interface. Herein, we use kinetic analyses together with *in situ* infrared spectroscopic studies and density functional theory (DFT) calculations to examine the activity of the Au sites as well as the Au and TiO₂ perimeter sites at the Au/TiO₂ interface and elucidate a plausible reaction mechanism.

II. Results and Discussion.

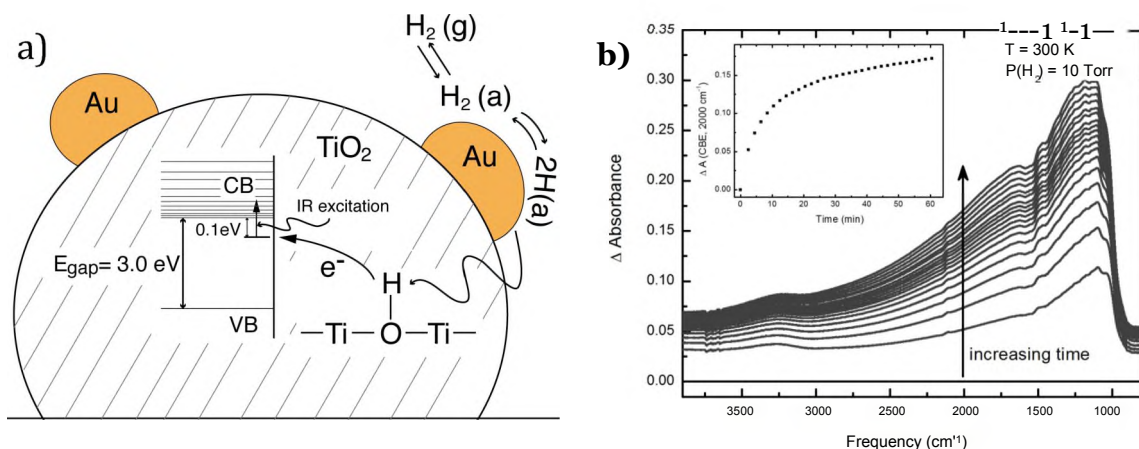


Figure 4.1. A. Schematic representation for the effect of atomic hydrogen spillover on Au/TiO₂ catalyst and the IR excitation of defect-bound electrons to and above the conduction band edge (CBE) of the TiO₂. B. Plot of the IR background shift of the Au/TiO₂ catalyst at 300 K under 10 Torr of H₂. The inset shows the development of the CBE effect at 2000 cm⁻¹ against time, as atomic H donates electrons to TiO₂ CBE defect sites.

It has been reported that atomic H dissolved in TiO₂²¹⁻²³ may be detected by the IR background upward shift, which is caused by trapped electrons from H in the Conduction Band Edge (CBE) states, as shown in Figure 4.1a.²⁴⁻²⁶ Examples of this phenomenon at room temperature are shown in Figures 4.1b and 4.2a, where a dramatic IR background up-shift is caused by molecular H₂ dissociation on Au followed by atomic H spillover to the TiO₂ support. Figure 4.2b shows that when a small quantity of O₂ is introduced to the H-rich surface, it drains the CBE electrons which results in an immediate background drop. Simultaneously, the oxidation reaction of the H₂ on the Au/TiO₂ surface to form H₂O(a) is observed by the absorption band at 1620 cm⁻¹ (5h2o).^{4'27} Removal of O₂ by reaction causes the CBE to return to an increased level in the H₂-rich environment (Figure 4.2c). The whole process is summarized in Figure 4.2d where both the CBE change and the H₂O formation are plotted with respect to time.

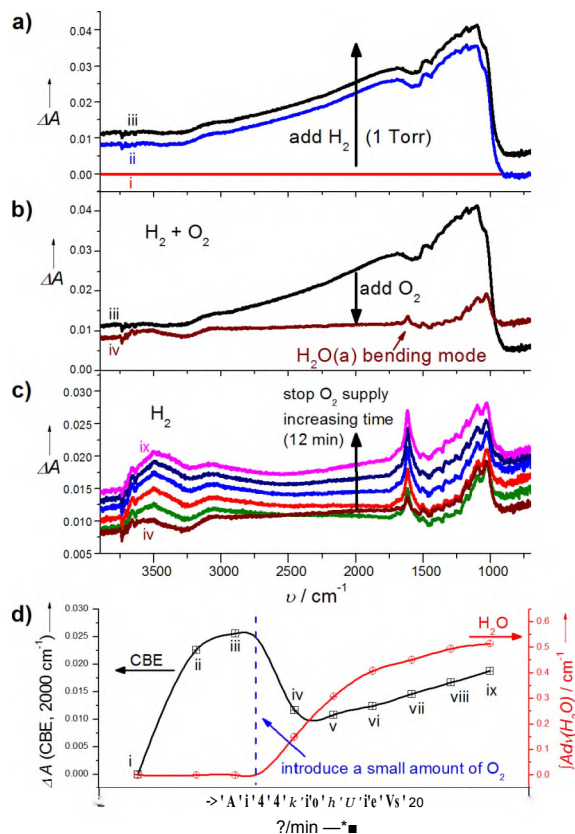


Figure 4.2. a). IR difference spectra of the H₂ spillover and CBE background shifting effect on the Au/TiO₂ at 295 K under 1 Torr of H₂. b). IR difference spectra of the H₂ oxidation by O₂ over the Au/TiO₂ at 295 K. c). IR difference spectra of the CBE background shifting effect on the (H₂O-partially covered) Au/TiO₂ surface when the O₂ supply is cut off. d). Plot of the CBE and H₂O development against time during the above processes.

In an effort to observe more details of the H₂-O₂ reaction, the catalyst was cooled to 210 K and a 1:100 mixture of O₂ and H₂ was added. The reaction progress is shown in Figure 4.3, indicating the production of both H₂O(a) and OH. A search for peroxide intermediate within the 1505-900 cm^{-1} region was inconclusive.²⁸ No products were observed on a pure TiO₂ sample mounted below the catalyst for the same reaction conditions, indicating that Au is necessary for the reaction. Similar experiments over the temperature range of 200-220 K were carried out and the kinetics studies as a function

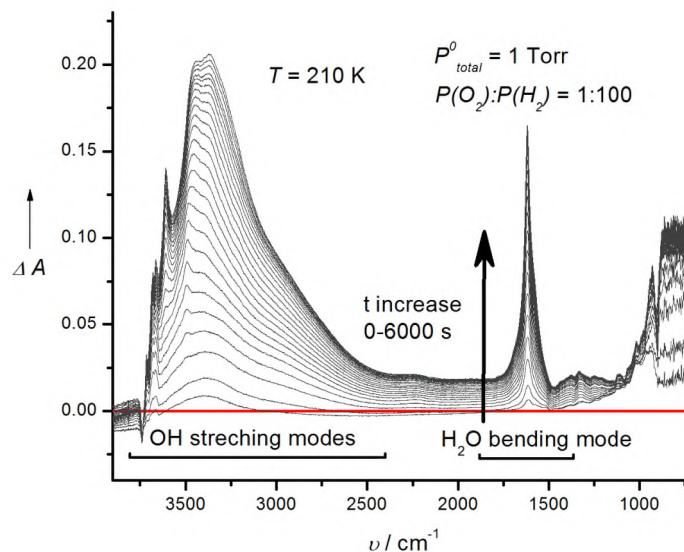


Figure 4.3. IR difference spectra of the Au/TiO₂ surface during H₂ oxidation by O₂ at 210 K.

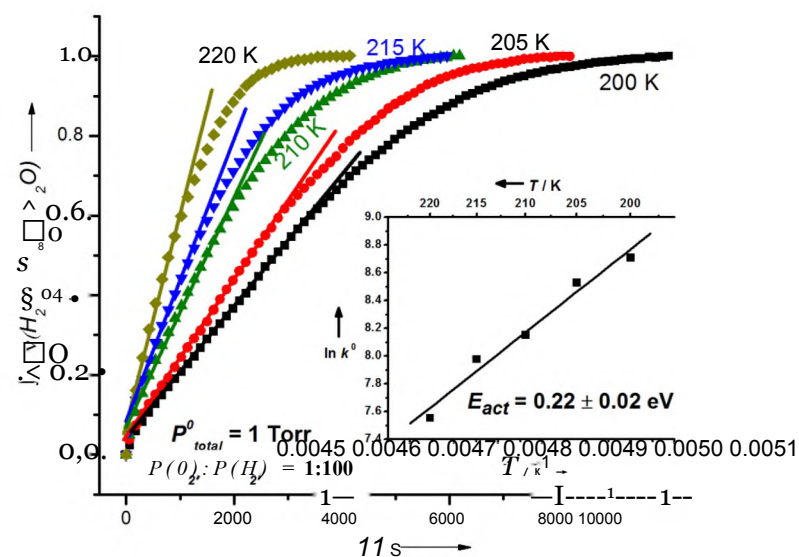


Figure 4.4. Kinetics for the oxidation of H₂ by O₂ over the Au/TiO₂ catalyst as measured by the change in the absorbance of H₂O as a function of time and temperature. The inset shows the Arrhenius plot.

of temperature are shown in Figure 4.4. An Arrhenius plot of the initial rate is shown in the inset, yielding an apparent activation energy of 0.22 ± 0.02 eV. This is the first report of the kinetics of H₂ oxidation over Au/TiO₂ below room temperature. Activation energies at temperatures above 300 K have been measured as 0.38 eV for H₂ + O₂²⁹ and

0.37 eV for H₂-D₂ exchange.¹⁰ The rate of reaction maximizes to nearly the same limit at particular pressures of O₂ (~0.08 Torr) and H₂ (~1.4 Torr), as shown in Figure 4.5, indicating site saturation for both reactants.

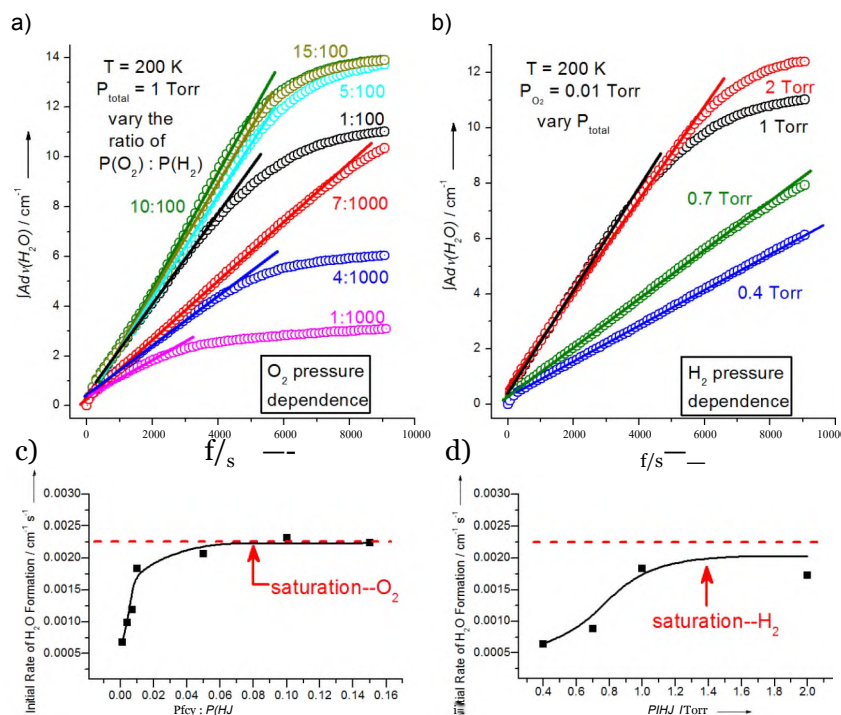


Figure 4.5. The effects of: a) O₂ pressure and b) H₂ pressure on the H₂ oxidation kinetics over Au/TiO₂. c). Plot of the initial rate of H₂O formation as a function of increasing O₂ partial pressure. d). Plot of the initial rate of H₂O formation as a function of the increasing H₂ pressure.

DFT calculations were carried out to help elucidate the reaction mechanism and identify possible active sites for the low temperature H₂ oxidation. Details of the model system employed to simulate the Au/TiO₂ catalyst can be found in Chapter 3, Section II (page 27). H₂ oxidation is thought to proceed by the formation of two H adatoms. Our DFT results as well as previous experiments²⁴ show that the lowest H-H dissociation barrier on Au *in the absence of O₂* is ~0.5 eV (Figure 4.6). As a result, we studied the

influence of the co-existing O₂ to the reaction. The calculated adsorption energies for O₂ at various possible Au and TiO₂ sites are shown in Figure 4.7. The most favorite binding

Initial TS	E _a [eV]
	0.48
	0.95
	0.16

Figure 4.6. DFT-calculated results for H₂ dissociation on: (a) Au site with lowest CN (CN=7); (b) Au site with highest CN (CN=9); (c) on Au site (CN=9) in the presence of O₂ where a Ti-OOH species is formed. Au is yellow. Ti is grey. Oxygen in the TiO₂ lattice is pink. Adsorbed oxygen is red. Hydrogen is cyan. E_a is the activation energy.

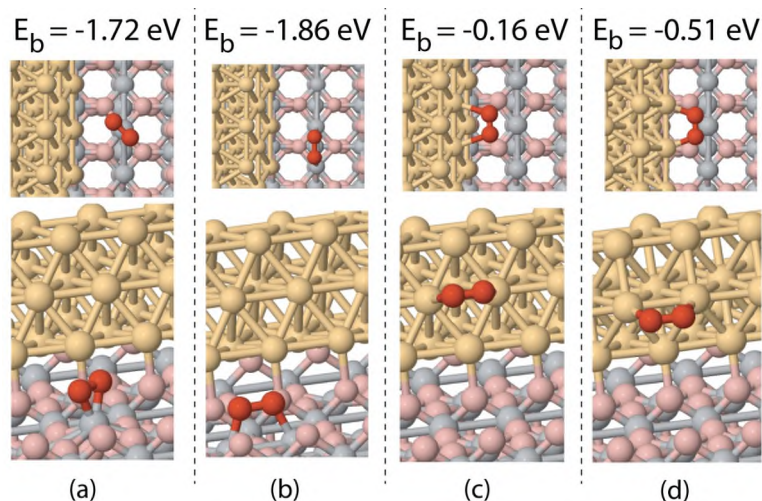


Figure 4.7. O₂ adsorption configurations and binding energies, E_b, on: (a) perimeter TiO₂ site; (b) perimeter TiO₂ sites with other configurations; (c) Au with low coordination number (CN=7); (d) Au with high coordination number (CN=9). Au is yellow. Ti is grey. Oxygen in oxide is pink. Oxygen is red.

site for O₂ is at the perimeter on TiO₂ where it has a binding energy of ~1.8 eV (Figure 4.7b). This is consistent with previous theoretical calculations reported in the literature which show a strong and preferential binding of O₂ to the Ti_{5c} cation sites at the Au/TiO₂ interface.³⁰ Figure 4.7c shows that the binding energy for O₂ on the terrace of the Au nano rod is rather weak, thus indicating a very low probability for adsorption at this site. Previous calculations about O₂ adsorption on Au agree with this conclusion.³¹ The adsorption of O₂ on the coordinatively unsaturated edge sites (CN=7) results in stronger adsorption with an adsorption energy of -0.51 eV, as shown in Figure 4.7d. The adsorption of O₂, however, is still weaker as compared to the binding energy on the TiO₂ perimeter site (-1.86 eV, Figure 4.7b).

The presence of O₂ in the system can significantly lower the barrier to dissociate H₂, as is shown in Figure 4.6. The barrier to activate H₂ on the Au/TiO₂ system in the absence of oxygen is 0.48 eV for H₂ on the low coordination Au sites (CN=7) and 0.95 eV on high coordination Au sites (CN=9), as shown in Figures 4.6a and 4.6b. The presence of O₂, however, can considerably lower the barrier for the activation of H₂ by stabilizing the transition state that results in stabilizing Ti-OOH formation. As a result, the H₂ dissociation barrier is decreased to 0.16 eV, as shown in Figure 4.6c. The calculations indicate that the local presence of adsorbed O₂ can promote H₂ dissociation to yield the activation energy of 0.22 eV measured experimentally.

A H₂ catalytic oxidation cycle is proposed by DFT calculation, as shown in Figure 4.8. The adsorption of O₂ at the Ti_{5c} perimeter site, the most favored of all of the sites shown in Figure 4.7, lowers the barrier for the dissociative adsorption of H₂(g) at the neighboring Au perimeter site down to 0.16 eV, as shown in Figure 4.8a-b. The dissociative adsorption of H₂ at this dual perimeter site thus produces Ti-OOH intermediate and Au-H surface intermediates. Dissociation of the Ti-OOH to form Ti-OH

and Ti-O was calculated to have a barrier of 0.20 eV (Figure 4.8c). The resulting O(a) activates and dissociates a second incident H₂(g) at the dual perimeter site, with a barrier of 0.13 eV, as shown in Figure 4.8e). The final hydrogenation of the two Ti-OH species by the two Au-H species proceeds with activation energies of 0.24 and 0.25 eV, as shown in Figure 4.8f-g.

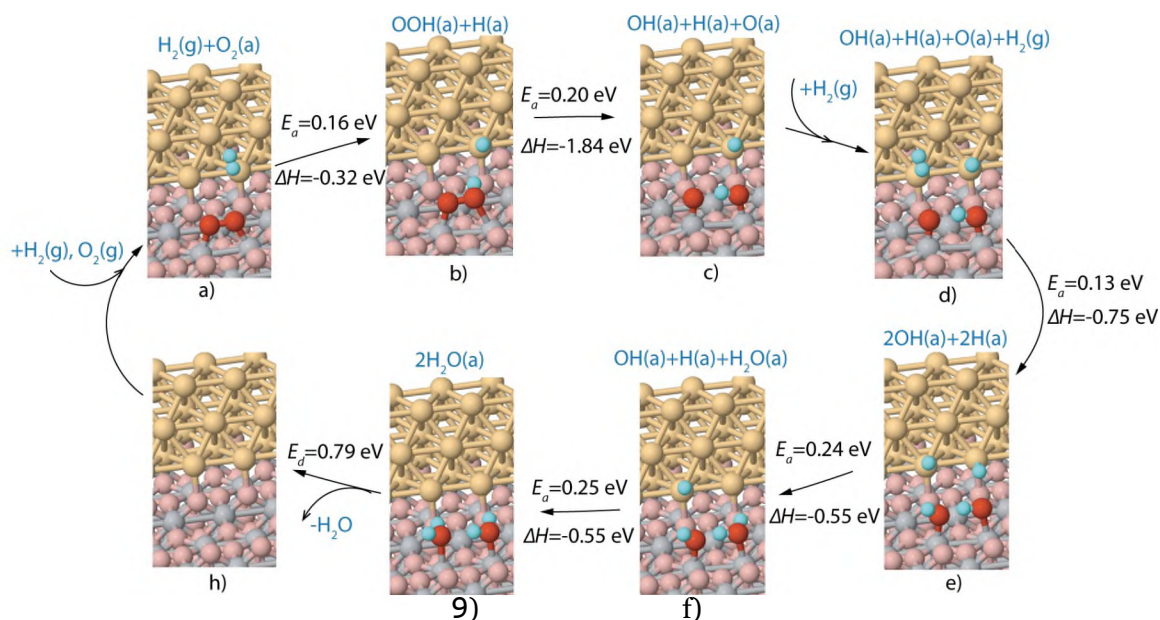


Figure 4.8. Catalytic reaction cycle and the corresponding activation barriers for the individual steps of the mechanism for the oxidation of H₂ to form H₂O over model Au/TiO₂ structures. The Au atoms and Ti atoms are shown in yellow and grey respectively, whereas the O in the TiO₂ lattice, adsorbed O and H atoms are shown in pink, red, and cyan respectively. E_a and ΔH represent activation barriers and reaction energies separately.

The initial rate of H₂O formation involves a sequence of elementary steps (Figure 4.8a-g) that have rather low activation energies in the range 0.13-0.25 eV. While it is difficult to rigorously distinguish a rate controlling step, the hydrogenation of OH(a) to form H₂O has the highest activation energy of 0.25 eV, in good agreement with the measured E_a of 0.22 eV. The low barriers of all other steps (Figure 4.8a-h) suggest that

the Au/TiO₂ perimeter sites serve as active sites for the H₂ oxidation at low temperature, via an O₂-assisted H-H dissociation mechanism.

Calculations of H₂O surface diffusion energies on TiO₂ (estimated to be 0.21, 0.32, and 0.43 eV at 1, 2/3, and 1/3 ML coverages) and desorption energy (0.79 eV in Figure 4.8g-h) suggest that H₂O will cluster and accumulate to block the active perimeter sites at low temperatures as the reaction proceeds. This is consistent with the results presented in Figure 4.4 where the reaction stops at longer times. Our measurements have therefore focused on the initial reaction rates where the effect of site blockage is minimal. This also means that the kinetic studies shown in Figure 4.4 are controlled by the disappearance of the active sites for H₂ oxidation.

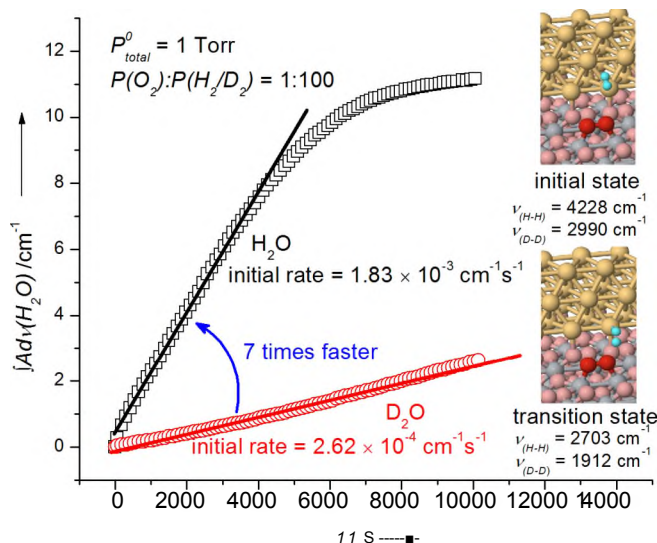


Figure 4.9. D₂ kinetic isotope effect for the oxidation of H₂ by O₂ over the Au/TiO₂ catalyst at 200 K. The insets show the ab initio calculated initial state and transition state frequencies for the O₂-assisted H₂ dissociation process.

To further elucidate the mechanism, we carried out D₂ labeling studies to measure the kinetic isotope effect (KIE). The rates of reaction of O₂ with H₂ and D₂ at 200 K, which are compared in Figure 4.9, show a ~7 fold increase in the initial rates for H₂ over

D2. The zero point energy (ZPE) differences for the reactant H₂ and D₂ and the corresponding transition states (TS) were considered in order to calculate the KIE to compare with the experimental results. The inset of Figure 4.9 shows the calculated initial state and TS and the corresponding vibrational frequencies of the H₂ dissociation reaction (steps a-b in Figure 4.8). If the ZPE difference is taken only for the initial state, the rate ratio, k_n/k_o , is calculated to be 87. Instead, using both initial and transition state frequencies, the calculated $k_n/k_o = 5$, in good agreement with the experimentally measured KIE value of 7, and indicating that an early TS is involved.

In summary, the active site for the H₂ + O₂ reaction over a Au/TiO₂ nanoparticle catalyst at low temperature was located at dual perimeter sites at the interface between Au and TiO₂ as schematically shown in the abstract drawing. An O₂-assisted H₂ dissociation via a Ti-OOH intermediate was proposed involving an early transition state. The calculated activation energies for sequential steps in the range 0.13-0.25 eV agree with the measured apparent activation energy of 0.22 eV.

III. Acknowledgement.

We gratefully acknowledge the support of this work by the U.S. Department of Energy-Office of Basic Energy Sciences, Grant Number DE-FG02-09ER16080 as well as the National Science Foundation and the Texas Advanced Computing Center for Teragrid resources. We also acknowledge the helpful discussion with Dr. Zhen Zhang of the University of Virginia.

Chapter 4 References:

1. Song, C. *Catalysis Today* 2002, 77, 17.

2. Bond, G. C.; Thompson, D. T. *Catalysis Reviews - Science and Engineering* **1999**, *41*, 319.
3. Collman, J. P.; Slaughter, L. M.; Eberspacher, T. A.; Strassner, T.; Brauman, J. I. *Inorganic Chemistry* **2001**, *40*, 6272.
4. Schumacher, B.; Denkwitz, Y.; Plzak, V.; Kinne, M.; Behm, R. J. *Journal of Catalysis* **2004**, *224*, 449.
5. Azar, M.; Caps, V.; Morfin, F.; Rousset, J.-L.; Piednoir, A.; Bertolini, J.-C.; Piccolo, L. *Journal of Catalysis* **2006**, *239*, 307.
6. Haruta, M.; Kobayashi, T.; Sano, H.; Yamada, N. *Chemistry Letters* **1987**, *2*, 405.
7. Valden, M.; Lai, X.; Goodman, D. W. *Science* **1998**, *281*, 1647.
8. Chen, M. S.; Goodman, D. W. *Science* **2004**, *306*, 252.
9. Kotobuki, M.; Leppelt, R.; Hansgen, D. A.; Widmann, D.; Behm, R. J. *Journal of Catalysis* **2009**, *264*, 67.
10. Fujitani, T.; Nakamura, I.; Akita, T.; Okumura, M.; Haruta, M. *Angewandte Chemie* **2009**, *48*, 9515.
11. Lopez, N.; Janssens, T. V. W.; Clausen, B. S.; Xu, Y.; Mavrikakis, M.; Bligaard, T.; Norskov, J. K. *Journal of Catalysis* **2004**, *223*, 232.
12. Cárdenas-Lizana, F.; Gómez-Quero, S.; Idriss, H.; Keane, M. A. *Journal of Catalysis* **2009**, *268*, 223.
13. Rodriguez, J. A.; Ma, S.; Liu, P.; Hrbek, J.; Evans, J.; Perez, M. *Science* **2007**, *318*, 1757.
14. Piccolo, L.; Daly, H.; Valcarcel, A.; Meunier, F. C. *Applied Catalysis B: Environmental* **2009**, *86*, 190.
15. Quinet, E.; Piccolo, L.; Morfin, F.; Avenier, P.; Diehl, F.; Caps, V.; Rousset, J.-L. *Journal of Catalysis* **2009**, *268*, 384.
16. Ford, D. C.; Nilekar, A. U.; Xu, Y.; Mavrikakis, M. *Surface Science* **2010**, *604*, 1565.
17. Barton, D. G.; Podkolzin, S. G. *The Journal of Physical Chemistry B* **2005**, *109*, 2262.
18. Joshi, A. M.; Delgass, W. N.; Thomson, K. T. *Journal of Physical Chemistry B* **2005**, *109*, 22392.
19. Wang, F.; Zhang, D.; Sun, H.; Ding, Y. *The Journal of Physical Chemistry C* **2007**, *111*, 11590.
20. Barrio, L.; Liu, P.; Rodriguez, J. A.; Campos-Martin, J. M.; Fierro, J. L. G. *Journal of Physical Chemistry C* **2007**, *111*, 19001.
21. Yin, X. L.; Calatayud, M.; Qiu, H.; Wang, Y.; Birkner, A.; Minot, C.; Woll, C. *ChemPhysChem* **2008**, *9*, 253.

22. Enevoldsen, G. H.; Pinto, H. P.; Foster, A. S.; Jensen, M. C. R.; Hofer, W. A.; Hammer, B.; Lauritsen, J. V.; Besenbacher, F. *Physical Review Letters* 2009, *102*, 136103.
23. Noei, H.; Qiu, H.; Wang, Y.; Muhler, M.; Woll, C. *ChemPhysChem* 2010, *11*, 3604.
24. Panayotov, D. A.; Yates, J. T., Jr. *Journal of Physical Chemistry C* 2007, *111*, 2959.
25. Panayotov, D. A.; Yates, J. T., Jr. *Chemical Physics Letters* 2005, *410*, 11.
26. Panayotov, D. A.; Yates, J. T., Jr. *Chemical Physics Letters* 2007, *436*, 204.
27. Wang, X.; Kim, S.; Buda, C.; Neurock, M.; Koper, O. B.; Yates, J. T., Jr. *Journal of Physical Chemistry C* 2009, *113*, 2228.
28. Sivadinarayana, C.; Choudhary, T. V.; Daemen, L. L.; Eckert, J.; Goodman, D. W. *Journal of the American Chemical Society* 2004, *126*, 38.
29. Walther, G.; Mowbray, D. J.; Jiang, T.; Johnes, G.; Jensen, S.; Quaade, U. J.; Horch, S. *Journal of Catalysis* 2008, *260*, 86.
30. Boronat, M.; Corma, A. *Dalton Transactions* 2010, *39*, 8538.
31. Barrio, L.; Liu, P.; Rodriguez, J. A.; Campos-Martin, J. M.; Fierro, J. L. G. *The Journal of Physical Chemistry C* 2007, *111*, 19001.

Chapter 5

Localized Partial Oxidation of Acetic Acid at the Dual

Perimeter Sites of the Au/TiO₂ Catalyst—Formation of Gold

Ketenylidene.*

[^]Modified with permission from I. X. Green, W. Tang, M. Neurock, and J. T. Yates, Jr., “*Localized Partial Oxidation of Acetic Acid at the Dual Perimeter Sites of the Au/TiO₂ Catalyst—Formation of Gold Ketenylidene*”, *Journal of the American Chemical Society*, Just Accepted, (2012). Copyright 2012 American Chemical Society. The theoretical work was performed by Dr. Wenjie Tang and Dr. Matthew Neurock and is included here for completeness.

Chemisorbed acetate species derived from the adsorption of acetic acid have been oxidized on a nano-Au/TiO₂ (~3 nm diameter Au) catalyst at 400 K in the presence of O₂(g). It was found that partial oxidation occurs to produce gold ketenylidene species, Au₂=C=C=O. The reactive acetate intermediates are bound at the TiO₂—perimeter sites of the supported Au/TiO₂ catalyst. The ketenylidene species is identified by its measured characteristic stretching frequency $\nu(\text{CO}) = 2040 \text{ cm}^{-1}$ and by ¹³C and ¹⁸O isotopic substitution comparing to calculated frequencies found from density functional theory. The involvement of dual catalytic Ti⁴⁺ and Au perimeter sites is postulated based on the absence of reaction on a similar nano-Au/SiO₂ catalyst. This observation excludes low coordination number Au sites as being active alone in the reaction. Upon raising the temperature to 473 K, the production of CO₂ and H₂O are observed as both acetate and ketenylidene species are further oxidized by O₂(g). The results show that partial oxidation of adsorbed acetate to adsorbed ketenylidyne can be cleanly carried out over Au/TiO₂ catalysts by control of temperature.

I. Introduction.

The scarcity of fossil fuels along with the increasing price of oil have stimulated significant efforts in the utilization of other forms of renewable energy such as biomass. Acetic acid, which is one of the most common products produced in the conversion of biomass, has gained considerable attention.¹ The transformation of acetic acid into other useful products is currently one of the key issues in the development of optimal economic strategies for the conversion of biomass. Novel Au oxidation catalysts which have demonstrated remarkable catalytic performance for the selective oxidation of CO and other hydrocarbon sources²⁻⁴ also show promising potential for oxidation processes that convert acetic acid to valuable unsaturated hydrocarbon intermediates via the selective removal of hydrogen.

Experiment as well as theory have shown that dual perimeter sites for nanometer Au/TiO₂ catalysts which involve both Au and Ti⁴⁺ centers, located at the interface of the Au nanoparticles and the TiO₂ support, catalyze oxidation reactions by dissociating O₂ molecules at these sites.⁵⁻⁸ In this paper, we show that these localized Au-Ti perimeter sites can catalytically oxidize acetic acid to a novel gold-ketenylidene surface intermediate (Au₂=C=C=O, also known as gold ketenide). This species is produced by the activation the C-H bonds in the methyl group of chemisorbed CH₃COO/TiO₂ at the Au/TiO₂ perimeter, subsequently following the breaking of one C=O bond.

The study of ketenylidene species (CCO) has taken place over a century since the first synthesis of ketene in 1905.⁹ It is considered as an important intermediate in hydrocarbon combustion,¹⁰⁻¹³ Fischer-Tropsch catalysis,¹⁴⁻¹⁸ (but see ref 19) and even in present-day astrochemistry.²⁰ Most metal ketenylidene species are synthesized as complexes with CCO ligands centered on transition metal atoms, such as Ru,¹⁴ Fe,²¹ Os,²¹ Ta,¹⁵ Zr,²² Hf,¹⁷ or Pt;²³ or observed during Cu thin film growth using a Cu organometallic complex.²⁴ A set of group 11 metal (Cu, Ag, Au) ketenylidenes was synthesized from

corresponding salts.²⁵⁻²⁷ The detection of ketenylidene species by spectroscopic measurements is typically confirmed by theoretical simulations.^{23,28-30} Since the proposal of possible surface ketenylidene species by Shriver *et al.* in 1987,¹⁴ only two documented cases of ketenylidene detection were reported on well-characterized surfaces: acetone was reacted with a pre-oxidized Ag(iii) surface;^{16,31} and CO was deposited on a W₂C(000i) surface.³² Herein, we show for the first time the spectroscopic observation of gold ketenylidene formation on a TiO₂-supported Au catalyst from the partial oxidation of acetic acid at Au-Ti dual perimeter sites at the interface using O₂(g). The reaction is particularly interesting mechanistically because the acetic acid reactant dissociatively adsorbs to form a carboxylate (CH₃COO⁻) intermediate on the TiO₂ support while the product, ketenylidene, is bound to the gold nanoparticles as a Au₂=C=C=O species.

II. Methodology.

The Au/TiO₂ catalyst (with Au particles possessing a mean diameter of ~3 nm) was synthesized using the deposition-precipitation protocol from HAuCl₄, TiO₂ powder (Degussa P 25) and urea as developed by Zanella *et al.*³³ Following synthesis, the Au/TiO₂ catalyst and a blank TiO₂ sample were pressed separately as 7 mm diameter spots into a tungsten grid and mounted into a high vacuum transmission IR cell that is described in detail previously.^{7,8} To activate and regenerate the catalyst before each experiment, a standard annealing treatment at 473 K was carried out. The treatment includes heating in vacuum for 30 min, oxidation by 18 Torr of O₂ for 210 min, followed by evacuation for 10 min. This annealing procedure removes most of the hydrocarbon species accumulated on the catalyst during its preparation, as observed by IR spectroscopy. Annealing at higher temperature was avoided to minimize possible sintering of Au particles during treatment. The samples were cooled to reaction

temperatures between 370 K and 400 K as described in each experiment after the annealing treatment.

Acetic acid (CH_3COOH , 99.9%) was purchased from Fisher Scientific. Ethylene (C_2H_4 , research purity) was purchased from Matheson TRI-GAS. Isotope labeled ethylene ($^{13}\text{C}_2\text{H}_4$, 99 atom% ^{13}C) was purchased from Sigma-Aldrich. Research purity oxygen gas (O_2 , 99.998%) was purchased from Matheson TRI-GAS. $^{18}\text{O}_2$ gas (99 atom%) was purchased from Isotec Inc. A Au/SiO₂ sample with ~3 nm Au particle diameter was generously provided by Professor R. Zanella, following the synthesis protocol described elsewhere.³⁴

In density functional theory (DFT) calculations, the ~3 nm diameter Au particles supported by TiO₂ was simulated by a 3-atomic-layer-high and 3-atom-wide Au nanorod structure bonded on top of a rutile TiO₂(110) slab, as was described in detail in Chapter 3, Section II (page 27).

III. Results and Discussion.

Figure 5.1 shows the IR spectra of saturated adsorbed acetate (from acetic acid) on the Au/TiO₂ catalyst and on the TiO₂ blank sample at 400 K after evacuation of gas phase acetic acid. The four main features observed at 2936 cm^{-1} (symmetric CH_3 stretching), 1532 cm^{-1} (asymmetric CO_2 stretching), 1454 cm^{-1} (symmetric CO_2 stretching), and 1338 cm^{-1} (CH_3 deformation) match well with other reported acetate ion adsorption features on TiO₂.³⁵ The resemblance between the two spectra indicates that acetic acid dissociatively adsorbs on the TiO₂ surface to produce acetate. A weak feature at 2040 cm^{-1} is uniquely observed on the Au/TiO₂ sample and is attributed to the acetate partial oxidation product—gold ketenylidene.³⁶ We postulate that this new species comes from acetate reacting with the adsorbed oxygen left over from the annealing treatment of

the Au/TiO₂ catalyst. The unique 2040 cm⁻¹ band corresponds to the C=O stretching motion, and falls into the observed frequency range of 2004-2076 cm⁻¹ for other reported ketenylidene ligands^{14,15,17,24,36} and the silver ketenylidene surface species.³¹ The other reported vibrational frequencies of gold ketenylidene species (VAU-C at 428 cm⁻¹; 6CCO at 562 cm⁻¹)³⁶ are below the natural spectral cut off of TiO₂ (~1000 cm⁻¹), and thus are not observed.

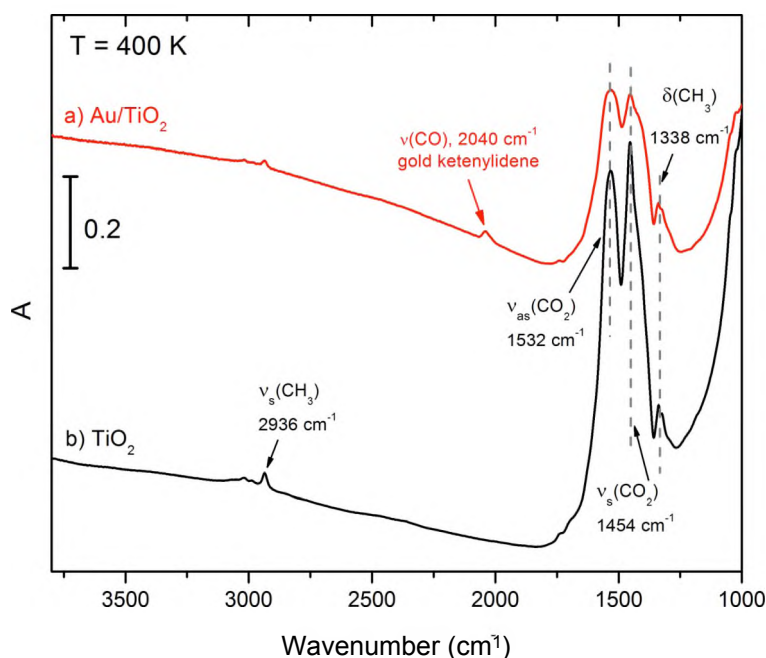


Figure 5.1. IR spectra of acetate species (from acetic acid) adsorbed on (a) Au/TiO₂ and (b) TiO₂ at 400 K.

When the adsorbed acetate on the Au/TiO₂ catalyst as reported in Figure 5.1a comes into contact with 1 Torr of gas phase O₂ at 400 K, the band at 2040 cm⁻¹ increases immediately in absorbance as shown in Figure 5.2, indicating an increase in coverage of the surface ketenylidene species due to CH₃COO/TiO₂ oxidation. Gold ketenylidene appears to be the first and only oxidation product observed by IR from adsorbed acetate ion at 400 K. No gas phase CO₂ was detected during the 90 min experiment, indicating a

lack of total oxidation at 400 K on the Au/TiO₂ catalyst. However, during the annealing treatment in O₂ at 473 K carried out to restore the catalyst surface, all adsorbed acetate and ketenylidene species were oxidized to CO₂ and H₂O, judging from the IR spectra (not shown). This behavior gives evidence for temperature-controlled oxidation. No reaction was detected from the IR observations on the TiO₂ blank sample under the same experimental conditions for 90 min, indicating that gold is necessary for the catalytic oxidation of acetate.

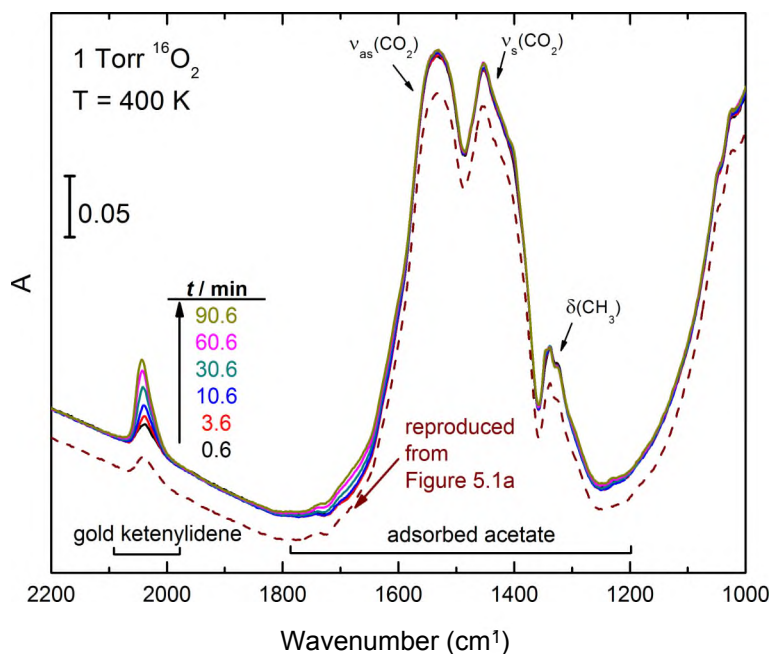


Figure 5.2. IR spectra (solid lines) of the acetate partial oxidation process on the Au/TiO₂ catalyst at 400 K under 1 Torr of O₂(g). Dotted spectrum: before O₂ exposure (reproduced spectrum from Figure 5.1a).

To further confirm the role of the Au-Ti dual perimeter sites, a Au/SiO₂ sample with a similar average gold particle size (~2.5 nm) was synthesized by Zanella *et al.*³⁴ and tested in our laboratory. Identical pre-treatment and experimental conditions to that employed for the Au/TiO₂ sample were used on the Au/SiO₂ sample, but no ketenylidene species

were detected at 400 K under 1 Torr of $O_2(g)$, as shown in Figure 5.3c. The adsorbed acetate in the SiO_2 spectrum matches with literature reports, where acetic acid deprotonates on the SiO_2 surface matches with literature reports, where acetic acid deprotonates on the SiO_2 surface.³⁷ Hydrogen bonding between the carbonyl group and the highly-hydroxylated SiO_2 surface also occurs, indicated by the intensity decrease of the isolated Si-OH band at 3735 cm^{-1} and the increase of the broad band $\sim 3571\text{ cm}^{-1}$ for hydrogen-bonded Si-OH groups.³⁷ The obvious differences between the acetate/Au/ SiO_2 spectrum (Figure 5.3b) and the acetate/Au/ TiO_2 spectrum (Figure 5.1) again confirm that the acetate observed in Figure 5.1 is adsorbed on TiO_2 and not on Au.

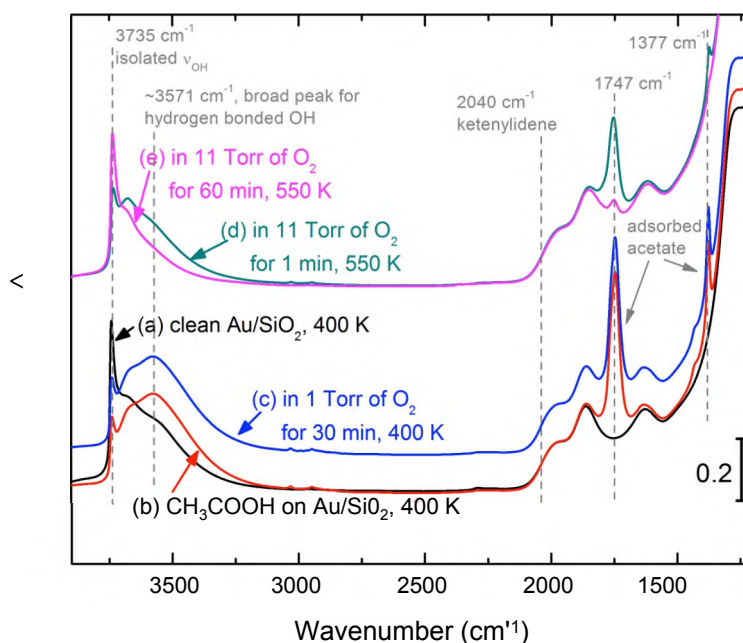


Figure 5.3. IR spectra of a similar acetic acid oxidation experiment as depicted in Figure 2 but on a Au/ SiO_2 sample. Spectra a-e are taken in one experiment sequentially: (a) clean hydroxylated Au/ SiO_2 sample at 400 K; (b) adsorbed acetic acid on Au/ SiO_2 at 400 K; (c) after contact with 1 Torr of O_2 at 400 K for 30 min; (d) ramp up temperature to 550 K and increase O_2 pressure to 11 Torr for 1 min; (e) in 11 Torr of O_2 at 550 K for 60 min.

To be sure that the Au/ SiO_2 sample is inactive towards acetic acid oxidation, the reaction temperature was increased to 550 K with an increased oxygen pressure of 11

Torr. Under these conditions, the loss of adsorbed acetate/SiO₂ species was observed during the 60 min experiment shown in Figure 5.3d-e, but no gold ketenylidene species were detected by IR spectroscopy. The negative result from the Au/SiO₂ sample shown in Figure 5.3 compared to the observed catalytic activity on the Au/TiO₂ catalytic sites for oxidation of CH₃COO/TiO₂ indicates that the oxidation requires both a Ti site and a Au site, and that low-coordinate Au sites present on Au/SiO₂ are insufficient for ketenylidene formation.

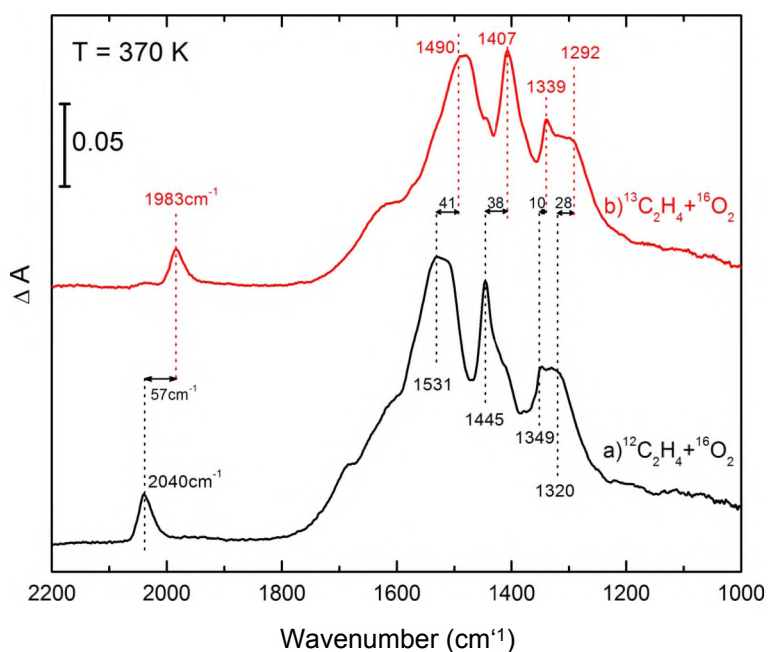


Figure 5.4. ¹³C-isotopic study of gold ketenylidene formation from ethylene oxidation on Au/TiO₂ catalyst. Spectra taken after 90 min of reaction at 370 K with 0.5 Torr of ethylene and 0.5 Torr of O₂. (a) ¹²C₂H₄ study. (b) ¹³C₂H₄ study.

In a separate set of experiments, we found that acetate and gold ketenylidene are also the final products of ethylene partial oxidation on a Au/TiO₂ catalyst at temperatures at 370 K. Utilizing this property, we used isotope-labeled ¹³C₂H₄ to confirm the vibrational assignment of gold ketenylidene. Figure 5.4 shows the oxidation products of a mixture of

0.5 Torr $^{12}\text{C}_2\text{H}_4$ and 0.5 Torr O_2 compared with the oxidation products of a mixture of 0.5 Torr $^{13}\text{C}_2\text{H}_4$ and 0.5 Torr O_2 , on the Au/TiO₂ catalyst at 370 K. Acetate and gold ketenylidene features are observed during the reaction as shown in Figure 5.4. The ^{13}C substitution caused a red shift for every vibrational feature observed in acetate and gold ketenylidene. A 57 cm^{-1} red shift was measured for $\text{Au}_2=^{13}\text{C}=^{13}\text{C}=^{16}\text{O}$ (1983 cm^{-1}) compared to $\text{Au}_2=^{12}\text{C}=^{12}\text{C}=^{16}\text{O}$ (2040 cm^{-1}). In addition to ^{13}C isotope labeling, we also used ^{18}O (99%) to oxidize ethylene. A $\text{Au}_2=^{12}\text{C}=^{12}\text{C}=^{18}\text{O}$ adsorption band at 2010 cm^{-1} was observed (spectrum not shown), red shifted 30 cm^{-1} from the non-labeled $\text{Au}_2=^{12}\text{C}=^{12}\text{C}=^{16}\text{O}$ species.

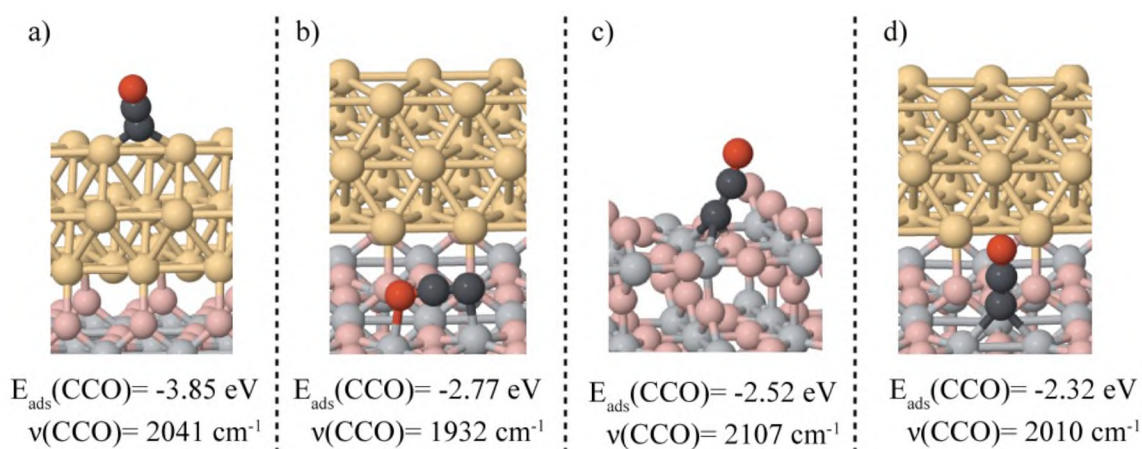
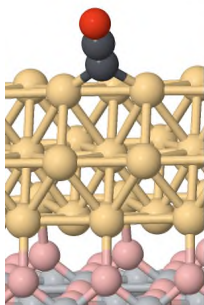


Figure 5.5. The adsorption energy and $\nu(\text{C}=\text{O})$ vibrational frequency for the most stable configurations of ketenylidene on different sites: a) on Au-Au edge site, b) on Ti5c sites at the Au/TiO₂ perimeter, c) on Ti5c site removed from the Au/TiO₂ interface. Panel d) shows the second most stable configuration of ketenylidene on a Ti5c site at the perimeter.

To rationalize these frequency shifts, we carried out first principles density functional theory (DFT) calculations to simulate the chemisorbed gold ketenylidene structure and its corresponding frequencies. We surveyed the entire Au/TiO₂ model surface and calculated the most probable adsorption sites in order to find the most stable configurations for the ketenylidene species, including the Au and Ti5c sites at the

Au/TiO₂ perimeter, as well as the Ti₅C sites removed from the interface. The linear ketenylidene species preferentially binds to the bridge Au-Au edge site (CN=7) at the top of the Au cluster to form a Au₂=C=C=O species that is oriented away from the edge as shown in Table 5.1. The adsorption energy of ketenylidene at this site was calculated to be -3.85 eV (Figure 5.5a) which is significantly larger than the other configurations examined, including the formation of a di-o bound Ti₅c-C=C=O-Ti₅c intermediate which lies parallel the TiO₂ surface (-2.77 eV, Figure 5.5b), the formation of (Ti₅c)₂-C=C=O intermediates oriented normal to the TiO₂ support removed from the Au nano-rod (-2.52 eV, Figure 5.5c) as well as at interfacial Ti₅c-Ti₅c sites at the Au perimeter (-2.32 eV, Figure 5.3d).

Table 5.1. Comparison of experimentally measured gold ketenylidene isotopically-labeled species frequencies, and DFT calculated frequencies.



Species	$\nu(\text{DFT})$ (cm ⁻¹)	$\nu(\text{Exp})$ (cm ⁻¹)
Au ₂ = ¹² C= ¹² C= ¹⁶ O	2041	2040
Au ₂ = ¹³ C= ¹³ C= ¹⁶ O	1980	1983
Au ₂ = ¹² C= ¹² C= ¹⁸ O	2016	2010

In addition to AU₂ being the most stable adsorption site for ketenylidene it also results in the closest theoretical $\nu(\text{C}=\text{O})$ vibrational frequency (2041 cm⁻¹) to the band frequency measured experimentally (2040 cm⁻¹) for the non-isotope-labeled gold ketenylidene species. The calculated vibrational frequencies for ketenylidene adsorbed on the various Ti₅C sites (Figure 5.5) differ from the experimental measured value by more than 30 cm⁻¹. The calculated isotopic shift of the $\nu(\text{C}=\text{O})$ frequency for the

$\text{Au}_2=\text{C}=\text{C}=\text{O}$ configuration compared to the experimental measurements are summarized in Table 5.1. The close match confirmed the observation of the production of gold ketenylidene chemisorbed species from the partial oxidation of $\text{CH}_3\text{COO}/\text{TiO}_2$.

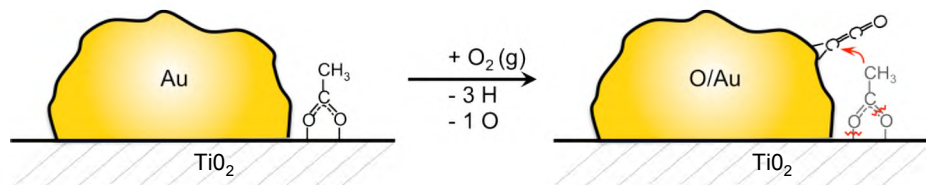


Figure 5.6. Scheme of the catalytic oxidation of $\text{CH}_3\text{COO}/\text{TiO}_2$ at the perimeter of the Au/TiO_2 particle, forming $\text{Au}_2=\text{C}=\text{C}=\text{O}$.

The catalytic partial oxidation of acetate ion adsorbed on TiO_2 to form gold ketenylidene at the dual perimeter sites of the Au/TiO_2 catalyst thus appears to proceed through a series of steps involving C-H bond scission and C-O bond scission. We postulate that the C-H bond scission is activated by the atomic O generated from $\text{O}_2(\text{g})$ dissociation at the Au-Ti dual perimeter sites.^{7,8} Following C-H bond scission, the Au-C bonds start to form, which facilitates the activation of the C-O bond at the Ti cationic sites. A schematic of the oxidation process from $\text{CH}_3\text{COO}/\text{TiO}_2$ to the $\text{O}=\text{C}=\text{C}/\text{Au}$ intermediate is shown in Figure 5.6.

To the best of our knowledge, this is the first report of the catalytic oxidation of acetate (and ethylene) to ketenylidene over a supported Au catalyst. The gold ketenylidene species formed at temperatures around 400 K can be further oxidized to CO_2 and H_2O at 473 K on the same catalyst, illustrating that the depth of the catalytic oxidation can be controlled by varying the reaction temperature. The acetate to ketenylidene formation path is a combination of dehydrogenation (oxidation) and

deoxygenation of chemisorbed acetate, which are crucial steps for biomass conversion into more valuable industrial chemicals.

IV. Acknowledgement.

We gratefully thank Dr. Rodolfo Zanella for generously providing us with the Au/SiO₂ sample. We also acknowledge the support of this work by Department of Energy—Office of Basic Energy Sciences, under grant number DE-FG02-09ER16080 as well as a fellowship for Mrs. Isabel Green from AES Corporation through the AES Graduate Fellowships in Energy Research Program at the University of Virginia, and the XSEDE computing resources from Texas Advanced Computing Center.

Chapter 5 References:

1. Munasinghe, P. C.; Khanal, S. K. *Bioresource Technology* **2010**, *101*, 5013.
2. Haruta, M.; Kobayashi, T.; Sano, H.; Yamada, N. *Chemistry Letters* **1987**, *2*, 405.
3. Meyer, R.; Lemire, C.; Shaikhutdinov, S. K.; Freund, H.-J. *Gold Bulletin* **2004**, *37*, 72.
4. Haruta, M. *CATTECH* **2002**, *6*, 102.
5. Laursen, S.; Linic, S. *Physical Chemistry Chemical Physics* **2009**, *11*, 11006.
6. Wang, J. G.; Hammer, B. *Physical Review Letters* **2006**, *97*, 136107.
7. Green, I. X.; Tang, W.; Neurock, M.; Yates, J. T., Jr. *Science* **2011**, *333*, 736.
8. Green, I. X.; Tang, W.; Neurock, M.; Yates, J. T., Jr. *Angewandte Chemie International Edition* **2011**, *50*, 10186.
9. Staudinger, H. *Berichte der deutschen chemischen Gesellschaft* **1905**, *38*, 1735.
10. Bayes, K. D. *The Journal of Chemical Physics* **1970**, *52*, 1093.
11. Fontijn, A.; Johnson, S. E. *The Journal of Chemical Physics* **1973**, *59*, 6193.
12. Sault, A. G.; Madix, R. J. *The Journal of Physical Chemistry* **1986**, *90*, 4723.
13. Sault, A. G.; Madix, R. J. *Surface Science* **1986**, *172*, 598.

14. Sailor, M. J.; Shriver, D. F. *Journal of the American Chemical Society* **1987**, *109*, 5039.
15. Neithamer, D. R.; LaPointe, R. E.; Wheeler, R. A.; Richeson, D. S.; Van Duyne, G. D.; Wolczanski, P. T. *Journal of the American Chemical Society* **1989**, *111*, 9056.
16. Sim, W. S.; King, D. A. *Journal of the American Chemical Society* **1995**, *117*, 10583.
17. Calderazzo, F.; Englert, U.; Guarini, A.; Marchetti, F.; Pampaloni, G.; Segre, A.; Tripepi, G. *Chemistry – A European Journal* **1996**, *2*, 412.
18. Deng, L.-J.; Huo, C.-F.; Liu, X.-W.; Zhao, X.-H.; Li, Y.-W.; Wang, J.; Jiao, H. *The Journal of Physical Chemistry C* **2010**, *114*, 21585.
19. Blyholder, G.; Emmett, P. H. *The Journal of Physical Chemistry* **1960**, *64*, 470.
20. Ohishi, M.; Suzuki, H.; Ishikawa, S. I.; Yamada, C.; Kanamori, H.; Irvine, W. M.; Brown, R. D.; Godfrey, P. D.; Kaifu, N. *Astrophysical Journal* **1991**, *380*, L39.
21. Shriver, D. F.; Sailor, M. J. *Accounts of Chemical Research* **1988**, *21*, 374.
22. Calderazzo, F.; Englert, U.; Guarini, A.; Marchetti, F.; Pampaloni, G.; Segre, A. *Angewandte Chemie International Edition in English* **1994**, *33*, 1188.
23. Bertani, R.; Casarin, M.; Ganis, P.; Maccato, C.; Pandolfo, L.; Venzo, A.; Vittadini, A.; Zanutto, L. *Organometallics* **2000**, *19*, 1373.
24. Girolami, G. S.; Jeffries, P. M.; Dubois, L. H. *Journal of the American Chemical Society* **1993**, *115*, 1015.
25. Blues, E. T.; Bryce-Smith, D.; Hirsch, H.; Simons, M. J. *Journal of the Chemical Society D: Chemical Communications* **1970**.
26. Blues, E. T.; Bryce-Smith, D.; Kettlewell, B.; Roy, M. *Journal of the Chemical Society, Chemical Communications* **1973**.
27. Blues, E. T.; Bryce-Smith, D.; Lawston, I. W.; Wall, G. D. *Journal of the Chemical Society, Chemical Communications* **1974**, 513.
28. Sailor, M. J.; Went, M. J.; Shriver, D. F. *Inorganic Chemistry* **1988**, *27*, 2666.
29. Li, J.; Bursten, B. E.; Zhou, M.; Andrews, L. *Inorganic Chemistry* **2001**, *40*, 5448.
30. Casarin, M.; Pandolfo, L. *Journal of Organometallic Chemistry* **2003**, *682*, 255.
31. Sim, W. S.; King, D. A. *The Journal of Physical Chemistry* **1996**, *100*, 14794.
32. Aizawa, T.; Otani, S. *The Journal of Chemical Physics* **2011**, *135*, 144704.
33. Zanella, R.; Giorgio, S.; Henry, C. R.; Louis, C. *Journal of Physical Chemistry B* **2002**, *106*, 7634.
34. Zanella, R.; Sandoval, A.; Santiago, P.; Basiuk, V. A.; Saniger, J. M. *The Journal of Physical Chemistry B* **2006**, *110*, 8559.

35. Liao, L.-F.; Lien, C.-F.; Lin, J.-L. *Physical Chemistry Chemical Physics* 2001, 3, 3831.
36. Blues, E.; Bryce-Smith, D.; Lawston, I. *Gold Bulletin* 1976, 9, 88.
37. Young, R. P. *Canadian Journal of Chemistry* 1969, 47, 2237.

Chapter 6

Mechanism of the Partial Oxidation of Acetic Acid by O₂ at the Dual Perimeter Sites of a Au/TiO₂ Catalyst.*

*Modified version of that prepared for The Journal of Physical Chemistry C. The theoretical work was performed by Dr. Wenjie Tang and Dr. Matthew Neurock and is included here for completeness.

A novel gold ketenylidene species ($\text{Au}_2=\text{C}=\text{C}=\text{O}$) was recently observed by infrared spectroscopy from the partial oxidation of acetic acid by O₂ on a Au/TiO₂ catalyst. The mechanism of this partial oxidation reaction is studied experimentally as well as theoretically by density functional theory (DFT). The reaction was found to be localized at the dual perimeter sites of the Au/TiO₂ catalyst, where O₂ was activated. No ketenylidene formation was observed on the Au/SiO₂ catalyst or a TiO₂ blank sample. The mechanism involves multiple C-H bonds and C-O bond scission at the Au-Ti⁴⁺ dual perimeter sites, where C-H bonds scission occurs on Au sites and C-O bond scission occurs on neighbor TiO₂ sites. An ¹⁸O₂ isotopic labeling experiment indicated that the O moiety of the ketenylidene species originated from the acetic acid. The rate-limiting step was found to be the C-O bond scission. An overall activation energy of 1.80 eV was found from the DFT calculation, which matched the experimentally measured apparent activation energy of 1.7 ± 0.2 eV. A deuterium kinetic isotope effect of ~4 indicates that the C-H bonds activation is important in the overall acetate oxidation reaction.

I. Introduction.

Since organic acids are one of the common products from biomass conversion, research on the decarboxylation, reduction, and partial oxidation of organic acids such as acetic acid, yielding high value feedstock molecules, is of importance.¹ Acetic acid is a

good model molecule for organic acids due to its simplicity and characteristic carboxylate functional group. As a result, the total oxidation of acetic acid over metal oxide catalysts such as TiO₂ and SnO₂ has been studied extensively as a model reaction for volatile organic molecule removal from polluted air.²⁻⁴

As a novel oxidation catalyst, gold nanoparticles supported on TiO₂ have shown fascinating activity in reactions involving molecular O₂, such as CO oxidation,⁵⁻⁸ H₂ oxidation,⁹ and propene epoxidation.¹⁰ Various density functional theory (DFT) simulations,^{7,9,11,12} accompanying experimental results,^{7,9,13} pinpointed the active sites for O-O bond dissociation at the Au-Ti⁴⁺ dual perimeter sites where Au and TiO₂ meet. In low temperature H₂ oxidation⁹ and room temperature H₂-D₂ exchange¹⁴ experiments, it was demonstrated that the Au/TiO₂ catalyst can also activate H-H bond dissociation at the Au nanoparticle perimeter. The atomic H atoms generated at the perimeter can spill over to the TiO₂ support and cause a dramatic increase in IR background intensity due to the population of empty states near the bottom of the conduction band of TiO₂.^{9,15}

We have briefly reported the partial oxidation of acetic acid at the dual perimeter sites of a Au/TiO₂ catalyst, forming gold ketenylidene (Au₂CCO) species.¹⁶ The reactant, acetic acid, adsorbs on the TiO₂ support forming acetate/TiO₂, while the observed partial oxidation product, Au₂CCO, adsorbs on the Au nanoparticles. The change in adsorption sites during reaction indicates that the active sites for this partial oxidation correspond to the Au-Ti⁴⁺ dual perimeter sites which surround ~ 3 nm Au nanoparticles on TiO₂. Herein, we provide kinetic studies of the partial oxidation reaction using in situ transmission FTIR measurements. Together with DFT calculations, we present a reaction mechanism involving three C-H bond activation steps at the Au/TiO₂ dual perimeter sites. The C-H bond activation is aided by atomic O species, which are also formed at the perimeter sites.

II. Methodology.

The high vacuum transmission FTIR cell as well as the Au/TiO₂ catalyst has been described in great detail in Chapter 2. To test the necessity of the Au-Ti⁴⁺ dual perimeter sites for the catalytic reaction, a Au/SiO₂ sample with ~3 nm Au particle diameter was generously provided by Professor R. Zanella, following the synthesis protocol described elsewhere.¹⁷ Experiments related to the Au/SiO₂ catalyst were done separately from the Au/TiO₂ and TiO₂ catalysts, with similar pre-treatment and experimental parameters.

Before each use, the catalysts were treated at 473 K in vacuum for 30 min, in 18 Torr of O₂ for 210 min, followed by evacuation for 10 min. This treatment removes most of the IR-visible hydrocarbon impurities accumulated on the catalysts' surface during synthesis and assembly. Complete removal of the hydroxyl species requires more aggressive annealing at elevated temperatures (above 673 K for TiO₂^{18,19} and well above 1000 K for SiO₂²⁰). Such high temperature procedures were not performed to avoid Au particle aggregation. This treatment can also remove acetate from the Au/TiO₂ catalyst surface, but not for TiO₂ or Au/SiO₂, as will be discussed in Section III.C.

Acetic Acid (CH₃COOH, 99.9%) was purchased from Fisher Scientific. Isotope labeled acetic acid species, acetic acid-1-¹³C (CH₃¹³COOH, 99 atom% ¹³C) and acetic acid-D₄ (CD₃COOD, 99.9 atom% D), were purchased from Sigma-Aldrich. Freeze-pump-thaw cycles were performed before use on all three kinds of acetic acid. Urea (99.5%) and HAuCV₃H₂O were purchased from Acros. Research purity ¹⁶O₂ gas (99.998%) was purchased from Matheson TRI-GAS. ¹⁸O₂ gas (99% isotopic purity) was purchased from Isotec, Inc.

All simulations reported herein were carried out using density functional theory (DFT) calculations as implemented in the Vienna ab initio Simulation Package (VASP).²¹ Modeling details can be found in Chapter 3, Section II (page 27).

III. Results and Discussion.

A. FTIR Study of Acetic Acid Adsorption on Different Catalyst Surfaces.

Figure 6.1 shows the IR spectra of the three catalyst surfaces of interest, namely TiO_2 , Au/TiO_2 , and Au/SiO_2 , interacting with acetic acid at 400 K. Black spectra show the catalyst surfaces in vacuum after pre-treatment, before acetic acid exposure; red spectra show the catalysts in contact with 0.5 Torr of acetic acid gas, followed by evacuation for 30 min at 400 K. The adsorption features of acetic acid are similar comparing TiO_2 and Au/TiO_2 , but very different on the Au/SiO_2 surface. These observations indicate that acetic acid absorbs on TiO_2 and SiO_2 differently, and that Au nanoparticles make little contribution to the spectral features.²²

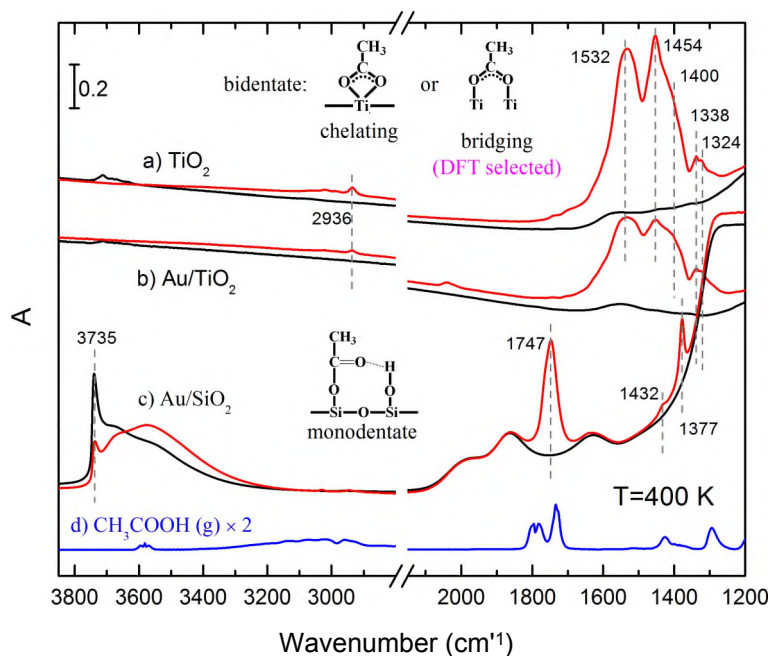


Figure 6.1. IR spectra of acetic acid adsorption at 400 K on a). TiO_2 ; b). Au/TiO_2 ; and c). Au/SiO_2 . Black spectra—clean catalysts surface; red spectra—0.5 Torr acetic acid followed by evacuation for 30 min. Spectrum d) shows 0.5 Torr gas phase acetic acid IR adsorption.

Figure 6.id shows the gas phase IR spectrum of acetic acid (0.5 Torr) at 400 K. When adsorbed at 400 K, acetic acid forms surface acetate species on all surfaces.^{4,23-30} According to other IR reports on acetate adsorption on TiO₂,^{4,23-26} the main features labeled on Figures 6.1a and 6.1b are assigned as following: 2936 cm⁻¹, symmetric CH₃ stretching (vs(CH₃)); 1532 cm⁻¹, asymmetric -COO stretching (vas(CO₂)); 1454 cm⁻¹, symmetric -COO stretching (vs(CO₂)); 1400 cm⁻¹, 1338 cm⁻¹, and 1324 cm⁻¹, CH₃ bending (δ (CH₃)). The frequency difference between symmetric and asymmetric ν (CO₂) is 78 cm⁻¹, indicating the acetate is adsorbed on the TiO₂ surface via a symmetrical bidentate orientation, as shown for chelating and bridging acetate species in the inset in Figure 6.1a.²³⁻²⁵ Clearly distinguishing between the chelating structure and the bridging structure by IR vibrational frequencies is difficult and under debate.²³⁻²⁵ However, DFT simulations of acetate adsorption on the TiO₂ rutile (110) surface (this work, Section III.B), the anatase (010) surface,³¹ and the anatase (101) surface,³² all indicate that the bridging configuration is more stable than the chelating structure.

Acetic acid adsorbs on the SiO₂ surface as acetate species at 400 K as well.²⁷⁻³⁰ However, the acetate/SiO₂ IR features are quite different from the acetate/TiO₂ features in the ν (CO₂) region: three bands at 1747 cm⁻¹, 1432 cm⁻¹, and 1377 cm⁻¹ are observed. Young has reported a careful IR comparison of the adsorption of acetic acid, acetyl chloride, and acetic anhydride on SiO₂ surfaces at 300 K and 423 K, and found the three bands described above in all cases.²⁹ It is then deduced that acetate adsorbs on SiO₂ via a monodentate configuration, where the 1747 cm⁻¹, 1432 cm⁻¹, and 1377 cm⁻¹ bands corresponding to C=O stretching (ν (CO)), asymmetrical CH₃ bending (δ as(CH₃)), and symmetrical CH₃ bending (δ s(CH₃)), respectively. The higher frequency bands at 3030 cm⁻¹ and 2946 cm⁻¹ correspond to Vas(CH₃) and Vs(CH₃), respectively. The highest frequency band at 3735 cm⁻¹, corresponding to isolated SiO-H stretching on the SiO₂

surface, is heavily perturbed by acetate adsorption, forming hydrogen bonds with the carbonyl moiety. One possible adsorption configuration of acetate on the SiO₂ surface is given in the inset to Figure 6.1c.

B. DFT Simulation of Acetate Formation and Most Stable Configuration on the Au/TiO₂ Catalyst.

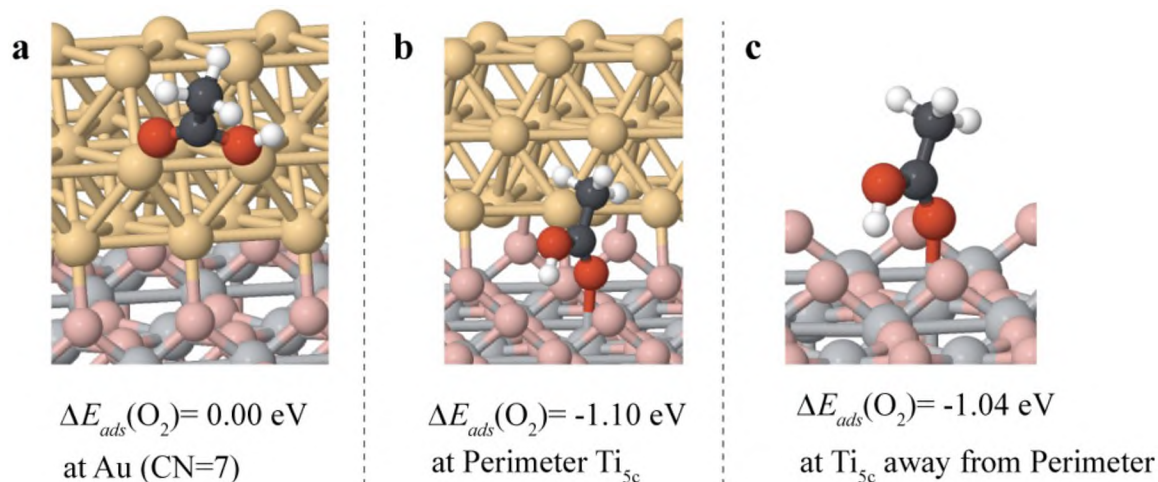


Figure 6.2. Acetic acid adsorption at different sites. The Au atoms and Ti atoms are shown in yellow and grey respectively, whereas the O in the TiO₂ lattice, adsorbed O, C atoms and H atoms are shown in pink, red, black and white respectively. ΔE_{ads} refers to the adsorption energy.

Since the IR bands observed for acetate/TiO₂ species cannot discriminate between chelating and bridging acetate adsorption configurations (Figure 6.1), we employed DFT simulation to locate the most favorable site for the acetic acid adsorption and acetate formation on the Au/TiO₂ catalyst. It is found that acetic acid does not bind to the Au nano-particle, even at the low coordinated Au site that has a coordination number (CN) of 7 (Figure 6.2a). A gas phase acetic acid molecule approaching the Au nano-particle needs to overcome a 0.95 eV OH group de-protonation barrier to form acetate, with an endothermic reaction heat of 0.04 eV, as shown in Figure 6.3a. The lack of stability of the

acetic acid molecule and the high barrier required for the acetate/Au formation exclude the Au site as the active site for adsorption or reaction, which agrees with the experimental observation shown in Figure 6.1.

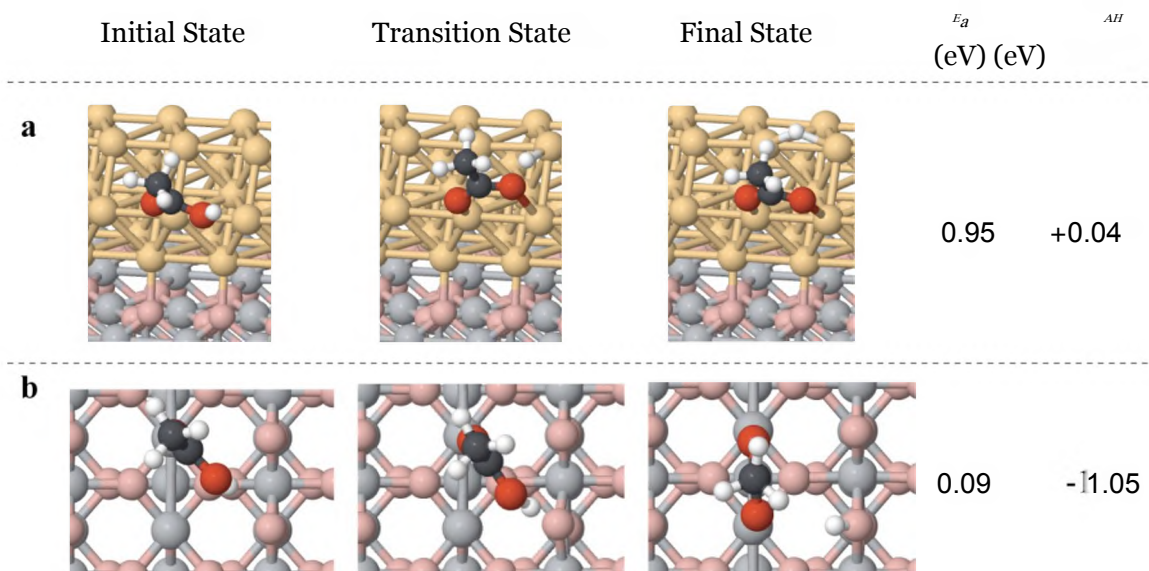


Figure 6.3. Acetate formation from acetic acid on a). TiO₂ and b). Au sites. E_a and ΔH refer to the activation barrier and reaction enthalpy, respectively.

Unlike on the Au nano-particles, the acetic acid molecule binds strongly to the TV sites of the TiO₂ support, with adsorption energies ranging from -1.04 eV to -1.10 eV (Figure 6.2b-c). The acetic acid molecule binds to the TiO₂ surface through the carbonyl O moiety to the Ti_{5c} sites, with the acidic proton forming a hydrogen bond with the bridging lattice oxygen from the TiO₂, as shown in Figure 6.2b-c. The de-protonation of adsorbed acetic acid to form acetate on TiO₂ proceeds easily with a small barrier of 0.09 eV and an exothermic reaction heat of 1.05 eV, as shown in Figure 6.3b.

We also compared the adsorption energy of the chelating and the bridging bidentate configuration of acetate/TiO₂ shown in Figure 6.1 and found that the bridging configuration (Figure 6.3b) is ~1.0 eV more stable than the chelating bidentate. A recent

STM study and DFT calculation of acetic acid adsorption on anatase TiO_2 surface also found the bridging configuration to be the stable adsorption state.³² Thus, we will use the bridging bidentate configuration to simulate acetate/ TiO_2 .

C. FTIR Study of the Interaction between Adsorbed Acetate and Oxygen on Different Catalyst Surfaces.

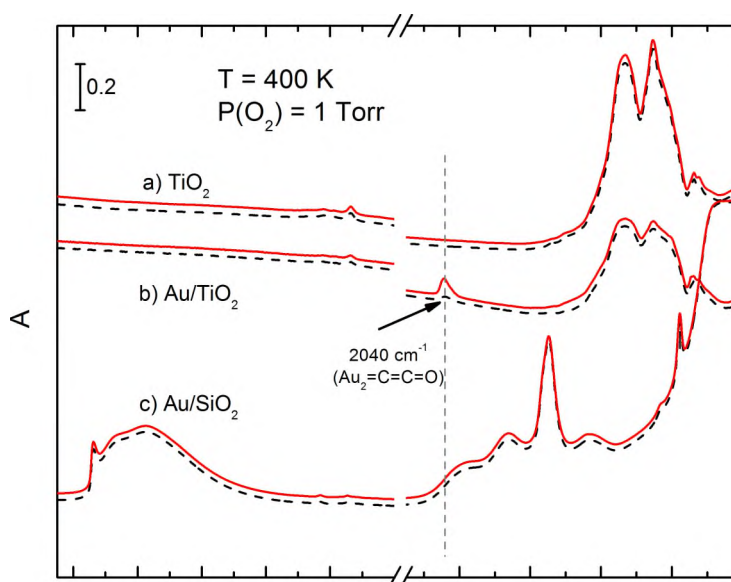


Figure 6.4. IR spectra of adsorbed acetate reacting with 1 Torr of O_2 on three catalysts at 400 K: a), on TiO_2 ; b), on Au/TiO_2 ; and c), on Au/SiO_2 . Black spectra—before O_2 exposure (reproduced from the red spectra of Figure 6.1a); red spectra—in contact with 1 Torr of O_2 at 400 K for 90 min.

The acetate-saturated surfaces shown in Figure 6.1 were exposed to 1 Torr of O_2 at 400 K and monitored for 90 min under steady state. Figure 6.4a shows the results on the TiO_2 sample, where little change developed after 90 min. In contrast, Figure 6.4b shows the development on the Au/TiO_2 catalyst, where the formation of the gold ketenylidene species (Au_2CCO) is observed by IR at 2040 cm^{-1} .¹⁶ A small amount of Au_2CCO was already formed after acetic acid adsorption in Figure 6.1b, showing that the high temperature O_2 pre-treatment (described in Section II.A) left a trace amount of adsorbed

O species on the catalyst surface which is reactive at 400 K.³³ Little change in the acetate features upon Au₂CCO formation were observed on the Au/TiO₂ sample in Figure 6.4b, indicating that the partial oxidation of acetate, forming Au₂CCO, is a minor reaction causing the majority of the acetate species to remain unaffected.

The interaction between acetate/SiO₂ and 1 Torr of O₂ at 400 K is minimal at 400 K, as shown in Figure 6.4c. The negative results on TiO₂ and Au/SiO₂ indicate that the partial oxidation of acetate/TiO₂ to form Au₂CCO is catalyzed at the Au-Ti⁴⁺ perimeter sites at 400 K. Since Au/SiO₂ contains coordinatively unsaturated Au atoms at the perimeter of the ~3 nm Au particles, this experiment indicates that sites of this kind alone are insufficient for acetate partial oxidation which can only be induced by dual sites involving both Au and TiO₂.

To further demonstrate the special properties of the Au-Ti⁴⁺ perimeter sites, a set of experiments investigating the interaction of acetate with O₂ at elevated temperatures on the three different surfaces were performed, as shown in Figure 6.5. Since the Au/TiO₂ and TiO₂ catalysts were held on the same tungsten mesh, the reaction temperature was chosen to be 473 K to protect the Au/TiO₂ catalyst from sintering. As shown in Figure 6.5a-b, after 210 min in 18 Torr of O₂, acetate intensity decreased only slightly on the TiO₂ sample, while most of the acetate disappeared on the Au/TiO₂ catalyst. Gas phase CO₂ was also detected in the cell, as highlighted in Figure 6.5. The CO₂ is believed to be the product of the total oxidation of acetate and ketenylidene on the Au/TiO₂ catalyst. The other total oxidation product, H₂O, is not detected on the surface at 473 K, and is also not detected in the gas phase, possibly due to adsorption on the room temperature-cell walls. The TiO₂ sample is held in the same experimental environment as the Au/TiO₂ catalyst, and thus gas phase CO₂ is also detected when the TiO₂ sample is observed, as shown in Figure 6.5a.

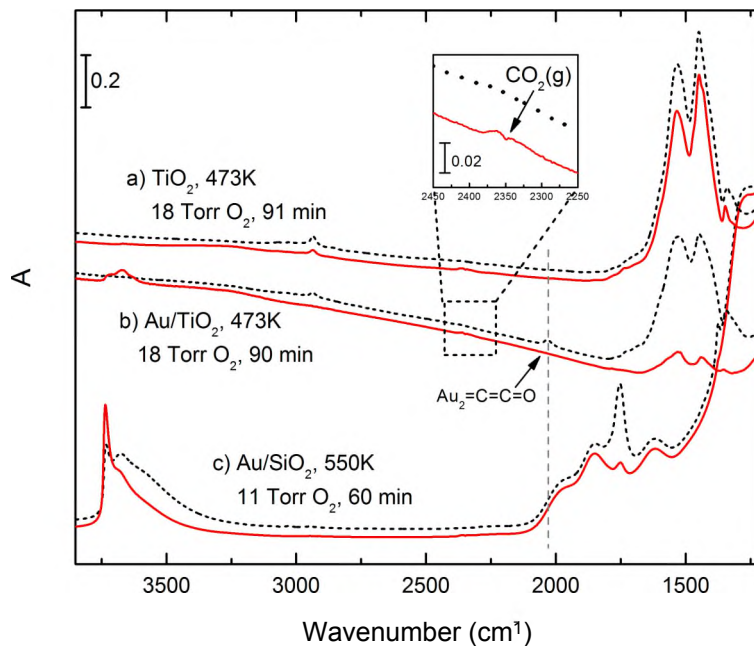


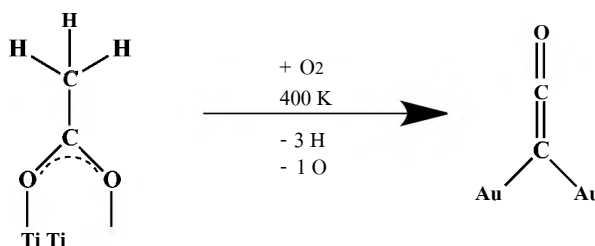
Figure 6.5. IR spectra of adsorbed acetate reacting with O_2 on three catalysts at elevated temperatures: a). on TiO_2 with 18 Torr of O_2 at 473 K; b). on Au/TiO_2 with 18 Torr of O_2 at 473 K; and c). on Au/SiO_2 with 11 Torr of O_2 at 550 K. Black spectra—upon just reaching target temperature, before O_2 exposure; red spectra—after reaction in O_2 .

More aggressive oxidation of acetate/ SiO_2 using 11 Torr of O_2 at 550 K on the Au/SiO_2 sample is shown in Figure 6.5c. Higher temperature is used here because no IR spectral change was detected at 473–500 K at all. At 550 K, during 60 min of reaction, most of the adsorbed acetate/ SiO_2 species disappeared from the IR spectrum, as indicated by the loss of acetate/ SiO_2 spectral features and the reappearance of isolated SiO-H groups, but little oxidation product (no Au_2CCO and little $CO_2(g)$) was detected.

The more aggressive high temperature studies shown in Figure 6.5 confirmed that without the $Au-Ti^{4+}$ dual perimeter sites, no ketenylidene species is produced from acetate partial oxidation. It also demonstrated that the oxidation depth of the acetate/ TiO_2 species on the Au/TiO_2 catalyst can be tuned by reaction temperature—partial oxidation at 400 K and total oxidation at 473 K.

D. Partial Oxidation of Acetate with $^{18}\text{O}_2$ Isotopic Species on Au/TiO₂.

The oxidative formation of Au₂CCO from acetate/TiO₂ on the Au/TiO₂ catalyst requires the synergistic action of TiO₂ sites and Au sites in close proximity on the multi-material catalyst: the reactant acetate is adsorbed on the TiO₂ support and the product ketenylidene is adsorbed on the Au nanoparticles, as shown in Scheme 6.1. The reaction involves multiple C-H and C-O bond activations. The partial oxidation would not proceed without oxygen, indicating that the activation of the C-H and/or the C-O bond is



Scheme 6.1. Acetate/TiO₂ partial oxidation forming Au₂CCO.

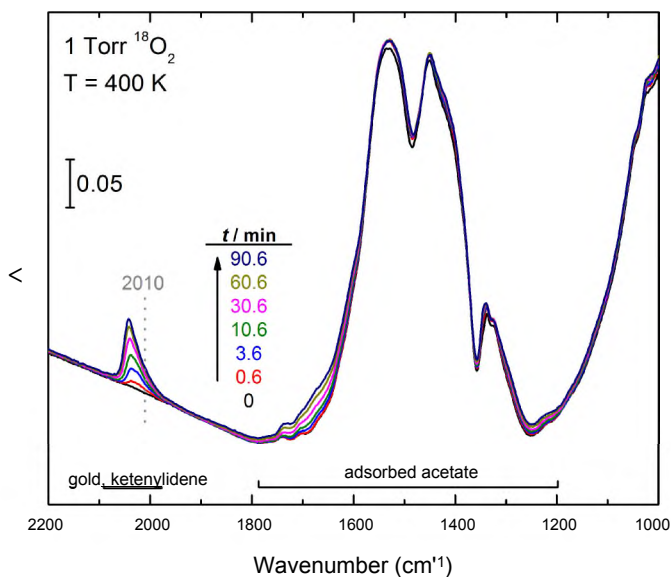


Figure 6.6. IR spectra of the partial oxidation of acetate by $^{18}\text{O}_2$ on Au/TiO₂. Dotted line indicates the absorption frequency of Au₂CC¹⁸O, which is not observed.

assisted by O₂. To identify the origin of the O atom in the final Au₂CCO product, a ¹⁸O₂ isotope experiment was carried out.

As shown in Figure 6.6, during the 90 min experiment with ¹⁸O₂ gas at 400 K, no ¹⁸O scrambled species (characteristic $\nu(\text{CO})=2010\text{ cm}^{-1}$)¹⁶ is detected. This confirms that the O in Au₂CCO comes from the original acetate species.

E. Kinetic Studies of the Formation of Ketenylidene.

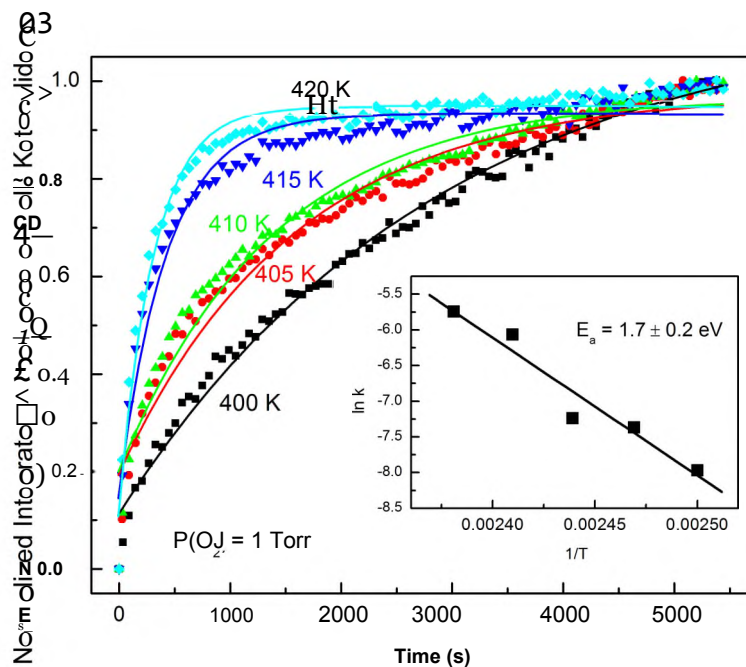


Figure 6.7. Kinetic studies of the partial oxidation of acetate to ketenylidene on the Au/TiO₂ catalyst. Solid curves underneath experimental data points are mathematical fits to first-order kinetics. Inset shows the Arrhenius plot.

Steady state partial oxidation of acetate on the Au/TiO₂ catalyst as shown in Figure 6.6 was carried out in the temperature range of 400–420 K for kinetic studies, under 1 Torr of O₂. The integrated absorbance of the Au₂CCO band centered at 2040 cm⁻¹ is used as a measure of the amount of product accumulated on the catalyst surface. The

oxidation reaction becomes significantly retarded after 90 min at all temperatures, indicated by the sluggish rate of growth of the Au₂CCO IR band when approaching the 90 min endpoint. Normalization of the integrated absorbance of Au₂CCO species to the maximum measured value is carried out to make experiments executed on different days more comparable. Plots of the reaction extent at five different temperatures are shown in Figure 6.7. The five experiments with various temperatures were carried out randomly in sequence.

Since the catalyst surface is saturated with acetate before reaction and since oxygen is abundant from the gas phase, the reaction is pseudo-first order in active site concentration located at the Au-Ti⁴⁺ perimeter, as shown in Equation 6.1.

$$R_{\text{ate}} = -\frac{d[\text{Au}_2\text{CCO}]}{dt} = k_x[\text{acetate}][\text{O}_2][\text{Active Site}] = k'_x[\text{Active Site}] \quad (6.1)$$

The solid lines under experimental data points shown in Figure 6.7 display the mathematical fit to first-order kinetics. The normalization described earlier does not alter the reaction constant k obtained from the mathematical fit. The Arrhenius plot is constructed as shown in the inset of Figure 6.7, yielding an apparent activation energy of 1.7 ± 0.2 eV.

F. Study of the Deuterium Kinetic Isotope Effect (DKIE) in the Partial Oxidation of Acetate Species.

As shown in Scheme 6.1, the partial oxidation of acetate/TiO₂ forming Au₂CCO involves multiple C-H bond scission steps and one C-O bond scission step. To elucidate the nature of the transition state, a DKIE study was designed, where a 1-to-1-ratio acetic acid-H₄ and acetic acid-D₄ mixture was pre-made in the gas-line and exposed to the Au/TiO₂ catalyst in a competitive experiment. In order to distinguish the partial

oxidation product from H- and D-labeled acetate, the hydrogen-free gold ketenylidene, ^{13}C labeling was employed for the acetic acid- H_4 species ($\text{CH}_3^{13}\text{COOH}$). As a result, observation of the formation of non-labeled Au_2CCO species at 2040 cm^{-1} allows the measurement of the rate of CD_3COO partial oxidation, while observation of the ^{13}C -isotopic labeled $\text{Au}_2\text{C}^{13}\text{CO}$ species at lower frequency ($\sim 1990\text{ cm}^{-1}$) allows the rate of $\text{CH}_3^{13}\text{COO}$ partial oxidation to be simultaneously measured.

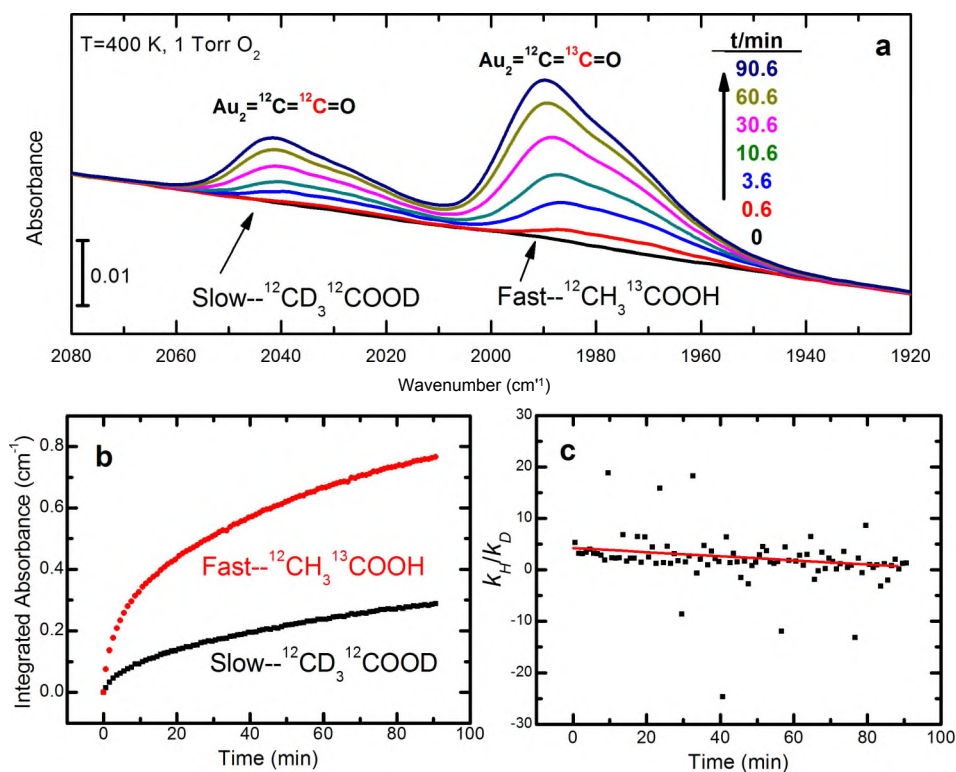


Figure 6.8. Deuterium kinetic isotope study, a). Partial oxidation of **1:1** ratio of adsorbed $\text{CH}_3^{13}\text{COO}/\text{TiO}_2$ and $\text{CD}_3\text{COO}/\text{TiO}_2$ at 400 K; b). plots of the integrated absorbance of $\text{Au}_2\text{C}^{13}\text{CO}$ from acetic acid- H_4 oxidation and Au_2CCO from acetic acid- D_4 oxidation as a function of reaction time; c). plots of $k_{\text{H}}/k_{\text{D}}$ as a function of the reaction time and the extent of reaction.

Figure 6.8a shows the IR spectra development in the gold ketenylidene region during the DKIE study. As expected, the deuterium labeled acetate partial oxidation proceeded at a slower rate compared to the non-labeled species as seen in the ketenylidene spectra

shown in Figure 6.8a. Figure 6.8b shows a plot of the integrated absorbance of the two gold ketenylidene species as a function of reaction time. As shown in Equation 6.1 and Figure 6.7, the reaction is pseudo-first order in the Au-Ti⁴⁺ dual perimeter site concentration. The rate of the two ketenylidene species formation can be represented by Equations 6.2 and 6.3:

$$\frac{d[Au_2C^{13}CO]}{dt} = k_H x [CH_3^{13}COO] x [O_2] x [Active Site] \quad (6.2)$$

$$\frac{d[Au_2CCO]}{dt} = k_D x [CD_3COO] x [O_2] x [Active Site] \quad (6.3)$$

Since the concentration of the two acetate species, the O₂ pressure, and the concentration of the active site are the same, dividing Equation 6.2 by Equation 6.3 yields Equation 6.4:

$$\frac{k_H}{k_D} = \frac{d[Au_2C^{13}CO]/dt}{d[Au_2CCO]/dt} \quad (6.4)$$

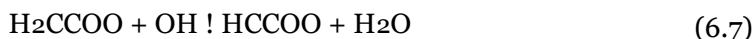
Figure 6.8c shows the DKIE, k_H/k_D , evaluated by point-by-point differentiation of the numerical data in Figure 6.8b. A linear least square fit of the DKIE data is shown in Figure 6.8c. A maximum k_H/k_D of 4.2 at full active site coverage ($t = 0$ min) is deduced from the linear fit. The DKIE falls to near unity as the reaction slows down. This observed initial DKIE value is consistent with the Hutchings team's report, where DKIE values in the 4-2 range was found for benzyl alcohol partial oxidation (forming benzaldehyde and toluene) over a Au-Pd/TiO₂ catalyst.³⁴

The observation of a DKIE means that C-H bond breaking in acetate/TiO₂ partial oxidation is of importance. The decrease in the overall DKIE during reaction may be due to a variation in the nature of the transition state on Au sites which are crowded by Au₂CCO species at later stages of the reaction. Possibly the frontier orbitals at the C-H bonds become less important for the reaction under crowded conditions on the Au sites and other factors become dominant, even though the activation energy remains constant.

G. DFT Proposed Mechanism of the Acetate Partial Oxidation

With the acetate adsorbed on the Ti_{5c} sites, O₂ was admitted to the system from the gas phase. It has been reported by us that the Au-Ti⁴⁺ dual perimeter sites can dissociate O₂ with a barrier of 0.4-0.6 eV, generating oxygen adatoms at the Au perimeter.³³ These oxygen adatoms can then diffuse on the Au nano-particle with barriers of 0.23-0.72 eV.^{7,33} At the experimental temperature in the current study (≥ 400 K), it is expected that the O adatoms can diffuse around the Au nano-rod and react when the appropriate reactant configuration is found. It is also reasonable to assume that the O adatoms are in abundance, at 1 Torr pressure. Since the reaction process, breaking C-H bonds and a C-O bond in acetate/TiO₂, only occurs in O₂, our mechanism involves O atom migration to Au perimeter sites followed by C-H bond activation on Au sites.

As shown in Scheme 6.1, the partial oxidation of acetate/TiO₂ forming Au₂CCO clearly involves both the Au surface sites and the TiO₂ support. As a result, it is natural to focus the mechanistic study at the Au/TiO₂ dual perimeter sites. From the reactant acetate (CH₃COO-) to the product ketenylidene (=C=C=O), a net of three C-H bonds and one C-O bond are broken. After testing different sequences of steps, the most favorable (lowest energy barrier) reaction pathway is summarized below:



The detailed structures of the initial state, transition state and the final state of each step shown above are summarized in Figure 6.8. After adsorption, the methyl moiety of the acetate/TiO₂ species first loses two hydrogens consecutively with barriers of ~0.8 eV

and starts to form Au-C bonds with the remaining -CH moiety to Au (Figure 6.9 a-b). The two dehydrogenation processes are assisted by an O adatom nearby, eventually forming an H₂O molecule on the Au. The H₂O molecule produced bonds weakly on the Au (-0.08 eV) and desorbs quickly. After the activation of the two C-H bonds, a C-O bond of the carboxylate moiety breaks with an ~0.7 eV barrier, resulting in the formation of Au₂CHCO that then detaches from the TiO₂ (Figure 6.9c). The last C-H bond is then broken at Au sites with the aid of another O adatom, forming Au₂CCO, as shown in Figure 6.9d. The final Au₂CCO configuration shown in Figure 6.9d theoretically gives $\nu(\text{CO})$ of 2041 cm⁻¹, consistent with the IR measurement (2040 cm⁻¹).¹⁶ This reaction pathway to Au₂CCO also retains the O moiety from the original acetate ion, as shown experimentally in Section III.D.

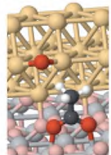
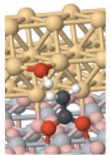
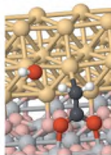
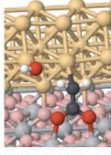
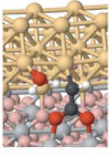
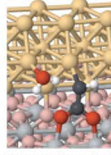
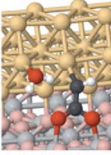
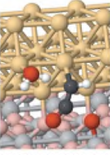
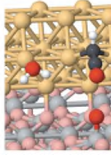
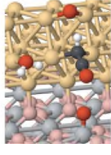
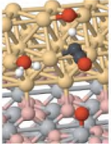
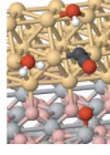
	Initial State	Transition State	Final State	E_a (eV)	ΔH (eV)	ΔKIE (k_H/k_D)
a				0.86	0.46	3.6
b				0.75	0.63	3.0
c				0.71	-0.13	N/A
d				0.21	-0.18	3.5

Figure 6.9. Key steps for the ketenylidene formation at perimeter. a-d corresponding to Equations 6.6-6.9.

Although the first dehydrogenation step has the highest intrinsic barrier (0.86 eV, Figure 6.9a), the highest overall barrier occurs at the C-O bond breaking step as the first two steps are endothermic, as shown in Figure 6.10 with black lines. In the overall calculated partial oxidation of acetate, the transition state for the C-O bond breaking step is 1.80 eV higher than the initial state involving acetate/TiO₂ at the perimeter and an O adatom on Au. This overall activation energy corresponds closely to the experimentally measured apparent activation energy of 1.7 eV, and is reasonable for an oxidation process occurring at 400 K. Thus, the C-O bond scission in the HCCOO/TiO₂ species is the rate limiting step for the reaction.

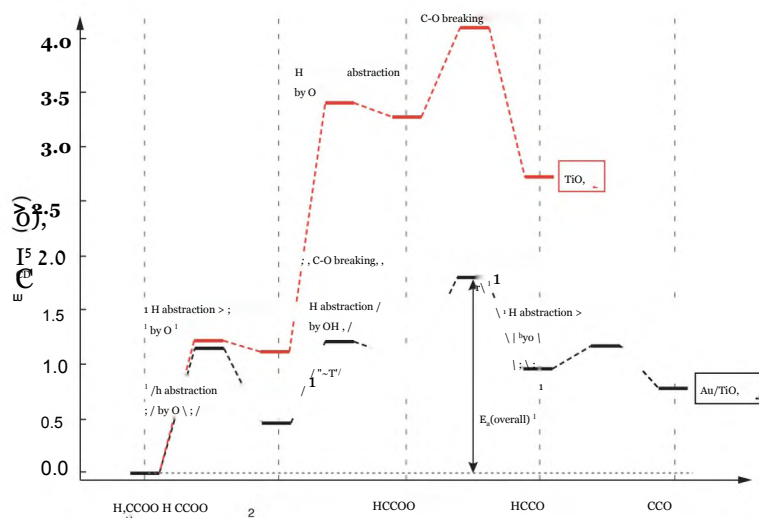


Figure 6.10. The energy diagram along the reaction pathway shown in Figure 6.9 for acetate oxidation on Au/TiO₂ sites and on TiO₂ sites. $E_a(\text{overall})$ refers to the overall barrier of the reaction.

The calculated DKIE of each C-H bond activation steps are also shown in Figure 6.9. The k_H/k_D value of 3-4 is consistent with other calculated DKIE reports for C-H bond activation.^{35,36} A sequence of three equally important C-H bond breaking steps, each with DKIE value of 3-4, would be expected to exhibit an overall DKIE greater than 3-4. The

fact that the observed overall DKIE is ~ 4.2 (Figure 6.8) indicates that the three C-H bond scission weigh differently to the final product. This could be due to the fact that the rate-limiting step (the C-O bond breaking step) does not involve C-H bond breaking.

H. Energy Barriers for Ketenylidene Formation on the TiO₂ Surface

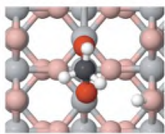
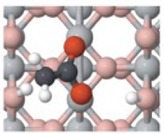
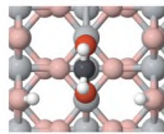
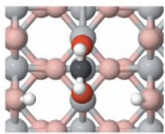
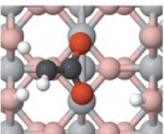
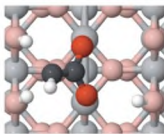
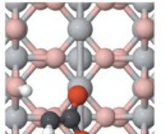
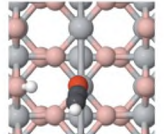
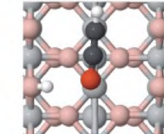
	Initial State	Transition State	Final State	E_a (eV)	ΔH (eV)
a				1.19	1.10
b				2.28	2.17
c				0.83	-0.57

Figure 6.11. Consecutive C-H bond and C-O bond scission (Equations 6.6-6.8) of acetate/TiO₂ away from the Au/TiO₂ dual perimeter site.

Since the Au/TiO₂ catalyst is fully-covered with acetate adsorbed on the TiO₂ sites, we also studied the possibility of ketenylidene formation on the TiO₂ support away from the Au-Ti⁺ perimeter, following the same mechanism depicted in Equations 6.6-6.9, as the red pathway shown in Figure 6.10. The reaction starts from the adsorbed acetate/TiO₂ configuration shown in Figure 6.3b. Due to the upright adsorption configuration of the acetate on TiO₂, interaction between the C-H bonds to adsorbed O atoms on the TiO₂ surface is excluded. As a result, the C-H bond scissions on TiO₂(110) is aided by bridging oxygen from the oxide surface. The calculated first three steps (Equations 6.6-6.8) of the

reaction, which all have high energy barriers, were shown in Figure 6.11. The dehydrogenation steps shown in Figure 6.11a-b generate very unstable CH_2 and CH moieties, since there is no Au nearby for stabilization. As a result, high activation barriers of 1.19 eV and 2.28 eV are obtained according to the Bronsted-Evans-Polanyi relationship.³⁷⁻³⁸ On top of these steps, the C-O bond scission step which follows the two C-H bonds breaking produces a HCCO group and an O adatom adsorbed on the Ti_{5c} site of TiO_2 (Figure 6.11c). The HCCO group is very unstable and some stabilization from the nearby Ti_{5c} site is observed, causing a small energy drop ($\Delta H = -0.57$ eV). However, the stabilization from the Ti_{5c} sites is not nearly as strong as that provided by the Au at the Au/ TiO_2 perimeter sites, resulting in a system that is still in a very high energy state, as shown in Figure 6.10. The C-O breaking step at the TiO_2 sites has a barrier of 0.83 eV, raising the overall barrier to 4.10 eV (Figure 6.10, red pathway). This overall barrier prohibits the reaction at ~ 400 K.

The advantages of the Au- Ti^{4+} dual perimeter comparing to TiO_2 or Au alone are that Au can strongly interact with the dehydrogenated species,^{16,39-41} while the Ti^{4+} sites stabilize the O moiety left from C-O bond scission on the carboxyl end.⁷ Since there is no Au to stabilize the CH_2 or CH moiety at the TiO_2 lattice sites, the products from the C-H or C-O bond breaking (Equations 6.6-6.8) are unstable and the energy required to proceed the reaction becomes formidable. These effects, together with the O adatoms generated at the Au- TiO_2 dual perimeter sites, help to promote the C-H and C-O bond cleavage. The combined activity of Au and TiO_2 sites is necessary for the formation of ketenylidene from acetate. The joint site activity supplies O atoms and OH radicals on Au sites which promote C-H bond scission in acetate species and eventually C-O bond scission on TiO_2 sites to produce chemisorbed gold ketenylidene with the steps shown in Equations 6.5-6.9.

IV. Summary of Results.

The adsorption and oxidation of acetic acid on a Au/TiO₂ catalyst has been studied experimentally and theoretically. The following results have been obtained:

1. Acetic acid dissociatively adsorbs on TiO₂ surface, forming bridging bidentate acetate/TiO₂.
2. The partial oxidation of acetate/TiO₂ to form Au₂CCO occurs near 400 K, at the Au-Ti⁴⁺ dual perimeter site present at ~3 nm Au nanoparticles. No ketenylidene formation occurs on Au/SiO₂ or TiO₂ under even more aggressive oxidation conditions, indicating that coordinative unsaturation in Au nanoparticles or TiO₂ alone is insufficient to support this reaction.
3. It was found by DFT simulation that the Au-Ti⁴⁺ dual perimeter site is crucial for three processes: (1) activating O₂; (2) promoting the dehydrogenation steps; and (3) stabilizing the O moiety after the C-O bond scission.
4. A ¹⁸O₂ isotope study revealed that the O moiety in the Au₂CCO intermediate species originated exclusively from the acetic acid, not from the gas phase oxygen.
5. The rate-limiting step for acetate partial oxidation was found to be the C-O bond scission of the HCCOO/TiO₂ intermediate. An initial deuterium kinetic isotope effect of ~4 was observed.
6. The overall calculated activation energy for ketenylidene formation on the Au/TiO₂ catalyst is 1.80 eV, matching with the 1.7 ± 0.2 eV apparent activation energy measured.
7. By raising the reaction temperature from ~400 K to 473 K, the partial oxidation process is converted to the total oxidation process for acetate/TiO₂, on the Au/TiO₂ catalyst, forming CO₂ and water.

V. Acknowledgement.

We gratefully thank Dr. Rodolfo Zanella for kindly providing us the Au/SiO₂ sample. We acknowledge the support of this work by DOC-Office of Basic Energy Sciences under grant number DE-FG02-09ER16080, as well as the XSEDE computing resources from Texas Advanced Computing Center. We also acknowledge a fellowship for Mrs. Isabel Green from AES Corporation through the AES Graduate Fellowships in Energy Research Program at the University of Virginia.

Chapter 6 References:

1. Munasinghe, P. C.; Khanal, S. K. *Bioresource Technology* **2010**, *101*, 5013.
2. Kohl, D.; Thoren, W.; Schnakenberg, U.; Schull, G.; Heiland, G. *Journal of the Chemical Society, Faraday Transactions* **1991**, *87*, 2647.
3. Liao, L.-F.; Lien, C.-F.; Lin, J.-L. *Physical Chemistry Chemical Physics* **2001**, *3*, 3831.
4. Backes, M. J.; Lukaski, A. C.; Muggli, D. S. *Applied Catalysis B: Environmental* **2005**, *61*, 21.
5. Haruta, M.; Kobayashi, T.; Sano, H.; Yamada, N. *Chemistry Letters* **1987**, *2*, 405.
6. Valden, M.; Lai, X.; Goodman, D. W. *Science* **1998**, *281*, 1647.
7. Green, I. X.; Tang, W.; Neurock, M.; Yates, J. T., Jr. *Science* **2011**, *333*, 736.
8. Meyer, R.; Lemire, C.; Shaikhutdinov, S. K.; Freund, H.-J. *Gold Bulletin* **2004**, *37*, 72.
9. Green, I. X.; Tang, W.; Neurock, M.; Yates, J. T., Jr. *Angewandte Chemie International Edition* **2011**, *50*, 10186.
10. Huang, J.; Haruta, M. *Research on Chemical Intermediates* **2012**, *38*, 1.
11. Wang, J.; Hammer, B. *Topics in Catalysis* **2007**, *44*, 49.
12. Laursen, S.; Linic, S. *Physical Chemistry Chemical Physics* **2009**, *11*, 11006.
13. Kotobuki, M.; Leppelt, R.; Hansgen, D. A.; Widmann, D.; Behm, R. J. *Journal of Catalysis* **2009**, *264*, 67.
14. Fujitani, T.; Nakamura, I.; Akita, T.; Okumura, M.; Haruta, M. *Angewandte Chemie* **2009**, *48*, 9515.

- 15- Panayotov, D. A.; Yates, J. T., Jr. *Journal of Physical Chemistry C* **2007**, *111*, 2959.
16. Green, I. X.; Tang, W.; Neurock, M.; J. T. Yates, J. *Journal of the American Chemical Society* **2012**, *In preparation*.
17. Zanella, R.; Sandoval, A.; Santiago, P.; Basiuk, V. A.; Saniger, J. M. *The Journal of Physical Chemistry B* **2006**, *110*, 8559.
18. Green, I. X.; Yates, J. T., Jr. *The Journal of Physical Chemistry C* **2010**, *114*, 11924.
19. Green, I. X.; Buda, C.; Zhang, Z.; Neurock, M.; Yates, J. T., Jr. *The Journal of Physical Chemistry C* **2010**, *114*, 16649.
20. Panayotov, D. A.; Paul, D. K.; Yates, J. T., Jr. *Journal of Physical Chemistry* **2003**, *107*, 10571.
21. Kresse, G. *Physical Review B* **2000**, *62*, 8295.
22. Sato, S.; Ueda, K.; Kawasaki, Y.; Nakamura, R. *The Journal of Physical Chemistry B* **2002**, *106*, 9054.
23. Gonzalez, F.; Munuera, G.; Prieto, J. A. *Journal of the Chemical Society, Faraday Transactions 1: Physical Chemistry in Condensed Phases* **1978**, *74*, 1517.
24. Hasan, M. A.; Zaki, M. I.; Pasupulety, L. *Applied Catalysis A: General* **2003**, *243*, 81.
25. Pei, Z. F.; Ponc, V. *Applied Surface Science* **1996**, *103*, 171.
26. Sanchez Escibano, V.; Busca, G.; Lorenzelli, V. *The Journal of Physical Chemistry* **1990**, *94*, 8945.
27. Fukushima, T.; Arakawa, H.; Ichikawa, M. *Journal of the Chemical Society, Chemical Communications* **1985**, 729.
28. Eischens, R. P. *Science* **1964**, *146*, 486.
29. Young, R. P. *Canadian Journal of Chemistry* **1969**, *47*, 2237.
30. Robietti, A. G.; Thompson, J. C. *Spectrochimica Acta* **1965**, *21*, 2023.
31. Capecchi, G.; Faga, M.; Martra, G.; Coluccia, S.; Iozzi, M.; Cossi, M. *Research on Chemical Intermediates* **2007**, *33*, 269.
32. Grinter, D. C.; Nicotra, M.; Thornton, G. *The Journal of Physical Chemistry C* **2012**.
33. Green, I. X.; Tang, W.; McEntee, M.; Neurock, M.; J. T. Yates, J. *Journal of the American Chemical Society* **2012**, *In preparation*.
34. Meenakshisundaram, S.; Nowicka, E.; Miedziak, P. J.; Brett, G. L.; Jenkins, R. L.; Dimitratos, N.; Taylor, S. H.; Knight, D. W.; Bethell, D.; Hutchings, G. J. *Faraday Discussions* **2010**, *145*, 341.
35. Hu, R.; Zhang, Q.; Chen, Y. *The Journal of Chemical Physics* **2010**, *133*, 114306.

36. Gronert, S.; Keeffe, J. R. *The Journal of Organic Chemistry* **2006**, 71, 5959.
37. Bronsted, J. N. *Chemical Reviews* **1928**, 5, 231.
38. Evans, M. G.; Polanyi, M. *Transactions of the Faraday Society* **1938**, 34, 11.
39. Olivera, P. P.; Patrino, E. M.; Sellers, H. *Surface Science* **1995**, 327, 330.
40. Zeigarnik, A. V.; Valdes-Peréz, R. E.; Myatkovskaya, O. N. *The Journal of Physical Chemistry B* **2000**, 104, 10578.
41. Xing, B.; Pang, X.-Y.; Wang, G.-C. *Journal of Catalysis* **2011**, 282, 74.

Chapter 7

Inhibition at Perimeter Sites of Au/TiO₂ Oxidation Catalyst by Reactant Oxygen.*

*Adapted with permission from I. X. Green, W. Tang, M. McEntee, M. Neurock, and J. T. Yates, Jr., *"Inhibition at Perimeter Sites of Au/TiO₂ Oxidation Catalyst by Reactant Oxygen"*, Journal of the American Chemical Society, ASAP, 2012. Copyright 2012 American Chemical Society. The theoretical work was performed by Dr. Wenjie Tang and Dr. Matthew Neurock and is included here for completeness.

TiO₂-supported gold nanoparticles exhibit surprising catalytic activity for oxidation reactions compared to noble bulk gold which is inactive. The catalytic activity is localized at the perimeter of the Au nanoparticles where Au atoms are atomically adjacent to the TiO₂ support. At these dual catalytic sites, an oxygen molecule is efficiently activated through chemical bonding to both Au and Ti⁴⁺ sites. A significant inhibition by a factor of 22 in the CO oxidation reaction rate is observed at 120 K when the Au is pre-oxidized, caused by the oxygen-induced positive charge produced on the perimeter Au atoms. Theoretical calculations indicate that induced positive charge occurs in the Au atoms which are adjacent to chemisorbed oxygen atoms, almost doubling the activation energy for CO oxidation at the dual catalytic sites in agreement with the experiments. This is an example of self-inhibition in catalysis by a reactant species.

I. Introduction.

The origin of the activity of oxide-supported nanoparticle Au catalysts has been of great interest over the last two decades.^{1,2} This activity contrasts markedly with the inactivity of the bulk metal. Nanoparticle Au catalysts exhibit extraordinary efficiency and selectivity in key industrial oxidation reactions involving molecular oxygen.³

Understanding the mechanisms by which these catalysts carry out oxidation reactions will provide valuable insights and guidance toward the design of new catalytic materials. Joining the effort of unraveling the CO oxidation process on the Au/TiO₂ catalyst lead by others,⁴⁻⁸ we have shown spectroscopically that on a catalyst comprised of ~3 nm Au particles supported on TiO₂ the catalytic activity is localized at the Au perimeter, where dual catalytic sites involving Au atoms and Ti⁴⁺ ions work together at very low temperatures to activate molecular oxygen and oxidize both H₂ as well as CO.^{9,10} More research is needed as many aspects of the dual-catalytic system are still unclear and under debate.

The charge state of active Au species during the catalytic reaction is one area that has been greatly debated, with different reports citing the active sites as being either negative, neutral or positively charged Au species. For instance, Au clusters deposited on oxide F-centers were reported to be negatively charged and highly active for CO oxidation;^{8,11-13} other experiments, however, suggest that the active sites for CO oxidation are comprised of partially oxidized (positively charged) Au centers.¹⁴⁻¹⁷ In addition, there are also various reports that suggest as-synthesized cationic Au(III) is not active for CO oxidation at room temperature until reduced to metallic Au³⁺¹⁸ and that the metallic Au is the active species.^{18,19} Previous theoretical calculations of charge effects on Au also provided mixed conclusions as to the relationship between the Au oxidation state and the catalytic activity.⁷⁻²⁰⁻³⁵

Two important challenges associated with establishing the charged state of the active sites experimentally are: (1) it was hard to measure the partial charge state (oxidation states between 0 and ± 1) of localized Au atoms *in situ* directly via common techniques such as X-ray photoelectron spectroscopy, X-ray absorption near edge structure spectroscopy, or Mössbauer spectroscopy until recently;¹⁵⁻³⁶ and (2) the reactant for the

standard catalyst activity test, the CO molecule, is a strong reducing agent for Au nanoparticles at room temperature or lower.³⁷⁻³⁹ To avoid these complications, we use the reactant CO molecule as a surface probe at very low temperatures (~120 K) to detect the Au oxidation state during the catalytic reaction, and in addition, to kinetically track the reaction progress via *in situ* infrared (IR) spectroscopy. At these low temperatures the reduction of cationic Au by CO does not occur during the catalytic reaction.

We have previously demonstrated that at temperatures in the range 110-130 K, CO molecules adsorbed on the TiO₂ support (CO/TiO₂) are the active species for CO oxidation and are delivered to the dual catalytic perimeter sites by diffusion across TiO₂.⁹ By working at low temperatures the reaction is kinetically simplified via the exclusion of higher activation energy processes. In contrast, CO adsorbed on Au sites is essentially unreactive at 120 K.⁹ In the work reported here we show that pre-oxidation of the Au perimeter sites of the Au/TiO₂ catalyst at high temperature (473 K), to produce Au^{s+} sites, reduced the CO oxidation activity by a factor of 22 at 120 K. The apparent activation energy for CO oxidation over the Au/TiO₂ catalyst increases from 0.16 eV to 0.27 eV when Au^{s+} sites are produced by pre-oxidation of the catalyst. Density functional theory (DFT) calculations indicate that the origin of the local catalytic inhibition or site poisoning is the conversion of Au⁰ to Au^{s+} at the Au nanoparticle perimeter that results from the strong chemisorption of oxygen atoms at these sites. Understanding the inhibition of the active Au sites in the low-temperature regime provides insight into the mechanism of the CO oxidation reaction on Au/TiO₂ catalysts at higher temperatures, thus coupling low temperature studies to catalysis at higher temperatures.

II. Methodology.

Detailed description of the synthetic method of the Au/TiO₂ catalyst and the vacuum transmission FTIR cell can be found in Chapter 2. After the catalyst was installed and activated in the vacuum cell, pre-oxidation of the catalyst to various stages was carried out at temperatures from 295 K to 473 K in 5 Torr of O₂ for 30 min. Pre-reduction of the catalyst to different degrees was carried out in 0.07 Torr of CO for 5 min at temperatures in the range 120-473 K, as indicated in each experiment reported. All experiments described in this study were carried out on the same catalyst prepared by repeated oxidation in O₂ followed by reduction in CO, i.e. the catalyst was reusable for many experiments. No heating above 473 K was performed to avoid the known effect of sintering of Au nanoparticles.^{6,40} Thus, a “fully-oxidized Au⁵⁺/TiO₂ catalyst” or a “fully-reduced Au⁰/TiO₂ catalyst” were made by O₂ oxidation or CO reduction at 473 K. Transmission electron microscope measurements of the catalyst after repeated oxidation/reduction cycles show a Au particle size distribution similar to the as-prepared catalyst (2-8 nm diameter, with a most probable diameter of 3 nm, Figure 2.3).^{9,10,41} The catalyst, oxidized and reduced at different temperatures, was cooled to 120 K in vacuum for the CO adsorption and oxidation reaction.

CO adsorption on the catalyst to saturation coverage at temperatures between 110 K and 130 K was achieved by back filling the cell with 0.07 Torr of CO gas. For the CO oxidation studies, after reaching saturation, the CO gas was evacuated from the cell for approximately 10 min to produce one monolayer (ML) coverage. An IR spectrum was taken after 8.6 min of CO evacuation in each experiment and was used as the point of time zero for the reaction kinetics study. One Torr of O₂ was then introduced to the cell and the CO oxidation reaction immediately began. FTIR spectra were taken every minute until the CO/TiO₂ adsorption feature was gone from the IR spectra (~20 min for Au⁰/TiO₂ catalyst and ~60 min for Au⁵⁺/TiO₂ catalyst).

First principle plane wave density functional theory (DFT) calculations carried out using the generalized gradient approximation (GGA)⁴² were used herein to explore the influence of oxidized Au sites on CO oxidation. The Au/TiO₂ system was simulated herein by a Au nano-rod supported on a rutile TiO₂ surface. Detailed information about the calculation can be found in Chapter 3, Section II (page 27).

III. Results and Discussion.

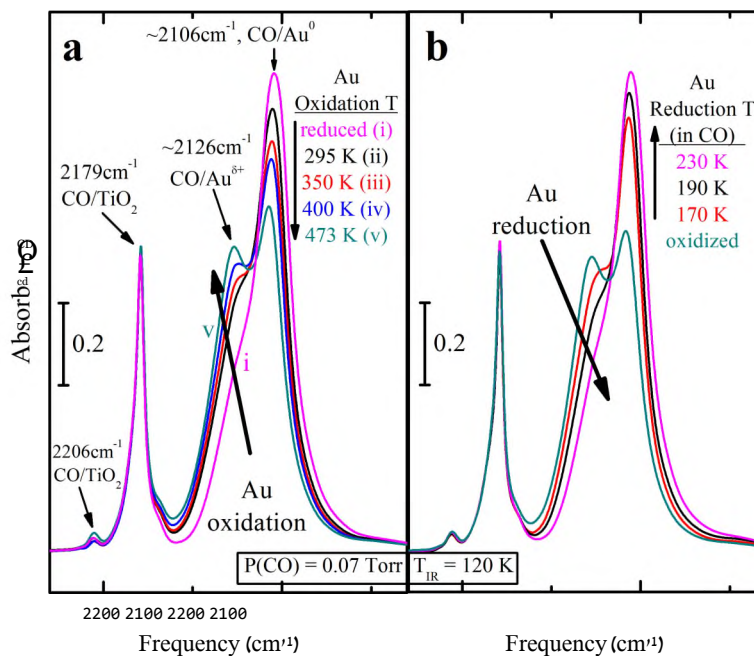


Figure 7.1. IR spectra of 120 K-saturated CO adsorption of the Au/TiO₂ catalyst surface modification by (a) oxidation in O₂ and (b) reduction in CO at different temperatures.

The step-wise oxidation of the catalyst was carried out to examine the Au⁰ to Au⁸⁺ species conversion. Figure 7.1a shows the IR spectra in the CO stretching region of a reduced catalyst pre-oxidized to different levels. The IR absorption bands at 2179 cm⁻¹ and 2206 cm⁻¹ are assigned to CO adsorbed on Ti⁴⁺ sites (denoted as CO/TiO₂) because

identical bands are observed on a TiO₂ blank sample also held in the IR cell. The IR band at $\sim 2106\text{ cm}^{-1}$ is assigned to CO terminally adsorbed on metallic Au⁰ sites based on previous investigations (denoted as CO/Au⁰).^{9,39,43-45} The high frequency shoulder at $\sim 2126\text{ cm}^{-1}$ is generally assigned to CO adsorbed on positively charged Au^{s+} sites ($0 < s < 1$, denoted as CO/Au^{s+}).^{39,44-46} As the pre-oxidation temperature increases from 295 K to 473 K, the 2106 cm^{-1} band decreases in absorbance at saturation coverage, while the 2126 cm^{-1} band increases in absorbance, indicating a transition from CO/Au⁰ species to CO/Au^{s+} species under increasingly aggressive oxidation conditions.

The Au-catalyst pre-oxidation process was shown to be completely reversible by observation of ν_{CO} during reduction of the oxidized Au⁵⁺/TiO₂ catalyst in gas phase CO. Figure 7.1b shows the 120 K-CO IR absorption spectra of the pre-oxidized catalyst reduced at temperatures from 170 K to 230 K in 0.07 Torr of CO, where an increase of CO/Au⁰ species is accompanied by a decrease of CO/Au^{s+} species, just opposite from Figure 7.1a. It is noted that the Au oxidation state produced by pretreatment has no influence on the neighboring CO/TiO₂ species, since the band frequency, band shape, and saturation absorbance of the CO/TiO₂ species remains unchanged upon Au oxidation/reduction. We denote the catalyst in Figure 7.1a(i) as the “fully-reduced Au⁰/TiO₂” sample and the catalyst in Figure 7.1a(v) as the “fully-oxidized Au⁵⁺/TiO₂” sample. The CO/Au¹⁺ ($\nu_{\text{CO}}=2186\text{-}2159\text{ cm}^{-1}$),^{38,43,47} CO/Au³⁺ ($\nu_{\text{CO}}=\sim 2207\text{ cm}^{-1}$),⁴⁷ and CO/Au⁵⁻ ($\nu_{\text{CO}}=2038\text{-}1900\text{ cm}^{-1}$)^{46,48} species reported by others on Au nanoparticle catalysts using IR or other measurement techniques^{11,12,14} are not found in our IR observations.

To gain quantitative knowledge of the conversion between Au⁰ and Au^{s+} species, the overlapping CO/Au⁰ and CO/Au^{s+} bands have been deconvoluted using a Lorentz function in all measurements made during the CO reduction process (part of which are

presented in Figure 7.1b). The integrated absorbance of each deconvoluted band is used as a measurement of the amount of the corresponding species on the surface. Figure 7.2 depicts the conversion of CO/Au^{5+} to CO/Au^0 as a function of increasing reduction temperature in CO. The reduction process starts above 147 K in 0.07 Torr of CO, before which little change in integrated absorbance is observed for either species. The total integrated CO absorbance on the Au^0 and Au^{5+} sites remains constant during the reduction (Figure 7.2, right axis) indicating that the saturation coverage of adsorbed CO (1 ML) on the Au nanoparticles is constant for various stages of reduction, and supports the idea that the extinction coefficients of CO/Au^0 species and CO/Au^{5+} species are quite similar. The oxidation/reduction procedures using O_2 and CO provide a very convenient method to reproducibly modify the Au/TiO_2 catalyst.

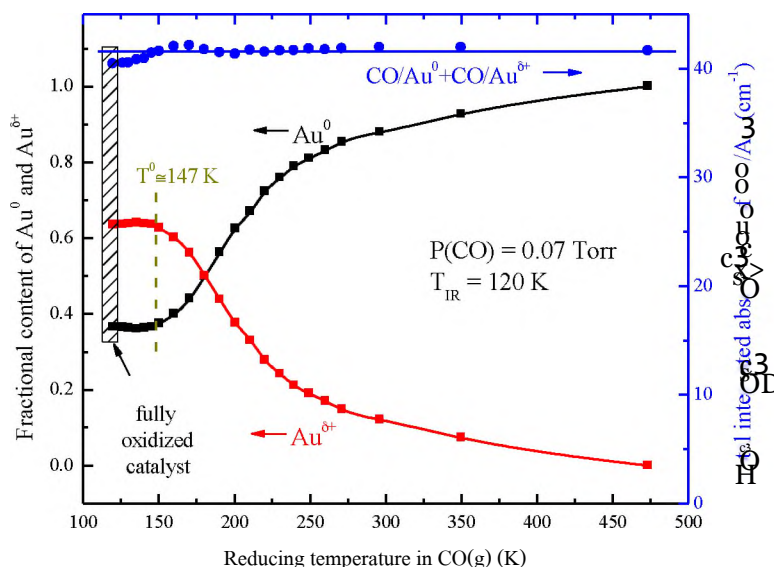


Figure 7.2. Left axis: plots of the CO/Au^{5+} fractional conversion to CO/Au^0 species monitored by deconvolution of IR bands from Figure 7.1b using the Lorentz vco line shape function and comparing the integrated absorbance of each deconvoluted band. Right axis: plot of the total integrated IR absorbance of CO/Au^{5+} and CO/Au^0 species combined, versus catalyst reduction temperature.

To determine the kinetic influence of oxidation of the Au/TiO₂ catalyst, we performed low temperature CO oxidation reactions on the fully-reduced catalyst and on the fully-oxidized catalyst separately. Infrared spectra taken during the first 1200 s of the two experiments are shown in Figure 7.3. Consistent with our previous findings on Au⁰/TiO₂ catalysts,⁹ CO/TiO₂ is the main active species undergoing oxidation at 120 K judging by the disappearance of CO/TiO₂ feature from the IR spectra. An absorption band near 2350 cm⁻¹, corresponding to the production of CO₂/TiO₂, is observed to increase. At 120 K, the CO₂ product is captured on the catalyst surface. The CO/Au⁰ and CO/Au^{s+} bands are slightly blue shifted during the reaction, indicating partial charge transfer by adsorbed oxygen atoms on nearby Au sites at 120 K. But these CO/Au⁰ and CO/Au^{s+} species are not significantly consumed during the CO oxidation reaction due to their limited diffusional motion on Au sites at such low temperature.⁹ This small blue shift disappears upon evacuation of O₂ and readsorption of CO at 120 K (spectra not shown).

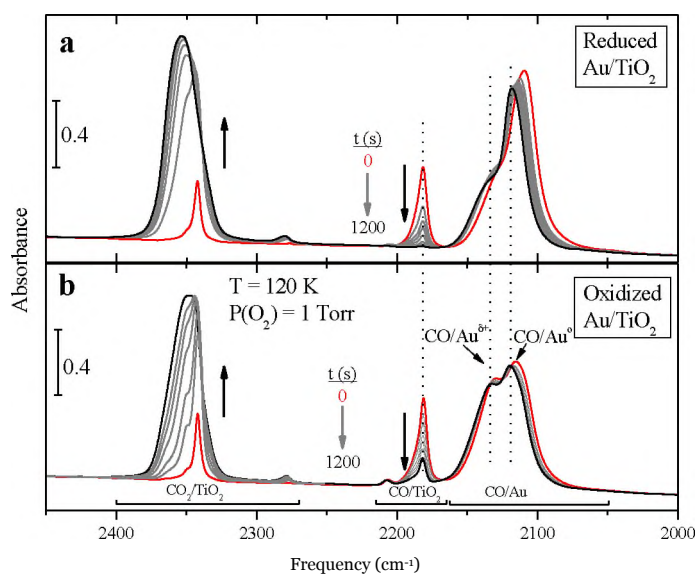


Figure 7.3. Comparison of low temperature CO oxidation on the (a) fully-reduced Au⁰/TiO₂ catalyst and on the (b) fully-oxidized Au^{s+}/TiO₂ catalyst.

The main kinetic difference in the two experiments in Figure 7.3 is the decrease of the rate of CO/TiO₂ consumption (as well as CO₂/TiO₂ generation) on the fully-oxidized Au⁵⁺/TiO₂ catalyst. In 1200 s at 120 K, the CO/TiO₂ oxidation reaction is complete on the fully-reduced Au⁰/TiO₂ catalyst (Figure 7.3a), while ~20% of CO/TiO₂ remains on the Au⁵⁺/TiO₂ catalyst (Figure 7.3b). Kinetic plots of the CO/TiO₂ consumption on fully-reduced and fully-oxidized Au/TiO₂ are shown in Figure 7.4, where a reversibility test for the catalyst during multiple reduction/oxidation cycles is also shown. The CO/TiO₂ oxidation reaction follows accurate first-order kinetics in CO coverage in both cases, indicated by the fitted solid lines in Figure 7.4. The catalyst performance is reproducible

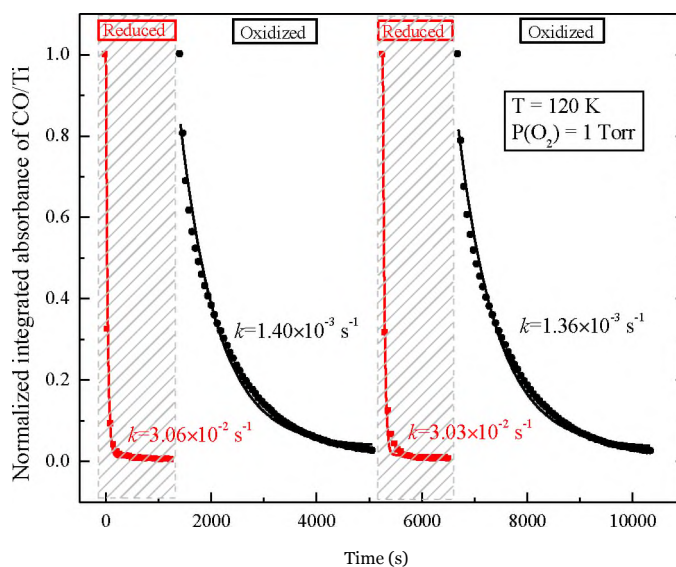


Figure 7.4. Representative kinetic plots of the CO/TiO₂ oxidation process on the fully-reduced Au⁰/TiO₂ catalyst (red, corresponding to Figure 7.3a), and on the fully-oxidized Au⁵⁺/TiO₂ catalyst (black, corresponding to Figure 7.3b). Solid lines represent the first-order kinetics fit for the experimental data.

for the mild oxidation-reduction cycles used in this study. The first-order CO oxidation rate constant at 120 K is ~22 times larger on the fully-reduced Au⁰/TiO₂ catalyst compared to the Au⁵⁺/TiO₂ catalyst, indicating an inhibition effect associated with the

formation of Au^{5+} species. A similar reduction in the CO oxidation rate was also reported on a O_2 -treated Au/SiO_2 catalyst working at room temperature.⁴⁹ It is noteworthy that the inhibition on $\text{Au}^{5+}/\text{TiO}_2$ is detected by the decrease of the rate of consumption of the CO/ TiO_2 species, which is the only participant for CO oxidation at 120 K, showing again the unique activity of dual catalyst sites at the Au perimeter for CO/ TiO_2 oxidation on the Au/TiO_2 catalyst. As shown previously⁹ and below, these sites involve Au and Ti centers which have a special capability to activate molecular O_2 at the perimeter of Au nanoparticles on TiO_2 .

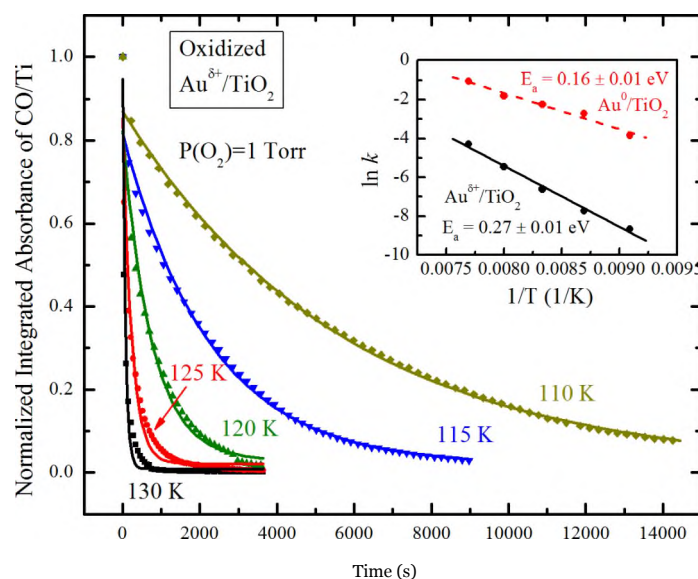


Figure 7.5. Plots of the integrated absorbance of CO/ TiO_2 against time during reaction with O_2 at various temperatures fitted to first-order kinetics. Inset: the Arrhenius plot comparing activation energies on Au^0/TiO_2 (red) and $\text{Au}^{5+}/\text{TiO}_2$ (black). Data for Au^0/TiO_2 was taken from Chapter 3 (ref. 9).

Previously we reported the apparent activation energy for CO oxidation on the Au^0/TiO_2 catalyst to be 0.16 ± 0.01 eV.⁹ For comparison we carried out a study of the effect of temperature on the CO/ TiO_2 oxidation on the fully-oxidized $\text{Au}^{5+}/\text{TiO}_2$ catalyst in the temperature range of 110-130 K as shown in Figure 7.5a. The resulting apparent

activation energy for the oxidation of CO/TiO₂ was found to be 0.27 ± 0.01 eV (Figure 7.5b), a near doubling of apparent activation energy. The ratio of pre-exponential factors, $A_{ox}/A_{red} \ll 10^3$, indicates that the O-inhibition of Au catalytic activity is likely not due to site blocking by adsorbed O atoms. We had postulated previously that the lower activation energy process measured for CO oxidation over the Au⁰/TiO₂ catalyst may be heavily influenced by the CO/TiO₂ species' diffusion energy across the TiO₂ surface.⁹ The large difference in the pre-exponential factors therefore may indicate that the two Arrhenius plots are likely describing processes that differ in mechanism and activation entropy, where CO oxidation on Au^{s+} sites is entropically more favorable. It is worth noting that working at low temperatures is important to see the reduction of catalytic activity associated with the presence of the Au^{s+} site. At elevated temperatures near room temperature, the inhibition by chemisorbed oxygen will not be observed as the CO can migrate to the oxidized Au site and easily reduce it (Figure 7.2).

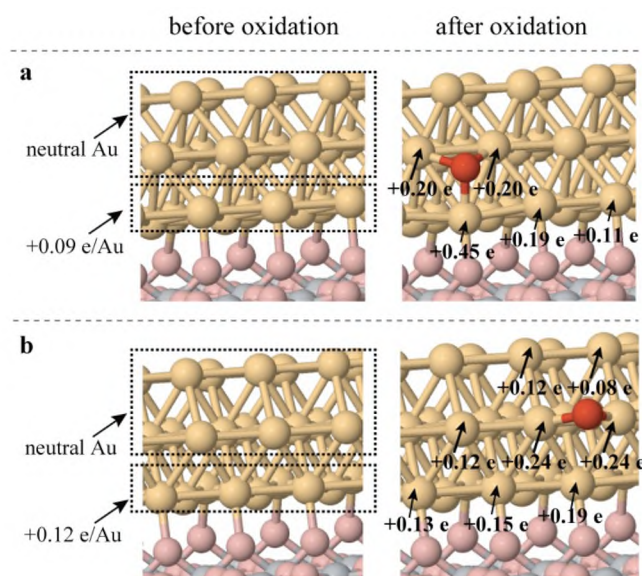


Figure 7.6. Au charge state changes at the interface perimeter sites.

Density functional theory (DFT) calculations provided detailed insight into the mechanism for CO oxidation at the dual catalytic sites of the Au^0/TiO_2 perimeter.⁹ We carry out similar calculations herein to follow the influence of partially oxidized Au on the oxidation of CO at the dual Au/TiO_2 sites using the same Au/TiO_2 interface model presented previously.⁹ A detailed charge analysis of the Au sites on the fully-reduced Au/TiO_2 surface shows that all of the surface Au atoms are neutral, except for those that are in direct contact with the bridge oxygen atoms of the TiO_2 support which have a charge of $\sim +0.1\text{ e}$ as shown in Figure 7.6.

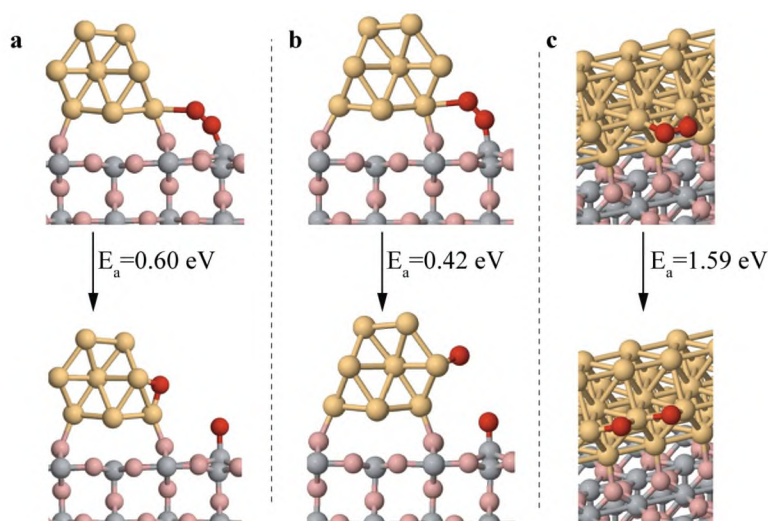


Figure 7.7. Calculated barrier for Au oxidation at different sites.

Some previous theoretical studies have suggested the importance of Au^{s+} for CO oxidation on the Au/TiO_2 catalyst.^{7,28-30,32} The models that were used examined only the influence of charge transfer between the TiO_2 support and the Au nanoparticles. There are no studies, however, of which we are aware, that examine the influence of the pre-oxidation of Au nanoparticles by chemisorbed oxygen on Au/TiO_2 catalysts. These sites involving chemisorbed oxygen, however, are more likely to be the relevant sites

associated with the inhibition phenomena that occur at O₂-rich conditions. We start by examining the Au sites where direct O₂ activation most likely proceeds. We showed previously that O₂ preferentially adsorbs at the perimeter sites along the Au/TiO₂ interface where it is partially activated by its interaction with the Au, thus forming a Ti-O-O-Au, peroxo type intermediate.⁹ The direct activation of O₂ at these perimeter sites, where no assistance by other molecules is involved, proceeds with a barrier of 0.4-0.6 eV (Figure 7.7), resulting in the production of O adatoms at the Au perimeter. Once formed,

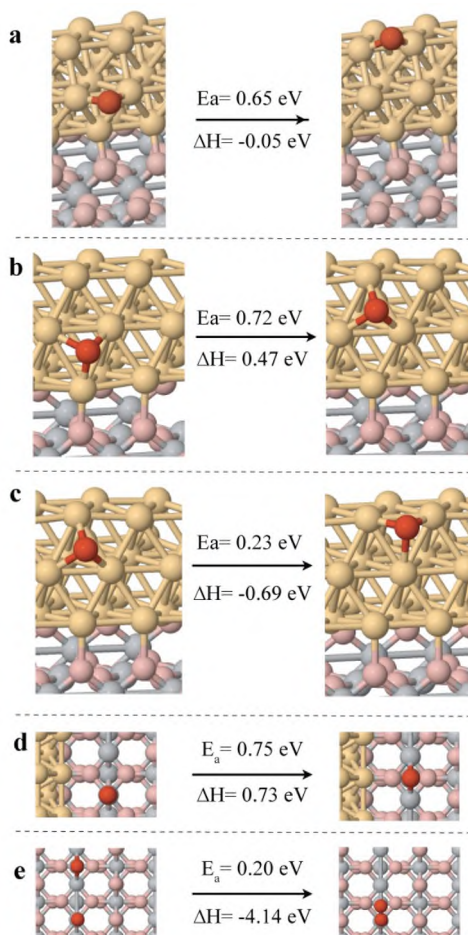


Figure 7.8. (a-c)-O atom diffusion on Au nanorod; (d)-O atom diffusion on Ti5c and (e)-recombination to O₂. ΔH refers to the reaction energy. The O atom diffusion on Ti5c data comes from Chapter 3 (ref. 9).

these O adatoms can diffuse to Au sites that are further removed from the perimeter as shown in Figure 7.8. The favorable binding sites for these atomic O species is either on a FCC three-fold hollow or on the edge bridge site, as shown in Figure 7.8a-c. The binding energies for these chemisorbed O adatoms are -0.3 to -0.4 eV with respect to one half of the O₂ molecule in gas phase, indicating that the O₂ dissociative adsorption is exothermic and chemisorbed O adatoms resulting from the O₂ dissociation are stable. The higher

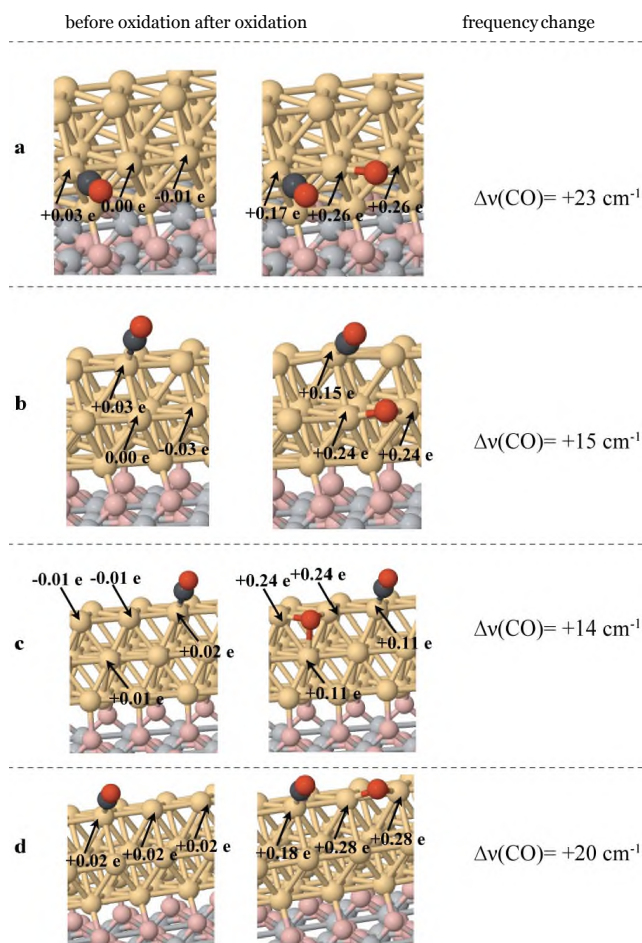


Figure 7.9. Theoretical predictions of the CO vibrational frequency change before and after oxidation. a, b, c, and d represent different CO and O adsorption configurations on the Au nanorod.

activation barriers for O surface diffusion on Au are consistent with the fact that these sites form only at the higher pre-oxidation temperatures (≥ 295 K). These O adatoms inductively increase the positive charge of the neighboring Au atoms as shown in Figure 7.9 ($\text{Au}^{\text{s}+}$, $\delta=0.1-0.3$) and directly influence the vibrational frequency of CO adsorbed on these electropositive Au sites. The vibrational frequency calculation results are reported in Figure 7.9. Calculated CO/ $\text{Au}^{\text{s}+}$ frequencies reveal a blue shift of $+14-23$ cm^{-1} from CO/ Au^0 , which is in very good agreement with the $+20$ cm^{-1} shift observed



Figure 7.10. Oxygen inhibition effect for O-O bond scission at the Au/TiO₂ perimeter from DFT calculation. a,b-CO-assisted O₂ dissociation at Au-Site I (a) before and (b) after Au oxidation by an O adatom. c, d-CO-assisted O₂ dissociation at Au-Site II (a) before and (b) after Au oxidation by an O adatom.

experimentally (from ~ 2106 to ~ 2126 cm^{-1} , Figure 7.1).

CO oxidation at the Au^0/TiO_2 perimeter was found to follow a path where molecular O_2 is activated in the presence of a nearby CO molecule at a dual catalytic site via a Au-O-O-Ti precursor.^{9'23'28} We examine the two characteristically different perimeter sites present in our model as shown in Figure 7.10 which reveal the differences that result from the different coordination numbers (CN) of the Au atoms that bind to the TiO_2 support. The first site (site I, Figure 7.10a) involves a more coordinatively unsaturated Au atom (CN=6) and is anchored to the support by a TiO_2 -bridging oxygen atom. The second site (site II, Figure 7.10c) involves a Au atom with CN=7 which also interacts with a TiO_2 -bridging oxygen atom. The different coordination numbers at these sites provide insights into the behavior of Au atoms with different coordination numbers in contact with the TiO_2 support of actual catalysts. When the Au was not oxidized, the activation energies calculated for the O-O bond scission (assisted by CO at the perimeter) are 0.16 eV (site I) and 0.27 eV (site II), as shown in Figures 7.10a and 7.10c. The lower barrier for CO oxidation reported at site I is the result of the less-coordinatively saturated Au atom⁵⁰ in site I, strongly stabilizing the terminal O of O_2 on TiO_2 . Similarly the higher barrier for CO oxidation at site II, compared to site I, is due to the weaker interaction of Au with O_2 that arises from the increased CN of the Au atom at site II over that at site I. In this case for the reduced Au^0/TiO_2 catalyst, CO oxidation can proceed at either site at 120 K, with site I being kinetically dominant. The presence of partially-oxidized Au atoms that result upon the formation of chemisorbed oxygen atoms reduces the ability of Au^{s+} to stabilize the CO- O_2 formation in the transition state upon reaction with CO, thus increasing the activation barrier (Figures 7.10b and 7.10d). The CO oxidation activation barrier for Au^{s+} at site I is now markedly higher at 0.65 eV as shown in Figure 7.10b. The activation barrier for site II shown in Figure 7.10d is only 0.32 eV. This significant

activation barrier increase at site I is the result of the much stronger binding of the chemisorbed oxygen atom due to the lower CN of Au at site I (CN=6) than at site II (CN=7). The strong chemisorption of atomic oxygen at site I prohibits site I from carrying out catalytic oxidation whereas site II can still catalyze CO oxidation at temperatures in the range 110-130 K. Since the pre-oxidation of the Au/TiO₂ catalyst was performed in 5 Torr of O₂ at elevated temperature (473 K), it is reasonable to assume the majority of perimeter sites are covered with O adatoms after oxidation. In fact, based on the changes in CO/Au and CO/Au^{s+} absorbance in Figure 7.2, about 60% of the Au⁰ sites on the surface of the Au nanoparticles become Au^{s+} sites for the particular size distribution of the Au nanoparticles used in the experiment. As a result, Au-Site I is poisoned whereas Au-Site II becomes the most active site for CO oxidation at low temperatures. The reaction of CO with the first oxygen of O₂ at Au-Site II results in the formation of CO₂ and an O adatom on the TiO₂ perimeter. This bound oxygen atom reacts with a second CO molecule on the TiO₂ support to form CO₂ with a barrier of only ~0.1 eV to regenerate the active site.

The end result from the theoretical simulations is that the formation of strongly chemisorbed oxygen bound to coordinatively unsaturated Au atoms inhibits these sites for low temperature CO oxidation. The more coordinatively saturated Au atoms associated with bound oxygen atoms can still oxidize CO but the barrier is increased to 0.32 eV which is consistent with the experimentally observed inhibition of the Au/TiO₂ catalyst by pre-oxidation and agrees with the 0.27 eV measured apparent activation energy.

The pre-oxidation is carried out in a temperature range where Au-based catalytic reactions are usually performed (295-473 K). At these temperatures, Au^{s+} species formed from oxygen chemisorption are likely to be involved. The apparent activation energy of

0.27 eV on the $\text{Au}^{5+}/\text{TiO}_2$ catalyst agrees with previously-reported 0.2-0.3 eV activation energies for CO oxidation on Au/TiO_2 catalysts measured at higher temperatures (200-350 K).^{51,52} While these partially oxidized sites demonstrate reactivity that is consistent with that reported over working catalysts, the higher temperature used here to activate O_2 also promotes the diffusion of adsorbed atomic oxygen from the interface where it can react with CO on Au^0 sites. In our low-temperature experiments, the more active Au^0 metal sites at the Au perimeter are only present at temperatures below 200 K. This argument is confirmed by the extension of the Arrhenius plots shown in Figure 5b, where CO oxidation activity on the Au^{s+} sites surpasses the Au^0 sites at 198 K. In the temperature range of $T > 198$ K, CO reacts with the O adatoms on the Au nano-rod, constantly reducing the Au^{s+} sites to Au^0 sites, and the activity increases above that observed when Au^{s+} sites remain unreduced, below 147 K (Figure 7.2). The Au^{s+} sites exhibit lower reactivity than Au^0 sites which is consistent with the results from *in situ* X-ray absorption studies of CO oxidation over Au/TiO_2 catalysts at higher temperatures.^{3,18,19,53,54}

IV. Conclusion.

The activity of Au catalytic sites located at the boundary between Au nanoparticles and a TiO_2 support have been studied experimentally and theoretically in order to understand the influence of oxygen adsorption on the model low-temperature oxidation reaction, $\text{CO} + 1/2\text{O}_2 \rightarrow \text{CO}_2$. As on the reduced Au/TiO_2 catalyst, CO is found to be supplied from TiO_2 sites surrounding the pre-oxidized Au nanoparticles at catalytic reaction temperatures near 120 K, confirming the general picture of catalytic activity at the nanoparticle perimeter. It is found that on the oxygen-treated catalyst the reaction rate is considerably reduced and the activation energy is nearly doubled by electronic

effects which involve the induction of positive charge into the perimeter Au atoms by O atom adsorption. The activation of O₂ on the inhibited Au^{s+} catalyst is assisted by a neighboring CO molecule at low temperatures. The ability of the catalyst to activate molecular O₂ at dual perimeter sites involving Au^{s+} atoms and neighbor Ti⁴⁺ ions in the support is retarded significantly for the CN=6 Au^{s+} atoms, causing the catalytic site to shift to the CN=7 Au^{s+} sites. It is likely that the higher temperature and higher O₂ pressure regimes for CO oxidation involve these Au^{s+} perimeter sites, where the oxidation of Au^o to Au^{s+} by O₂ and the reduction of Au^{s+} to Au^o by CO occur constantly.

V. Acknowledgement.

We gratefully acknowledge the financial support by DOE, Office of Basic Energy Sciences, under grant number DE-FG02-09ER16080 as well as a fellowship for Mrs. Isabel Green from AES Corporation through the AES Graduate Fellowships in Energy Research Program at the University of Virginia. We also acknowledge the XSEDE computing resources from the Texas Advanced Computing Center.

Chapter 7 References:

1. Haruta, M.; Kobayashi, T.; Sano, H.; Yamada, N. *Chemistry Letters* **1987**, 2, 405.
2. Meyer, R.; Lemire, C.; Shaikhutdinov, S. K.; Freund, H.-J. *Gold Bulletin* **2004**, 37, 72.
3. Kung, M. C.; Davis, R. J.; Kung, H. H. *The Journal of Physical Chemistry C* **2007**, 111, 11767.
4. Widmann, D.; Behm, R. J. *Angewandte Chemie International Edition* **2011**, 50, 10241.
5. Chen, M. S.; Goodman, D. W. *Science* **2004**, 306, 252.
6. Kotobuki, M.; Leppelt, R.; Hansgen, D. A.; Widmann, D.; Behm, R. J. *Journal of Catalysis* **2009**, 264, 67.
7. Laursen, S.; Linic, S. *The Journal of Physical Chemistry C* **2009**, 113, 6689.

8. Wang, J.; Hammer, B. *Topics in Catalysis* **2007**, *44*, 49.
9. Green, I. X.; Tang, W.; Neurock, M.; Yates, J. T., Jr. *Science* **2011**, *333*, 736.
10. Green, I. X.; Tang, W.; Neurock, M.; Yates, J. T., Jr. *Angewandte Chemie International Edition* **2011**, *50*, 10186.
11. Yan, Z.; Chinta, S.; Mohamed, A. A.; Fackler, J. P.; Goodman, D. W. *Journal of the American Chemical Society* **2005**, *127*, 1604.
12. Sanchez, A.; Abbet, S.; Heiz, U.; Schneider, W. D.; Hakkinen, H.; Barnett, R. N.; Landman, U. *The Journal of Physical Chemistry A* **1999**, *103*, 9573.
13. Vijay, A.; Mills, G.; Metiu, H. *Journal of Chemical Physics* **2003**, *118*, 6536.
14. Fu, Q.; Saltsburg, H.; Flytzani-Stephanopoulos, M. *Science* **2003**, *301*, 935.
15. Fierro-Gonzalez, J. C.; Guzman, J.; Gates, B. C. *Topics in Catalysis* **2007**, *44*, 103.
16. Frondelius, P.; Hakkinen, H.; Honkala, K. *Angewandte Chemie International Edition* **2010**, *49*, 7913-
17. Venezia, A. M.; Pantaleo, G.; Longo, A.; Di Carlo, G.; Casaletto, M. P.; Liotta, F. L.; Deganello, G. *The Journal of Physical Chemistry B* **2005**, *109*, 2821.
18. Calla, J. T.; Bore, M. T.; Datye, A. K.; Davis, R. J. *Journal of Catalysis* **2006**, *238*, 458.
19. Calla, J.; Davis, R. *Catalysis Letters* **2005**, *99*, 21.
20. Laursen, S.; Linic, S. *Physical Review Letters* **2006**, *97*, 026101.
21. Molina, L. M.; Hammer, B. *Applied Catalysis A: General* **2005**, *291*, 21.
22. Vilhelmsen, L. B.; Hammer, B. *Physical Review Letters* **2012**, *108*, 126101.
23. Liu, Z.-P.; Hu, P.; Alavi, A. *Journal of the American Chemical Society* **2002**, *124*, 14770.
24. Okazaki, K.; Morikawa, Y.; Tanaka, S.; Tanaka, K.; Kohyama, M. *Physical Review B* **2004**, *69*, 235404.
25. Madsen, G. K. H.; Hammer, B. *Journal of Chemical Physics* **2009**, *130*, 044704.
26. Okumura, M.; Kitagawa, Y.; Haruta, M.; Yamaguchi, K. *Applied Catalysis A: General* **2005**, *291*, 37-
27. Okumura, M.; Kitagawa, Y.; Haruta, M.; Yamaguchi, K. *Chemical Physics Letters* **2001**, *346*, 163.
28. Molina, L. M.; Rasmussen, M. D.; Hammer, B. *Journal of Chemical Physics* **2004**, *120*, 7673.
29. Wang, J. G.; Hammer, B. *Physical Review Letters* **2006**, *97*, 136107.

30. Liu, Z.-P.; Gong, X.-Q.; Kohanoff, J.; Sanchez, C.; Hu, P. *Physical Review Letters* 2003, 91, 266102.
31. Boronat, M.; Concepción, P.; Corma, A. *Journal of Physical Chemistry C* 2009, 113, 16772.
32. Chrétien, S.; Metiu, H. *Journal of Chemical Physics* 2008, 128, 044714.
33. Remediakis, I. N.; Lopez, N.; Norskov, J. K. *Applied Catalysis A: General* 2005, 291, 13.
34. Tang, D.; Hu, C. *The Journal of Physical Chemistry Letters* 2011, 2972.
35. Laursen, S.; Linic, S. *Physical Chemistry Chemical Physics* 2009, 11, 11006.
36. van Bokhoven, J. A.; Louis, C.; Miller, J. T.; Tromp, M.; Safonova, O. V.; Glatzel, P. *Angewandte Chemie International Edition* 2006, 45, 4651.
37. Li, M.; Wu, Z.; Ma, Z.; Schwartz, V.; Mullins, D. R.; Dai, S.; Overbury, S. H. *Journal of Catalysis* 2009, 266, 98.
38. Minicò, S.; Scire, S.; Crisafulli, C.; Visco, A. M.; Galvagno, S. *Catalysis Letters* 1997, 47, 273.
39. Dekkers, M. A. P.; Lippits, M. J.; Nieuwenhuys, B. E. *Catalysis Letters* 1998, 56, 195.
40. Lee, I.; Joo, J. B.; Yin, Y.; Zaera, F. *Angewandte Chemie International Edition* 2011, 50, 10208.
41. Zanella, R.; Giorgio, S.; Henry, C. R.; Louis, C. *Journal of Physical Chemistry B* 2002, 106, 7634-
42. Perdew, J. P.; Wang, Y. *Physical Review B* 1992, 45, 13244.
43. Henao, J. D.; Caputo, T.; Yang, J. H.; Kung, M. C.; Kung, H. H. *The Journal of Physical Chemistry B* 2006, 110, 8689.
44. Carrettin, S.; Concepción, P.; Corma, A.; Lopez Nieto, J. M.; Puentes, V. F. *Angewandte Chemie International Edition* 2004, 43, 2538.
45. Chen, M.; Goodman, D. W. *Accounts of Chemical Research* 2006, 39, 739.
46. Hao, Y.; Mihaylov, M.; Ivanova, E.; Hadjiivanov, K.; Knozinger, H.; Gates, B. C. *Journal of Catalysis* 2009, 261, 137.
47. Mihaylov, M.; Knozinger, H.; Hadjiivanov, K.; Gates, B. C. *Chemie Ingenieur Technik* 2007, 79, 795-
48. Boccuzzi, F.; Chiorino, A.; Manzoli, M. *Surface Science* 2000, 454-456, 942.
49. Wu, Z.; Zhou, S.; Zhu, H.; Dai, S.; Overbury, S. H. *The Journal of Physical Chemistry C* 2009, 113, 3726.

50. Williams, W. D.; Shekhar, M.; Lee, W. S.; Kispersky, V.; Delgass, W. N.; Ribeiro, F. H.; Kim, S. M.; Stach, E. A.; Miller, J. T.; Allard, L. F. *Journal of the American Chemical Society* 2010, *132*, 14018.
51. Daté, M.; Okumura, M.; Tsubota, S.; Haruta, M. *Angewandte Chemie International Edition* 2004, *43*, 2129.
52. Long, C. G.; Gilbertson, J. D.; Vijayaraghavan, G.; Stevenson, K. J.; Pursell, C. J.; Chandler, B. D. *Journal of the American Chemical Society* 2008, *130*, 10103.
53. Weiher, N.; Bus, E.; Delannoy, L.; Louis, C.; Ramaker, D. E.; Miller, J. T.; van Bokhoven, J. A. *Journal of Catalysis* 2006, *240*, 100.
54. Schwartz, V.; Mullins, D. R.; Yan, W.; Chen, B.; Dai, S.; Overbury, S. H. *The Journal of Physical Chemistry B* 2004, *108*, 15782.

Part II

Adsorption, Diffusion, and Desorption Properties of Metal Oxides

Chapter 8

IR Spectroscopic Measurement of Chemisorbed Pyridine

Diffusion Kinetics through MgO Nanoparticles — The

Involvement of Surface Defect Sites in Slow Diffusion.*

[^]Reprinted with permission from S. Kim, X. Wang, C. Buda, M. Neurock, O. B. Koper, and J. T. Yates, Jr., “*IR Spectroscopic Measurement of Diffusion Kinetics of Chemisorbed Pyridine through Nanocrystalline MgO Particles. The Involvement of Surface Defect Sites in Slow Diffusion*”, *The Journal of Physical Chemistry C* 2009, 113, 2219-2227. Copyright 2009 American Chemical Society. The theoretical work was performed by Dr. Corneliu Buda and Dr. Matthew Neurock and is included here for completeness.

The molecular transport of pyridine through nanosized MgO particles has been investigated by Fourier transform IR spectroscopy. Two regimes of chemisorbed pyridine diffusion are observed. A fast diffusion process is associated with pyridine bound to nondefective smooth MgO(100) facets which exhibit an activation energy barrier of 35.7 kJ mol⁻¹ for escape into a mobile precursor. The slow pyridine diffusion process occurs from defect sites, where the activation energy of escape to the mobile precursor is measured to be 64.6 kJ mol⁻¹. The escape barriers controlling pyridine diffusion through MgO powders are similar to the calculated adsorption energy on MgO(100) and to the calculated adsorption energies on various defect sites on MgO(100) having lower Mg²⁺ coordination numbers than those on MgO(100) facets.

I. Introduction.

Molecular transport in porous solids has been conventionally considered as the diffusion through the pores with a rate which is modified by the presence of pore walls which bind molecules at adsorption sites.¹⁻⁴ The diffusivity is determined by the textural properties of the porous materials such as the pore volume, pore size distribution, and

surface area, as well as the surface chemical properties of the pore walls. For adsorbed molecules the transport has been explained by surface diffusion along the internal surface within the pore structure.⁵⁶ The bound molecules are activated into a mobile precursor state in which they move laterally and then desorb into vacuum, as shown in Figure 8.1.⁷⁸ The activation energy controlling the rate of surface diffusion, which is denoted as the escape barrier, has been found to be near the desorption activation energy in accordance with Figure 8.1. Therefore, the rate of the overall transport process is controlled by the escape barrier leading to the mobile precursor state.

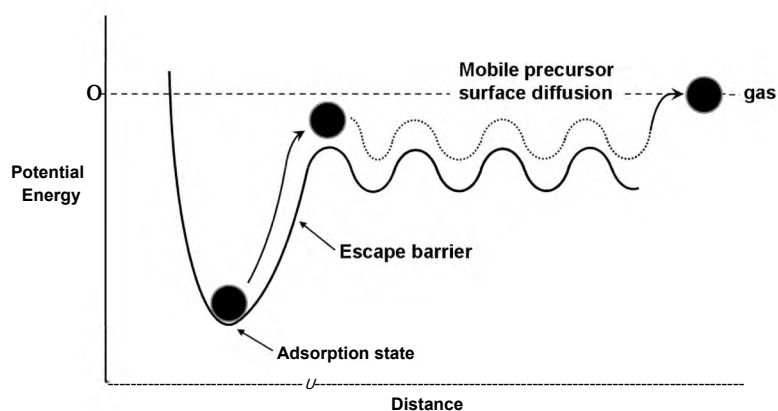


Figure 8.1. Schematic potential energy diagram of the mobile precursor state model for activated surface diffusion. The coordinate describing motion from site to site in the mobile precursor diffusion is a lateral coordinate across the surface.

Infrared spectroscopy has been used to study the long range Fickian diffusion kinetics in powders by monitoring the absorbance change in the vibrational modes of diffusing molecules *in-situ*.⁹⁻¹² In our previous report using transmission IR spectroscopy,¹³ we developed a new method to study the diffusion properties of molecules moving from the condensed phase *inward* into high area γ - Al_2O_3 powders. With this technique the diffusion of organic molecules from a condensed film (formed at low temperature on the outer geometrical surface of the powder) into the interior of the

compressed powder was monitored by using a characteristic IR band as a spectroscopic sensor of the arrival of diffusing molecules at new adsorption sites within the bulk of the powder. The diffusivity was determined by fitting the change in absorbance due to chemically bound molecules to Fick's second law, lending agreement with theory.

In the present work, we have studied molecular transport properties through nanosized MgO powders by using chemisorbed pyridine as a probe molecule. In these measurements diffusion *outwards* was employed. We found that molecular transport of pyridine through porous MgO is governed by two separable activated escape processes into the mobile precursor state which are associated with two types of pyridine chemisorption binding sites on the MgO surface. The molecule in the mobile precursor state may desorb into vacuum or readsorb on a chemisorption site. Density functional theoretical calculations find two predominant modes of pyridine adsorption with adsorption energies that agree with those found experimentally to within the expected accuracy.

II. Methodology.

A. Experimental.

MgO powder is compressed into the grid (0.005 cm thickness) using a hydraulic press (60,000 psi).¹⁴⁻¹⁶ In separate studies, an unpressed MgO sample was prepared by spraying a slurry of MgO in acetone + water mixture onto the grid through a temporary mask which is designed to locate the sample spot position.^{17,18} While the slurry was sprayed, the grid was maintained at 50 °C by electric heating with a dc power supply to rapidly evaporate the solvents.

The powdered MgO was obtained from Nanoscale Corporation (Manhattan, KS). The synthetic process used for producing such powders is described elsewhere.¹⁹ The MgO is

composed of hexagonal platelet particles with individual crystallite sizes of less than 8 nm. The major physical characteristics of the MgO sample for different treatment conditions are listed in Table 8.1. Compared to the “as-received” material, the specific surface area and the pore volume have significantly decreased in samples treated at 1200 K for dehydroxylation. Figure 8.2 shows the pore size distribution of the corresponding MgO samples. The BET (Brunauer-Emmett-Teller) method was employed using a Quantachrome Nova 2200 BET instrument. The BJH method, developed by Barrett, Joyner and Halenda in 1951 was used to calculate the pore size distribution (PSD). The method is based on the Kelvin equation and corrected for multilayer adsorption.²⁰ It is most widely used for calculations of the PSD over the mesopore (2-50 nm) and part of the macropore range. The mesopore size distribution function gives the volume of pores as a function of their diameter. When the MgO is heat-treated before or after compression, most of pores less than 10 nm in size disappear due to the agglomeration of the particles, as seen in Figure 8.2.

Table 8.1: Typical Properties of the MgO Nanoparticles

	uncompressed MgO		compressed MgO ^a	
	treated at 1200 K with untreated N ₂ flowing		treated at 1200 K with untreated N ₂ flowing	
SSA (m ² /g)	241	13	19	23
av pore diameter (nm)	5.0	14.1	20.5	23.4
pore volume (cm ³ /g)	0.3	0.04	0.10	0.14

^a Compressed with 60000 psi.

The compressed/uncompressed MgO sample was annealed to 1100 K in vacuum for 0.5-2 hours to produce a dehydroxylated surface. Figure 8.3 shows the IR spectral changes of the compressed MgO sample upon heating, where the surface hydroxyl groups and surface carbonate species disappear from the MgO.

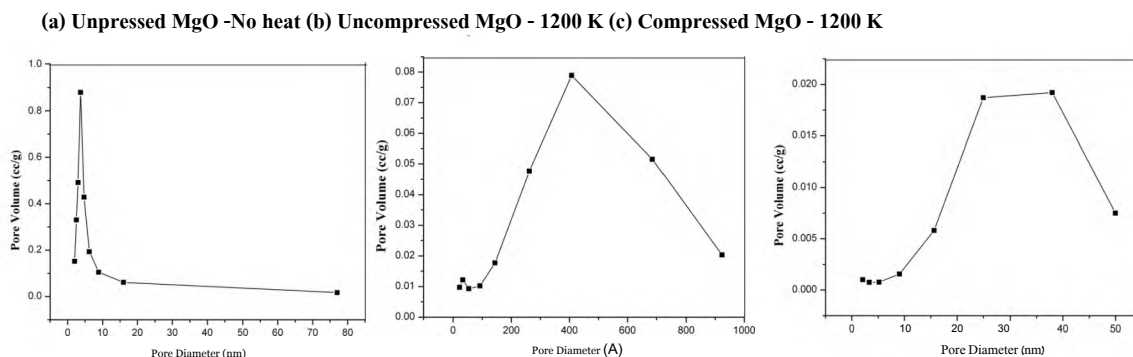


Figure 8.2. Pore size distribution of MgO powder samples: (a) uncompressed; (b) uncompressed with heat treatment at 1200 K; (c) compressed with heat treatment at 1200 K.

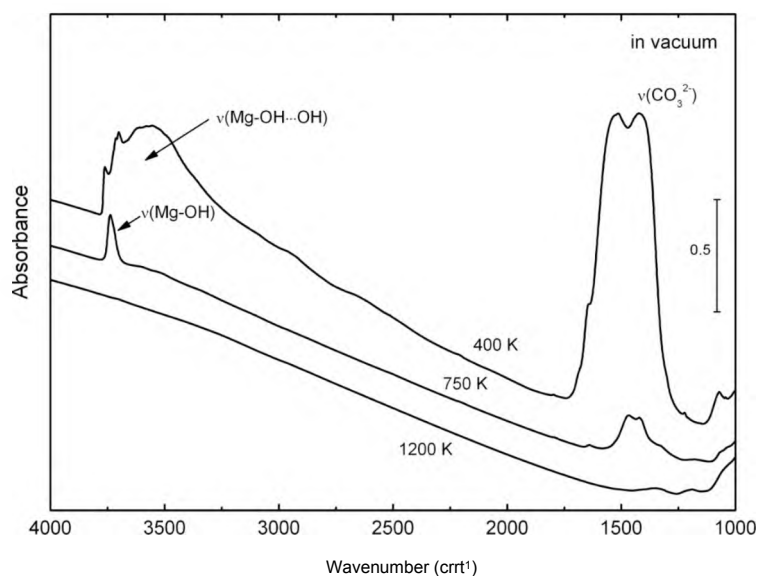


Figure 8.3. FT-IR spectra of compressed MgO during heat treatment up to 1200 K. The loss of surface Mg-OH and Mg-CO₃ species is observed.

Pyridine was obtained from Sigma-Aldrich (anhydrous, 99.8 % purity) and further purified with freeze-pump-thaw cycles using liquid nitrogen. The MgO was exposed to pyridine at 260 K to form a saturated chemisorbed phase. Spectroscopic measurements show that no physisorbed pyridine forms under these adsorption conditions. The IR measurements versus time of pyridine diffusion were carried out in vacuum at 270-300 K, and the diffusion of pyridine from the MgO was monitored by plotting the absorbance

decrease of several pyridine vibrational modes. The temperature range used herein was near the onset temperature for desorption of chemisorbed pyridine.

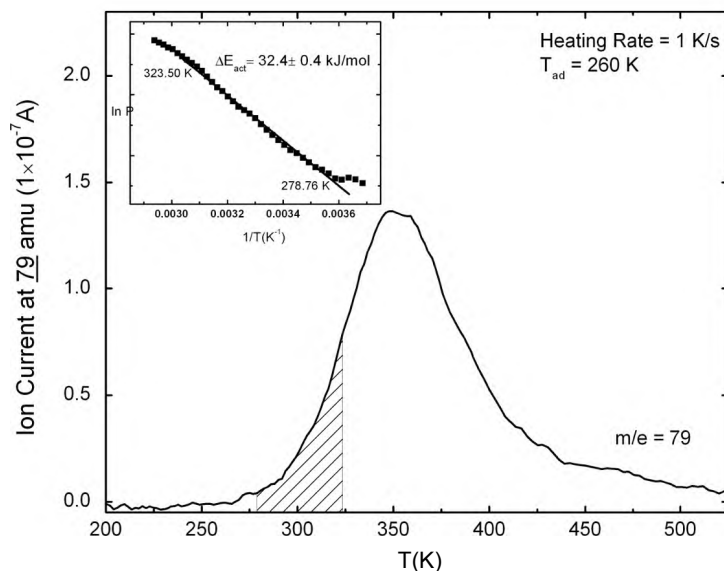


Figure 8.4. TPD spectra of chemisorbed pyridine from compressed MgO. The kinetic fit to the leading edge, depicted by crosshatching in the TPD spectra, yields $\Delta E_{act} = \sim 32.4 \pm 0.4$ kJ/mol.

Figure 8.4 shows temperature-programmed desorption (TPD) from a chemisorbed pyridine layer which is initially near saturation coverage. Thermal desorption at $m/e = 79$ (parent) was recorded at an electron energy of 70 eV. Measurements near the onset temperature for desorption, 270 K, provide an estimate of the lowest activation energy for pyridine escape by desorption from the powdered surface. This process is probably kinetically controlled by the escape barrier from the most weakly bound chemisorbed state to the mobile precursor state and then to vacuum. An exponential fit to the leading edge of the desorption curve yields an activation energy of 32.4 ± 0.4 kJ mol⁻¹ for pyridine desorption, over the temperature range 278-323 K, as shown by the cross-hatched region.

B. Computational.

Nonlocal gradient corrected periodic density functional theoretical (DFT) calculations were carried out to determine the optimal pyridine adsorption sites on the MgO(100) surface and their corresponding adsorption energies. All of the calculations were performed using Vienna Ab-initio Simulation Program (VASP), a periodic DFT code which expands the wave function as a series of plane waves.²¹⁻²³ The interactions between the core and the valence electrons were described by Vanderbilt ultrasoft pseudopotentials (US-PP).²⁴ The calculations were all carried out within the Generalized Gradient Approximation where the Perdew-Wang 91 (PW91) functional²⁵ form was used to calculate the exchange and correlation energies. The electronic energies were converged to within 10^{-4} eV, whereas the geometry was optimized such that the forces on each atom were below the threshold value of 0.05 eV/Å. A $3 \times 3 \times 1$ Monkhorst-Pack k -point mesh²⁶ was used to sample the first Brillouin zone.

The MgO(100) surface was modeled using a 3×3 unit cell comprised of four layers, each of which contained nine Mg and nine O atoms. A vacuum region of 15 Å was placed between each of the MgO slabs. The bottom two layers of the slab were held fixed to their optimized bulk configuration, while the top two layers along with the pyridine molecule were optimized. Both Mg^{2+} and O^{2-} defect sites were created by removing Mg and O atoms from the top surface. The pyridine adsorption energies were calculated using Equation 8.1:

$$^4E_{\text{ads}} \equiv E_{\text{pyridine/MgO}} - E_{\text{pyridine}} - E_{\text{MgO}} \quad (8.1)$$

where $E_{\text{pyridine/MgO}}$, E_{pyridine} , and E_{MgO} refer to the energy of pyridine bound to the MgO surface, pyridine alone in the gas phase, and the bare MgO(100) surface, respectively. The theoretical estimates of adsorption energy do not include small van der Waals contributions.

III. Results.

A. Spectroscopic Measurements.

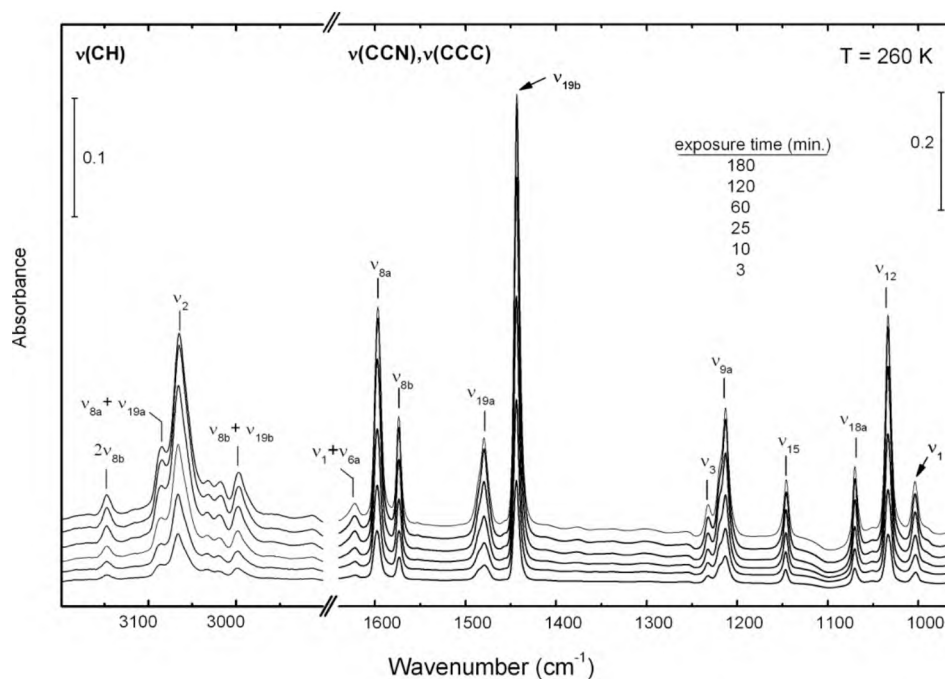


Figure 8.5. FT-IR spectra of chemisorbed pyridine on compressed MgO with increasing exposure time at 260 K and ~15 mTorr.

Figure 8.5 shows IR spectral developments as pyridine is adsorbed on MgO from the gas phase (~ 15 mTorr) at 260 K. The assignments in Figure 8.5 are based on published results following Wilson's notation.²⁷⁻³¹ The IR absorbance develops monotonically as chemisorbed pyridine molecules saturate the surface. Figure 8.6 shows the normalized integrated absorbances of two specific vibrational modes, ν_{19b} (the C-C, C-N stretching mode) at 1443 cm^{-1} and ν_1 (the sym. ring breathing mode) at 1003 cm^{-1} (these modes are denoted by arrows in Figure 8.5), plotted as a function of increasing pyridine exposure at ~15 mTorr pressure and 260 K. The modes develop and their absorbance saturates in about 2-4 hours. Since the MgO is totally dehydroxylated (see Figure 8.3) by the 1200 K

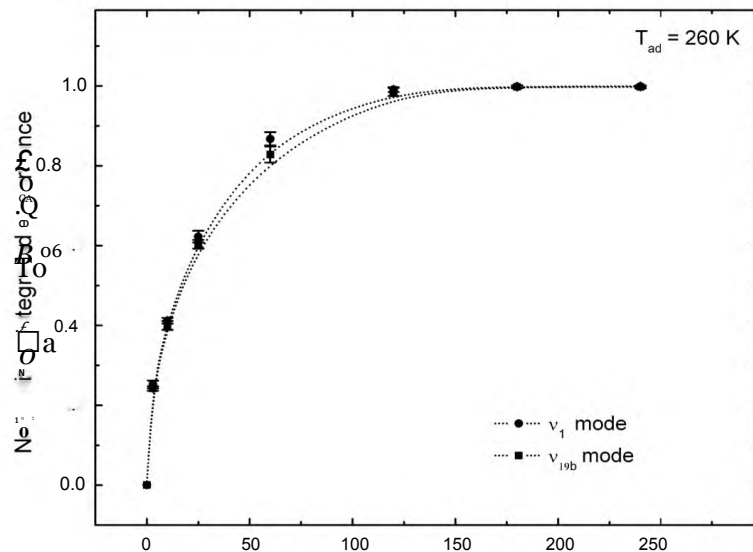


Figure 8.6. Plots of the integrated absorbance of two pyridine vibrational modes upon increasing exposure time up to saturation coverage. The diffusion measurements are made from the saturated pyridine layer.

pre-treatment process, the pyridine adsorption occurs at Mg^{2+} Lewis acid sites via the nitrogen atom and the vibrational frequencies observed for the adsorbed pyridine are near those found for pyridine chemisorbed on Lewis acid sites of metal oxides in published reports.³²⁻³⁴ The pyridine sym. ring breathing mode (ν_i) shows a distinct blue shift when the pyridine molecule adsorbs to a metal ion caused by the interaction between the metal ion and the pyridine's nitrogen.³⁵⁻³⁷ Upon adsorption on Mg^{2+} sites the mode shifts by $+12\text{ cm}^{-1}$, compared to the frequency in the gas phase, so that the chemisorbed pyridine is clearly separated from physisorbed pyridine species which can only be populated at lower adsorption temperature or higher pressure. Similar adsorption behavior is observed for the ν_{19b} mode which is also an indicator of the coverage of chemisorbed pyridine.

Figure 8.7 shows, starting with the saturated surface, the spectral changes as a function of time for two pyridine vibrational modes, ν_{19b} and ν_i , after heating to two fixed temperatures in vacuum (270 K and 300 K). The absorbance of the pyridine modes

decreases as the adsorbed pyridine molecules diffuse out of the interior of the compressed MgO samples at the elevated temperatures. The line shape changed during desorption are related to the involvement of two chemisorption sites, as will be discussed later.

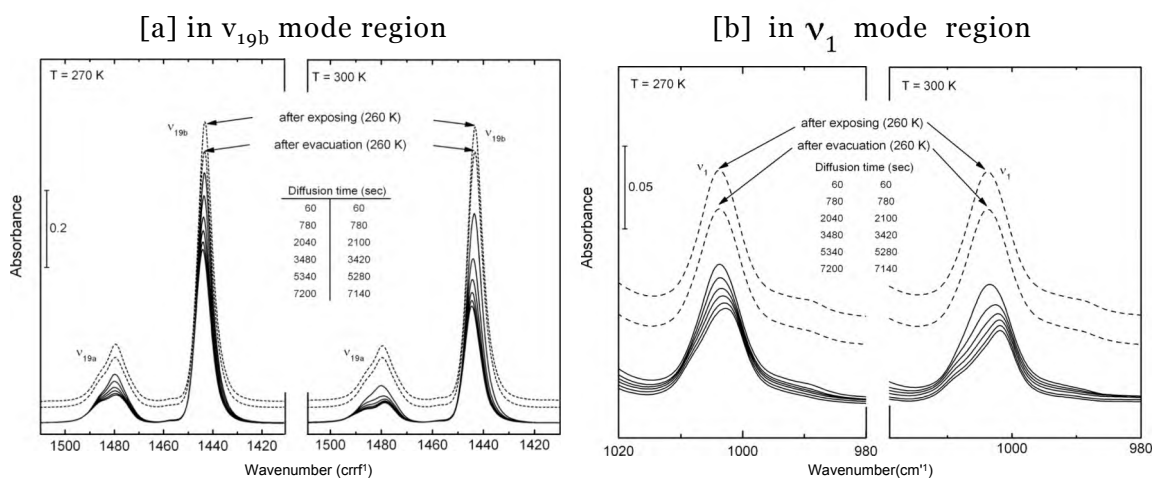


Figure 8.7. FT-IR spectra of pyridine on compressed MgO at 270 K and 300 K for increasing diffusion time in vacuum in the region of (a) the ν_{19} vibrational mode and (b) the ν_1 vibrational mode.

B. Diffusion Studies - Compressed MgO.

The spectra of the depleting pyridine chemisorbed layer were taken every 2-5 min for over 2 h at several fixed temperatures (270, 280, 290 and 300 K). The integrated absorbances, which are normalized to a point measured 5 min after evacuation at 260 K, are plotted as a function of time at each temperature, as shown in Figure 8.8. The points can be fitted to Fick's Second Law in one dimension.³⁸

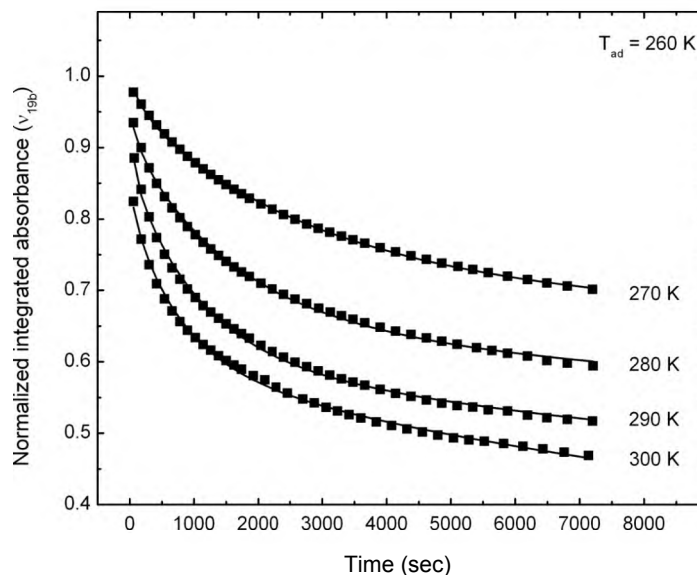


Figure 8.8. Plots of normalized absorbance of pyridine remaining during diffusion from compressed MgO at 270 K - 300 K. Symbols are experimental results and solid lines are the best fit to the double diffusion Equation 8.4. The normalization was done to the data point measured after exposure at 260 K followed by evacuation for 5 min.

The total amount of pyridine remaining adsorbed on the MgO at time t , M_t , is for a single diffusion process³⁸

$$M_t = \int_0^l C(x, t) dx = M_0 \sum_{n=0}^{\infty} \frac{8}{(2n+1)^2 \pi^2} \exp \left\{ -D(2n+1)^2 \pi^2 t / l^2 \right\} \quad (8.2)$$

where, l = thickness of compressed MgO, $C(x, t)$ = pyridine concentration at position x and time t , and M_0 = total amount adsorbed at saturation point (mol g^{-1} MgO) at $t = 0$.

Then, the normalized amount of pyridine remaining at time t for a single diffusion process is given by Equation 8.3:

$$\frac{M_t}{M_0} = \sum_{n=0}^{\infty} \frac{8}{(2n+1)^2 \pi^2} \exp \left\{ -D(2n+1)^2 \pi^2 t / l^2 \right\} \quad (8.3)$$

where $\frac{M_t}{M_0}$ = the fraction of sites occupied by pyridine; A_t is the absorbance of pyridine as measured by IR during diffusion, and A_0 is absorbance of the saturated layer.

The diffusivity was not defined successfully in our measurements by a single diffusion process. In the depletion of pyridine from the MgO, there is initially a very rapid diffusion stage, followed by a much slower process, as seen in Figure 8.8. Therefore the data points are fitted to a diffusion model involving two parallel diffusion processes, as shown in Equation 8.4:

$$A_{\theta} = A_{\infty} \left\{ \frac{1}{2} \left[1 + \frac{1}{\sqrt{1 + \frac{D_s}{D_f}}} \right] \exp \left\{ -\frac{D_s t}{x^2} \right\} + \frac{1}{2} \left[1 - \frac{1}{\sqrt{1 + \frac{D_s}{D_f}}} \right] \exp \left\{ -\frac{D_f t}{x^2} \right\} \right\} \quad (8.4)$$

where θ , θ_{∞} = the fractional coverage of pyridine initially involved in the fast and slow processes, and D_f , D_s = diffusion coefficient of pyridine in each process.

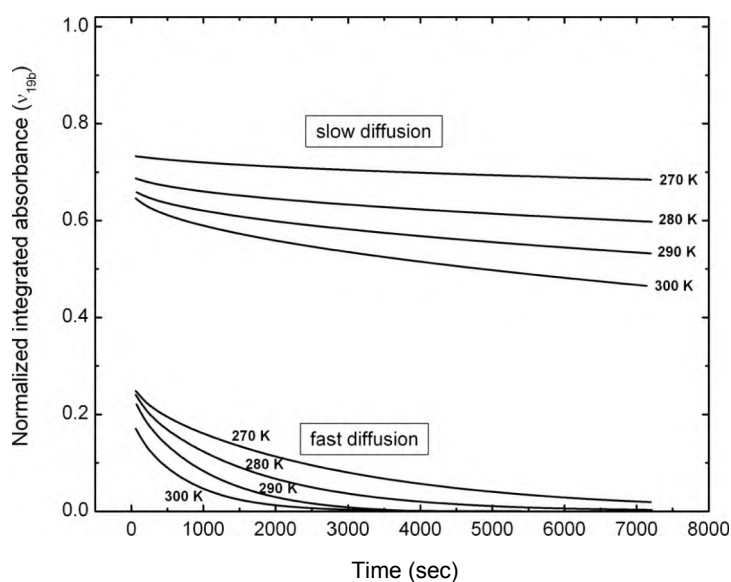


Figure 8.9. Separation of the slow and fast diffusion processes at each temperature as obtained by mathematical fits in Figure 8.8.

The best-fit curve at each temperature is shown as a solid line in Figure 8.8 correspondingly closely to the experimental points. The high quality of the fit indicates

that the diffusion process is well described by the two parallel rate processes. Figure 8.9 shows the separation of the fast and slow diffusion processes. It may be seen from the starting points that at 300 K about 64 % of the pyridine experiences the slow diffusion process, whereas at 300 K about 18 % experiences the fast diffusion process. These coverages do not add to 100 % because the first points were measured following some initial desorption. It is likely that the fraction of pyridine participating in the fast process is underestimated.

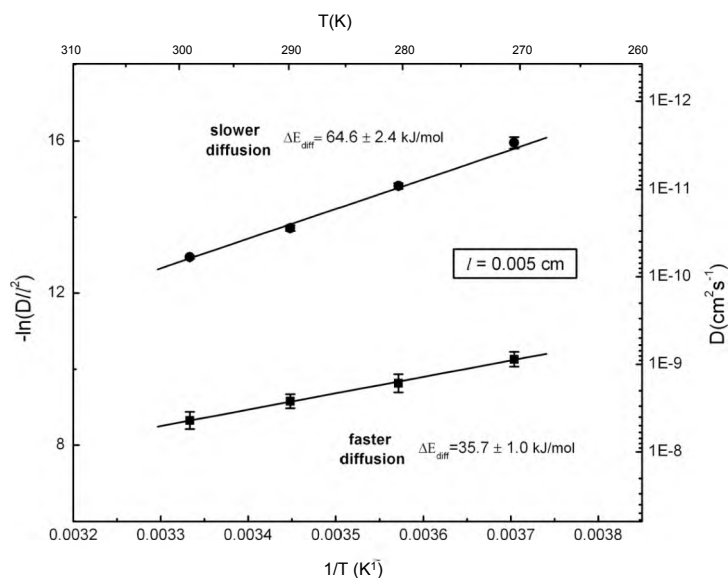


Figure 8.10. Arrhenius plots for the slow diffusion and the fast diffusion processes for pyridine from compressed MgO. The diffusivity values at various temperatures in each process is shown on the right hand axis.

Arrhenius plots for the two diffusion processes yield the corresponding activation energy values, as shown in Figure 8.10. The values of diffusion coefficients obtained at various temperatures are shown on the right-hand side of the graph, where the value of $l = 0.005$ cm, which is the thickness of the MgO deposit. Each point is an average from the data obtained from two pyridine vibrational modes, V19b and V1, in two separate diffusion

measurements, with the standard deviation. The diffusivity D_s in the slow process is in the range of 3.0×10^{-12} to $6.0 \times 10^{-11} \text{ cm}^2 \text{ s}^{-1}$ with an activation energy of $\sim 64.6 \pm 2.4 \text{ kJ mol}^{-1}$, which is about twice the activation energy in the initial fast process. The fast process exhibits D_f in the range of 8.9×10^{-10} to $4.5 \times 10^{-9} \text{ cm}^2 \text{ s}^{-1}$ with an activation energy of $\sim 35.7 \pm 1.0 \text{ kJ mol}^{-1}$. The two processes are postulated to be due to the activation of different kinds of chemically bound pyridine species to the mobile precursor state, which is controlled by the escape barrier for each species. The fast kinetic process is associated with flat and non-defective MgO sites, and the slow process is attributed to defect sites where the pyridine molecules bind strongly.

C. Comparison of Compressed and Uncompressed MgO Powders.

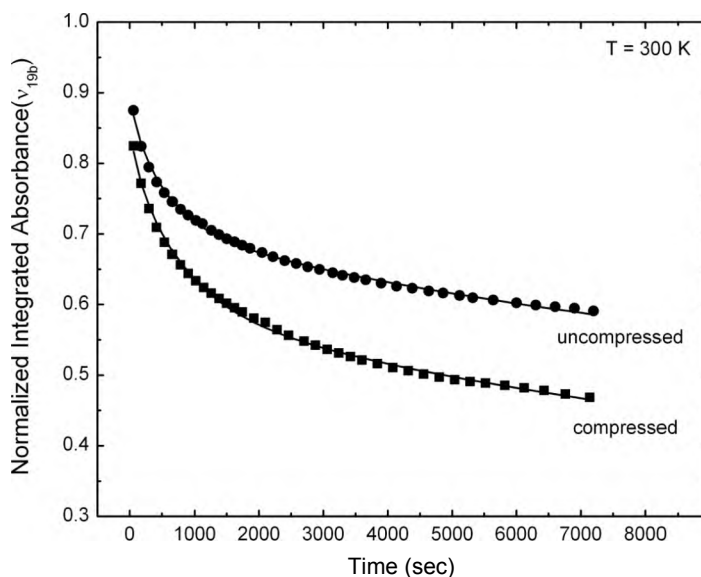


Figure 8.11. Plots of normalized diffusion amount of pyridine remaining during diffusion on uncompressed MgO at 300 K, compared to that on compressed MgO. Symbols are experimental results and solid lines are the best fit to the double diffusion Equation 8.4. The normalization was done as in Figure 8.8.

Figure 8.11 shows the diffusion rate of pyridine from a sprayed (uncompressed) MgO sample at 300 K, compared to that from the compressed MgO (reproduced from Figure 8.8). The diffusion coefficients in the uncompressed MgO are obtained by the best fit to the diffusion Equation 8.4 at 300 K, and found to be $3.8 \times 10^{-11} \text{ cm}^2 \text{ s}^{-1}$ (compared to $6.0 \times 10^{-11} \text{ cm}^2 \text{ s}^{-1}$ (compressed)) and $4.8 \times 10^{-9} \text{ cm}^2 \text{ s}^{-1}$ (compared to $4.5 \times 10^{-9} \text{ cm}^2 \text{ s}^{-1}$ (compressed)) for the slow and fast processes, respectively. The diffusivity for the slow process in the uncompressed MgO is slightly lower than in the compressed sample, while the value for the fast process is within the measurement error range. Moreover, the molecular fraction involved in the slow process increases up to $\sim 75 \%$ for the uncompressed MgO, as compared to $\sim 64 \%$ in the compressed sample, suggesting that physical compression of the nanoscale particles may remove defect sites to a small degree.

D. Spectroscopic Detection of Defect Site Adsorption.

IR spectral changes during pyridine depletion from the two MgO samples are compared for two specific vibrational modes, ν_{8b} (the C-C, C-N stretching mode) and ν_{12} (the asym. ring breathing mode), as shown in Figure 8.12. As the depletion from the compressed MgO continues (see upper spectra in Figure 8.12), the species which are associated with the fast process disappear more rapidly and the more strongly bound pyridine increases in relative coverage. Two overlapping spectral features are associated with the fast and slow diffusion processes. This indicates the presence of two kinds of adsorbed pyridine species associated with the two diffusion processes. It is clearly seen that IR spectral features on the uncompressed MgO (see lower spectra in Figure 8.12) are very close to that of strongly bound pyridine which participates in slow diffusion, as seen as a slowly decreasing shoulder on the compressed MgO (upper spectra). This means

that the fraction of the strongly bound species observed spectroscopically is initially larger on the uncompressed MgO, which is consistent with the higher fraction of slowly diffusing pyridine molecules (75 % in uncompressed MgO vs 64 % in compressed MgO) obtained from the previous kinetic analyses.

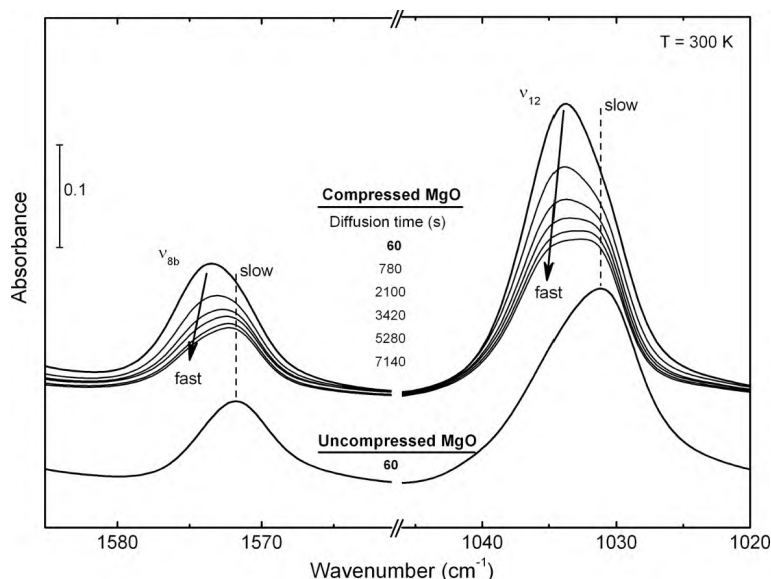


Figure 8.12. FT-IR spectra of pyridine on compressed and uncompressed MgO at 300 K with increasing diffusion time in the region of (a) the V_{8b} vibrational mode; and (b) the V_{12} vibrational mode.

E. Theoretical Results.

Pyridine adsorption on the MgO surface is predominantly electrostatic in character involving the donation of the lone pair of electrons on the basic nitrogen atom to the charged Mg center. The strength of electrostatic interaction with pyridine increases as the positive charge on MgO increases. In general, we find that the interaction energies increases as the metal coordination number decreases, as might be expected.

The preferred mode of adsorption of pyridine was found to be in an atop configuration on top of a Mg atom, with the pyridine molecule oriented perpendicular to

the MgO surface. This results in a Mg-N bond length of 2.313 Å and an adsorption energy of $-41.5 \text{ kJ mol}^{-1}$. In a second stable configuration, pyridine adsorbs tilted from the surface normal by 45.9° and has a Mg-N bond length of 2.392 Å. It is more weakly held to Mg in this state with a calculated adsorption energy of $-21.2 \text{ kJ mol}^{-1}$. The final possible configuration of adsorption of pyridine is one in which the pyridine aromatic ring lies parallel to the surface. This adsorption configuration is associated with a very weak binding energy of -5.8 kJ mol^{-1} .

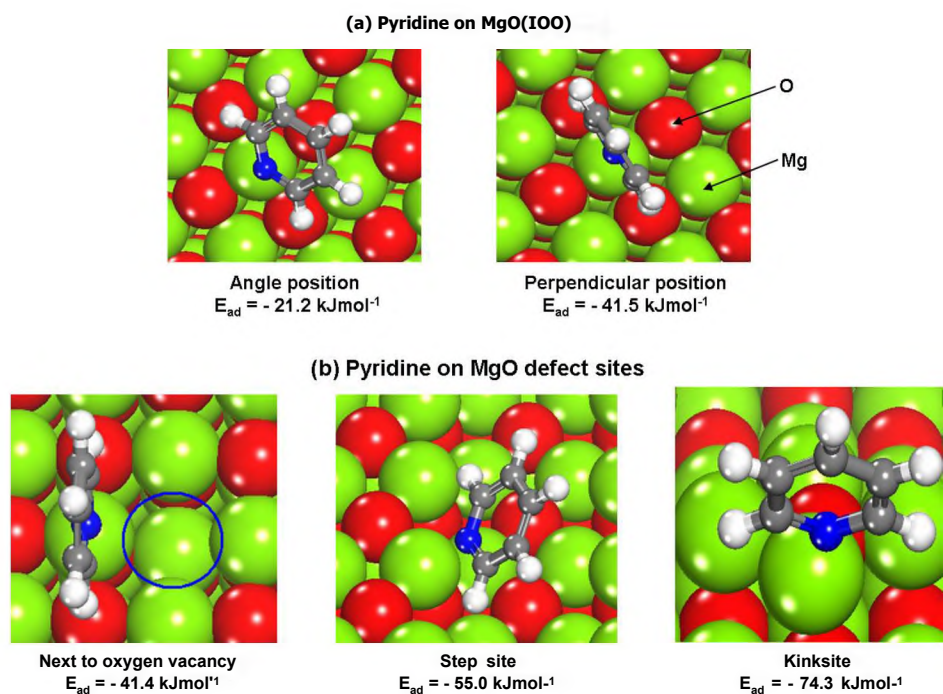


Figure 8.13. DFT calculation of the configuration and adsorption energy of chemisorbed pyridine (a) on MgO(100); and (b) on representative MgO defect sites.

In order to probe the nonideality of the MgO surface, we examined the adsorption of pyridine on MgO at different Mg coordination sites created by introducing O vacancy defect sites (CN = 4), step sites (CN = 3), and kink sites (CN = 2). The adsorption energy of pyridine adjacent to an O defect site ($-41.4 \text{ kJ mol}^{-1}$) was found to be quite similar to

that for pyridine on the ideal MgO(100) surface at $-41.5 \text{ kJ mol}^{-1}$ for the perpendicular mode of adsorption and $-21.2 \text{ kJ mol}^{-1}$ for the tilted orientation. The reduction of the coordination number from 5 to 4 increased the positive charge on the Mg atom, but this was compensated by repulsive interactions between the negatively charged neighboring O atoms, which ultimately resulted of step and kink sites in the MgO surface decreased the Mg coordination numbers from 4 to 3 and from 3 to 2, respectively. The decrease in coordination number of Mg on the step and kink surfaces is no longer compensated by the repulsive influences of the neighboring oxygen and as such the pyridine adsorption becomes energetically more favorable. The pyridine adsorption energy increases from $-41.5 \text{ kJ mol}^{-1}$ on MgO(100) to $-55.0 \text{ kJ mol}^{-1}$ (Mg-N = 2.180 Å) at the step site and to $-74.3 \text{ kJ mol}^{-1}$ (Mg-N = 2.135 Å) at the kink site. The representative adsorption configurations of pyridine adsorbed on MgO surfaces are depicted in Figure 8.13.

IV. Discussion.

A. Observation of Mobile Precursor Diffusion Kinetics.

The kinetic behavior observed for pyridine diffusion through MgO powder may be described accurately by a mobile precursor model, as shown in Figure 8.14. Here, a strongly chemisorbed pyridine molecule, localized on its adsorption site, can enter a weakly bound adsorption configuration at molecule-surface distances which are larger than those characteristic of the chemisorptive binding. This mobile precursor moves rapidly over the surface over low barriers. The molecule in the precursor state can either undergo desorption or return to a strong binding adsorption site. During adsorption through the precursor intermediate, the sticking coefficient will remain constant over most of the coverage range.⁷

In the mobile precursor mechanism for surface diffusion, the activation energy controlling surface diffusion will be the escape barrier height, separating the chemisorbed species from the diffusing precursor species. The observation of two overlapping activated processes for pyridine diffusion through MgO powder indicates that two MgO binding sites, having different escape barriers, are involved, as shown in Figure 8.14. It would be expected that the escape barrier in both cases will be smaller than the barrier to direct desorption from the chemisorption binding site.

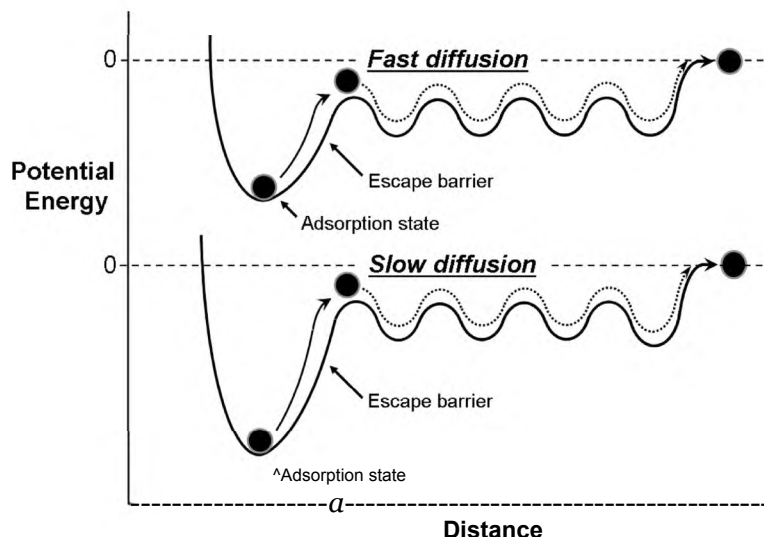


Figure 8.14. Schematic potential energy diagram of the slow and fast diffusion processes for pyridine through MgO based on the mobile precursor state model.

In this model the fast process will dominate at higher pyridine coverages, followed by the slow process as the surface coverage decreases, as is experimentally observed. After the majority of the fast diffusing molecules have been depleted from the weaker binding sites, the slow process will dominate and will be controlled by the escape barrier from the stronger binding sites.

B. Crystallographic Issues on MgO Particles. Pyridine Adsorption Sites.

The original uncompressed MgO studied here consists of hexagonal platelets about 80 nm in length and 10 nm thick, characterized by a high fraction of cubic crystal faces of (100) orientation. In addition to these faces, atomic steps, atomic step kinks, and oxygen vacancy defects are likely present on the surface and these defects will provide higher pyridine binding energy sites, compared to the smooth MgO(100) facets.

It is noted that the measured activation energy for fast diffusion ($35.7 \pm 1.0 \text{ kJ mol}^{-1}$) is slightly less than the calculated binding energy from the MgO(100) sites (41.5 kJ mol^{-1}), consistent with the teachings of Figure 8.1 and 8.14. the slow diffusion process, fed by the more strongly bound pyridine into mobile precursor diffusion from the defect sites ($64.6 \pm 2.4 \text{ kJ mol}^{-1}$). The calculated energy range for desorption from defect sites ranges from 41.4 to 74.3 kJ mol^{-1} therefore includes in its range the activation energy measured for the slow diffusion process.

C. MgO Powder Compression Effects.

Under the vacuum condition used in this experiment, surface diffusion predominates over Knudsen diffusion effects, since the mean free path of gas molecules is enormous compared to the pore sizes.

The uncompressed MgO powder exhibits a high surface area and a narrow pore size distribution centered at $\sim 5 \text{ nm}$ diameter (see Table 8.1 and Figure 8.2). Heating or compression of the powder causes a large decrease in surface area and a large *increase* in the average pore size. This is interpreted as being due to agglomeration of the nanometer-size MgO crystallites, producing larger clusters which have lost most of the small pores, leaving only larger pores with an average diameter of 14-23 nm (see Table 8.1). Compression of the MgO powder is also found to slightly increase the fraction of

rapidly diffusing pyridine molecules from 16% to 22% (see Table 8.2), and this is attributed to the removal of some of the active defect sites through agglomeration from small crystals to larger clusters. Similar effects due to aggregation processes have been reported by others.³⁹⁻⁴¹ Alternately, the enhancement of the rate of surface diffusion in the compressed powder can also be related to a decrease in the diffusion pathway tortuosity of the compressed MgO powder, compared to the uncompressed powder.

Table 8.2: Diffusion Parameter for Pyridine Diffusion on MgO in Compressed and Uncompressed Samples at 300K.

	D_f (10^{-9} cm ² s ⁻¹)		θ_t (%)	D_s (10^{-11} cm ² s ⁻¹),		θ_s (%)
compressed MgO	4.5		22	6.0		64
uncompressed MgO	4.8		16	3.8		75

D. Observation of the Elementary Surface Diffusion Processes by Spectroscopic Measurements.

The dehydroxylation and compression treated, significantly reducing the ~ 5 nm pores, might be considered to have a major influence on the kinetics of molecular transport through the powder. In fact, following compression, only relatively small changes in the diffusion coefficients for $\text{C}_5\text{H}_5\text{N}$; fast adsorption processes are observed as shown in Table 8.2. In addition, a significant change is observed in the ratio of these two transport processes following compression. These observations suggest that the kinetic measurements primarily reflect molecular behavior on the MgO surfaces related to site heterogeneity at the atomic level, and the kinetic behavior observed is only slightly modified by significant changes in the pore size distribution produced upon compression. Compression is a macroscopic phenomenon, which is relatively

unimportant in governing the two microscopic processes which control surface diffusion for two general types of MgO sites.

Another observation supports the conclusion that two states of adsorbed pyridine are responsible for the fast and slow diffusion processes. In Figure 8.12, where the spectral line shape of two pyridine vibrational modes is monitored as diffusion occurs, there is strong evidence that the ν_{sb} mode and the ν_{12} modes contain two overlapping components. On the compressed MgO, diffusion of pyridine followed by desorption first consumes the species associated with the high frequency components; the other component is slow to disappear as diffusion/desorption continues. On the uncompressed MgO, where diffusion is somewhat slower, a higher fraction of the pyridine is observed as the slow diffusion species, judging by the comparison of spectral lineshapes. This observation is consistent with the idea that compression to produce larger agglomerates also removes some defect sites from the powdered material but that the inherent site inhomogeneity governs the ratio of the fast and slow surface diffusion processes at the atomic level.

V. Summary of Results.

The following observations about pyridine diffusion through dehydroxylated MgO powder have been made:

1. Diffusion of chemisorbed pyridine, adsorbed on Mg^{2+} Lewis acid sites, occurs via the operation of a mobile precursor mechanism involving highly mobile species fed by strongly chemisorbed species.
2. The rate-determining step for diffusion through the powder followed by desorption into vacuum involves activation over an escape barrier from the chemisorbed species

into the mobile precursor state. The escape behavior is smaller than the adsorption energy.

3. Two different pyridine chemisorbed species are associated with a fast and slow diffusion process on MgO. The escape barrier for the fast process is 35.7 kJmol⁻¹, and for the slow process the escape barrier is 64.6 kJmol⁻¹.

4. DFT calculations show that the binding energy for pyridine to MgO(100) is 41.5 kJmol⁻¹. On defective MgO sites, the pyridine binding energy is calculated to be in the approximate range of 41.4-74.3 kJmol⁻¹. These values are quantitatively consistent with the postulate that slow diffusion originates from pyridine molecules bound to MgO defect sites, where the coordination number for Mg²⁺ ions at these sites is lower than CN = 5 for the MgO(100) crystal facet.

5. Extreme compression of the MgO powder to remove most of the ~5 nm diameter pores causes only a relatively small increase in the diffusion speed and produces little change in the magnitude of the two diffusion coefficients involved, or in the observed ratio of pyridine participating in the fast and slow pyridine diffusion processes.

6. Small frequency differences in the V8b and the V12 modes are associated with pyridine binding to weak binding (MgO(100)) and strong binding MgO (defect) sites.

VI. Acknowledgement.

We acknowledge, with thanks, the support of this work by DTRA through Contract HDTRA1-07-C-0085.

Chapter 8 References:

1. Barrer, R. M. *Hydrothermal Chemistry of Zeolites*; Academic Press: London, 1982.
2. Cornner, W. C. In *Fluid Transport in Nanoporous Materials*; Cornner, W. C., Fraissard, J., Eds.; Springer: Dordrecht, 2006.
3. Crittenden, B.; Thomas, W. J. *Adsorption Technology & Design*; Butterworth-Heinemann 1998; Vol. Boston.
4. Ruthven, D. M. *Principles of Adsorption and Adsorption Process*; John Wiley & Sons: New York, 1984.
5. Boer, J. H. *The Dynamical Character of Adsorption* Oxford University Press: London, 1968.
6. Do, D. D. *Adsorption Analysis Equilibria and Kinetics*; Imperial College Press: London, 1998; Vol. 2.
7. Weinberg, W. H. In *Kinetics of Interface Reactions*; M. Grunze, H. J. K., Ed.; Springer-Verlag: New York, London 1986.
8. Cassuto, A.; King, D. A. *Surf. Sci.* **1981**, 102, 388.
9. Karge, H. G. *Comptes Rendus Chimie* **2005**, 8, 303.
10. Meunier, F. C.; Domokos, L.; Seshan, K.; Lercher, J. A. *J. Catal.* **2002**, 211, 366.
11. Niessen, W.; Karge, H. G. *Studies Surf. Sci. Catal.* **1991**, 60, 213.
12. Niessen, W.; Karge, H. G. *Studies Surf. Sci. Catal.* **1994**, 84B, 1191.
13. Kim, S.; Byl, O.; Liu, J.-C.; Johnson, J. K.; Yates, J. T., Jr *J. Phys. Chem. B* **2006**, 110, 9204.
14. Kim, S.; Byl, O.; Yates, J. T., Jr. *Journal of Physical Chemistry B* **2005**, 109, 3499.
15. Ballinger, T. H.; Wong, J. C. S.; Yates, J. T., Jr *Langmuir* **1992**, 8, 1676.
16. Ballinger, T. H.; Yates, J. T., Jr *Langmuir* **1991**, 7, 3041.
17. Basu, P.; Ballinger, T. H.; Yates, J. T., Jr *Rev. Sci. Instrum.* **1988**, 59, 1321.
18. Yates, J. T., Jr; Duncan, T. M.; Worley, S. D.; Vaughan, R. W. *J. Chem. Phys.* **1979**, 70, 1219.
19. Utamapanya, S.; Klabunde, K. J.; Schlup, J. R. *Chemistry of Materials* **1991**, 3, 175.
20. Barrett, E. P.; Joyner, L. G.; Ealenda, P. P. *J. Am. Chem. Soc.* **1951**, 73, 373.
21. Kresse, G.; Furthmuller, J. *Computational Materials Science* **1996**, 6, 15.
22. Kresse, G.; Furthmuller, J. *Physical Review B* **1996**, 54, 11169.
23. Kresse, G.; Hafner, J. *Physical Review B* **1994**, 49, 14251.
24. Vanderbilt, D. *Physical Review B* **1990**, 41, 7892.

25. Perdew, J. P.; Chevary, J. A.; Vosko, S. H.; Jackson, K. A.; Pederson, M. R.; Singh, D. J.; Fiolhais, C. *Physical Review B* **1992**, *46*, 6671.
26. Monkhorst, H. J.; Pack, J. D. *Physical Review B* **1976**, *13*, 5188.
27. Wilson, E. B., Jr. *Physical Review* **1934**, *45*, 706.
28. Corrsin, L.; Fax, B. J.; Lord, R. C. *J. Chem. Phys.* **1953**, *21*, 1170.
29. Kline, C. H., Jr; Turkevich, J. *J. Chem. Phys.* **1944**, *12*, 300.
30. Klots, T. D. *Spectrochim. Acta A* **1998**, *54*, 1481.
31. Wiberg, K. B.; Walters, V. A.; Wong, K. N.; Colson, S. D. *J. Phys. Chem.* **1984**, *88*, 6067.
32. Parry, E. P. *J. Catal.* **1963**, *2*, 371.
33. Travert, A.; Vimont, A.; Sahibed-Dine, A.; Daturi, M.; Lavalley, J.-C. *Appl. Catal. A: General* **2006**, *307*, 98.
34. Zaki, M. I.; Hasan, M. A.; Al-Sagheer, F. A.; Pasupulety, L. *Colloids and Surfaces A: Physicochem. Eng. Aspects* **2001**, *190*, 261.
35. Mizutani, G.; Ushioda, S. *J. Chem. Phys.* **1989**, *91*, 598.
36. Wu, D.-Y.; Ren, B.; Jiang, Y.-X.; Xu, X.; Tian, Z.-Q. *J. Phys. Chem. A* **2002**, *106*, 9042.
37. Ferwerda, R.; Mass, J. H. v. d.; Duijneveldt, F. B. v. *J. Mol. Catal. A: Chemical* **1996**, *104*, 319.
38. Crank, J. *The Mathematics of Diffusion*; 2 ed.; Oxford University Press: New York, 1980.
39. Coluccia, S.; Baricco, M.; Marches, L.; Martra, G.; Zecchina, A. *Spectrochim. Acta* **1993**, *49A*, 1289.
40. Stankic, S.; Muller, M.; Diwald, O.; Sterrer, M.; Knoziñger, E.; Bernardi, J. *Angew. Chem. Int. Ed.* **2005**, *44*, 4917.
41. Zecchina, A.; Scarano, D.; Bordiga, S.; Ricchiardi, G.; Spoto, G.; Geobaldo, F. *Catal. Today* **1996**, *27*, 403.

Chapter 9

Direct Spectroscopic Observation of the Role of Humidity in Surface Diffusion through an Ionic Adsorbent Powder—The Behavior of Adsorbed Pyridine on Nanocrystalline MgO.*

*Adapted with permission from X. Wang, S. Kim, C. Buda, M. Neurock, O. B. Koper, and J. T. Yates, Jr., “Direct Spectroscopic Observation of the Role of Humidity in Surface Diffusion through an Ionic Adsorbent Powder. The Behavior of Adsorbed Pyridine on Nanocrystalline MgO.”, *The Journal of Physical Chemistry C* **2009**, 113, 2228-2234. Copyright 2009 American Chemical Society. The theoretical work was performed by Dr. Corneliu Buda and Dr. Matthew Neurock and is included here for completeness.

The influence of water vapor on the surface diffusion behavior of pyridine adsorbed on powdered MgO surfaces has been studied by FTIR absorption spectroscopy. It has been found that the introduction of water vapor significantly increases the pyridine surface diffusion coefficient. FTIR spectra showed that water vapor converted Lewis acid Mg^{2+} sites to Bronsted Mg-OH sites. These measurements also detected the change in surface bonding of pyridine to the two types of sites. The activation energy for escape of chemisorbed pyridine into a mobile precursor state is lower for pyridine bound to Mg-OH sites than for binding to Mg^{2+} sites, causing the hydroxylated MgO to exhibit a higher diffusivity than found for dry MgO containing no surface hydroxyl groups. This effect was confirmed by DFT calculations of the binding energy of pyridine to MgO(100) sites and to defect sites on MgO(100), where hydroxylation decreases the binding energy by $\sim 30 \text{ kJmol}^{-1}$ on each type of site.

I. Introduction.

The adsorption of trace contaminants from gas mixtures onto high area oxide surfaces is often compromised by the coadsorption of water in gas streams being

purified.¹⁻⁷ In the testing of sorbents for personnel protection, the breakthrough time of the toxic reagent is often used as a measure of the efficacy of the sorbent.² The introduction of water vapor into the gas stream often reduces the breakthrough time considerably. This decrease in breakthrough time is thus used as a practical measure of the influence of water on the sorption efficiency of high surface area materials.

These changes are likely the result of the molecular interactions that occur between water and the high surface area sorbent for which a number of questions exist. Does water preferentially occupy strong adsorption sites, thus resulting in a decreased sorption efficiency (decreased effective surface area), or does water occupy these sites and thus weaken the binding of the toxic reagents? Herein we present infrared spectroscopic evidence for an adsorbed molecule, pyridine, obtained during its surface diffusion/desorption through high surface area MgO powder, showing that the injection of water significantly increases the pyridine surface diffusion coefficient by displacement of the pyridine from strong adsorption sites (Lewis acid sites) to weaker hydrogen-bonded sites.

The method of using transmission IR spectroscopy as a kinetic probe for the study of surface diffusion is employed in our laboratory, using a thin deposit of powdered material in which molecular diffusion can be studied. The *in situ* absorbance changes in the vibrational modes of diffusing molecules can be fit to long range Fickian diffusion kinetics very well.⁸⁻¹³ Our original method, used in the study of diffusion *inward* into high area Y-ALO₃, starting from a condensed film of the molecule of interest on the outer geometrical surface of the powder, was successful in measuring the coefficient of diffusion at a single temperature.¹¹ Recent developments of this method involve measuring diffusion *outward* from a saturated adsorbed layer. Following adsorption to saturation, the surface is exposed to vacuum, which results in a slow depletion of the

adsorbed layer which can be monitored conveniently by IR spectroscopy.¹² This method has the advantage that the temperature dependence of surface diffusion can be measured over a short range of temperature, permitting the activation energy for the diffusion process to be measured.

We observed two different pyridine diffusion regimes for the pyridine/MgO system.¹² The first is the fast diffusion regime associated with diffusion of pyridine absorbed on terrace MgO(100) sites. The second regime is the slow diffusion regime which is associated with pyridine adsorbed onto defect Mg^{2+} sites, where the pyridine binding energy is larger than on terrace MgO(100) sites. The thermal excitation of chemisorbed pyridine allows it to overcome the escape barrier and form a mobile precursor state which can either rapidly diffuse along the surface until it desorbs or re-adsorbs onto another chemisorption site.^{12,14,15}

Using this method we have examined the role of injected water on the diffusion of pyridine through MgO powder. Dissociation of water molecules produces Mg-OH groups⁴⁻⁷ which convert the Lewis acid sites to Brønsted acid sites. Instead of bonding to the Lewis acid Mg^{2+} sites on the hydroxyl-free MgO surface through the lone pair of electrons on the nitrogen atom in pyridine, weaker hydrogen bonds form between the hydroxyl-covered MgO surface and the pyridine molecules, thus resulting in a more rapid diffusion/desorption process.

II. Methodology.

A. Experimental.

The experimental methods used in this work are described in detail elsewhere.^{12,16} The powdered MgO, which was provided by NanoScale Corporation, (Manhattan, KS), consists of hexagonal platelet particles with individual crystallite sizes smaller than 8

nm.¹⁷ In order to prepare a coherent sample disk, the MgO powder was pressed into the grid using a special die under 60,000 psi,^{18,19} achieving a density of 0.008 g cm⁻³. The compressed MgO sample was annealed to 1200 K in vacuum for 30 minutes to cause complete dehydroxylation prior to pyridine adsorption. The N₂-BET surface area of the compressed material is 23 m²g⁻¹ and the pore size distribution is reported elsewhere.¹² We believe that the predominant surface planes on the MgO crystallites have the MgO(100) orientation.¹²

Pyridine was obtained from Sigma-Aldrich (anhydrous, 99.8% purity) and further purified with freeze-pump-thaw cycles using liquid nitrogen. In the pyridine diffusion/desorption experiment without water (experiment I), the MgO sample was exposed to pyridine vapor at about 1 Torr pressure and 295 K to form a saturated chemisorbed layer, as determined by reaching a maximum in pyridine absorbance. The chamber was pumped ($< 1 \times 10^{-7}$ Torr) at 295 K by a turbo-molecular pump for 10 minutes. The sample was then heated to 300 K and infrared spectra were continuously recorded over time immediately after 300 K was achieved. The process was monitored by plotting the absorbance decrease versus time for one pyridine vibrational mode, the ν_{19b} mode. In the water displacement experiment (experiment II), after pyridine diffusion/desorption without water for 1800 s, the sample was suddenly exposed to water vapor pressure at 53 mTorr. Pumping was then quickly started after the IR spectrum showed a clear saturation of hydroxyl group absorbance and the pyridine diffusion/desorption experiment was continued. In a separate water-pretreatment experiment (experiment III), after annealing, the MgO sample was exposed to water vapor at 53 mTorr and 295 K for 600 s. The chamber was then pumped out for 1800 s before pyridine exposure. A pyridine diffusion/desorption experiment was then carried out at 300 K.

The infrared spectra were recorded with a Bruker TENSOR 27 FT-IR spectrometer, using a liquid nitrogen cooled MCT detector. Each spectrum was obtained in 12 s by averaging 32 interferograms at 2 cm⁻¹ resolution. The background spectrum was taken through the empty grid region and was subtracted from the measured IR spectrum. Each diffusion/desorption experiment was observed for 2 hours, with IR spectra being taken every 2-5 minutes.

B. Computational.

Nonlocal gradient corrected periodic density functional theory (DFT) calculations were carried out using the Vienna Ab-initio Simulation Program (VASP)²⁰⁻²² to determine the adsorption energies of pyridine on the terraces and steps of the dehydroxylated and hydroxylated Mg(100) surfaces. All of the calculations were performed within the Generalized Gradient Approximation using the Perdew Wang 91 (PW91) functional²³ form to account for the corrections to the exchange and correlation energies. Vanderbilt ultrasoft pseudopotentials were used to describe the interactions between the core and the valence electrons.²⁴ The electronic energies for all of the calculations reported were converged to within 10⁻⁴ eV, whereas the geometry was optimized such that the forces on each atom were below the threshold value of 0.05 eVÅ⁻¹. A 3x3x1 Monkhorst-Pack k-point mesh²⁵ was used to sample the first Brillouin zone.

The MgO (100) surface was modeled using a 3x3 unit cell comprised of 4 layers, each of which contained 9 Mg and 9 O atoms. A vacuum region of 15 Å was placed between each of the MgO slabs. The bottom two layers of the slab were held fixed to their optimized bulk configuration, while the top two layers along with the pyridine molecule were optimized. The pyridine adsorption energies were calculated using Equation 9.1:

$$AE_{ads} = E_{pyridine/MgO(H)} \sim E_{pyridine} \sim E_{MgO(H)} \quad (9.1)$$

where $E_{\text{pyridine/Mgo}}$, E_{pyridine} and $E_{\text{Mgo(H)}}$ refer to the energy pyridine bound to the Mg^{2+} (or Mg-OH) site on the MgO surface, pyridine alone in the gas phase and the bare (or hydroxylated) $\text{MgO}(100)$ surface, respectively. Pyridine adsorption was examined at the Mg^{2+} sites on the bare $\text{MgO}(100)$ surface, OH sites on the hydroxylated $\text{MgO}(100)$ surface, Mg^{2+} sites at the bare step edge of the $\text{MgO}(100)$ surface and at the hydroxylated step edge of the $\text{MgO}(100)$ surface.

III. Results.

A. Influence of Surface Hydroxylation on Kinetics of Pyridine Diffusion.

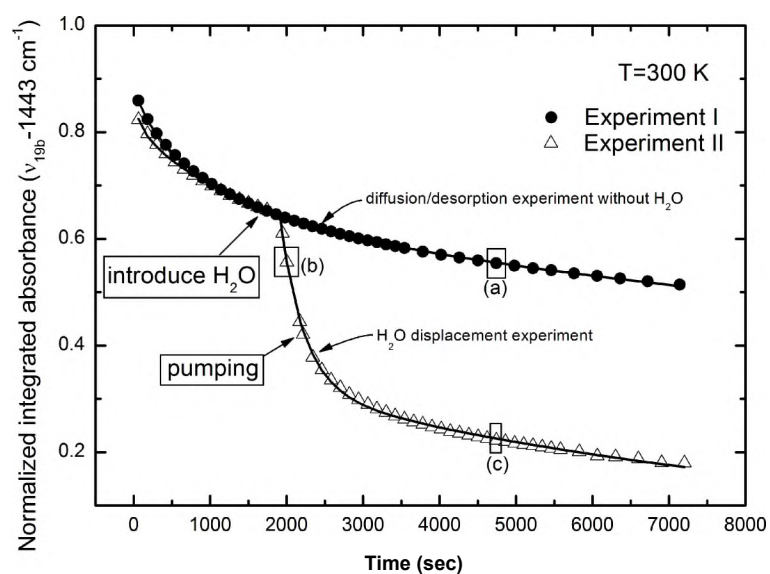


Figure 9.1. Plots of the integrated absorbances of the pyridine ring-breathing vibrational mode V19b (1443 cm^{-1}) as a function of increasing diffusion time at 300 K for experiments I and II. Dark circles are data points from experiment I while triangles are data points from experiment II. Solid lines through experimental data points are the best fit lines to the double diffusion Equation 9.2.

Figure 9.1 shows the normalized, integrated absorbances of the pyridine ring-breathing (ν_{CCN}) vibrational mode, V19b in the Wilson notation²⁶⁻²⁹ (1443 cm^{-1}), versus time for the pyridine diffusion/desorption experiment without water and the H_2O

displacement experiment on the dehydroxylated MgO, respectively, at 300 K. The integrated absorbances are normalized to the corresponding baseline measured 300 s after pyridine evacuation. The diffusion/desorption experiment without water yields results similar to results reported elsewhere,¹² which reveal two diffusion processes: an initial process which is quite fast, followed by a slower process.

We have shown previously that the experimental data can best be fit to model based on Fick's Second Law by assuming two different diffusion processes.¹² This results in Equation 9.2:

$$6 \frac{A}{A_{\infty}} = 9_f V \sum_{n=0}^{\infty} \frac{8}{(2n+1)^2 n^2} \exp \left\{ -D_f (2n+1)^2 n^2 t / l^2 \right\} + 6 \frac{8}{V \sum_{n=0}^{\infty} (2n+1)^2 n^2} \exp \left\{ -D_s (2n+1)^2 n^2 t / l^2 \right\} \quad (9.2)$$

where $9a$ = the fraction of sites occupied by the absorbate (pyridine in this case); At = total absorbance for the pyridine remaining after desorption time t , A_{∞} = total absorbance of pyridine after adsorption for infinite time; 9_f , 9_s = fractional coverage of pyridine involved in the initial fast or slow diffusion process; D_f , D_s = diffusion coefficient of pyridine in the fast and slow process; t = time (s); and l = thickness of the compressed MgO sample (0.005 cm in our case). On the dehydroxylated surface, about 74% of the pyridine follows a slow diffusion process with the diffusivity $D_s = 7 \times 10^{-11} \text{ cm}^2 \text{ s}^{-1}$, whereas about 17% of the pyridine follows a fast diffusion process with $D_f = 3 \times 10^{-9} \text{ cm}^2 \text{ s}^{-1}$ in good agreement with previous measurements.¹² The percentages do not add to 100% because of a delay time before beginning the diffusion measurement. The best-fit curve to Equation 9.2 is drawn as a solid line through the experimental points of the diffusion/desorption experiment without water (dark circles).

Compared to the diffusion/desorption experiment without water on dehydroxylated MgO, the sudden introduction of water vapor in Figure 9.1 rapidly accelerates the

depletion of pyridine from the MgO surface. In order to fit the experimental data points to Fick's Second Law, we divided the data into two sections: (i) points from 0 to 1740 s as the combination of fast and slow diffusion on the hydroxyl-free surface; and (ii) points from 1940 s to the end as another combination of fast and slow diffusion processes on the water-treated surface. The 200 s vacancy in between the two sections was due to experiment delay when we introduced water vapor. The best-fit curve is drawn as a solid line through the triangular experimental points from the H₂O displacement experiment in Figure 9.1. In section (i), about 77% of the pyridine is in the slow diffusion process with $D_s = 7 \times 10^{-10} \text{ cm}^2\text{s}^{-1}$ and 10% of the pyridine is in the fast diffusion process with $D_f = 3 \times 10^{-9} \text{ cm}^2\text{s}^{-1}$. For the water-treated MgO in section (ii), about 38% of the pyridine participates in a slow diffusion process with $D_s = 3 \times 10^{-10} \text{ cm}^2\text{s}^{-1}$ and 45% of the pyridine is in a fast diffusion process with $D_f = 8 \times 10^{-9} \text{ cm}^2\text{s}^{-1}$. Thus the introduction of water *increases the fraction of fast diffusing molecules by a factor of about 5, and results in an increase in the fast diffusion coefficient by a factor of 3.*

Figure 9.2 shows the normalized integrated absorbances of the V_{19b} vibrational mode of pyridine versus time at 300 K, for the hydroxyl-free diffusion/desorption experiment, as well as for the diffusion/desorption experiment on a MgO surface previously exposed to H₂O. The best fit models derived from Fick's Second Law are drawn as solid lines through the corresponding experimental data points. There are still two diffusion processes in the case of the H₂O pre-treated MgO surface: about 53% of the pyridine is in the slow diffusion process with $D_s = 2 \times 10^{-10} \text{ cm}^2\text{s}^{-1}$ and 32% of the pyridine is in the fast diffusion process with $D_f = 3 \times 10^{-9} \text{ cm}^2\text{s}^{-1}$. Compared to the diffusion/desorption experiment from a dehydroxylated MgO surface, the initial absolute amount of pyridine adsorbed is smaller on the H₂O pre-treated MgO surface. Furthermore, diffusion/desorption from the H₂O pre-treated MgO surface involves a larger fraction of

pyridine participating in the fast diffusion process, thus causing pyridine depletion to be more complete within the two-hour experiment.

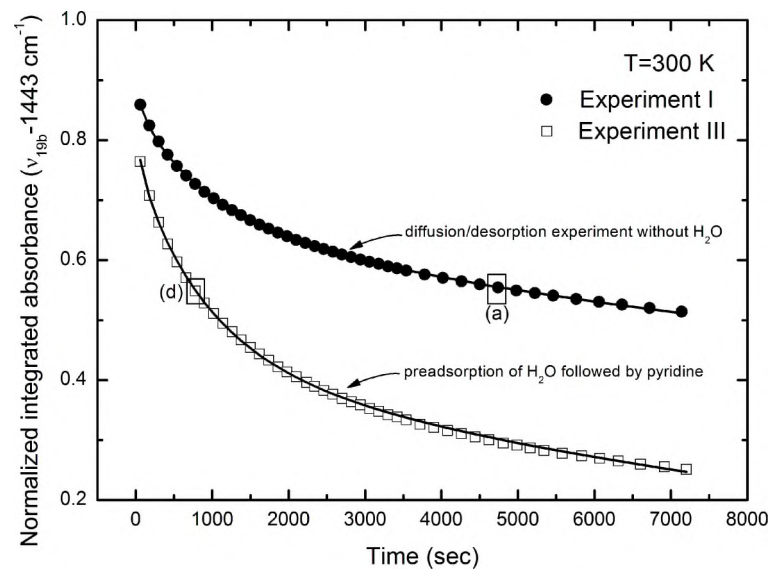


Figure 9.2. The integrated absorbances of the pyridine ring-breathing vibrational mode ν_{1443} (1443 cm^{-1}) as a function of increasing diffusion time; at 300 K for experiments I and III. Dark circles are data points from experiment I while squares are data points from experiment III. Solid lines through experimental data points are the best fits to the diffusion equation 9.2.

As the calculated diffusion coefficients for the diffusion of pyridine on MgO and Mg-OH surfaces measured in Figure 9.1 and 9.2 are summarized in Table 9.1, the different sample surfaces MgO (in dehydroxylated), the influence of the delay times before the diffusion experiment is different. Thus this deviation of the sum of the percentage coverage from 100% varies.

Table 9.1: Diffusion Parameters for Pyridine Diffusion on MgO and on Mg-OH surfaces.

experiment		$D_p (10^{-11} \text{ m}^2 \text{ s}^{-1})$	$\theta_p (\%)$	$D_s (10^{-11} \text{ m}^2 \text{ s}^{-1})$	$\theta_s (\%)$
diffusion/desorption experiment (I)		3	17	7	74
H_2O displacement experiment (II)	diffusion/desorption experiment (i)	3	10	7	77
	diffusion/desorption experiment (ii)	8	45	27	38
diffusion/desorption experiment with H_2O (III)		3	32	22	53

B. Spectroscopic Effects following H₂O Introduction to Dehydroxylated MgO.

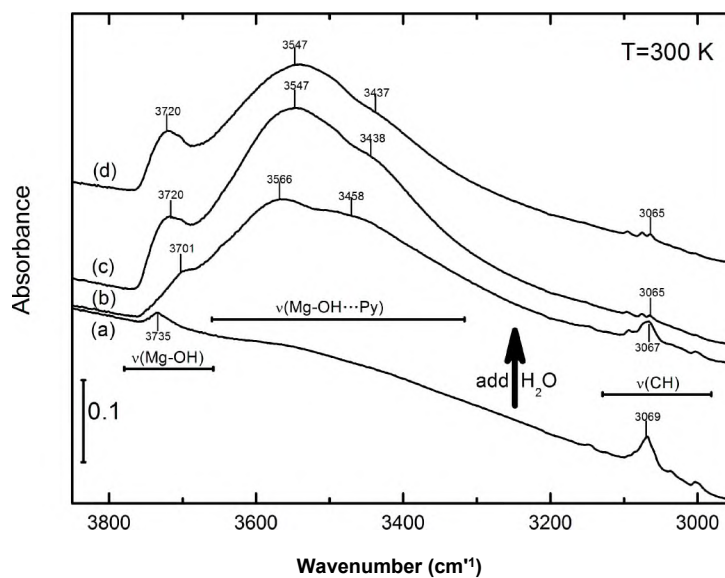


Figure 9.3. FTIR spectra of $\nu(\text{OH})$ region and $\nu(\text{CH})$ region of pyridine molecules adsorbed on hydroxyl-free MgO ((a)) and hydroxyl-covered MgO ((b)-(d)) at 300 K. Spectra (a), (b), (c), and (d) were taken at corresponding point in Figures 9.1 and 9.2.

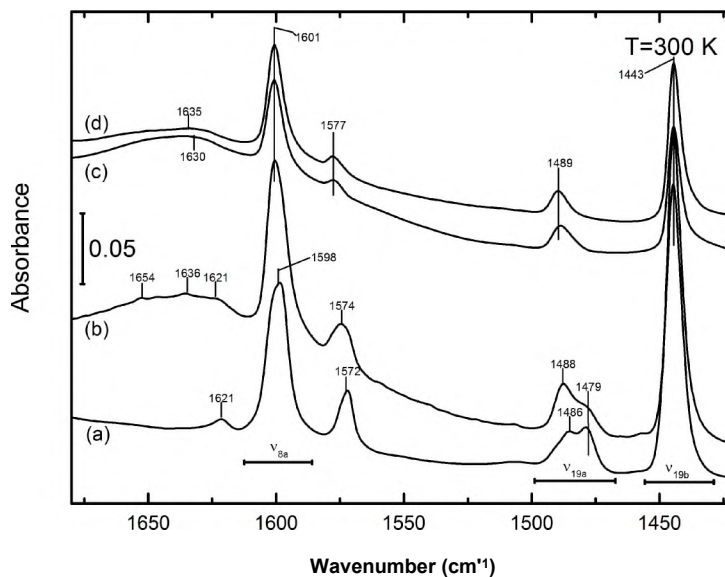


Figure 9.4. FTIR spectra of $\nu(\text{CCN})$ region of pyridine molecules adsorbed on hydroxyl-free MgO (a) and hydroxyl-covered MgO (b-d) at 300 K.

Figures 9.3 and 9.4 present IR spectra at points (a), (b) and (c) from Figure 9.1 and point (d) from Figure 9.2. Point (a) is almost at the end of the diffusion/desorption experiment without water (4740 s) on dehydroxylated MgO where the primary diffusion occurs by the slow diffusion process. Point (b) is at the middle of the process induced by H₂O (2000 s) where the diffusion is mainly in the fast diffusion regime, with approximately the same pyridine coverage as at point (a). The spectrum at point (c) in the H₂O displacement experiment is taken at the same diffusion time as point (a). In Figure 9.2, point (d) in the pyridine diffusion/desorption experiment on the H₂O pre-treated MgO surface (780 s) has almost the same pyridine coverage as at point (a) in Figure 9.1. Spectra (c) and (d) are almost identical to each other, in both Figures 9.3 and 9.4, as a result of the involvement of surface Mg-OH groups in hydrogen bonding to pyridine in both cases.

Figure 9.3 shows the IR spectra of the O-H stretching mode ($\nu(\text{OH})$) and the C-H stretching mode for adsorbed pyridine ($\nu(\text{CH})$ region). Compared to spectrum (a), spectra (b), (c), and (d) result in a downward shift of the vibrational peak frequency for the isolated OH group vibrational mode, from 3735 cm^{-1} to 3701 cm^{-1} , 3720 cm^{-1} and 3720 cm^{-1} , respectively. This is accompanied by the formation of a broad, intense OH band in the region $3680\text{--}3150\text{ cm}^{-1}$ that results from hydrogen bonding of Mg-OH surface species to pyridine. In the $\nu(\text{CH})$ region ($3120\text{--}2950\text{ cm}^{-1}$) in Figure 9.3, the most intense and sharp peak at 3069 cm^{-1} in spectrum (a) decreases in absorbance due to pyridine depletion and shifts slightly to lower wavenumber (3069 cm^{-1} \wedge 3065 cm^{-1}) in (b) and (c), (d), respectively.

Figure 9.4 shows the IR spectra in the pyridine ring-breathing mode ($\nu(\text{CCN})$) region. The most intense mode, V19b, experiences only a decrease in intensity but no frequency change from (a) to (d), making the integrated absorbance of this spectral feature

excellent for judging the relative coverage of pyridine during the experiment. In contrast, the second most intense spectral mode, V8a, experiences both a decrease in intensity and a small upward shift from 1598 cm^{-1} in spectrum (a) to 1601 cm^{-1} in spectra (b)-(d). The small peak on the lower wavenumber side of V8a also decreases in absorbance and shifts upward from (a) to (d) as the surface is hydroxylated. A broad low intensity band around 1630 cm^{-1} appears in spectra (b)-(d) due to the introduction of H_2O . The peak at 1479 cm^{-1} decreases in absorbance from (a) to (d), while the peak at 1486 cm^{-1} shifts to the higher wavenumber, and initially increases slightly in absorbance upon introduction of H_2O .

Associated OH groups are produced on the MgO surface by H_2O adsorption and dissociation. The $\nu(\text{OH})$ frequency shifts, shown in Figures 9.3 and 9.4, can be interpreted as a hydrogen bonding interaction between pyridine and the Mg-OH group. We will discuss this in detail in the Discussion section. In addition, the introduction of H_2O to dehydroxylated MgO surfaces in these experiments may result in a low coverage of adsorbed H_2O molecules as evidenced by the observation of an intense H_2O bending mode peak at about 1630 cm^{-1} immediately after H_2O introduction. However, this spectral peak due to adsorbed H_2O almost disappeared after evacuation. Thus, there is little influence of adsorbed H_2O molecules on pyridine diffusion/desorption on the MgO surface. The enhanced pyridine diffusion rate is, instead, attributed to the conversion of Lewis acid Mg^{2+} sites to Brønsted Mg-OH sites.

Thus, the induction of a fast pyridine diffusion process is associated with the formation of weak hydrogen bonds to pyridine when Mg-OH surface sites are present. The Mg-OH groups eliminate Lewis acid Mg^{2+} sites which strongly bond to pyridine.

IV. Discussion.

It is reported elsewhere^{12,30,31} that pyridine mainly adsorbs on two different types of Lewis acid sites (designated LPy and L*Py) on a dehydroxylated MgO surface: 5-fold Mg²⁺ sites (terrace sites) and 3 or 4-fold Mg²⁺ sites (defect sites). The binding energy of pyridine at the defect Mg²⁺ sites is higher than that of the terrace Mg²⁺ sites so the activation energy for pyridine adsorbed on the stronger bonding sites (L*) to form the mobile precursor active for diffusion is larger than for pyridine adsorbed onto weaker bonding sites (L).¹² Two different escape barrier energies for pyridine from the two types of Lewis acid sites lead to two parallel diffusion/desorption processes from the dehydroxylated MgO surface, as illustrated in Figure 9.5. The excellent fit between the data and the model for the diffusion/desorption experiment involving two kinetic processes, as shown in Figures 9.1 and 9.2 (dark circles), helps to confirm this theory.

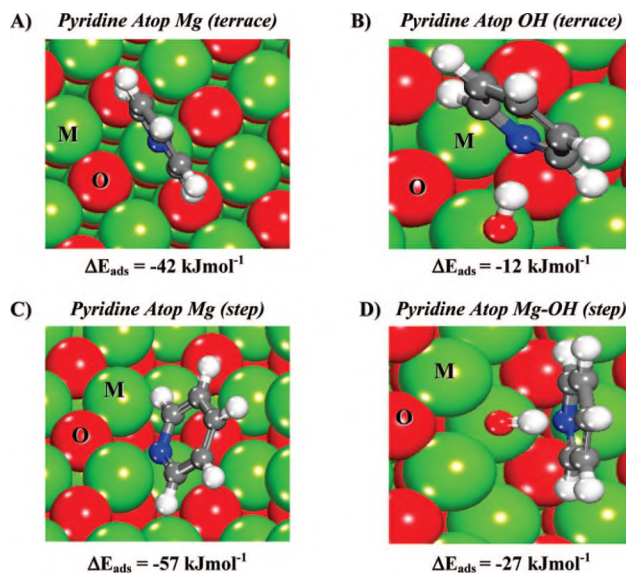


Figure 9.5. DFT calculations of the adsorption energies of pyridine chemisorbed on A. dehydroxylated MgO(100) terrace; B. hydroxylated MgO(100) terrace; C. dehydroxylated MgO(100) step; and D. hydroxylated MgO(100) step.

The results in Figure 9.1 show that the sudden introduction of water vapor dramatically increases the diffusion/desorption behavior of pyridine from the MgO surface. Comparing the diffusion coefficients shown in Table 9.1, we see that the results from the pyridine diffusion/desorption experiment on a hydroxyl-free MgO surface are essentially identical in the two separate experiments, I and II; an initial fast diffusion stage followed by a slower process. The introduction of water vapor mid way in experiment II (section (ii)) increased the diffusivity of pyridine ($D_f = 8 \times 10^{-9} \text{ cm}^2\text{s}^{-1}$) as compared to the diffusivity of pyridine found in diffusion/desorption without water ($D_f = 3 \times 10^{-9} \text{ cm}^2\text{s}^{-1}$). After the new condition was reached on the hydroxyl-covered MgO surface, a greater diffusivity of pyridine in the slow process was also observed ($D_s = 3 \times 10^{-10} \text{ cm}^2\text{s}^{-1}$) as compared to diffusivity on the dehydroxylated MgO ($D_s = 7 \times 10^{-11} \text{ cm}^2\text{s}^{-1}$). Note that in experiment III, where a separate pyridine diffusion/desorption experiment on a water pre-treated MgO surface was carried out, a D_f similar to pyridine diffusion/desorption from the hydroxyl-free MgO surface and a D_s similar to pyridine diffusion/desorption from the hydroxyl-covered MgO surface were found.

The new adsorption sites appear to be created by water vapor adsorption and dissociation on MgO since both the fast and the slow diffusion processes are modified in favor of fast diffusion. The introduction of water vapor changes the environment on the MgO surface, which changes both the amount of pyridine adsorbed on the different types of sites as well as the characteristics of the diffusion processes. Further analysis of the IR spectra supports this conclusion, as discussed below.

Spectrum (a) in Figure 9.3 shows a small peak at 3735 cm^{-1} which indicates a low coverage of isolated hydroxyl groups on the surface. The pressed MgO sample used in our experiment was annealed at 1200 K under vacuum for 30 minutes in order to produce an almost completely dehydroxylated surface. It is known that annealing at

1200 K for 2 hours can produce a totally dehydroxylated MgO surface.¹² By comparing the experimental results from the MgO samples annealed to 1200 K under vacuum for 30 minutes and 2 hours, respectively, we conclude that the low residual coverages of hydroxyl intermediates will not significantly influence the diffusion/desorption behavior of pyridine. The appearance of a broad band around 3550 cm^{-1} in spectra (b)-(d) is due to the formation of associated OH—Py adsorbed species, which will now be denoted as H-bonded pyridine (HPy). In addition, Mg-OH—HO-Mg hydrogen bonding between neighboring species will also contribute to the broad band.

In the C-H stretching mode region in Figure 9.3 (lower wavenumber region), the shape of spectrum (a) (several small peaks with the largest peak around 3069 cm^{-1}) is very similar to other reported IR spectra³² and shows that pyridine molecules are adsorbed on Lewis acid sites (denoted as LPy regardless of whether terrace or defect sites are involved). After the introduction of water vapor, in spectra (b)-(d) of Figure 9.3, the intensity of the most intense peak in the C-H stretching region decreased and the whole C-H stretching band is broadened and shifted slightly to lower wavenumbers. These changes indicate pyridine displacement and the formation of H-bonded pyridine (HPy), which is taking the place of LPy.³²

The peak positions of ν_{sa} and $\nu_{19\text{b}}$ of the ring-breathing modes may also be used to analyze the pyridine adsorption sites.^{30'33'34} Spectrum (a) in Figure 9.4 shows the $\nu(\text{CCN})$ region of LPy species on the MgO surface at 300 K. The ν_{sa} peak at 1598 cm^{-1} and $\nu_{19\text{b}}$ peak at 1443 cm^{-1} are indicative of the LPy species on an MgO surface.^{33,34} After the sudden introduction of water vapor, there is a small upward frequency shift of ν_{sa} , as seen in spectrum (b) of Figure 9.4, suggesting the conversion of LPy species to HPy species. The ν_{sa} frequency at 1601 cm^{-1} of spectra (b)-(d) also indicates the existence of HPy species.³³

Additional evidence for the conversion of LPy species to HPy species can be seen in the features of Figure 9.4 around 1480 cm^{-1} in the V19a region of the pyridine vibrational spectrum. The V19a split features at 1486 cm^{-1} and 1479 cm^{-1} in spectrum (a) are indicative of the fast-diffusing and slow-diffusing LPy species¹² on dehydroxylated MgO(100) facets and on defective surface sites, respectively, which possess different diffusion coefficients. Hydroxylation eliminates the split features and produces a single peak in the $1488\text{--}1489\text{ cm}^{-1}$ range in spectra (b)–(d). This shows that upon hydroxylation, the LPy species are replaced by the HPy species with even larger diffusivities and with an upward shifted, unsplit feature.

After the introduction of water vapor, the original Lewis acid sites on the MgO surface become covered with -OH groups making them Bronsted acid sites. For the dehydroxylated MgO(100) surface, the calculated binding energy for pyridine chemisorption, which occurs via the electron donation from the lone pair of electrons on the pyridinic nitrogen atom to the surface Mg^{2+} cation, was calculated to be -42 kJmol^{-1} , as shown in Figure 9.5A. On the hydroxylated MgO(100) surface, pyridine adsorbs atop of the surface hydroxyl creating a hydrogen bond between the proton of the OH group and the nitrogen atom on pyridine, which is shown in Figure 9.5B. The calculated binding energy for pyridine chemisorption through this hydrogen bond was -12 kJmol^{-1} .

^{1,35} Thus, pyridine adsorbed on an Mg-OH site (HPy) is more weakly bound by 30 kJmol^{-1} than the LPy species. Similar calculations were carried out for pyridine adsorption at the dehydroxylated and hydroxylated step edges of MgO(100). The results, which are shown in Figures 9.5C and 9.5D, indicate that the adsorption energy of pyridine increased on both the dehydroxylated and hydroxylated atomic steps by about -15 kJmol^{-1} over those reported on the ideal terraces of MgO(100), resulting in adsorption energies of -57 kJmol^{-1} and -27 kJmol^{-1} for the dehydroxylated and hydroxylated surfaces,

respectively. After the injection of water onto the MgO surface, pyridine experiences a ~ 3 -fold increase in its surface diffusion coefficient, D_f , and a ~ 5 -fold increase in the population of the rapidly diffusing pyridine.

In experiment III, where pyridine is initially adsorbed onto a previously hydroxylated surface, the fast diffusion coefficient, D_f , remains the same as on the dehydroxylated surface ($= 3 \times 10^{-9} \text{ cm}^2 \text{ s}^{-1}$), and the slow diffusion coefficient increases by a factor of about 3, from $7 \times 10^{-11} \text{ cm}^2 \text{ s}^{-1}$ to $22 \times 10^{-11} \text{ cm}^2 \text{ s}^{-1}$. The fraction of fast-moving pyridine molecules, O_f , increases by about a factor of 2 or 3 to 32%. Hydroxylation also produces a 30% decrease in the fraction of slow-moving molecules. Thus the hydroxylation of the MgO surface leads to a general increase in both the pyridine surface diffusion coefficients, as well as an increase in the fraction of fast-moving molecules.

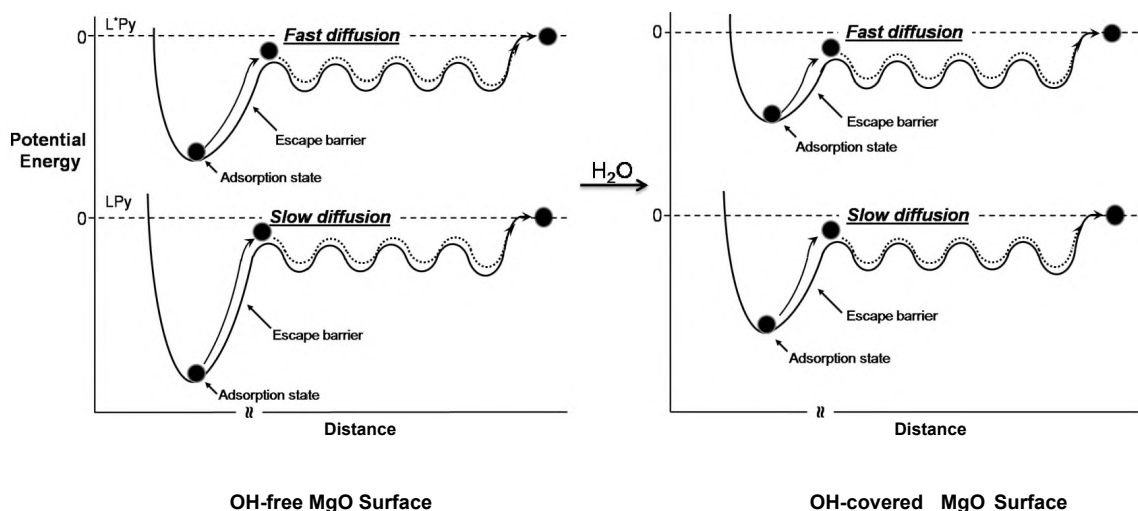


Figure 9.6. Schematic potential energy diagrams of the slow and fast diffusion processes for pyridine through MgO before and after the adsorption and dissociation of water, based on the mobile precursor state model.

A schematic which highlights the influence of water vapor on pyridine diffusion/desorption is shown in Figure 9.6. Water vapor converts the Lewis acid sites to

Brensted acid sites on an MgO surface. The rate of diffusion/desorption of pyridine on a dehydroxylated MgO surface is based on the pyridine adsorbing to terrace Mg^{2+} sites denoted as LPy and to defect Mg^{2+} sites denoted as L^*Py in Figure 9.6, while the diffusion/desorption on a hydroxylated MgO surface is mainly based on pyridine adsorbing to OH groups through hydrogen bonding. The chemisorbed LPy or hydrogen-bonded HPy species are activated over a characteristic escape barrier into a mobile precursor state which has high surface mobility. The process of surface diffusion is kinetically controlled by the passage over the escape barrier into the mobile precursor from which pyridine can desorb. The weaker surface binding in HPy species as compared to LPy and L^*Py species result in the greatly enhanced surface diffusion rate of pyridine when the MgO surface is hydroxylated.

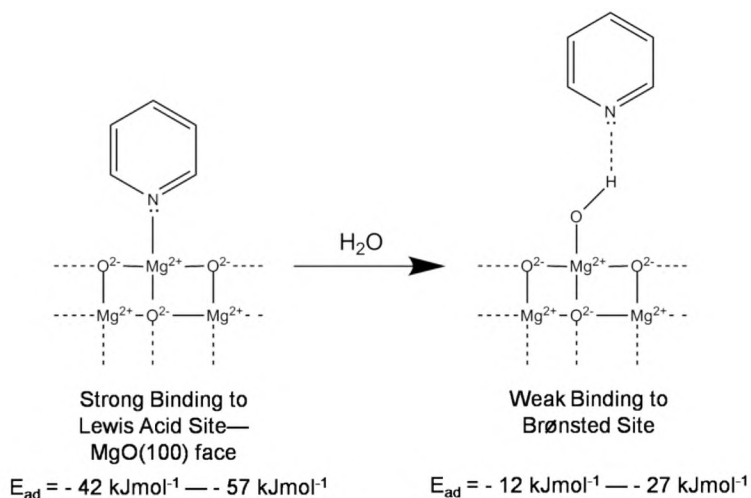


Figure 9.7. Schematic diagram of the effect of water on pyridine surface binding to MgO.

The overall effect of the introduction of water vapor on the binding properties of pyridine to an MgO surface is described in Figure 9.7. The pyridine adsorption to the

MgO surface is weakened due to the water vapor converting Lewis acid sites to Brønsted sites.

V. Summary of Results.

The main results from this study are summarized below:

1. Infrared spectroscopy has been used to monitor the kinetics of surface diffusion of pyridine molecules through nanocrystalline MgO particles at 300 K.
2. The hydroxylation of MgO by water vapor adsorption and dissociation at 300 K enhances both the rate of pyridine surface diffusion and the fraction of fast-diffusing molecules compared to the dehydroxylated surface.
3. IR spectroscopic studies of the shifts of selected pyridine vibrational modes and of the formation of hydrogen-bonded Mg-OH-Py modes reveal that the formation of the weakly-bond hydrogen-bonded pyridine species increases the surface diffusion rate of pyridine.
4. DFT calculations show that the binding energy for pyridine to dehydroxylated MgO(100) surface is -42 kJmol^{-1} ; the binding energy for pyridine to the hydroxylated MgO (100) surface is -12 kJmol^{-1} . Both binding energies increase by -15 kJmol^{-1} at the step edge leading to pyridine chemisorption energies of -57 and -27 kJmol^{-1} for the dehydroxylated and hydroxylated surfaces, respectively. These values support the postulate that the formation of the hydroxyl group on the MgO surface causes the enhancement of the pyridine surface diffusion rate.
5. Diffusion occurs via a mobile precursor mechanism which rapidly conducts molecules to vacuum by processes kinetically controlled by the escape barrier height for the adsorbed species into the mobile precursor state.

VI. Acknowledgement.

We acknowledge, with thanks, the support of this research from the Defense Threat Reduction Agency (DTRA) through contract HDTRA1-07-C-0085.

Chapter 9 References:

1. Comte, S.; Calvet, R.; Dodds, J. A.; Balard, H. *Powder Tech.* **2005**, 157, 39.
2. Wood, G. O. *Carbon* **2002**, 40, 685.
3. Hao, N.; Ruthven, D. M. *J. Colloid Interface Sci.* **1986**, 112, 154.
4. Giordano, L.; Goniakowski, J.; Suzanne, J. *Phys. Rev. Lett.* **1998**, 81, 1271.
5. Langel, W.; Parrinello, M. *Phys. Rev. Lett.* **1994**, 73, 504.
6. Langel, W.; Parrinello, M. *J. Chem. Phys* **1995**, 103, 3240.
7. Odelius, M. *Phys. Rev. Lett.* **1998**, 82, 3919.
8. Meunier, F. C.; Domokos, L.; Seshan, K.; Lercher, J. A. *J. Catal.* **2002**, 211, 366.
9. Niessen, W.; Karge, H. G. *Studies Surf. Sci. Catal.* **1994**, 84, 1191.
10. Karge, H. G. *C. R. Chimie* **2005**, 8, 303.
11. Kim, S.; Byl, O.; Liu, J.-C.; Johnson, J. K.; Yates, J. T., Jr *J. Phys. Chem. B* **2006**, 110, 9204.
12. Kim, S.; Wang, X.; Buda, C.; Neurock, M.; Koper, O. B.; Yates, J. T., Jr. *The Journal of Physical Chemistry C* **2009**, 113, 2219.
13. Bludau, H.; Karge, H. G.; Niessen, W. *Microporous and Mesoporous Materials* **1998**, 22, 297.
14. Weinberg, W. H. In *Kinetics of Interface Reactions*; Grunze, M., Kreuzer, H. J., Eds.; Springer-Verlag: New York, London, 1986.
15. Cassuto, A.; King, D. A. *Surf. Sci.* **1981**, 102, 388.
16. Kim, S.; Byl, O.; Yates, J. T., Jr *J. Phys. Chem. B* **2005**, 109, 3499.
17. Utamapanya, S.; Klabunde, K. J.; Schlup, J. R. *Chem. Mater.* **1991**, 3, 175.
18. Ballinger, T. H.; Wong, J. C. S.; Yates, J. T., Jr *Langmuir* **1993**, 8, 1676.
19. Ballinger, T. H.; Yates, J. T., Jr *Langmuir* **1991**, 7, 3041.

20. Kresse, G.; Hafner, J. *Phys. Rev. B* 1994, 49, 14251.
21. Kresse, G.; Furthmuller, J. *Comput. Mater. Sci.* 1996, 6, 15.
22. Kresse, G.; Furthmuller, J. *Phys. Rev. B* 1996, 54, 11169.
23. Perdew, J. P.; Chevary, J. A.; Vosko, S. H.; Jackson, K. A.; Pederson, M. R.; Singh, D. J.; Fiolhais, C. *Phys. Rev. B* 1992, 46, 6671.
24. Vanderbilt, D. *Phys. Rev. B* 1990, 41, 7892.
25. Monkhorst, H. J.; Pack, J. D. *Phys. Rev. B* 1976, 13, 5188.
26. Corrsin, L.; Fax, B. J.; Lord, R. C. *J. Chem. Phys* 1953, 21, 1170.
27. Kline, C. H., Jr; Turkevich, J. *J. Chem. Phys* 1944, 12, 300.
28. Klots, T. D. *Spectrochim. Acta A* 1998, 54, 1481.
29. Wiberg, K. B.; Walters, V. A.; Wong, K. N.; Colson, S. D. *J. phys. Chem.* 1984, 88, 6067.
30. López, T.; Gómez, R.; Navarrete, J.; López-Salinas, E. *J. Sol-Gel Sci. Technol.* 1998, 13, 1043.
31. Peng, X. D.; Barteau, M. A. *Langmuir* 1991, 7, 1426.
32. Travert, A.; Vimont, A.; Sahibed-Dine, A.; Dature, M.; Lavalley, J.-C. *Appl. Catal. A: General* 2006, 307, 98.
33. Zaki, M. I.; Hasan, M. A.; Al-Sagheer, F. A.; Pasupulety, L. *Colloids and Surfaces A: Physicochem. Eng. Aspects* 2001, 190, 261.
34. Mekheimer, G. A. H.; Halawy, S. A.; Mohamed, M. A.; Zaki, M. I. *J. Phys. Chem. B* 2004, 108, 13379.
35. Jeffrey, G. A. *An Introduction to Hydrogen Bonding*; Oxford University Press: New York, 1997.

Chapter 10

IR Spectroscopic Measurement of Diffusion Kinetics of Chemisorbed Pyridine through TiO₂ Particles.*

[^]Reprinted with permission from I. X. Green, C. Buda, Z. Zhang, M. Neurock, and J. T. Yates, Jr., *"IR Spectroscopic Measurement of Diffusion Kinetics of Chemisorbed Pyridine through TiO₂ Particles"*, The Journal of Physical Chemistry C 2010, 114, 16649-16659. Copyright 2010 American Chemical Society. The theoretical work was performed by Dr. Corneliu Buda and Dr. Matthew Neurock and is included here for completeness.

The chemisorption and surface diffusion/desorption of pyridine from TiO₂ powder (P 25) has been measured as a function of temperature using transmission IR spectroscopy. Two classes of diffusion have been measured with activation energies of 36 kJ/mol (fast) and 90 kJ/mol (slow). By comparing density functional theory (DFT) calculations of bonding energies on TiO₂ rutile (110) and anatase (101), the dominant crystal planes expected in P 25 TiO₂, it is found that fast diffusion would be expected on the rutile phase and that much slower diffusion would be expected on the anatase phase. In addition the presence of oxygen defect sites will produce more strongly bound pyridine than either of the model crystal planes selected for investigation. To both types of TiO₂ surfaces, pyridine bonding occurs to coordinatively unsaturated Ti cation sites through the N lone pair of the pyridine molecule. More than 85% of the molecules exhibit slow surface diffusion and this is attributed to diffusion on the dominant anatase crystallites as well as to diffusion on defective sites. Diffusing molecules exhibit a ν_{19b} ring-breathing mode, with the rapidly-diffusing molecules exhibiting a mode frequency of ~ 1438 cm⁻¹ and the slowly-diffusing species exhibiting a mode frequency of ~ 1445 cm⁻¹. Electron stimulated desorption ion angular distribution (ESDIAD) studies of the C-D bond directions for pyridine on the rutile TiO₂(110)-1 x 1 surface show that the ring plane is

rotated by $37 \pm 1^\circ$ with respect to the [001] azimuth on the crystal surface, in good agreement with the 39° rotational angle calculated by DFT. Several ring breathing modes of pyridine are slightly broadened on rutile sites compared to anatase sites and this may be due to more freedom for librational vibrations of the more weakly-bound pyridine molecules.

I. Introduction.

TiO₂ is a widely studied metal oxide due to its catalytic properties in both traditional chemistry¹, photochemistry,²⁻⁶ and other applications such as photovoltaic devices,⁴ gas sensors⁷ and as a white pigment.² A fundamental understanding of the elementary adsorption and transport processes along with the catalytic properties of TiO₂ powders is critical in its use as an active catalyst as well as a support. Single crystal TiO₂, as a simple and more controllable system, is one of the most intensively investigated model oxides.^{3,5,6} However, powdered TiO₂ polycrystalline samples are widely employed for heterogeneous catalysis due to large surface area, multiple adsorption sites and ease of handling.^{3,8} This paper investigates the bonding and activated diffusion of pyridine on and through TiO₂ powders and follows a similar study on powdered MgO.⁹

A commercial TiO₂ polycrystalline powder, Aeroxide® P 25 (or Degussa P 25), is known and well accepted as a standard material used in both industry and research, due to its chemical/photochemical activity and stability. It contains TiO₂ nanoparticles in both anatase ($d \sim 25$ nm) and rutile ($d \sim 85$ nm) phases with a ratio of about 4:1.¹⁰ However, it has been shown that TiO₂ nanoparticles with anatase and rutile phases have different adsorption ability,¹¹ photocatalytic activity,^{12,13} and behave differently for the dispersion of supported molybdena.¹⁴

The surface diffusion of adsorbed molecules in porous materials is influenced by the properties of both the porous material and the adsorbed molecules. These properties include pore volume, pore size distribution, surface area, and the interaction between the adsorbate and the various types of surface sites.¹⁵ The transport of adsorbed molecules through porous solids can be described as the thermally activated hopping of molecules from one adsorption site to another along pore walls.¹⁶ The bound molecules are thought to be activated via the formation of a mobile precursor state in which they can move laterally along the surface until they either desorb into the vacuum or readsorb onto another trapping site.^{9,17-19} In the mobile precursor model, the activation barrier for diffusion is defined as the energy necessary to activate the adsorbed molecule from its chemisorbed state into the weakly bound mobile precursor mode, which is known as the “escape barrier”.^{9,19} The energy needed to further activate the molecule from the mobile precursor state to vacuum is relatively low since the mobile precursor is governed by the weak van der Waals interactions between the adsorbate and the adsorbent surface. The surface transport of molecules through the powdered surface is therefore activated by overcoming the “escape barrier”, instead of the conventional “desorption barrier”.

TIR (transmission infrared spectroscopy) is a powerful tool for studying the surface diffusion of probe molecules through powdered nano size materials.^{9,19,20} The vibrational mode frequencies of an adsorbed molecule are sensitive to its chemical environment, allowing different adsorption sites and condensed phases to be distinguished. The surface sensitivity of TIR employed to study adsorbates on high surface area solids is quite high resulting in a detection limit of $\sim 10^{-4}$ ML (monolayer) for the adsorbate. The integrated absorbance change in the infrared bands of diffusing molecules gives information about the fraction of molecules lost by diffusion and desorption from the powder sample and this information can be used to fit the diffusion kinetics through

Fick's Second Law of diffusion.^{9,19,21} Changes in the infrared band lineshapes and frequency provide information about species' surface bonding changes during the diffusion process.

The aromatic structure together with the nitrogen functional group of pyridine (Py) makes it an ideal mimic of certain other toxic organic molecules. The lone pair of electrons that reside on the nitrogen atom provide significant basic character and pyridine is often used as a probe of the acid sites on metal oxide surfaces and their degree of acidity.²²⁻²⁴

In this paper, we use transmission FTIR with pyridine as a probe molecule to study the adsorption and diffusion/desorption behavior of pyridine on powdered TiO₂ to reveal the surface properties of powdered polycrystalline TiO₂. The results show that there is a distribution of sites with different Lewis acid character found on the powdered sample. The results are compared with theoretical results in order to understand and quantify the different adsorption states and modes of diffusion.

II. Methodology.

A. Experimental.

1. FTIR and XRD Measurements on Powdered TiO₂.

The experimental system used in this paper was described in detail previously.²⁰ Powdered TiO₂ was provided by Evonik Industries (Aeroxide® TiO₂ P 25). The sample as received was polycrystalline composed of ~80% anatase and ~20% rutile phases.^{10,25,26} Although the literature records that a phase change from anatase to rutile occurs during calcinations (in air) around and above 900 K,²⁵⁻²⁷ XRD results shown in Figure 10.1 indicate that the treatment used in this work does not change the anatase to rutile ratio significantly. This is possibly due to the lack of oxygen in the high vacuum cell which

retarded the phase transformation from anatase to rutile. The specific surface area (SSA) of the sample, before further treatment, was $49 \text{ m}^2\text{g}^{-1}$. The powdered material was hydraulically pressed at 100,000 psi into a circular spot 7 mm in diameter onto the tungsten grid which is 0.0508 mm in thickness containing about 1370 windows ($0.22 \text{ mm} \times 0.22 \text{ mm}$) per cm^2 that are filled with the compressed TiO_2 powder. The total amount of TiO_2 powder on the tungsten grid after compressing was 0.0054 g with a density of 0.014 g cm^{-3} .

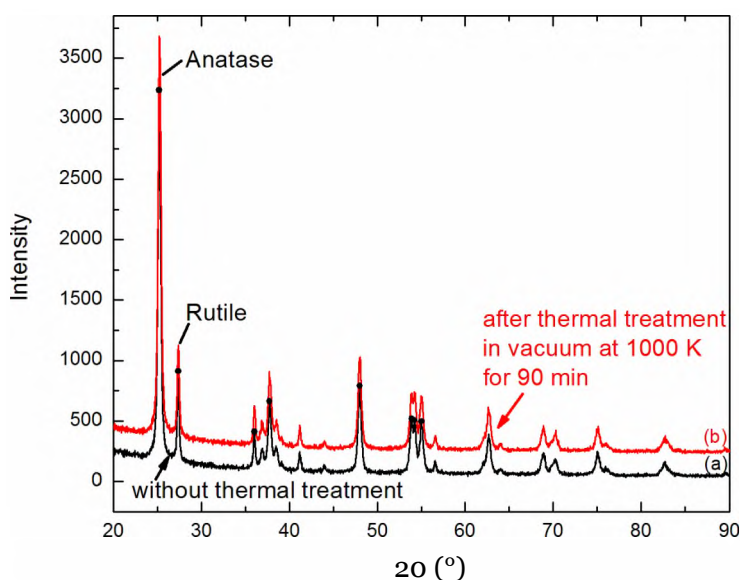


Figure 10.1. XRD patterns of the TiO_2 P 25 polycrystalline sample used in this work. Black pattern (a) represents the P 25 sample as received and red pattern (b) shows the sample after heating in vacuum to 1000 K for 90 min. Black dots are added to spectrum (a) where the maxima in the diffraction lines are overlapped with pattern (b).

The compressed sample was then mounted in the high vacuum IR chamber. Before each experiment, a sample cleaning cycle was carried out. The sample was first heated in vacuum to 680 K at a heating rate of 30 K/min. Oxygen gas was then introduced to the chamber at 680 K until a chamber pressure of 2 Torr was reached. The sample was maintained under oxygen for 1 hour to oxidize and remove any organic residue as

monitored by IR spectroscopy. The sample was then heated up to 780 K at 2 Torr O₂ pressure for further oxygen treatment for 0.5 hour. The chamber was then pumped back to vacuum with the TiO₂, at 780 K, and the sample was heated up to 1000 K for 1.5 hours in vacuum for hydroxyl removal and thermal reduction. This procedure will produce a TiO₂ surface containing oxygen vacancy defect sites.^{3,28} The IR spectrum (not shown) reveals that after the treatment cycle, the TiO₂ surface is free of detectable organic molecules as well as hydroxyl species. The sample was then cooled to the desired temperature at a cooling rate of 30 K/min.

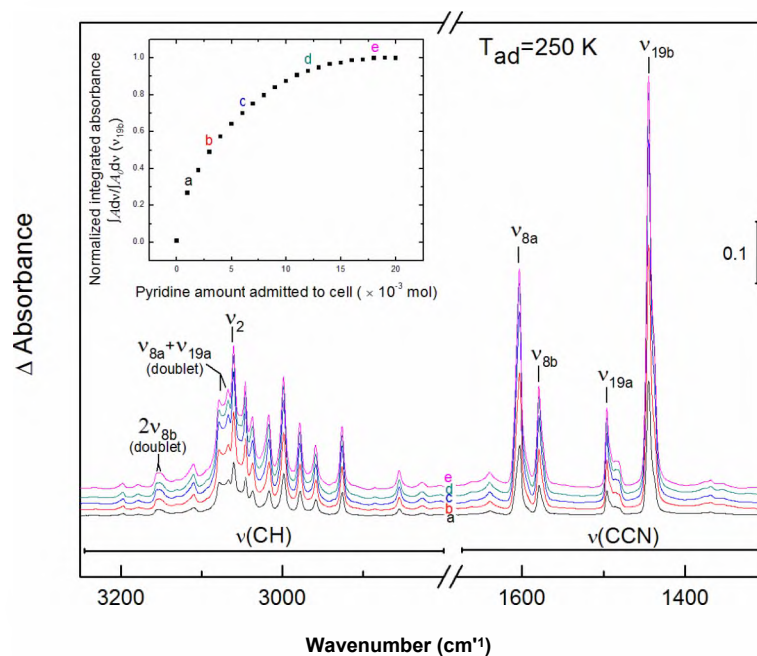


Figure 10.2. FTIR spectra of chemisorbed pyridine molecules on the TiO₂ polycrystalline surface showing increasing amounts of adsorbed pyridine at 250 K. Spectra a-e are taken with 1, 3, 6, 12, or 18×10^{-3} mole of pyridine molecules introduced to the chamber, respectively. The inset plots the integrated absorbance of the pyridine ring-breathing mode ν_{19b} (1445 cm⁻¹) as a function of increasing pyridine exposure. Saturation is reached at 1.8×10^{-3} mole exposure.

Pyridine was obtained from Sigma-Aldrich (anhydrous, 99.8% purity) and further purified with freeze-pump-thaw cycles using Z-N₂. After the cleaning cycle, the TiO₂

sample was exposed to pyridine gas at 250 K until saturation of the chemisorbed species was observed to cause the IR spectra to reach the maximum pyridine absorbance, as shown in the inset to Figure 10.2. At the saturation point, 1.8×10^{-3} moles of pyridine molecules had been introduced to the chamber. However, due to the *I-N*₂ cooling of the reentrant dewar holding the grid, only a fraction of the introduced pyridine molecules actually reached the TiO₂ sample. The chamber was then pumped at a TiO₂ temperature of 250 K (to a pressure $<5 \times 10^{-6}$ Torr) by a turbo-molecular pump. A reference spectrum, to which spectra measured during diffusion were ratioed, was taken 7 min after pumping. After 10 min of pumping, the sample was heated up to a constant temperature in the range from 260 to 290 K for diffusion experiments. The temperatures for the diffusion experiments were chosen based on TPD results on TiO₂(110)-1x1 (not shown) which revealed that the onset temperature for chemisorbed pyridine desorption was around 255 K. IR spectra were taken continuously over time once the desired diffusion temperature was achieved. The diffusion/desorption process was monitored by plotting the integrated absorbance decrease versus time for one pyridine vibrational mode, the ν_{19b} mode.

The IR spectra were recorded with a purged Bruker TENSOR 27 FTIR spectrometer, using a liquid nitrogen cooled MCT detector. Each spectrum was obtained in 51 s by averaging 128 interferograms at 2 cm⁻¹ resolution. A background spectrum, taken through the empty tungsten grid, was subtracted from the measured IR spectrum. Each diffusion/desorption experiment was carried out for 2 hours, with IR spectra taken every 2 min.

Powder X-ray diffraction (XRD) data were collected using Cu K α radiation on a PANalytical X'Pert PRO powder diffractometer equipped with an X'Celerator detector.

The TiO_2 sample was treated in the high vacuum IR cell with the sample cleaning cycle described above and then cooled to room temperature and transferred to the diffractometer. Data were collected between $5\text{--}90^\circ$ 2θ in scanning mode with a step size of 0.0167° and a count time of 20 s.

2. Adsorption Configuration Study on Single Crystal Rutile $\text{TiO}_2(110)\text{-}1\times 1$ Surface.

The adsorption configuration of pyridine on rutile $\text{TiO}_2(110)$ single crystal has been studied in a separate ultrahigh vacuum (UHV) chamber equipped with electron-stimulated desorption ion angular distribution (ESDIAD), low energy electron diffraction (LEED), Auger electron spectroscopy (AES), and a quadrupole mass spectrometer (QMS). The base pressure is below 3×10^{-10} Torr, as described elsewhere.^{29,30} The time-of-flight ESDIAD (TOF-ESDIAD) has been carried out using a pulse electron gun operating at 40 kHz with incident electron energy of 210 eV. The $\text{TiO}_2(110)\text{-}1\times 1$ surface can be reproducibly produced by Ar^+ sputtering followed by annealing at 900 K in vacuum, and has been characterized by LEED and AES.³⁰ Deuterated pyridine ($\text{C}_5\text{D}_5\text{N}$) was dosed to the $\text{TiO}_2(110)$ surface at 85 K through an absolutely-calibrated capillary array doser.³¹ After dosing, the $\text{C}_5\text{D}_5\text{N}/\text{TiO}_2(110)$ surface was annealed at 300 K for a short time to remove the physical adsorption layer, and then returned to 85 K for TOF-ESDIAD experiments. The angular distribution of the D^+ ions ejected from oriented $\text{C}_5\text{D}_5\text{N}$ molecules was used to determine the azimuthal orientation of the pyridine ring by observing the direction of the 3,4, and 5 C-D bonds.

Deuterated pyridine ($\text{C}_5\text{D}_5\text{N}$) was purchased from Aldrich with 99.9% atom D purity and was purified by freeze-pump-thaw treatment.

A rutile $\text{TiO}_2(110)$ single crystal was purchased from Princeton Scientific Corp.

B. Computational.

In an effort to complement the experimental results, first principle density functional theoretical calculations were carried out to examine the adsorption of pyridine at different sites on two model TiO₂ surfaces in order to establish the modes of adsorption and the adsorption energies. All of the calculations reported herein were carried out using periodic plane wave density functional theory (DFT) code VASP by Kresse and Hafner.³²⁻³⁴ The non-local exchange and correlation effects were modeled within the generalized gradient approximation (GGA) using the Perdew Wang (PW91)³⁵ functional. In order to reduce the number of plane-waves needed, the interaction between valence and core electrons were described by the use of Vanderbilt Ultrasoft Pseudopotentials (US-PP)³⁶ with a plane-wave basis cutoff energy of 396 eV. A (3 x 3 x 1) Monkhorst-Pack k-point mesh³⁷ was used to sample the first Brillouin zone. The convergence criteria for electronic energy was set to 10⁻⁶ eV, while geometries for each atomic configuration were optimized until the forces on each atom were less than 0.05 eV/Å. For this study both anatase and rutile TiO₂ crystal forms were used to examine pyridine adsorption. The unit cells were cleaved along the 101 (anatase) and 110 (rutile) directions respectively, with a crystal slab of 8 atomic layers separated by a 10 Å vacuum space between slabs. The lowest two layers of the TiO₂ slab were held fixed, while the remaining six were optimized along with adsorbents to their lowest energy configuration. The average adsorption energy (E_{Ads}), defined as the overall adsorption energy divided by total number of adsorbed pyridine molecules, for the following reaction (TiO₂ + nPy → TiO₂-Py_n) was calculated using Equation 10.1:

$$E_{Ads} = [E(\text{TiO}_2\text{-Py}_n) - E(\text{TiO}_2) - nE(\text{Py})]/n \quad (10.1)$$

where n refers to the number of pyridine molecules adsorbed and E(TiO₂-Py_n), E(TiO₂), and E(Py) refer to the total energies for n-molecules of pyridine adsorbed on TiO₂, bare

TiO₂ surface and the pyridine molecule calculated in the gas phase, respectively. In order to compare with the experimental thermal heats of desorption we define the heat of adsorption of pyridine per mole (Q) to be the absolute value of the calculated energies of adsorption as shown in Equation 10.2:

$$Q = - (DE_{ads}) \quad (10.2)$$

This conforms to the experimental definition that the heat liberated during adsorption is a positive value. In addition, we make the approximation that the changes in the zero point energy, vibrational, rotational and translational energies and the volume, contributed to the enthalpy, can be neglected.

III. Results and Discussion.

A. Pyridine Chemisorption on TiO₂ Surfaces.

Figure 10.2 shows the IR absorbance development for pyridine molecules chemisorbing on the TiO₂ surface at 250 K. The C-H vibrational mode region around 3000 cm⁻¹ and the C-C-N ring breathing vibrational mode region around 1500 cm⁻¹ are indicated. Several important spectral features that will be discussed in more detail later are labeled in Figure 10.2, based on Wilson's notation³⁸ and other published results following Wilson's notation.^{9,39,40}

All of the pyridine vibrational features increase monotonically in absorbance as the number of pyridine molecules chemisorbed on the TiO₂ surface increases. Since after the sample cleaning cycle the TiO₂ surface is fully dehydroxylated, the chemisorption sites for pyridine are the Ti cations which serve as Lewis acid centers to which pyridine can bind via its lone pair of electrons on the nitrogen atom. The peak frequency and lineshape of the strong V19b absorbance which appears at 1445 cm⁻¹ corresponds to the C-N-C stretching mode and is termed a pyridine ring breathing mode. The position of the

ν_{19b} absorbance at 1445 cm^{-1} confirms that pyridine molecules chemisorb on the surface Lewis acid centers (Ti cation sites).^{9,23} The frequency of this mode is most strongly affected by the interaction between the nitrogen lone pair from the pyridine molecule and the substrate surface.^{11,23,24} Thus, it has been chosen to monitor the relative amount of pyridine chemisorbed on the TiO_2 surface. The integrated absorbance of the ν_{19b} mode is assumed to be proportional to the amount of pyridine chemisorbed on the metal oxide surface.^{9,19} The inlay on Figure 10.2 shows the integrated absorbances of the ν_{19b} mode normalized to the maximum integrated absorbance during pyridine exposure as a function of the increasing amount of pyridine introduced into the chamber.

In the $\nu(\text{CCN})$ region, a shoulder on the lower wavenumber side is seen on both the ν_{19a} (peak at 1496 cm^{-1} , shoulder at 1480 cm^{-1}) and the ν_{19b} (peak at 1445 cm^{-1} , shoulder at 1438 cm^{-1}), indicating that there is more than one type of Lewis acid site on the TiO_2 surface. It is also noted that the features in the $\nu(\text{CH})$ region are more complicated when compared to pyridine chemisorbed on the Lewis acid sites of other metal oxide surfaces.^{9,11,23,41} More C-H vibrational features and multiple combination modes are observed. These spectra will be discussed in Section III.H.

B. Diffusion/Desorption Studies at Different Temperatures.

The pyridine-saturated TiO_2 surface at 250 K, whose infrared spectrum is shown in Figure 10.2, is programmed upwards in temperature after evacuation for 10 min, and then held at a constant temperature between 260 and 290 K for diffusion studies lasting 2 hours with spectra taken every 2 min. In an actively pumped vacuum system, with temperatures higher than the adsorption temperature (250 K), pyridine molecules begin to diffuse and desorb from the TiO_2 surface, causing the corresponding IR absorbances

to decrease. The integrated absorbances of ν_{igb} , normalized to a point measured 7 min after evacuation at 250 K, are plotted as a function of diffusion time at each temperature, as shown in Figure 10.3.

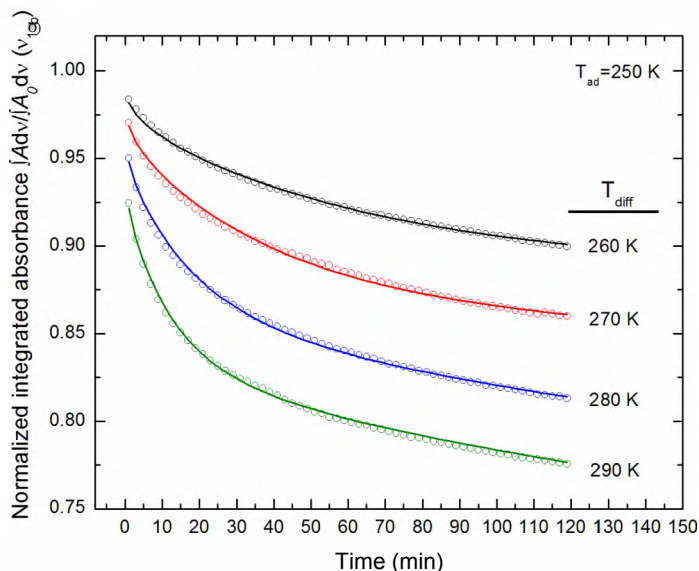


Figure 10.3. Normalized integrated absorbance of the ν_{igb} mode as a function of increasing diffusion time at different temperatures. Hollow circles show experimental data points taken at each temperature from 260 to 290 K. Solid lines of the same respective colors underneath the data points show the best fit curves to the double diffusion Equation 10.3 at each temperature. The curves are normalized to the data point taken after pyridine saturation at 250 K followed by evacuation for 7 min.

We have shown previously in a study concerning the adsorption and diffusion of pyridine on MgO that the experimental diffusion curve can be fit to a model based on Fick's second law by assuming two different diffusion processes.^{9,19} The mathematical expression is shown in Equation 10.3,²¹

$$\begin{aligned}
 \frac{6A - A_0}{A_0} = \frac{6}{V} \sum_{n=0}^{\infty} \frac{8}{(2n+1)^2} \exp \left\{ -\frac{60 D_s (2n+1)^2 \pi^2 f}{l^2} \right\} \\
 + \frac{6 S^2}{\sum_{n=0}^{\infty} (2n+1)^2} \exp \left\{ -\frac{60 D_s (2n+1)^2 \pi^2 f}{l^2} \right\}
 \end{aligned}
 \quad (10.3)$$

where $\theta =$ the fraction of sites occupied by the adsorbate (pyridine in this case); $A_t =$ total integrated absorbance for the pyridine remaining after desorption time t , $A_0 =$ total integrated absorbance of pyridine after adsorption for infinite time; θ_f , $\theta_s =$ fractional coverage of pyridine involved in the initial fast or slow diffusion process; D_f , $D_s =$ diffusion coefficient of pyridine in the fast and slow process; $t =$ time (min); and $l =$ thickness of the compressed TiO_2 sample (0.00508 cm in our case). The best-fit curve at each temperature is shown as a solid line in Figure 10.3 corresponding closely to the experimental points shown in the same color. The best fit for all four diffusion curves requires the use of two characteristic diffusion processes to fit the fast and slow processes.

Table 10.1: Diffusion Parameters for Pyridine Diffusion on TiO_2 surfaces.

Temp (K)	$D_f (10^{-10} \text{ cm}^2 \text{ s}^{-1})$	$\theta_f (\%)$	$D_s (10^{-13} \text{ cm}^2 \text{ s}^{-1})$	$\theta_s (\%)$
260	6.6	9.8	1.0	90
270	11	9.9	9.1	89
280	23	8.5	50	89
290	35	8.4	65	86

The parameters for the two-site model are summarized in Table 10.1. The diffusion coefficient of the fast process is in the range of 6.6 to $3.5 \times 10^{-9} \text{ cm}^2 \text{ s}^{-1}$ and the diffusion coefficient of the slow process is in the range of 1.0×10^{-3} to $6.5 \times 10^{-12} \text{ cm}^2 \text{ s}^{-1}$ over the studied temperature range. Overall, about 9% of the pyridine molecules on the surface at the beginning of the diffusion experiment participate in fast diffusion and more than 85% of the pyridine molecules experience slow diffusion. The total coverage of pyridine on the TiO_2 surface is $\theta = \theta_f + \theta_s$, combining d_f and d_s is; not 100% since some of the sites are occupied by other species. Since adsorption and during the ramping up of the temperature to the chosen diffusion temperature, there is a deviation from 100%

increases as the diffusion temperature is set higher because longer temperature ramping times are needed to reach the beginning diffusion temperature.

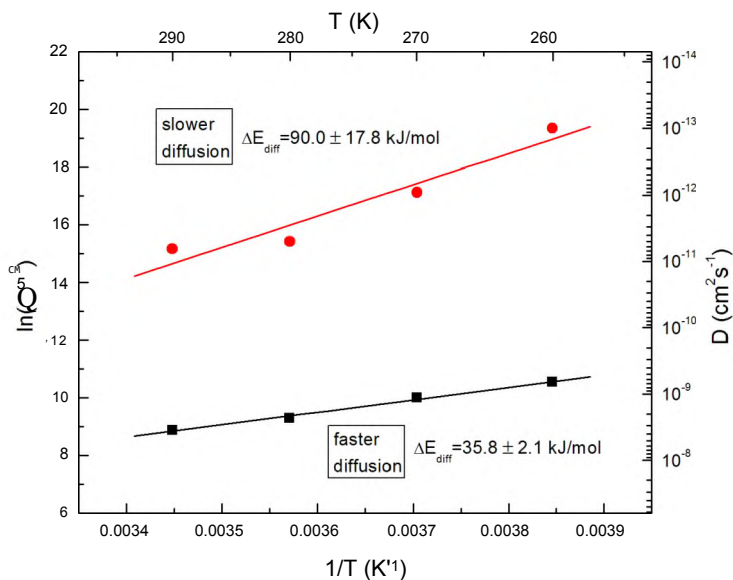


Figure 10.4. Arrhenius plots for the fast diffusion and the slow diffusion processes for pyridine from the TiO₂ polycrystalline surface.

Arrhenius plots for the two diffusion processes are shown in Figure 10.4. Activation energies of the fast and slow diffusion are calculated to be 35.8 ± 2.1 kJ/mol and 90.0 ± 17.8 kJ/mol, respectively.

The TiO₂ P 25 sample used in this work contains polycrystalline phases of both anatase (~80%) and rutile (~20%) as shown in Figure 10.1. Thus, the measured activation energies are averages among a series of different adsorption environments, including different crystal structures, surface defect types, and adsorbate structures.

C. Spectroscopic Evidence for the Two-Process Diffusion.

Infrared spectra from all 4 diffusion studies from 260 K to 290 K have the same development trend. Data collected at 280 K are chosen as representative of the 4 diffusion studies. The V19b vibrational mode's lineshape changes during pyridine's

diffusion/desorption from the TiO_2 surface at 280 K are shown in the upper panel of Figure 10.5. The main peak at $\sim 1445 \text{ cm}^{-1}$ and the shoulder at $\sim 1438 \text{ cm}^{-1}$ both decrease

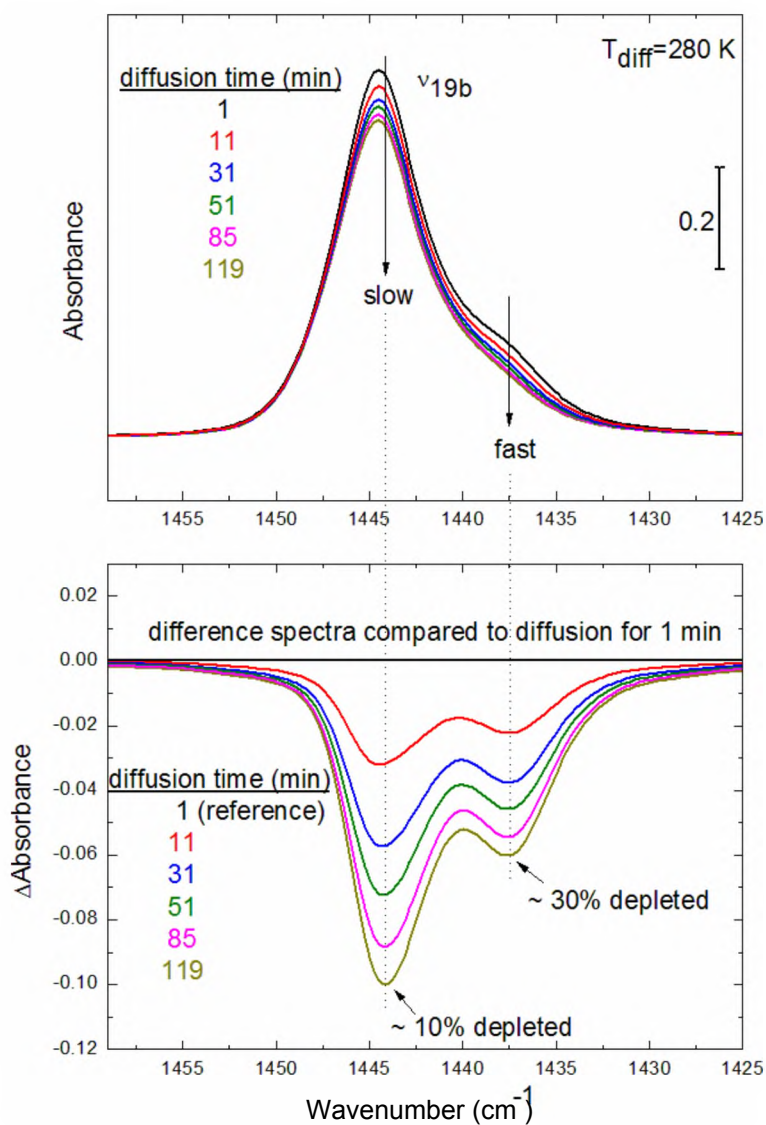


Figure 10.5. FTIR spectra (upper panel) and difference spectra (lower panel) of the ν_{19b} mode lineshape changes during pyridine diffusion on a TiO_2 polycrystalline surface at 280 K. Spectra shown in black, red, blue, green, pink and yellow green correspond to diffusion for 1, 11, 31, 51, 85, and 119 min respectively. Difference spectra are referenced to the first spectrum (black) shown in the upper panel.

in absorbance as the diffusion process proceeds. This ν_{19b} ring-breathing vibrational mode is typically seen as a sharp, strong, single peak in pyridine chemisorbed on Lewis

acid sites of various powdered metal oxide surfaces, such as ZrO_2 ,²³ Al_2O_3 ,²³ and MgO ,⁹ in the 1440-1447 cm^{-1} region. The appearance of the lower wavenumber shoulder indicates that multiple types of Lewis acid adsorption sites exist on the TiO_2 particles.

Difference spectra shown on the bottom panels of Figure 10.5 show the spectra from the top panels each subtracted from the first spectrum of the diffusion experiment on the same panel. Over the 2 hour experiment, ~30% of the shoulder was depleted, with only a 10% reduction in the main peak absorbance. Thus, we propose that for the $\text{V}_{19\text{b}}$ vibrational mode, the main absorbance at 1445 cm^{-1} corresponds to molecules undergoing the slow diffusion process, while the shoulder at 1438 cm^{-1} corresponds to molecules undergoing the fast diffusion process.

D. Computational Results.

1. Adsorption of Pyridine at the $\text{Ti}_{5\text{c}}$ site-Rutile $\text{TiO}_2(110)$.

Density functional theoretical calculations were carried out to determine the adsorption modes of pyridine and their corresponding adsorption energies at a range of different sites on both the anatase (101) and rutile (110) TiO_2 surfaces. The calculated adsorption energies were used to establish the most stable adsorption sites in order to compare with the experimental results and help identify the possible sites responsible for the fast and slow diffusion regimes found experimentally. A rigorous quantitative comparison of the result between theory and experiment is difficult due to range of different adsorption sites that may be present on rutile and anatase TiO_2 surfaces. The results can also be obscured due to the fact that DFT and in particular the PW91 functional used here tend to overestimate the adsorption energies.⁴² The adsorption of pyridine on the rutile $\text{TiO}_2(110)$ surface occurs at the exposed cation Ti sites which have a coordination number 5. This is often termed the $\text{Ti}_{5\text{C}^{4+}}$ site.³ Pyridine adsorbs atop of the

Ti cation site whereby the plane of the molecule is perpendicular to the surface.⁴² Pyridine adsorption involves the transfer of electrons from the lone pair on the nitrogen atom into the unfilled states of the Ti cation.

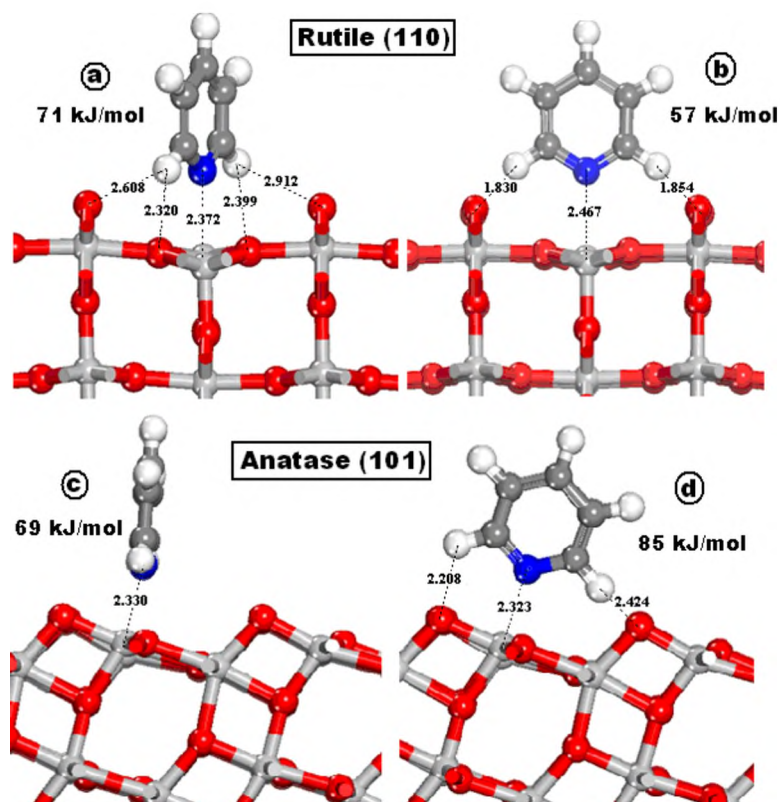


Figure 10.6. Pyridine adsorption on the rutile $\text{TiO}_2(110)$ single crystal surface: (a) rotated and (b) perpendicular orientations relative the plane of bridging oxygen atoms, respectively. The rotated species exhibit $\pm 39^\circ$ ring rotation with respect to the $[110]$ azimuth. Pyridine adsorption on the anatase $\text{TiO}_2(101)$ single crystal surface: (c) parallel and (d) perpendicular orientations.

The calculations here reveal that the most stable adsorption configurations on the rutile $\text{TiO}_2(110)$ surface are on the exposed Ti cations. The pyridine molecule rotates around its central axis in order to gain an enhanced stabilization as a result of the weaker interactions between the hydrogen atoms on the pyridine and the exposed bridging oxygen of the rutile surface. When pyridine adsorbs on the rutile (110) surface perpendicularly, the hydrogen atoms bound to the carbon atoms adjacent to the nitrogen

within the pyridine ring point towards the surface. Pyridine rotates around the Ti-N bond in order to allow these two hydrogen atoms to form weak hydrogen-bond interactions with the bridging 2 coordinate oxygen anions which sit on the surface and the 5 coordinate oxygen anions in the plane of the surface. The lowest energy adsorption state on rutile (110) is shown in Figure 10.6a resulting in a pyridine adsorption energy of 71 kJ/mol (exothermic). The adsorption of the pyridine molecule is almost exclusively a result of an electrostatic interaction between N and Ti atoms ($\text{Ti-N} = 2.37 \text{ \AA}$). The distances between pyridine H atoms and surface O atoms are all greater than a standard hydrogen bond (2 \AA) and therefore only very weakly contribute to the overall adsorption process. In this configuration, the rotation angle between the pyridine molecular plane and the bridging oxygen row is calculated to be 39° . Further discussion and experimental measurements of this angle will be provided in Section III.E.

If pyridine is rotated around the Ti-N axis in order to place it directly within the plane of the two bridging oxygen anions that sit in adjacent rows and the Ti adsorption center (as shown in Figure 10.6b), the bond distances between the bridging oxygen and the hydrogen reduce to 1.85 \AA . The rotation weakly enhances the hydrogen bonding between the pyridine and the bridging oxygen, but this occurs at the expense of the strong electrostatic interaction between the Ti and the N. The Ti-N bond distance increases to 2.47 \AA which weakens the overall adsorption energy by 14 kJ/mol down to 57 kJ/mol. This decrease in overall adsorption energy supports our initial statement that the main contribution to adsorption of pyridine on the rutile $\text{TiO}_2(110)$ surface is via the donation of electrons from the N to the Ti cation.

2. Adsorption of Pyridine on the Anatase $\text{TiO}_2(101)$ Surface.

The adsorption energy of pyridine on the anatase $\text{TiO}_2(101)$ surface is 85 kJ/mol (as shown in Figure 10.6d) which is 14 kJ/mol stronger than on the rutile surface (shown in

Figure 10.6a) despite the fact that the Ti-N bond lengths on the two surfaces are within 0.04 Å of one another and that both sites involve a Ti_5C^{4+} site. The increased adsorption appears to be the result of an increased hydrogen bonding on the anatase surface. For example, the adsorption of pyridine is 16 kJ/mol stronger when the plane of the pyridine is aligned perpendicular to the plane of the bridging oxygens and the Ti center (Figure 10.6d) such that the hydrogen atoms can interact with the bridging oxygen anions (H—O distances are 2.21 and 2.42 Å) compared to when the pyridine is oriented normal to the Obr-Ti-Obr plane (Figure 10.6c) which results in no hydrogen bonding and an adsorption energy of 69 kJ/mol. This 16 kJ/mol difference which is attributed solely to hydrogen bonding is very close to the differences between the calculated pyridine adsorption energies on the anatase surface in the absence of hydrogen bonding (69 kJ/mol, Figure 10.6c) and on the rutile surface (71 kJ/mol, Figure 10.6a). This suggests that the more open channels that form as a result of the rows of the exposed bridging oxygen atoms allow for hydrogen bonds to form without inhibiting the approach of pyridine to the surface and sacrificing the strong N-Ti interaction, causing pyridine to adsorb more strongly on the anatase $TiO_2(101)$ surface. As such the oxygen atoms on the anatase surface are more attractive toward the H atoms of the pyridine molecule than those located on rutile.

3. Adsorption of Pyridine at Oxygen Vacancy Sites on Rutile and Anatase.

The experimental results for pyridine diffusion on TiO_2 , shown in Figures 10.3 and 10.4, suggest that there is a distribution of different adsorption sites. While the clear distinction between the rutile and anatase surfaces can account for some of the observed experimental results, other possible adsorption sites, such as the oxygen vacancy defect sites, also play an important role. The Ti sites adjacent to an O vacancy defect should be considerably more reactive to pyridine than those of stoichiometric anatase or rutile. We

carried out herein a number of calculations whereby we remove 1-2 oxygen atoms directly connected to the Ti centers responsible for pyridine adsorption, in order to understand the influence of the defect sites on the adsorption of pyridine.

The removal of one of the bridging oxygen atoms on the rutile (110) surface in the form of $V_2 O_2(g)$ was calculated to be highly endothermic ($Q = -401$ kJ/mol) as the coordination number (CN) of the Ti center is reduced from 6 to 5. The subsequent removal of a second oxygen bound to the same Ti was found to be slightly more endothermic ($Q = -407$ kJ/mol) as the CN of the Ti is reduced to 4. In contrast to the removal of the first oxygen atom, the removal of a second oxygen atom resulted in significant reconstruction whereby the Ti center moves inward toward the second layer to help compensate for its lower coordination number. On anatase (101) the energy required for removal of the first oxygen was calculated to be -440 kJ/mol, which is significantly more endothermic than that on rutile (110). The results found here for the removal of oxygen from the surface of TiO_2 agree very well with previous results reported in the literature on both rutile⁴³ and anatase.⁴⁴

The adsorption of pyridine at the defect sites on the reduced TiO_2 surface was found to be more exothermic as a result of the lower CN and enhanced acidity of the Ti sites. Pyridine adsorbs at the oxygen vacancy of rutile $TiO_2(110)$ with its C2 axis tilted by 45° from the surface normal as is shown in Figure 10.7a. The optimized structure has a Ti-N bond length of 2.34 Å which is similar to that found on the defect free surface. The adsorption energy of pyridine at the defect site (CN = 5) on the rutile (110) surface was calculated to be 92 kJ/mol, which is 21 kJ/mol stronger than that on the defect-free TiO_2 rutile (110) surface. The adsorption of pyridine at the same Ti center with two oxygen vacancies (CN = 4) resulted in a minor weakening of the pyridine binding energy, as the adsorption energy decreases from 92 kJ/mol to a value of 84 kJ/mol. The reduced

affinity of the Ti cation in this surface for pyridine is the result of the surface reconstruction. The orientation of pyridine on the doubly reduced rutile $\text{TiO}_2(\text{ii}0)$ surface was found to be perpendicular to surface normal with a Ti-N bond distance of 2.36 Å as is shown in Figure 10.7b.

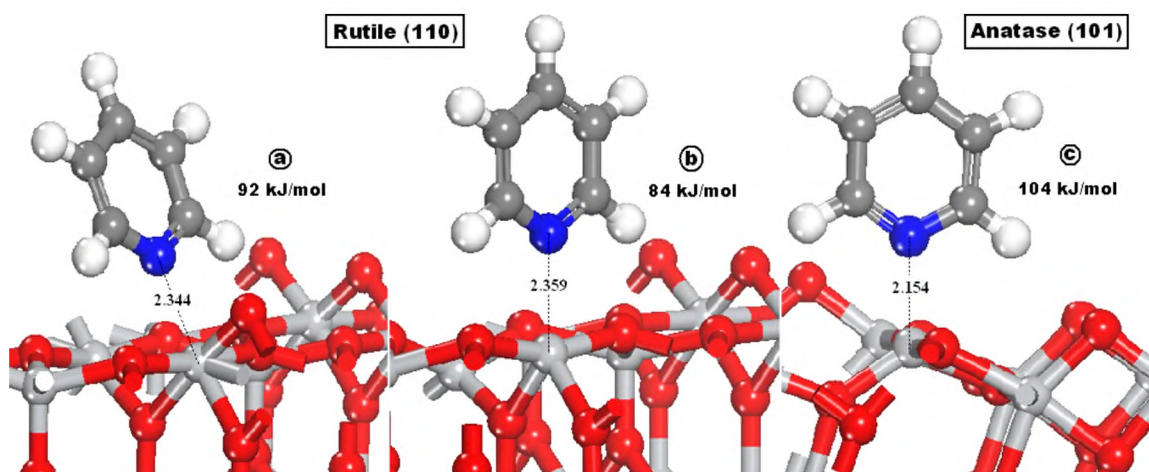


Figure 10.7. Pyridine adsorption over O vacancy defects on TiO_2 single crystal surfaces: (a) one oxygen defect, rutile (110); (b) two oxygen defects, rutile (110); and (c) one oxygen defect, anatase (101).

The adsorption of pyridine at the defect site on anatase (101) was found to be 104 kJ/mol which is 12 kJ/mol stronger than that at the defect site on rutile (110). This was the highest affinity for pyridine we found for all of the sites examined. The optimized Ti-N bond here was found to be 2.15 Å as seen in Figure 10.7c which is significantly smaller than that on the rutile (110) surface.

4. Summary of the Energetics of Adsorption of Pyridine on TiO_2 .

The calculations reported here reveal that a wide range of pyridine adsorption energies (from 57 kJ/mol to 104 kJ/mol) on TiO_2 are possible. These energies, which are summarized in Figure 10.8, depend strongly on the bulk crystal structure (rutile *vs.*

anatase), surface orientation, and the presence of oxygen-vacancy defects reducing the surface Ti cation coordination number (CN = 4-6). A summary of the calculated

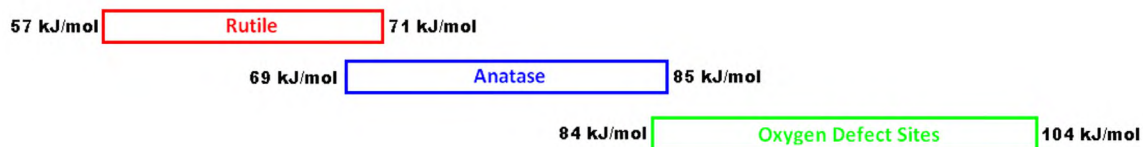


Figure 10.8. Range of pyridine adsorption energies over non-defective and O vacancy defects on TiO₂ rutile and anatase single crystal surfaces. The interval of adsorption energy values for rutile and anatase are associated with different pyridine ring orientations relative to the TiO₂ surface. The calculated adsorption energy values of pyridine on TiO₂ are slightly overestimated by PW91 DFT functional.

adsorption energies on different sites on the rutile and anatase surfaces and the role of oxygen defect sites is given in Figure 10.8. This calculated span of adsorption energies from 57 to 104 kJ/mol is in rough agreement with the distribution of activation energies for diffusion as reported in section III.B from experiments (36 to 90 kJ/mol), especially considering the well known tendency of the PW91 functional to overestimate adsorption energies. The distribution of pyridine molecules bound at different angular orientations to the coordinatively saturated Ti cation sites on the rutile surface, as well as those species on the anatase surface that do not form hydrogen bonds, are the most weakly held species with a distribution of adsorption energies that range from 57 to 71 kJ/mol. The most strongly held pyridine molecules are those found on anatase which are hydrogen bonded and those found at the defect sites of both surfaces which have adsorption energies on the order of 84 to 104 kJ/mol. These two types of adsorption modes (weak and strong) likely result in the fast and slow diffusion modes identified experimentally although the exact identification of adsorption sites is beyond the scope of this work. The more rapidly diffusing species may be due to the pyridine bound to the defect-free surfaces of rutile whereas those which diffuse more slowly may be the result

of pyridine diffusion on the anatase surfaces or near oxygen-defect sites on either rutile or anatase crystals. In the mobile precursor model for surface diffusion, the “escape barrier” is smaller than the “desorption barrier” as a result of weak van der Waals bonding of the mobile molecule. Within this model, our experimental results (36 kJ/mol for fast diffusion and 90 kJ/mol for slow diffusion) and theoretical results (adsorption energies ranging between 57 kJ/mol to 104 kJ/mol) are consistent with each other.

E. ESDIAD Study of the Pyridine Adsorption Configuration on the Rutile $\text{TiO}_2(\text{iio})$ Single Crystal Surface.

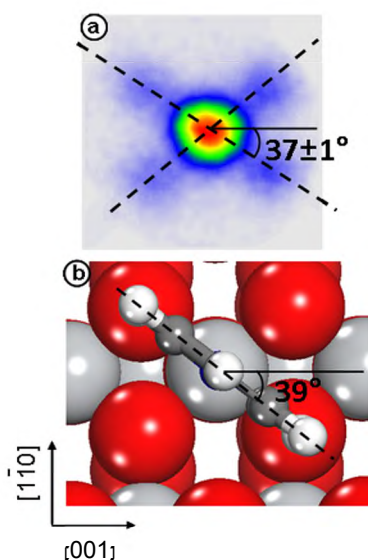


Figure 10.9. (a): D+ ESDIAD pattern obtained from $\text{C}_5\text{D}_5\text{N}$ adsorbed on the rutile $\text{TiO}_2(110)$ single crystal surface. The beam colors from red to blue indicating descending D+ ion yield from the oriented molecules. The crystal axes orientation on the $\text{TiO}_2(110)\text{-}1 \times 1$ surface is also indicated by the arrow. (b): Theoretical simulation of the configuration of pyridine adsorbed on the $\text{TiO}_2(110)\text{-}1 \times 1$ surface.

The ESDIAD pattern of the angular distribution of D+ from the $\text{C}_5\text{D}_5\text{N}/\text{TiO}_2(110)\text{-}1 \times 1$ surface is shown in Figure 10.9a. The beam colors from red to blue indicate descending

D⁺ ion yield from the various C-D bonds sampled. Five beams, a strong central beam and four weaker side beams, are observed. The crystal azimuthal orientation of the TiO₂(110) substrate, which was measured by LEED, is also labeled in Figure 10.9a. The central stronger beam comes from the D⁺ desorption from the *para* D atoms (position 4 on the pyridine ring), and the side weaker beams come from the D⁺ desorption from the *meta* D atoms (position 3 and 5). The ESDIAD pattern shows that the chemisorbed pyridine molecular plane is not perpendicular to the bridging oxygen row direction ([001]), but rotates around its central axis (Ti-N bond direction) to form an angle. Due to the symmetry of the TiO₂(110) surface with respect to the [001] or $[11\bar{0}]$ azimuth, the pyridine molecule can rotate either clockwise or anti-clockwise, which leads to four side beams instead of two. The angle between the pyridine molecular plane and the [001] azimuth is measured to be $37 \pm 1^\circ$, which agrees very well within measurement and theoretical error with the theoretical results (39°) reported in section III.D.1. For easy comparison, the top view of the theoretical simulation of pyridine adsorbed on the rutile TiO₂(110)-1x1 surface is shown in Figure 10.9b (same configuration of Figure 10.6a). The high electron-stimulated desorption (ESD) yield of the *para* D atom compared with the *meta* D atoms is due to less neutralization of the electron-excited ionization process at the central position than that of the side positions by the charge transfer from the TiO₂(110) substrate,⁴⁸ as well as to the fact that both ring orientations will contribute to the central D⁺ ion yield originating from the *para* position.

F. Computational Results for Pyridine Adsorption to Higher Coverages.

The comparisons made between the theoretically calculated adsorption energies and the measured diffusion barriers did not consider the potential differences in coverage that may take place between the calculations carried out at a low coverage and the

experiments. To better understand the influence of pyridine coverage on the adsorption energies on TiO_2 , we carried out a series of calculations where we successively increased the number of pyridine molecules adsorbed on the rutile $\text{TiO}_2(110)$ surface and varied their specific locations. The results are shown in Figure 10.10 where empty circles (O) represent empty Ti cation sites that are available for pyridine adsorption and solid circles (•) represent pyridine-occupied sites. Pyridine molecules adsorb on the rutile (110) surface with the most stable configuration shown in Figure 10.6a. A fully occupied surface as shown in Figure 10.10g is given for illustration.

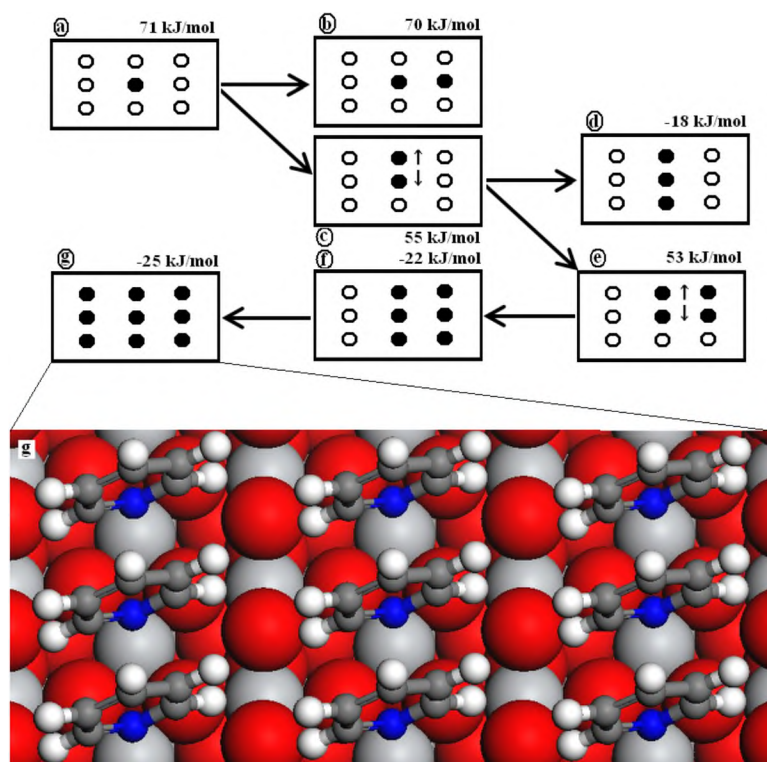


Figure 10.10. Map of sequential pyridine adsorption on the rutile $\text{TiO}_2(110)\text{-}1\times 1$ surface. The empty circles (O) represent empty sites, while solid circles (•) illustrate the pyridine adsorption locations.

From the most stable configuration of one pyridine molecule adsorbed on rutile (110) surface, as shown in Figure 10.10a, the addition of a second pyridine molecule in one of

the adjacent Ti channels divided by a row of bridging oxygen anions at the surface (Figure 10.10b), did not appreciably alter the average adsorption energy (70 kJ/mol) from that of the single pyridine molecule (71 kJ/mol). In contrast, when two Py molecules share the same channel and are adsorbed at two neighboring Ti cation sites (Figure 10.10c), the average adsorption energy decreases by 16 kJ/mol to 55 kJ/mol. Upon optimization, both pyridine molecules bend away from each other by about 7° from the normal of the substrate in order to minimize the repulsion between the rings (as indicated by black arrows), but both still remain adsorbed at neighboring Ti atoms on the rutile (110) surface. As the coverage increases to four pyridine molecules adsorbed on the slab, where two of the pyridine molecules are placed in neighboring channels (Figure 10.10e), the average adsorption energy decreases by only 2 kJ/mol to 53 kJ/mol. This suggests that pyridine can occupy up to 67% of available Ti sites on the terrace rutile (110) TiO₂ surface without major changes in average adsorption energy.

Further increases in the pyridine coverage results in the co-adsorption of pyridine at Ti sites within the same channel (Figure 10.10d) whereby there are significant repulsive interactions between the pyridine molecules which make the overall process endothermic with an adsorption energy value of -18 kJ/mol. The successive adsorption of pyridine molecules in adjacent channels (Figure 10.10f-g), replicating maximum pyridine coverage, results in only minor decreases in average adsorption energy (-22 and -25 kJ/mol) relative to a full occupied channel (Figure 10.10d). We conclude that pyridine molecules adsorb at Ti sites in a discontinuous manner (occupied-occupied-unoccupied) along the channels delimited by O planes, which allows pyridine molecules to avoid the repulsion between the adjacent rings.

G. Postulate for Fast and Slow Diffusion Sites in the Mobile Precursor Model.

From the experimental results, the fast diffusion route dominates the overall diffusion process in the beginning with the participation of a total fraction of ~9% of the adsorbed pyridine. According to the theoretical results, pyridine molecules adsorbed on the terrace rutile (110) surface are the most weakly held with an adsorption energy of 57 kJ/mol. The theoretical results also showed that at full coverage, due to the repulsion from adjacent pyridine-pyridine interactions, only a maximum of 67% of the terrace sites on rutile (110) could be available to pyridine molecules. The TiO₂ P 25 sample used in this work contains ~20% rutile and ~80% anatase phase. Thus, we postulate that the fast diffusion is attributed to pyridine molecules adsorbed on terrace rutile sites.

Since the activation barrier for the fast diffusion is lower by more than 2-fold compared to the barrier for the slow process, initially the majority of the mobile precursor state will be populated from those sites—terrace rutile Ti cation sites. As diffusion proceeds, slow diffusion begins to dominate the process because the population of pyridine molecules shifts toward those adsorbed on anatase TiO₂ and to sites on both rutile and anatase containing 3 and 4 coordinated Ti defective sites with a stronger binding energy and a higher escape barrier.

H. Spectroscopic Evidence of Pyridine Adsorption on Rutile and Anatase Surfaces.

It is very difficult by infrared spectroscopy to accurately characterize the adsorbed pyridine species when a mixture of two crystalline phases of TiO₂ (anatase and rutile) is being investigated. While the (101) and (110) faces of the anatase and rutile crystals, respectively, are the dominant faces, other faces and admixed faces are also present. In

addition, defect sites on both anatase and rutile surfaces are likely present. Despite this problem of mixed phases, studies of the variation in the infrared lineshape for several of the pyridine ring-breathing modes offer glimpses of the pyridine binding to anatase and rutile phases of TiO₂. In Figure 10.11, a study of the infrared lineshape of the overtone of one ring-breathing mode, $2\nu_{8b}$ mode, is shown during experiments where adsorption is being carried out and also when diffusion/desorption occurs. In addition, lineshape studies are shown when readsorption of pyridine is investigated.

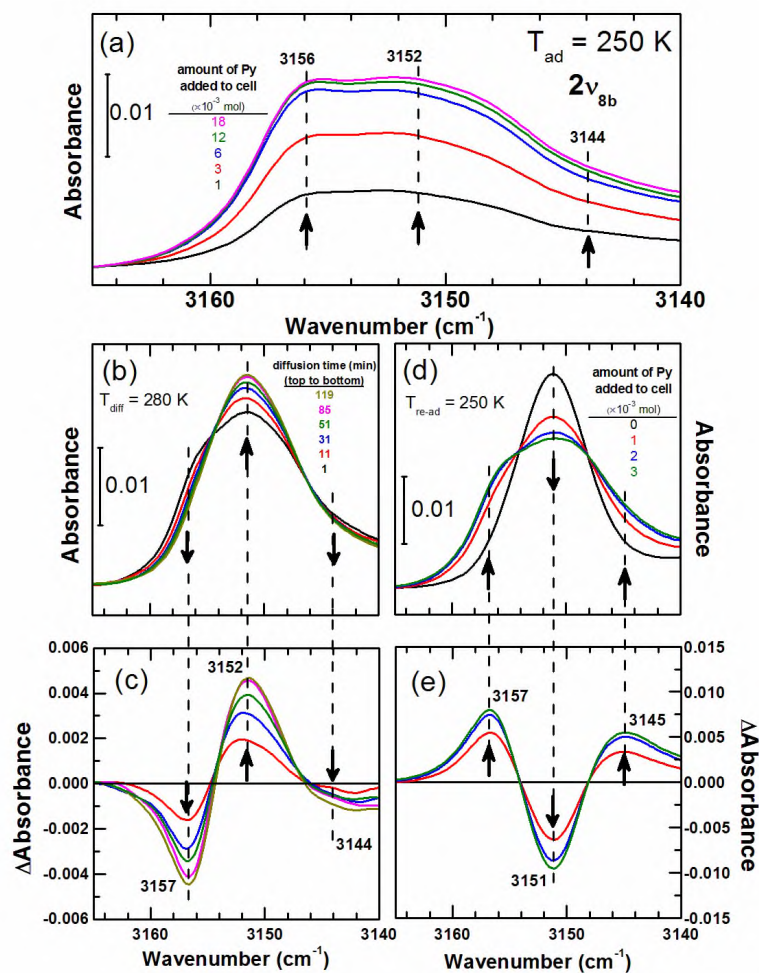


Figure 10.11. FTIR spectra and difference spectra of the $2\nu_{sb}$ mode lineshape changes during: (a) pyridine adsorption at 250 K; (b, c) diffusion/desorption at 280 K; and (d, e) re-adsorption at 250 K, on the TiO_2 polycrystalline surface.

Figure 10.11a shows the IR absorbance development of the $2\nu_{sb}$ mode during pyridine adsorption at 250 K (zoomed in from Figure 10.2). As more pyridine molecules arrive on the TiO_2 surface, in the $2\nu_{sb}$ mode region, three bands at 3156, 3152, and 3144 cm^{-1} grow side by side. However, during the diffusion experiments, as shown in Figure 10.11b, the two wings at 3156 cm^{-1} and 3144 cm^{-1} decrease as the diffusion/desorption process continues, while the center peak at 3152 cm^{-1} increases. We consider the “wing” development to be indicative of line broadening of the $2\nu_{sb}$ mode. The broad $2\nu_{sb}$ mode, present throughout the pyridine adsorption process, sharpened in response to the diffusion/desorption process. This change can be better seen in difference spectra, as shown in Figure 10.11c, where the spectra from Figure 10.11b are each subtracted from the first spectrum of the diffusion experiment (1 min) in the same figure. The disappearance of “wing” spectral components seen at 3156 and 3144 cm^{-1} and the growth of the central band at 3152 cm^{-1} can be clearly seen, indicating that the $2\nu_{sb}$ mode sharpens as the fast-diffusing pyridine species leave the sample by desorption.

After one diffusion/desorption experiment has taken place, when the $2\nu_{sb}$ mode had been converted to a sharper single band, the sample was cooled back to 250 K and pyridine was reintroduced to the chamber. The broadened multi-peak feature reappeared immediately, as shown in Figure 10.11d. As the number of pyridine molecules introduced into the chamber increases, a completely reversed trend from Figure 10.11b develops. The difference spectra of Figure 11d are shown in Figure 10.11e. The central $2\nu_{sb}$ component decreases in intensity while the two “wing” components develop as shoulders, indicating line-broadening.

A similar line-broadening during adsorption and sharpening during desorption phenomenon is also observed for the V8b, V19a, and V8a + V19a modes, but the spectra are not shown here.

To rule out the influence of temperature differences between the adsorption experiment and the diffusion experiment on the pyridine spectral lineshape change, a separate adsorption experiment was carried out at 300 K (not shown) proving that the broad band also exists at 300 K when the chamber is filled with 0.4 Torr of pyridine. Thus the broadened absorption spectrum is associated with pyridine adsorption over a wide temperature range, whereas desorption at constant temperature leads to sharpening of the spectrum.

These spectral developments are consistent with the following hypotheses: (1). The chemical bond strength for pyridine chemisorbed on anatase is generally stronger than for rutile surfaces as shown in Figure 10.8. The escape energy from the adsorption site to the mobile precursor species will therefore also generally be larger for pyridine bound to anatase surfaces compared to rutile surfaces. (2). Adsorption from the gas phase at 250 K fills both anatase and rutile sites to saturation. (3). Diffusion/desorption preferentially removes pyridine from the rutile sites. (4). Exchange of pyridine molecules between anatase and rutile crystallites is slow at 250 K. (5). Broadening of the ring breathing modes occurs preferentially on rutile sites.

The activation energies for diffusion measured here may be used to estimate the lifetime of a pyridine molecule on a TiO₂ particle of a particular diameter. (The average particle size for anatase particles are ~ 25 nm; the average particle size for rutile particles are ~85 nm.¹⁰) For the fast moving pyridine molecules, assumed to be mainly on rutile sites and associated with a diffusion activation energy of 36 kJ mol⁻¹, we use the equation

for a random walk in two-dimensional diffusion, $l = \sqrt{4Dt}$, where l is the step length; D is the diffusion coefficient; t is the lifetime. Using $D_{fast, 250 K} = 3.4 \times 10^{-10} \text{ cm}^2\text{s}^{-1}$ for fast diffusion at 250 K and 85 nm as the step length, the time required for diffusion from a rutile particle to a neighboring particle will be of ~ 0.2 s. Similarly, using $D_{slow, 250 K} = 2.7 \times 10^{-14} \text{ cm}^2\text{s}^{-1}$ and $l = 25$ nm, the time for particle-to-particle diffusion by the slow process is ~ 230 s. This is the order of time for diffusion across an anatase particle to a neighboring particle. For adsorption at 250 K from the gas phase, achievement of full coverage occurs on both rutile and anatase sites and broadened ring breathing modes are observed. As diffusion/desorption occurs, the rutile-bound pyridine is preferentially depleted in short times, causing the narrowing of the infrared features. Upon pyridine readsorption, where empty rutile sites are preferentially repopulated, the modes are again observed to broaden.

The spectroscopic separation observed for pyridine molecules, between rutile and anatase sites, is certainly only an approximation. Defect sites on either rutile or anatase crystal faces will have enhanced binding and therefore are also likely to contribute to the slow diffusion process. However, the long time (~ 230 s) calculated for pyridine molecule diffusion across TiO₂ anatase crystallites suggests that we are, in the main, observing separate diffusion processes occurring on separate crystallites, with rutile crystallite having much shorter retention times compared to anatase.

The reasons for enhanced 2v8b line width for pyridine adsorbed on rutile crystal surfaces compared to anatase crystal surfaces is difficult to explain. Lifetime broadening of the vibrationally-excited 2v8b mode would be associated with more strongly-bonded pyridine species (on anatase sites) which could more rapidly exchange energy with the TiO₂ substrate. This is just opposite to the experimental observation, where the more

freely-moving pyridine molecules, exhibiting the lowest activation energy for diffusion, also exhibit the broadened 2v8b line shape. The broadened IR modes observed for the pyridine molecules on the rutile sites may indicate the preferential presence of low frequency librational modes for the more weakly-bound pyridine species giving line broadening effects for some higher frequency internal vibrational modes of chemisorbed pyridine. The higher librational freedom postulated for pyridine on rutile (110) surfaces (due to reduced hydrogen bonding compared to anatase (101)) may be involved in causing the broadened ring breathing modes for the fast diffusing pyridine molecules.

IV. Summary.

The following observations have been made about the adsorption and surface diffusion of pyridine through TiO₂ powder:

1. Heat treatment at 1000 K in vacuum to completely dehydroxylate the TiO₂ does not change the crystalline structure of the mixture significantly.
2. Pyridine chemisorbs to a saturation coverage on Lewis acid sites on dehydroxylated TiO₂.
3. The saturated pyridine layer diffuses and desorbs at experimentally observable rates in the temperature range 260 - 290 K.
4. Diffusion occurs with a mixture of kinetics which can be accurately simulated using Fick's second law. Two kinetic processes for pyridine diffusion are found with an activation energy of 35.8 ± 2.1 kJ/mol (fast process) and an activation energy of 90.0 ± 17.8 kJ/mol (slow process).
5. More than 85% of the molecules experience the slow diffusion process. This is comparable to the relative abundance of anatase crystallites.

6. The ν_{9b} ring breathing mode exhibits two components at -1445 cm^{-1} and -1438 cm^{-1} . The -1445 cm^{-1} band is associated with molecules undergoing the slow diffusion process involving more strongly-bound pyridine molecules mainly from anatase sites; the -1438 cm^{-1} band is associated with the molecules undergoing a faster diffusion process on rutile sites.

7. Comparison of pyridine chemisorption energies by DFT calculations indicates that rutile TiO_2 surfaces chemisorb pyridine more weakly than anatase.

8. Pyridine adsorption occurs at coordinatively unsaturated Lewis acid Ti sites via the donation of electrons from the N lone pair of the pyridine molecule to the Ti cation. Oxygen vacancy defect sites enhance pyridine bonding on both anatase and rutile surfaces. Hydrogen bonding effects between C-H bonds adjacent to the N in pyridine and the bridging O atoms on the rutile $\text{TiO}_2(110)\text{-}1\times 1$ crystal plane contribute only weakly to the formation of the chemisorption bond. Stronger hydrogen bonding to surface oxygen sites occurs on anatase (101) surfaces.

9. Pyridine molecules chemisorb perpendicularly on Ti^{4+} cation sites on the rutile $\text{TiO}_2(110)\text{-}1\times 1$ surface with a -37° angle of the ring plane with respect to the [001] azimuth, as confirmed by both ESDIAD measurements and DFT calculations.

10. Lateral repulsive interactions between coadsorbed pyridine molecules on TiO_2 (as calculated from DFT) limit the pyridine coverages to 67% of the available Ti cation surface sites on the $\text{TiO}_2(110)\text{-}1\times 1$ surface.

11. The ring breathing modes ν_{8b} , ν_{19a} , $2\nu_{8b}$, and $(\nu_{8a}+\nu_{19b})$ are broadened on rutile sites compared to anatase sites, possibly due to more freedom for molecular libration on rutile sites. This is consistent with reduced hydrogen bonding of the 2- and 6- C-H bonds to surface oxygen atoms on rutile (110) surfaces.

12. The large difference in pyridine's chemisorption and diffusion energies for anatase and rutile suggests that the transport of many gases through polycrystalline TiO₂ will be similarly affected. This is of importance in the use of TiO₂ as a catalyst support as well as a sorbent powder.

V. Acknowledgement.

We thank the Defense Threat Reduction Agency (DTRA) for support of this work under DTRA contract number HDTRA1-09-1-0008 and HDTRA1-07-C-008. We also thank Dr. Michael Sabat (University of Virginia) and Dr. Barbara A. Reisner (James Madison University) for performing the XRD measurements. We also kindly acknowledge the computational resources provided by the EMSL, a national scientific user facility sponsored by the Office of Biological and Environmental Research of the U.S. Department of Energy and located at the Pacific Northwest National Laboratory.

Chapter 10 References:

1. Beck, F.; Schulz, H. *Electrochimica Acta* 1984, 29, 1569.
2. Fujishima, A.; Zhang, X.; Tryk, D. A. *Surface Science Reports* 2008, 63, 515.
3. Diebold, U. *Surface Science Reports* 2003, 48, 53.
4. Grätzel, M. *Energy Resources Through Photochemistry and Catalysis*; Academic Press: New York, 1983.
5. Thompson, T. L.; Yates, J. T., Jr. *Chemical Reviews* 2006, 106, 4428.
6. Linsebigler, A. L.; Lu, G.; Yates, J. T., Jr. *Chemical Reviews* 1995, 95, 735.
7. Schierbaum, K. D.; Kirner, U. K.; Geiger, J. F.; Gopel, W. *Sensors and Actuators B: Chemical* 1991, 4, 87.
8. Martra, G. *Applied Catalysis A: General* 2000, 200, 275.

9. Kim, S.; Wang, X.; Buda, C.; Neurock, M.; Koper, O. B.; Yates, J. T. J. *Journal of Physical Chemistry C* **2009**, *113*, 2219.
10. Ohno, T.; Sarukawa, K.; Tokieda, K.; Matsumura, M. *Journal of Catalysis* **2001**, *203*, 82.
11. Bezrodna, T.; Puchkovska, G.; Shimanovska, V.; Chashechnikova, I.; Khalyavka, T.; Baran, J. *Applied Surface Science* **2003**, *214*, 222.
12. van der Meulen, T.; Mattson, A.; Osterlund, L. *Journal of Catalysis* **2007**, *251*, 131.
13. Tayade, R. J.; Surolia, P. K.; Kulkarni, R. G.; Jasra, R. V. *Science and Technology of Advanced Materials* **2007**, *8*, 455.
14. Zhu, H.; Shen, M.; Wu, Y.; Li, X.; Hong, J.; Liu, B.; Wu, X.; Dong, L.; Chen, Y. *Journal of Physical Chemistry B* **2005**, *109*, 11720.
15. Do, D. D. *Absorption Analysis: Equilibria and Kinetics*; Imperial College Press, 1998; Vol. 2.
16. DeBoer, J. H. *The Dynamical Character of Adsorption*; Oxford University Press: London, 1968.
17. Weinberg, W. H. *Kinetics of Interface Reactions*; Springer-Verlag: New York and London, 1986.
18. Cassuto, A.; King, D. A. *Surface Science* **1981**, *102*, 388.
19. Wang, X.; Kim, S.; Buda, C.; Neurock, M.; Koper, O. B.; Yates, J. T., Jr. *Journal of Physical Chemistry C* **2009**, *113*, 2228.
20. Kim, S.; Byl, O.; Yates, J. T., Jr. *Journal of Physical Chemistry B* **2005**, *109*, 3499.
21. Crank, J. *The Mathematics of Diffusion*; 2nd ed.; Oxford University Press: New York, 1980.
22. Bludau, H.; Karge, H. G.; Wilhelm, N. *Microporous and Mesoporous Materials* **1998**, *22*, 297.
23. Zaki, M. I.; Hasan, M. A.; Al-Sagheer, F. A.; Pasupulety, L. *Colloids and Surfaces A: Physicochem. Eng. Aspects* **2001**, *190*, 261.
24. Knözinger, H. *Advances in Catalysis* **1976**, *25*, 184.
25. Raj, K. J. A.; Viswanathan, B. *Indian Journal of Chemistry* **2009**, *48A*, 1378.
26. Su, W.; Zhang, J.; Feng, Z.; Chen, T.; Ying, P.; Can, L. *Journal of Physical Chemistry C* **2008**, *112*, 7710.
27. Zhang, H.; Banfield, J. F. *Journal of Materials Research* **2000**, *15*, 437.
28. Pizzio, L. R. *Materials Letters* **2005**, *59*, 994.
29. Ahner, J.; Mocuta, D.; Yates, J. T., Jr. *Journal of Vacuum Science and Technology A* **1999**, *17*, 2333.

30. Lee, J.; Zhang, Z.; Yates, J. T., Jr. *Physical Review B* 2009, 79, 08i408(R).
31. Yates, J. T., Jr. *Experimental Innovations in Surface Science: A Guide to Practical Laboratory Methods and Instruments*; Springer: New York, 1998.
32. Kresse, G.; Hafner, J. *Physical Review B* 1994, 49, 14251.
33. Kresse, G.; Furthmuller, J. *Computational Materials Science* 1996, 6, 15.
34. Kresse, G.; Furthmuller, J. *Physical Review B* 1996, 54, 11169.
35. Perdew, J. P.; Chevary, J. A.; Vosko, S. H.; Jackson, K. A.; Pederson, M. R.; Singh, D. J.; Fiolhais, C. *Physical Review B* 1992, 46, 6671.
36. Vanderbilt, D. *Physical Review B* 1990, 41, 7892.
37. Monkhorst, H. J.; Pack, J. D. *Physical Review B* 1976, 13, 5188.
38. Wilson, E. B. *Physical Review* 1934, 45, 706.
39. Wiberg, K. B.; Walters, V. A.; Wong, K. N.; Colson, S. D. *The Journal of Physical Chemistry* 1984, 88, 6067.
40. Wong, K. N.; Colson, S. D. *Journal of Molecular Spectroscopy* 1984, 104, 129.
41. Paola, A. D.; Garda-López, E.; Marci, G.; Martin, C.; Palmisano, L.; Rives, V.; Venezia, A. M. *Applied Catalysis B: Environmental* 2004, 48, 223.
42. Hammer, B.; Hansen, L. B.; Norskov, J. K. *Physical Review B* 1999, 59, 7413.
43. Vijay, A.; Mills, G.; Metiu, H. *Journal of Chemical Physics* 2003, 118, 6536.
44. Vittadini, A.; Selloni, A. *Journal of Chemical Physics* 2002, 117, 353.
45. Lee, J.; Balabin, I. A.; Beratan, D. N.; Lee, J. G.; Yates, J. T., Jr. *Chemical Physics Letters* 2005, 412, 171.

Chapter 11

Vibrational Spectroscopic Observation of Weakly-Bound

Adsorbed Molecular Oxygen on Powdered Titanium

Dioxide.*

[^]Reprinted with permission from I. X. Green and J. T. Yates, Jr., “*Vibrational Spectroscopic Observation of Weakly Bound Adsorbed Molecular Oxygen on Powdered Titanium Dioxide*”, The Journal of Physical Chemistry C 2010, 114, 11924-11930. Copyright 2010 American Chemical Society.

The adsorption of O₂ from air is an essential step in the use of TiO₂ as a photo-oxidation catalyst. This work explores the properties of a weakly-bound O₂ species which is probably the precursor to “active” O₂ needed for the photo-oxidation of molecules by TiO₂. Adsorbed molecular oxygen was observed via FTIR for the first time on nano-sized TiO₂ particles. The observed O-O stretching mode frequency at 1550 cm⁻¹ is identical to the Raman displacement of O₂ gas, showing that the interaction between the IR active O₂ molecules and TiO₂ is relatively weak. It is noteworthy that weak adsorption of O₂ on TiO₂ is accompanied by the development of a weak IR absorption band due to the production of a small dipole in the molecule. In addition, the constant ν_{O_2} observed for increasing coverage indicates that the O₂ molecules exhibit only small interactions with each other in the adsorbed layer. The adsorption enthalpy of O₂ on TiO₂ is measured to be between -16 to -21 kJ mol⁻¹. The O₂⁻ species formed by O₂ adsorbing on TiO₂ surface defect sites (likely to be the active O₂ in photochemistry), with a calculated vibrational frequency of 1097 cm⁻¹, is not observed in this work. The influence of co-adsorbed CO, CO₂ and H₂O with the adsorbed O₂ species was also investigated. It is found that when the adsorbed surface species, such as CO, CO₂, and excess H₂O, screen the TiO₂ surface

electric field and TiO₂ surface dispersion forces, the IR active O₂ species are no longer observed.

I. Introduction.

TiO₂ has drawn vast interest due to its potential to catalyze photo-chemical reactions.¹⁻⁴ One important application of TiO₂ as a photo-catalyst lies in oxidizing hazardous organic materials into non-toxic molecules utilizing sunshine.¹⁻⁴ Thus, the adsorption of oxygen from air forms an important step since O₂ is the abundant oxidizing agent.

Stoichiometric TiO₂ is an insulator with little photo-catalytic capability.^{5,6} However, in reduced form, excess electrons located within the band gap cause the TiO_{2-x} to become an n-type semiconductor which can be used in various applications. TiO₂ can be easily reduced by thermally annealing, during which the TiO₂ surface exhibits a preferential loss of oxygen, generating bridging oxygen vacancies.⁶ These surface defect sites serve as strong-binding adsorption sites during photo-reactions. The study of weakly-bound O₂ molecules, which likely are precursors to strongly-bound photoactive O₂ molecules, allows us to better understand the sequence of elementary steps involved in TiO₂-mediated photo-oxidation.

Infrared spectroscopy is a powerful tool in exploring the photo-oxidation process involving organic materials on TiO₂ surfaces, since it can: 1) detect the *in situ* reaction mixture elements; 2) follow the change of reactant concentrations and record the build-up of products; and 3) distinguish adsorbed species and photo-chemical intermediates. It is a disadvantage that gas phase oxygen is IR inactive; O₂ is a diatomic molecule with a symmetric electron cloud configuration, unable to couple to incident IR light. However, it has been shown that the influence from ionic substrates, such as sodium zeolite,^{7,8} can induce IR activity for adsorbed diatomic molecules, such as H₂⁷ and N₂.⁸ Thus, the

interaction between adsorbed O₂ and the TiO₂ substrate can alter the symmetry of the oxygen molecule and generate an induced dipole and a dynamic dipole, making the O₂ species weakly IR visible.

In this work, the vibrational frequency of a weakly-adsorbed oxygen species on the TiO₂ surface at 1550 cm⁻¹ is observed by IR for the first time. Isotopic studies confirm the vibrational frequency belongs to the O-O stretching mode. CO, CO₂, and H₂O molecules are used to test the nature of the IR active O₂ species and its adsorption sites. The adsorption enthalpy of the IR active O₂ on TiO₂ is measured to be in the range of -16 to -21 kJ mol⁻¹, depending on coverage.

II. Methodology.

A high vacuum stainless steel transmission IR cell with a base pressure of $\sim 1 \times 10^{-8}$ Torr after bake out was employed in this work. A detailed description of the cell can be found elsewhere.^{9,10} The TiO₂ powdered sample used in this work was provided by Evonik Industries (Aeroxide® TiO₂ P 25). Before treatment, the sample was polycrystalline, composed of ~ 75 % anatase and ~ 25 % rutile phases with a specific surface area (SSA) of 49 m²g⁻¹.¹¹ The powdered sample was pressed at 100,000 psi into a circular spot (0.7 cm in diameter) onto the tungsten grid by a hydraulic press. The total sample mass on the grid after pressing was 5.5×10^{-3} g with a density of 0.014 g cm⁻². The grid with sample was then mounted in the high vacuum IR cell.

In order to remove impurities from the TiO₂ sample, a cleaning cycle was performed before each experiment. The sample heating and cooling rate was set to 30 K min⁻¹ throughout the cleaning cycle and experiments. The TiO₂ sample was first heated in vacuum to 680 K. Oxygen gas (2 Torr) was then introduced into the chamber to oxidize any impurities adsorbed on the TiO₂ sample. After 30 min of oxygen treatment, the

chamber was pumped back to vacuum and the sample was held at 680 K for another 30 min. The purpose of this procedure is to partially reduce the TiO_2 sample and to generate surface defect sites.¹⁶ IR spectra were taken at the end of the reduction process to make sure the surface was hydrocarbon, hydroxyl, and carbonate free. The sample was then cooled to the desired temperature.

Research purity $^{16}\text{O}_2$ gas (99.998 %) was purchased from Matheson TRI-GAS. $^{18}\text{O}_2$ gas (99 % isotopic purity) was purchased from Isotec Inc. The purity of the CO and CO_2 gas used was 99.999 %. Deionized water was employed and further purified with freeze-pump-thaw cycles before use.

The IR spectra were recorded with a Bruker TENSOR 27 FTIR spectrometer in combination with a liquid-nitrogen cooled MCT detector. The spectrometer, detector, and entire IR beam pathway not inside the vacuum cell were all purged continuously with H_2O - and CO_2 -free air. Each spectrum was obtained by averaging 256-1024 interferograms. The spectral resolution is set at 2 cm^{-1} . Integration of the IR absorbance near 1550 cm^{-1} was carried out in the wavenumber range 1559 cm^{-1} -1541 cm^{-1} using a linear baseline that connects the frequency limits of the peak envelope. A background spectrum, taken through the gas phase and empty tungsten grid, was subtracted from each measured IR spectrum under identical conditions to eliminate small interference from the gas phase and the grid. Each IR spectrum was taken after the gas phase and adsorbed phase had reached equilibrium, as judged by the IR spectral stability.

III. Results.

A. $^{16}\text{O}_2$ Adsorption on TiO_2 .

Figure 11.1 shows the IR absorbance development of $^{16}\text{O}_2$ adsorbed on the TiO_2 surface at 120 K. The spectra shown here are difference spectra generated by subtracting

the IR spectrum of the clean TiO_2 surface at 120 K without any oxygen adsorption from the spectra obtained after $^{16}\text{O}_2$ adsorption on TiO_2 at 120 K. As the $^{16}\text{O}_2$ chamber pressure increases, a weak sharp adsorption band at 1550 cm^{-1} develops. This band is assigned to the O-O stretching mode. The peak frequency is negligibly influenced by the oxygen pressure and coverage at 120 K as shown in Figure 11.1. Similar $^{16}\text{O}_2$ adsorption experiments at 140 K and 160 K show that the peak frequency is not influenced by temperature either.

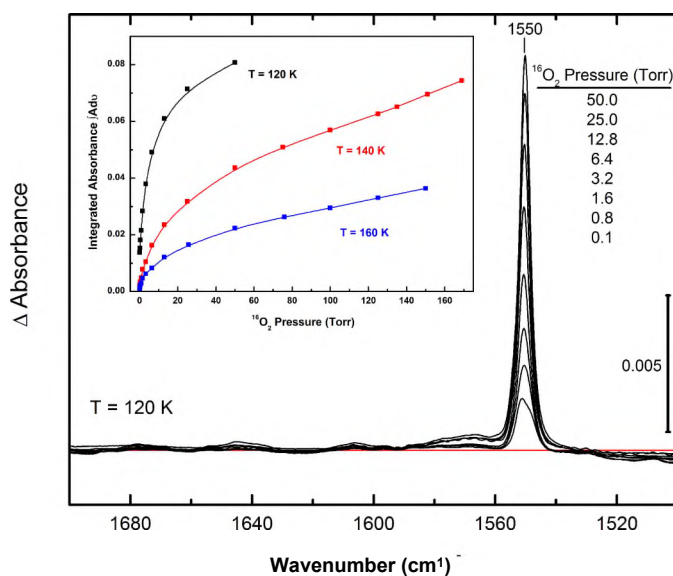


Figure 11.1. FTIR spectra of weakly-bound $^{16}\text{O}_2$ species on the TiO_2 surface with increasing $^{16}\text{O}_2$ pressure at 120 K. Each spectrum is differenced to the IR spectrum of the clean TiO_2 surface at 120 K without any oxygen adsorption. The inset plots the isotherms of $^{16}\text{O}_2$ adsorption on TiO_2 surface at 120 K (black), 140 K (red), and 160 K (blue).

The Raman displacement of $^{16}\text{O}_2$ gas is 1550 cm^{-1} .¹² The identical O-O stretching mode frequency observed in the IR spectra shows that the bond force constant is barely changed during the $^{16}\text{O}_2$ adsorption on TiO_2 . This suggests that the IR active O_2 species is very weakly bound on the surface in the sense that no obvious electron donation or withdrawal can be sensed by the O-O bond frequency.

The inset of Figure 11.1 shows the isotherm plots of the integrated absorbance of adsorbed $^{16}\text{O}_2$ in the 1550 cm^{-1} absorbance range as a function of increasing $^{16}\text{O}_2$ pressure at 120 K (black), 140 K (red) and 160 K (blue). (The maximum $^{16}\text{O}_2$ pressure reached at 120 K was 50 Torr; above this pressure a decrease in cooling rate was observed, causing accurate temperature control to be lost.) The integrated absorbance is proportional to the amount of $^{16}\text{O}_2$ that is adsorbed, becoming IR active due to interaction with the TiO_2 surface. Each data point on the isotherms represents the equilibrium amount of IR active $^{16}\text{O}_2$ adsorbed on the TiO_2 surface at the given oxygen gas pressure. It can be seen that at the same oxygen pressure, the integrated absorbance of $^{16}\text{O}_2$ decreases as temperature increases. In other words, to reach the same IR active $^{16}\text{O}_2$ coverage, higher oxygen gas pressure is required at higher temperature.

The O-O stretching mode of $^{16}\text{O}_2$ at 1550 cm^{-1} is only seen in equilibrium with gas phase oxygen. When pumped back to vacuum in the temperature range of 120 K - 160 K, complete O_2 desorption occurs as judged by the disappearance of the absorption band. This observation also indicates that the interaction between the IR active oxygen species and the TiO_2 surface is weak.

The adsorption enthalpy of $^{16}\text{O}_2$ adsorbing on TiO_2 follows van't Hoff's equation as shown in Equation 11.1:

$$Peq = \frac{e^{\frac{-\Delta H^\circ}{RT}}}{k} \quad (11.1)$$

where Peq is the equilibrium gas pressure (Torr) at a given oxygen coverage; k is a constant; ΔH° is the standard adsorption enthalpy, and T is the adsorption temperature (K). Figure 11.2 is a plot of the measured adsorption enthalpy as a function of the increasing integrated absorbance of $^{16}\text{O}_2$. The measured adsorption enthalpy is in the

range of -16 kJ mol^{-1} to -21 kJ mol^{-1} . The adsorption enthalpy decreases when the gas pressure and the O_2 coverage increase due to slightly repulsive $\text{O}_2\text{-O}_2$ interactions.

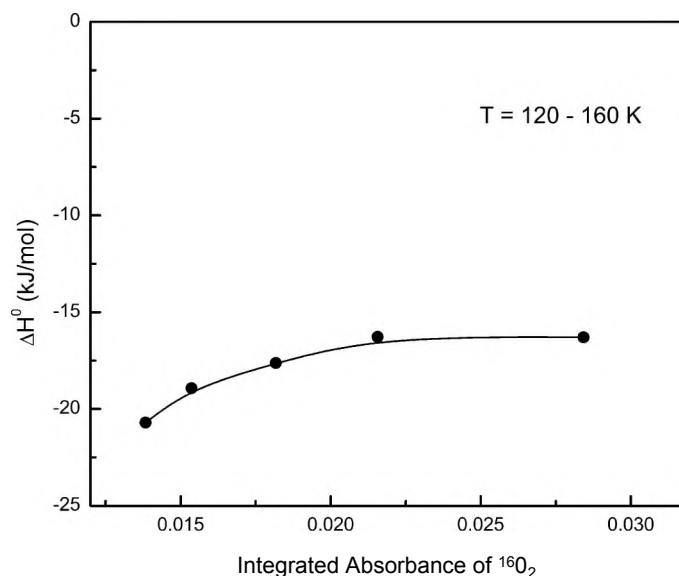


Figure 11.2. Plot of standard adsorption enthalpy obtained from analysis of the isotherms of $^{16}\text{O}_2$ on TiO_2 as a function of increasing integrated absorbance of $^{16}\text{O}_2$, in the temperature range of 120 - 160 K.

B. Isotopic Study of $^{18}\text{O}_2$ Adsorbed on TiO_2 .

To confirm the IR observation of the oxygen O-O stretching mode, a study involving $^{18}\text{O}_2$ was carried out, as shown in Figure 11.3. Figure 11.3a shows the IR spectrum of adsorbed $^{16}\text{O}_2$ at 1.6 Torr equilibrium pressure. Figure 11.3b shows the spectrum of a 1 : 1 mixture of $^{16}\text{O}_2$ and $^{18}\text{O}_2$ each at a partial pressure of 0.2 Torr. The $^{16}\text{O}_2$ exhibited an O-O stretching mode at 1550 cm^{-1} , while the $^{18}\text{O}_2$ exhibited an O-O stretching mode at 1463 cm^{-1} . The two frequencies are in accordance with the expected isotopic shift for an isolated molecule to within the accuracy of the wavenumber measurements ($\pm 1 \text{ cm}^{-1}$) indicating that the adsorbed molecule behaves almost as a free molecule without detectable modification by adsorption of the O-O force constant.

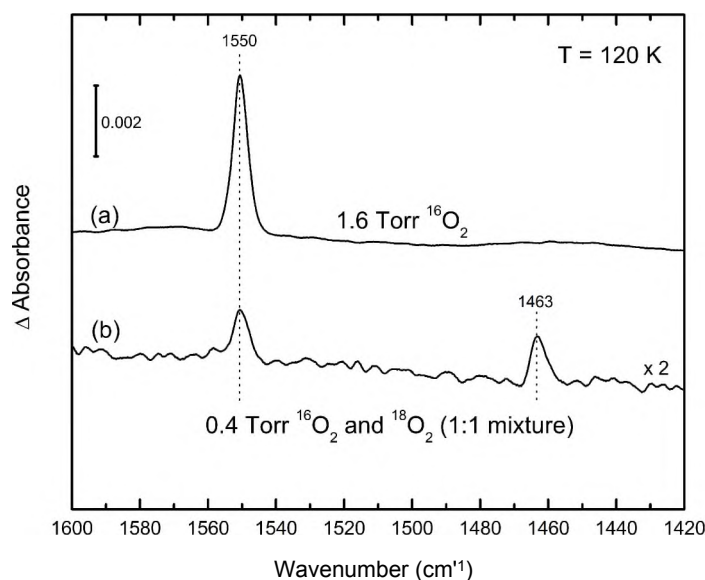


Figure 11.3. FTIR spectra of a), adsorption equilibrium between 1.6 Torr $^{16}\text{O}_2$ and TiO_2 at 120 K; and b). adsorption equilibrium between 0.4 Torr $^{16}\text{O}_2$ and $^{18}\text{O}_2$ (1 : 1 mixture) and TiO_2 at 120 K. The partial pressure of $^{16}\text{O}_2$ and $^{18}\text{O}_2$ in the mixture is 0.2 Torr. Each spectrum is differenced to the IR spectrum of the clean TiO_2 surface at 120 K without any oxygen adsorption.

C. $^{16}\text{O}_2$ Displacement by CO and CO_2 on TiO_2 .

In order to understand the properties of the TiO_2 surface region that cause oxygen molecules to become IR active, CO and CO_2 molecules were separately used to displace adsorbed $^{16}\text{O}_2$ molecules. Both CO and CO_2 are known to chemisorb on TiO_2 .¹³⁻¹⁷ CO interacts chemically with O_2 to oxidize photo-chemically on $\text{TiO}_2(110)$.¹⁸ CO_2 is known to interact with oxygen-vacancy defect sites on $\text{TiO}_2(110)$.¹⁹

I. $^{16}\text{O}_2$ Displacement by CO.

After the sample cleaning cycle, the TiO_2 sample was cooled to 120 K and 24 Torr of $^{16}\text{O}_2$ was introduced. Then CO was introduced through a leak valve from a storage vessel containing CO at 144 Torr. The leak valve was shut after every 2 min of CO leakage and an IR spectrum was taken after the leak valve had been closed for 10 min when equilibrium between the gas phase and the TiO_2 surface had been reached.

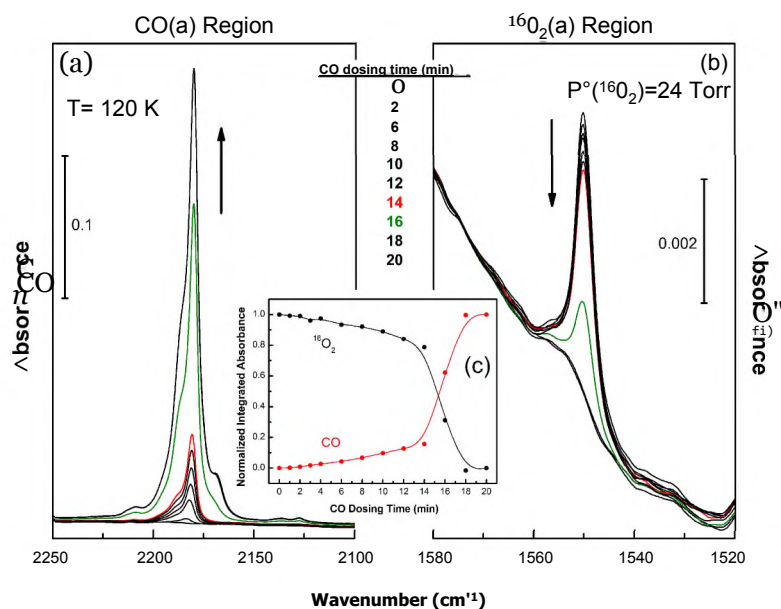


Figure 11.4. $^{16}\text{O}_2$ displacement by CO on the TiO_2 surface at 120 K. Panel a and b show the FTIR spectra of adsorbed CO increase and IR active $^{16}\text{O}_2$ absorbance decrease as the CO dosing time increases, respectively. Panel c shows the plot of normalized integrated absorbances of CO and $^{16}\text{O}_2$ as a function of increasing CO dosing time.

Figure 11.4 shows the IR spectra development in the C-O stretching mode region (panel (a)) and the O-O stretching mode region (panel (b)) as CO dosing time increases. As more CO molecules are introduced into the chamber, causing the CO absorbance to increase until saturation is reached (the spectra of CO dosing for 18 min and 20 min are overlapped with each other, indicating CO saturation was reached), and the $^{16}\text{O}_2$ absorbance to decrease until the absorption band disappears from the spectra. Adsorbed CO on TiO_2 causes complete displacement of adsorbed $^{16}\text{O}_2$ at 120 K.

A big decrease in absorbance is seen in Figure 11.4a-b between CO dosing for 14 min (red) and 16 min (green). At this point, the CO absorbance increased dramatically. This change is also clearly seen in Figure 11.4c which is a plot of the normalized integrated absorbance of CO and $^{16}\text{O}_2$ as a function of increasing CO dosing time. The $^{16}\text{O}_2$ absorbances are normalized to the initial point where only 24 Torr of $^{16}\text{O}_2$ and no CO

molecules are in the chamber. The CO absorbances are normalized to the CO saturation point (CO dosing for 18 min).

It is not known whether this effect is due to coverage induced changes for CO adsorbed on the liquid-N₂ cooled surfaces inside the cell, or to two sequential kinetic processes on the TiO₂ surface. The experiments show that an inverse relation exists between normalized O₂ and CO integrated absorbances.

2. ¹⁶O₂ Displacement by CO₂.

A CO₂-¹⁶O₂ displacement experiment was carried out similarly to the CO displacement experiment. After the sample cleaning cycle, the TiO₂ sample was cooled to 120 K, and 24.5 Torr of ¹⁶O₂ gas was introduced into the chamber. CO₂ gas was then leaked into the chamber through the same leak valve at an initial backing pressure of 144 Torr. IR spectra were taken periodically during the CO₂ dosing process, during which the leak valve was sequentially turned on and off and equilibrium between the gas phase and the TiO₂ surface had been reached at each CO₂ exposure.

Figure 11.5a shows the absorbance development of the CO₂ (ν_3 region), while Figure 11.5b shows the absorbance development of the carbonate (CO₃, ν_s and ν_{as} region) and the absorbance decrease of the O-O stretching region. Within the ν_3 region, the vibrational modes around 2400-2300 cm⁻¹ are attributed to the CO₂ molecule linearly adsorbed on the surface Ti cation sites through one O moiety.^{14,15} The small IR absorbance at 2280 cm⁻¹ is due to the natural abundance of adsorbed ¹³CO₂.^{14,15,17} In the carbonate region, bands at 1462 cm⁻¹ and 1376 cm⁻¹ are assigned to ν_{as} and ν_s of monodentate carbonate respectively; bands at 1612 cm⁻¹ and 1582 cm⁻¹ are assigned to the free carbonyl stretch in bidentate carbonate while the band at 1317 cm⁻¹ is assigned to the asymmetric stretch frequency (ν_{as}) of the bidentate carbonate.^{14,15,17}

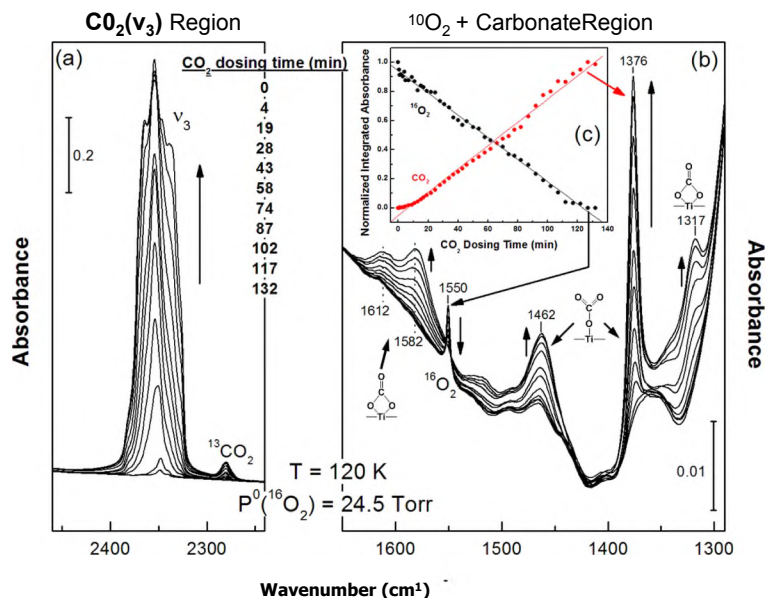


Figure 11.5. $^{16}\text{O}_2$ displacement by CO_2 on TiO_2 surface at 120 K. Panel a shows the $\text{CO}_2 \text{ v}_3$ region development with increasing CO_2 dosing time. Panel b shows the $^{16}\text{O}_2$ and carbonate region changes during the CO_2 dosing. Panel c shows the plot of normalized integrated absorbances of $\text{CO}_2(\text{v}_3 \text{ mode})$ and $^{16}\text{O}_2$ as a function of increasing CO_2 dosing time.

It is clear that CO_2 also displaces $^{16}\text{O}_2$, diminishing the absorbance of the O-O stretching mode in the IR spectra. However the displacement process is much more prolonged for the CO_2 molecules (about 130 min) compared to the CO molecules (about 18 min) under similar conditions of admission of the displacing molecule. Following CO_2 dosing for 127 min, the $\text{CO}_2(\text{V}_3 \text{ mode})$ reached saturation (as compared with CO_2 dosing for 132 min), and the O-O stretching mode disappeared from the IR spectra.

Figure 11.5c shows the normalized integrated absorbances of the $\text{CO}_2(\text{V}_3 \text{ mode})$, red and the O-O stretching mode (black) as a function of increasing CO_2 dosing time. Absorbances for $^{16}\text{O}_2$ are normalized to the initial point where only 24.5 Torr of $^{16}\text{O}_2$ and no CO_2 is in the chamber. The $\text{CO}_2(\text{V}_3 \text{ mode})$ absorbances are normalized to the saturation point (CO_2 dosing for 127 min). Both the CO_2 and $^{16}\text{O}_2$ development curves are

linear in response to increasing CO₂ dosing time. As with CO, the ¹⁶O₂ absorbance behaves inversely with the CO₂ absorbance.

D. Influence of Pre-Adsorbed H₂O on ¹⁶O₂ Adsorption.

The H₂O molecule is known to dissociate on a TiO₂ surface point vacancy defect at room temperature, leaving one -OH group filling the defect and the other H atom reacting with a nearby surface oxygen atom forming another -OH group.^{20,21} Thus, dissociated H₂O molecules can make the TiO₂ surface point defects unavailable to oxygen molecules. Since isolated OH groups (no extra hydrogen bond formed), associated OH groups (with hydrogen bonds), and molecularly adsorbed H₂O all show different characteristic features in the IR spectrum, H₂O molecules are an excellent probe to characterize the surface. Thus, in this work H₂O is used to modify the TiO₂ surface to different extents to determine the degree of surface screening required to prevent O₂ adsorption.

1. Influence of Excess H₂O on ¹⁶O₂ Adsorption on TiO₂.

After the sample cleaning cycle, the TiO₂ sample was cooled to 300 K. At this temperature, H₂O gas was introduced into the chamber gradually. Infrared spectra were taken periodically, during which the chamber was closed and 10 min was allowed for the H₂O(g) and the adsorbed species to reach equilibrium.

The group of black spectra in Figure 11.6 show the IR absorbance development of isolated OH stretching, associated OH stretching, and H-O-H bending modes during the H₂O exposure until a chamber pressure of 1×10^{-3} Torr of H₂O gas was reached in spectrum a, at 300 K. During this development, several characteristic IR features appeared: (i) the isolated OH stretching modes between 3750 cm⁻¹ and 3550 cm⁻¹. Adsorbed isolated OH groups usually exhibit sharp IR bands if the adsorption

environment is simple and uniform.^{9,22} However, the powdered TiO₂ sample employed here exposes multi-crystalline planes with various defects on the surface of each. This greatly complicates the isolated OH adsorption environment, leading to multiple sharp peaks in the high frequency region; (ii) the associated OH stretching band between 3500 cm⁻¹ and 2500 cm⁻¹. This is usually observed as a single broad band because the hydrogen bonding between OH groups and other surface species multiplies the complexity of the O-H intermolecular bonding situation leading to a general broadening of the band^{9, 23-23}; (iii) the H-O-H bending mode at 1620 cm⁻¹. The existence of this absorbance indicates that there are adsorbed H₂O molecules on the TiO₂ surface at 300 K.

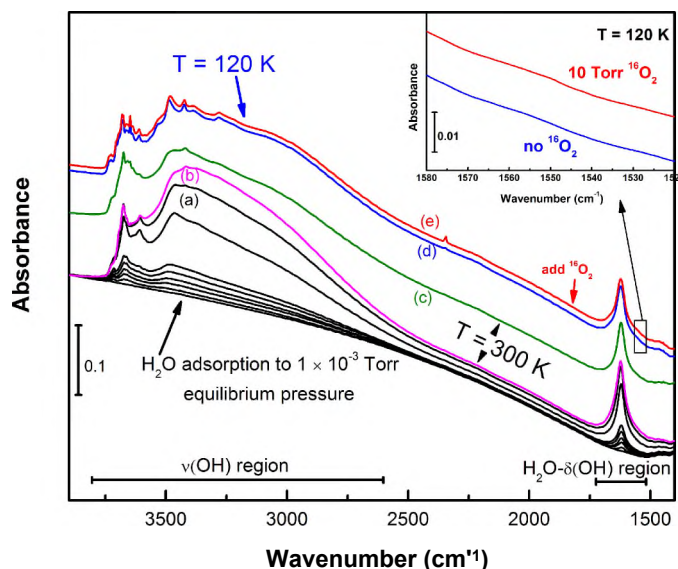


Figure 11.6. FTIR spectra of H₂O adsorption on TiO₂ surface at 300 K (a and the other 7 black spectra + b and c) and ¹⁶O₂ adsorption on H₂O covered TiO₂ surface at 120 K (d-e). Spectra a-b show the absorbance development with increasing H₂O dosing at 300 K. The equilibrium H₂O pressures at a and b are 1 × 10⁻³ Torr and 2.5 × 10⁻² Torr, respectively. Spectrum c shows the H₂O covered TiO₂ surface after evacuation for 10 min at 300 K. Spectra d and e show the H₂O covered TiO₂ surface at 120 K in vacuum and in 10 Torr of ¹⁶O₂, respectively. The inset shows magnified O-O stretching region of spectra d and e.

Spectrum b in Figure 11.6 (pink) shows the IR features when the H₂O chamber pressure is increased to 2.5×10^{-2} Torr. Compared to spectrum a (1×10^{-3} Torr H₂O pressure), a large increase in absorbance of the associated OH stretching mode is seen but little growth of isolated OH stretching or H-O-H bending modes is seen. This indicates that the TiO₂ surface is saturated with adsorbed OH groups and molecular H₂O. Enhanced hydrogen bonding occurs at 2.5×10^{-2} Torr H₂O equilibrium pressure.

The H₂O saturated TiO₂ sample was evacuated for 10 min at 300 K, as shown in Figure 11.6c (green spectrum). During evacuation, a slight decrease in absorbance was seen in all three characteristic spectral regions mentioned before. The sample was then cooled to 120 K, as shown in Figure 11.6d (blue spectrum). At low temperature, additional sharp peaks within the isolated OH stretching region appeared and may be due to the reduction of thermal motion of the OH group. A weak band at 2344 cm^{-1} developed (spectrum d) due to the CO₂ impurity from the chamber walls adsorbing onto the cooled TiO₂ surface.

¹⁶O₂ was then introduced into the chamber, in an attempt to observe adsorbed O₂. Figure 11.6e (red spectrum) shows the spectrum with 10 Torr of ¹⁶O₂ gas in the chamber. No O-O stretching feature can be detected. The inset of Figure 11.6 shows a magnified portion of spectra d and e in the O-O stretching mode region in which no ν_{O_2} absorbance developments are found at 10 Torr ¹⁶O₂. The adsorption channel for the IR active oxygen species is blocked by the excess H₂O adsorbed on the TiO₂ surface.

2. Influence of Isolated OH Groups on ¹⁶O₂ Adsorption.

Excess H₂O not only occupies the active defect sites on the TiO₂ surface, but also forms hydrogen bonded H₂O “network” among the OH groups and H₂O molecules that cover the surface. It is not unexpected that a layer such as this would block surface sites

capable of weakly bonding O₂ and activating the infrared absorption by means of a surface electric field at the TiO₂ surface. In order to further investigate the blockage of O₂ adsorption by water and OH groups, we studied O₂ adsorption on the surface containing only isolated OH groups.

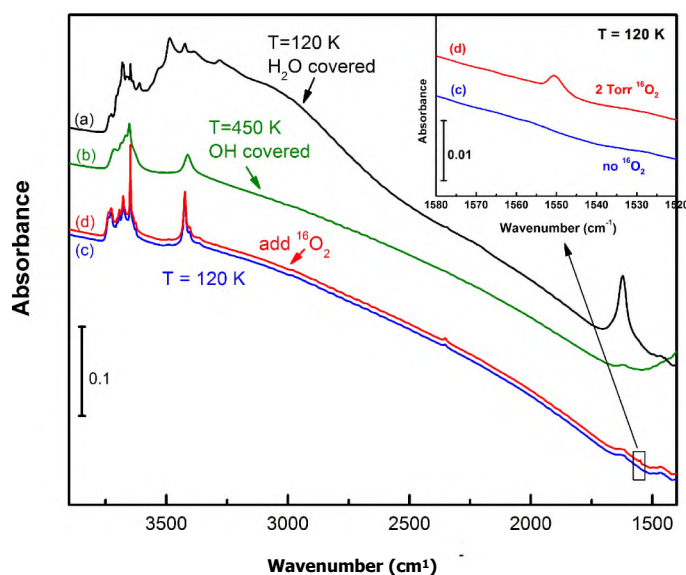


Figure 11.7. Spectrum a shows the H₂O covered TiO₂ surface at 120 K (duplicate from Figure 11.6d). Spectrum b shows the H₂O covered TiO₂ surface produced in spectrum a after annealing at 450 K for 10 min. Spectrum c and d shows the TiO₂ surface produced in spectrum b at 120 K in vacuum and in 2 Torr of ¹⁶O₂, respectively. The inset shows magnified O-O stretching region of spectra c and d.

Figure 11.7a (black spectrum) shows the same spectrum as in Figure 11.6d, which is the H₂O-covered TiO₂ surface at 120 K. The sample was heated to 450 K in vacuum for 10 min, giving the green spectrum shows in Figure 11.7b. Following annealing in vacuum at 450 K, only strongly-bound isolated OH groups remained on the surface.^{23,24} Associated OH groups and molecularly adsorbed H₂O either convert to isolated OH groups, or desorb from the surface in the form of H₂O(g).²⁵ After heating at 450 K for 10 min, most of the associated OH stretching and the H-O-H bending modes have

disappeared from the spectrum, as shown in Figure 11.7b. The characteristic spectral feature for OH groups adsorbed on a rutile TiO_2 surface is now seen at 3422 cm^{-1} as reported elsewhere²⁶ as well as other isolated OH species.

The sample was then cooled to 120 K for $^{18}\text{O}_2$ exposure. Figure 11.7c (blue spectrum) and d (red spectrum) show the TiO_2 surface before and after 2 Torr of $^{18}\text{O}_2$ gas exposure at 120 K, respectively. The inset of Figure 11.7 shows a magnified portion of spectrum c and d in the O-O stretching mode region. An IR absorbance at 1550 cm^{-1} is clearly seen in spectrum d indicating the existence of the IR active $^{18}\text{O}_2$ species on the surface. In other words, $^{18}\text{O}_2$ co-adsorbs with isolated OH groups on the TiO_2 surface. Knowing that isolated OH groups that survived the 450 K treatment are most likely adsorbed on and around the oxygen-vacancy defect sites,^{20,21,23} suggests that the IR active oxygen species is not the same species that adsorbs on and near the TiO_2 surface defect sites.

IV. Discussion.

A. Nature of the IR Active O_2 Species.

O_2 adsorption on TiO_2 has been studied by various techniques such as scanning tunneling microscopy (STM),^{26,27} temperature programmed desorption (TPD),^{28,29} photon stimulated desorption (PSD),^{18,30} and electron stimulated desorption (ESD).^{31,32} On rutile $\text{TiO}_2(110)$ single crystal surfaces, O_2 molecules can adsorb on surface oxygen-vacancy point defects.^{26,33} It is generally believed that vacancy defects on TiO_2 are electron rich, and O_2 molecules adsorbed on the TiO_2 surface will withdraw some electron density from the substrate and become slightly negatively charged as O_2^{5-} .^{28,34-36} This O_2^{5-} species is believed to play an important role in the photo-oxidation process on hydroxyl free TiO_2 . Due to the acceptance of a partial electron from the substrate, the vibrational frequency of the O-O stretch is expected to be greatly red shifted. It is noted

that the superoxide (O_2^-) species exhibits an O-O stretching mode at 1097 cm^{-1} and the peroxide (O_2^{2-}) species exhibits an O-O frequency of 802 cm^{-1} .³⁷

In our work, only a single vibrational frequency was found at 1550 cm^{-1} for $^{16}\text{O}_2$ adsorption (1463 cm^{-1} for $^{18}\text{O}_2$) as shown in Figure 11.1 and Figure 11.3. The lack of frequency shift from Raman observations indicates that the O-O bond is essentially identical to that in gas phase oxygen. This suggests that the influence of the TiO_2 surface on the adsorbed molecular O_2 observed here is primarily due to a physical effect and not to a chemical effect. The weak bonding (-16 to -21 kJ mol^{-1}) is in the range for O_2 physical adsorption on oxides and below the range for weak chemisorption.³⁸⁻³⁹ At the same time, the influence from the substrate has to be significant enough for the symmetric electron cloud of the O_2 molecule to deform slightly in order to generate a dipole moment change during bond length change (a dynamic dipole or dipole derivative ($d''g_r$)) to become IR active. We propose that this IR active O_2 species is weakly-bound to the TiO_2 surface via a general surface electric field. It is likely that hindered rotational freedom exists for this weakly-bound and slightly polarized O_2 molecule.

A schematic depicting O_2 adsorption on the TiO_2 surface is given in Figure 11.8. Three types of molecular oxygen species are shown on this scheme: (i) chemically bound oxygen, shown as red O_2^8 ; (ii) weakly-bound oxygen with slightly hindered rotational freedom, shown as blue O_2 species; (iii) gas phase oxygen that is not bound on the surface, shown as purple O_2 molecules. The chemically bound oxygen (red) is most likely to be the direct oxidizing agent when TiO_2 is used as a photo-catalyst, since direct bonding of the chemisorbed O_2 species occurs with the substrate. It is bound onto the TiO_2 surface strongly enough so that in vacuum it only desorbs after activation by either thermal energy at temperatures higher than 400 K according to TPD studies²⁸, or by

photon or electron stimulation in PSD³⁰ and ESD³¹ studies. As discussed before, this oxygen species is expected to have an O-O stretching frequency lower than 1550 cm^{-1} due to strong surface chemical bonding. On the other hand, the purple colored gas phase oxygen is not bound to the TiO_2 substrate and thus remains IR inactive.

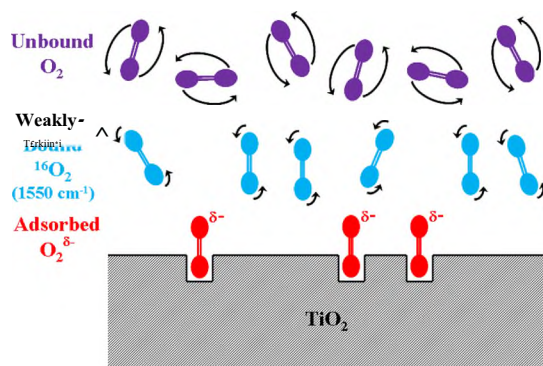


Figure 11.8. Scheme of the equilibrium of O_2 (g) with TiO_2 . The O_2^{6-} species are bound to oxygen-vacancy defect sites.

The blue colored weakly-bound oxygen molecules in Figure 11.8 are the IR active species. They are stabilized further away from the TiO_2 surface compared to the red colored chemically-bound oxygen. Their weak interaction with the TiO_2 surface is most likely not sufficient to strongly restrict the orientation of the molecule, giving it slightly hindered rotational freedom. The weakly-bound oxygen is in equilibrium with the gas phase oxygen; thus the IR absorbance of the O-O stretching mode increases monotonically with increasing oxygen gas pressure. As the oxygen gas pressure increases, more weakly-bound oxygen species squeeze into the near-surface layer, causing slightly increased repulsion between O_2 molecules and a slight decrease in adsorption enthalpy.

Although the IR active oxygen species is not in direct contact with the TiO_2 surface, it still holds research interest because it likely serves as the supply reservoir and precursor for the chemically bound oxygen species. Most of the photo-catalytic uses of TiO_2 are

performed in an oxygen-rich environment which allows the formation of weakly-bound O₂ species.

B. Confirmation of the Weakly-Bound Oxygen Model Using a Water Modified TiO₂ Surface.

Section III.D shows a set of O₂ adsorption experiments using excess water covering the TiO₂ surface and on a TiO₂ surface covered only with isolated OH groups. Figure 11.6 shows that no weakly-bound O₂ is observed in the IR spectrum of a TiO₂ surface covered by excessive water under 10 Torr of oxygen gas pressure, while Figure 11.7 shows that the IR active O₂ species produced in equilibrium with 2 Torr of oxygen gas exists on a TiO₂ surface containing only isolated OH species.

The difference between the surfaces in Figure 11.6 and Figure 11.7 is that in Figure 11.6, the surface is completely covered by OH groups, hydrogen bonding, and excessive water. In that case, not only the surface defect sites and adsorption sites for OH groups and water molecules are blocking oxygen adsorption, but other available sites are also blocked by hydrogen bonding between adsorbed water and OH groups. The excessive hydrogen bonding network makes direct interaction with the TiO₂ surface impossible for oxygen molecules. Thus, no oxygen was detected in the IR spectrum showed in Figure 11.6e. Under these conditions, screening of the electric field associated with the TiO₂ surface can both hinder O₂ adsorption as well as diminish O₂ polarization.

On the other hand, the surface in Figure 11.7 has only isolated OH on the surface. The adsorbed OH groups may block those sites where O₂ chemically adsorbs, but still leaves spaces for the weakly-bound O₂ species to interact with the TiO₂ directly. Thus, when exposed to 2 Torr of ¹⁶O₂ gas, the O-O stretching mode at 1550 cm⁻¹ appeared, as shown in Figure 11.7d.

C. Displacement of Surface-Bound Oxygen and Weakly-Bound Oxygen.

In section III.C, it is shown that both CO and CO₂ can displace the weakly-bound ¹⁶O₂. In both cases the absorbance of weakly-bound O₂ and either CO or CO₂ exhibit an accurate inverse relationship to each other. This suggests that the adsorbed CO or CO₂ molecules shield the O₂ molecules from the TiO₂ surface in a general manner, possibly by reducing the local electric field in their vicinity.

CO adsorbs on the TiO₂ surface with the carbon end interacting with the Ti cation via the σ orbital.¹⁵ All the adsorbed CO molecules contribute to the vibrational frequency between 2225 and 2150 cm⁻¹. CO₂ adsorption on the TiO₂ surface is more complicated since CO₂ can either adsorb linearly with bonding to one O moiety or form a carbonate. The V₃ mode was chosen to demonstrate the O₂ displacement by CO₂ in Figure 11.5c because it corresponds to the asymmetric stretching of linear CO₂ molecules. However, the carbonate species also shows an inverse displacement pattern with the weakly-bound O₂ species, as proven by integrating the absorbance at 1376 cm⁻¹ (not shown).

As more CO or CO₂ molecules adsorb on the TiO₂ surface, a screening layer between the substrate and the weakly-bound O₂ species starts to form. The CO and CO₂ adsorption can modify the electric field which the weakly-bound O₂ species senses by generating an induced opposite electric field. The difference between using CO and CO₂ molecules in displacing weakly-bound O₂ species lies in their ability to modify the electric field of the substrate.

V. Summary.

Transmission IR spectroscopy has been used to observe a weakly-bound molecular oxygen species which exhibits absorbance as a result of its interaction with bare sites on a powdered TiO₂ surface which has been thermally treated to produce a small fraction of

oxygen vacancy defect sites. The following properties of the adsorbed O₂ species have been observed:

1. The O₂(a) species exhibits a physical-adsorption enthalpy near -21 kJ mol⁻¹ at low coverage and experiences weak intermolecular repulsive forces as the coverage increases, causing an enthalpy increase of about 5 kJ mol⁻¹ at the highest coverage measured.
2. The ¹⁶O₂ species exhibits a vibrational frequency of 1550 cm⁻¹ that is identical to that of gas phase ¹⁶O₂. The lack of a frequency shift is consistent with the very weak van der Waals O₂ binding to TiO₂. The O-O stretching mode in the IR is likely turned on through interactions of the O₂ with an electric field which exists above bare TiO₂ sites on the surface.
3. The isotopic shift for ¹⁸O₂(a) compared to ¹⁶O₂(a) is consistent with the behavior of an essentially free molecule.
4. The O₂(a) stretching frequency is constant (± 1 cm⁻¹) over the coverage range investigated confirming that only weak intermolecular forces are developed as coverage increases.
5. Chemisorbed CO, CO₂ and H₂O block O₂ adsorption. However, partial coverages of hydroxyl groups are not completely effective in blocking O₂ adsorption.
6. The weakly-bound O₂ species is likely the precursor to more strongly-bound molecular O₂ species which are able to be electronically activated by electron-hole pairs made in TiO₂ by UV irradiation.

VI. Acknowledgement.

We acknowledge with thanks helpful discussions with Dr. Zhen Zhang on the properties of TiO₂ surfaces. We also acknowledge support from the Department of

Energy, Office of Basic Energy Sciences, under DOE grant number DE-FGo2-09ER16080.

Chapter 11 References:

1. Linsebigler, A. L.; Lu, G.; Yates, J. T., Jr. *Chemical Reviews* **1995**, 95, 735.
2. Thompson, T. L.; Yates, J. T., Jr. *Chemical Reviews* **2006**, 106, 4428.
3. Fujishima, A.; Zhang, X.; Tryk, D. A. *Surface Science Reports* **2008**, 63, 515.
4. Yates, J. T., Jr. *Surface Science* **2009**, 603, 1605.
5. Ganduglia-Pirovano, M. V.; Hofmann, A.; Sauer, J. *Surface Science Reports* **2007**, 62, 219.
6. Diebold, U. *Surface Science Reports* **2003**, 48, 53.
7. Beck, K.; Pfeifer, H.; Staudte, B. *Journal of the Chemical Society, Faraday Transactions* **1993**, 89, 3995.
8. Hadjiivanov, K.; Knožinger, H. *Chemical Physics Letters* **1999**, 303, 513.
9. Wang, X.; Kim, S.; Buda, C.; Neurock, M.; Koper, O. B.; Yates, J. T., Jr. *Journal of Physical Chemistry C* **2009**, 113, 2228.
10. Kim, S.; Byl, O.; Yates, J. T., Jr. *Journal of Physical Chemistry B* **2005**, 109, 3499.
11. Ohno, T.; Sarukawa, K.; Tokieda, K.; Matsumura, M. *Journal of Catalysis* **2001**, 203, 82.
12. G. Herzberg, F. R. S. *Molecular Spectra and Molecular Structure. I. Spectra of Diatomic Molecules*; Second ed.; Van Nostrand Reinhold Company, 1950.
13. Yates, D. J. C. *Journal of Physical Chemistry* **1961**, 65, 746.
14. Ramis, G.; Busca, G.; Lorenzelli, V. *Materials Chemistry and Physics* **1991**, 29, 425.
15. Liao, L. F.; Lien, C. F.; Shieh, D. L.; Chen, M. T.; Lin, J. L. *Journal of Physical Chemistry B* **2002**, 106, 11240.
16. Su, W.; Zhang, J.; Feng, Z.; Chen, T.; Ying, P.; Li, C. *Journal of Physical Chemistry C* **2008**, 112, 7710.
17. Turek, A. M.; Wachs, I. E.; DeCanio, E. *Journal of Physical Chemistry* **1992**, 96, 5000.
18. Lu, G.; Linsebigler, A.; Yates, J. T., Jr. *Journal of Chemical Physics* **1995**, 102, 3005.

19. Thompson, T. L.; Diwald, O.; Yates, J. T., Jr. *Journal of Physical Chemistry B* **2003**, *107*, 11700.
20. Bikondoa, O.; Pang, C. L.; Ithnin, R.; Murny, C. A.; Onishi, H.; Thornton, G. *Nature Materials* **2006**, *5*, 189.
21. Wendt, S.; Matthiesen, J.; Schaub, R.; Vestergaard, E. K.; Lmgsgaard, E.; Besenbacher, F.; Hammer, B. *Physical Review Letters* **2006**, *96*, 066107.
22. Takeuchi, M.; Bertinetti, L.; Martra, G.; Coluccia, S.; Anpo, M. *Applied Catalysis A: General* **2006**, *307*, 13.
23. Munuera, G.; Rives-Arnau, V.; Saucedo, A. *Journal of the Chemical Society-Faraday Transactions I* **1979**, *75*, 736.
24. Primet, M.; Pichat, P.; Mathieu, M. V. *Journal of Physical Chemistry* **1971**, *75*, 1216.
25. Henderson, M. A. *Langmuir* **1996**, *12*, 5093.
26. Wendt, S.; Schaub, R.; Matthiesen, J.; Vestergaard, E. K.; Wahlstrom, E.; Rasmussen, M. D.; Thostrup, P.; Molina, L. M.; Lmgsgaard, E.; Stensgaard, I.; Hammer, B.; Besenbacher, F. *Surface Science* **2005**, *598*, 226.
27. Wendt, S.; Sprunger, P. T.; Lira, E.; Madsen, G. K. H.; Li, Z.; Hansen, J. O.; Matthiesen, J.; Blekinge-Rasmussen, A.; Lmgsgaard, E.; Hammer, B.; Besenbacher, F. *Science* **2008**, *320*, 1755.
28. Henderson, M. A.; William, W. S.; Perkins, C. L.; Peden, C. H. F.; Diebold, U. *Journal of Physical Chemistry B* **1999**, *103*, 5328.
29. Sporleder, D.; Wilson, D. P.; White, M. G. *Journal of Physical Chemistry C* **2009**, *113*, 13180.
30. Thompson, T. L.; Yates, J. T., Jr. *Journal of Physical Chemistry B* **2005**, *109*, 18230.
31. Zhang, Z.; Yates, J. T., Jr. *Journal of Physical Chemistry C* **2010**, *114*, 3098.
32. Kimmel, G. A.; Petrik, N. G. *Physical Review Letters* **2008**, *100*, 196102.
33. Cui, X.; Wang, B.; Wang, Z.; Huang, T.; Zhao, Y.; Yang, J.; Hou, J. G. *Journal of Chemical Physics* **2008**, *129*, 044703.
34. Henderson, M. A.; Epling, W. S.; Peden, C. H. F.; Perkins, C. L. *Journal of Physical Chemistry B* **2003**, *107*, 534.
35. Anpo, M.; Che, M.; Fubini, B.; Garrone, E.; Giamello, E.; Paganini, M. C. *Topics in Catalysis* **1999**, *8*, 189.
36. de Lara-Castells, M. P.; Krause, J. L. *Journal of Chemical Physics* **2001**, *115*, 4798.
37. Vaska, L. *Accounts of Chemical Research* **1976**, *9*, 175.
38. Somorjai, G. A. *Introduction to Surface Chemistry and Catalysis*; Wiley Interscience, 1994.

39. Wandelt, K. *Surface Science Reports* **1982**, 2,1.

Part III

Appendices

Appendix A

Geometry of the Cell — Position of the Sample, Width of the IR Beam, and the Calibration and Installation of the Fiber Optics.

The vacuum IR cell is constructed using of a 3% in stainless steel cube which has six 3/8" ports. The transmission IR beam passes the cell through the Y-direction, via 2 differentially pumped KBr windows, as shown in Figure 2.1. A vacuum UV fiber optical cable is installed in the cell from the X-direction. The sample holder enters the cell from the Z-direction. Ideally, all three axes should intersect in the center of the cube. However, the sample is slightly off-centered since the IR sample feed-through where the Ni sample holder clamps are installed on has 4 electrical connectors—two for the thermocouple and two for the Ni clamps. It is crucial to know the exact location of the center of the sample on the X-Y plane, in order to focus the IR and UV beams appropriately. A set of careful measurements was made to obtain this information and will be summarized in this section. This section will be divided into 3 parts: A.1 the physical position of the center of the sample in relation to the 3/8 in cube cell; A.2 the width of the IR beam at the focus point and its relationship to the aperture size; and A.3 the fiber optic output beam width and power as a function of distance to the sample.

A.1. The Position of the Sample Center. (Notebook #10, pages 22-23)

Figure A.1 shows the physical position of the center of the sample on the X-Y plane (top view). Since the sample manipulator has vertical motion, information on the Z-direction is not useful at this point. The measurements were made on the bare cell cube

without the differentially pumped windows. As shown in Figure A.2, a ruler with known thickness (measured by caliper) was pressed tightly against the cell's outer-wall to create a spacer plate for the flat side of the caliper to rest against. This arrangement assured that the caliper pin is perpendicular to the W-mesh. The thickness of the ruler was later deducted from the total length measured. It is important to note the orientation of the Ni-clamps when making the measurements as shown in Figure A.1, since the distance will be different when the Ni-clamps are turned 180° . A similar method was used for the y-direction measurements.

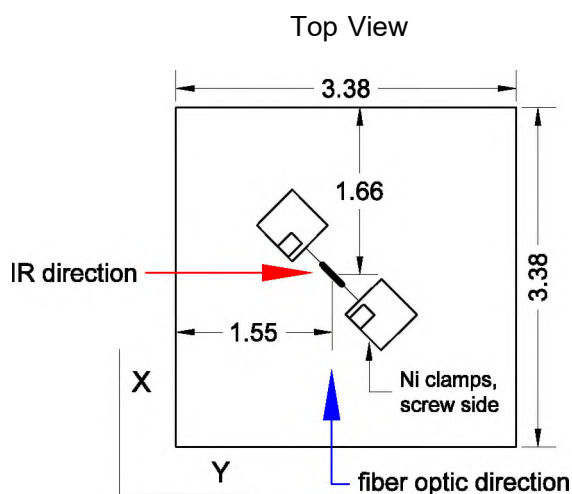


Figure A.1. Top view of the cell with the sample center position labeled (dimensions in inches).

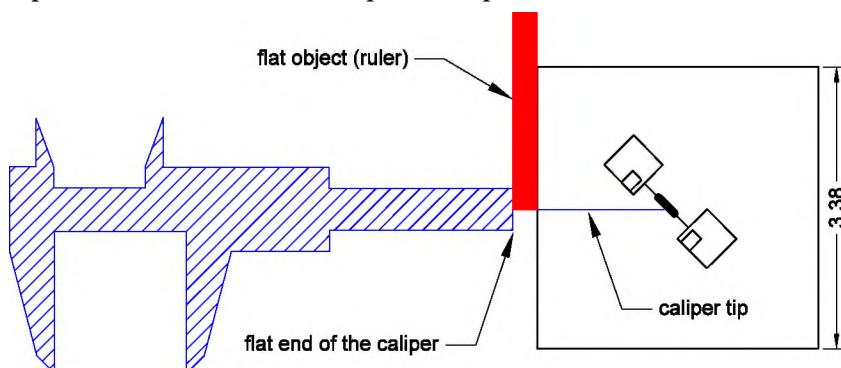


Figure A.2. Scheme of the measurement setup.

The measured values shown in Figure A.1 are only for reference use and rough estimation for future users, since each individual feed-through employed should give a unique (but similar) sample position.

A.2. The Width of the IR Beam at the Sample Position and Its Relationship to the Aperture Size. (Notebook #10, pages 8-21)

The FTIR spectrometer is equipped with an aperture wheel that can control the IR beam width. The aperture can be set to a value between 0.5 mm and 6 mm. Ideally, one should be able to choose an appropriate aperture size that is slightly smaller than the sample size to obtain a high signal to noise ratio without incident light missing the sample. However, it was found that the actual IR beam size at the center of the cell is not directly proportional to the aperture size. The aperture size shown on the computer should only be used as a reference to the trend of the actual IR beam. This session explains the method used to measure the IR beam size near the center of the IR cell and the measured values.

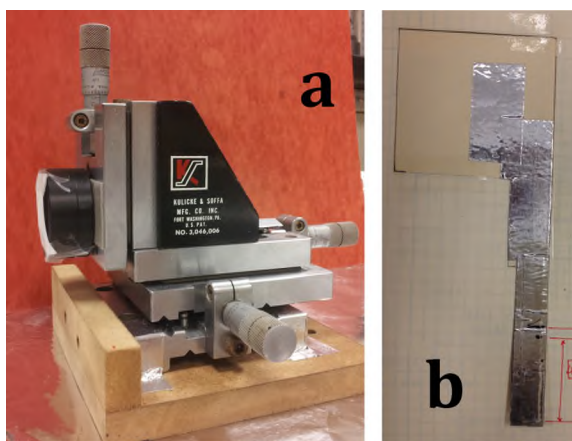


Figure A.3. Tools used to calibrate the IR beam size. A, manipulation stage; b, cardboard mask.

A manipulator stage with separate X, Y, Z-direction motions was employed, as shown in Figure A.3a. The graduated scales on the manipulator stage are labeled to 1/1000" increments. A number-9-shaped cardboard mask was made and glued to the manipulator, as shown in Figure A.3b. The width of the mask was enough to block the entire IR beam at the widest measurements. Aluminum tape was used to add more weight and stiffness to the cardboard, so the mask remained straight and still during the measurements. A set of separate rulers was drawn on the empty cell edges, as shown in the inset of Figure A.4. A Y-value was fixed for each set of X and Z direction measurements.

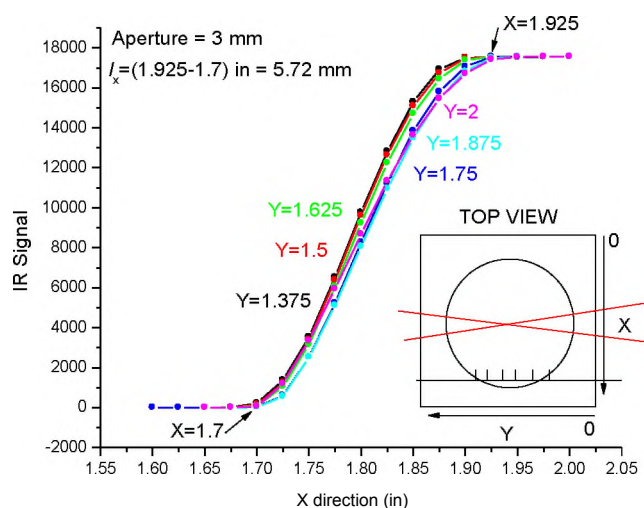


Figure A.4. IR beam width calibration at 3 mm aperture size. Each curve shows the IR beam width at the indicated Y-position.

Aperture sizes 0.5 mm, 1 mm, 3 mm, and 5 mm were tested. The final results are plotted in Figures 4-6, and are summarized below:

1.) The beam size does not change much through the cell (along the Y-direction), as shown in Figure A.4. In other words, the focus point is not sharp.

2.) The beam size increases as the aperture setting increases, but not proportionally, as shown in Figures A.5-6. With a 7-mm (0.28 in) diameter sample spot, the 3 mm aperture setting is the optimal value (5.7 mm).

3.) The beam width on the x-direction and the z-direction are similar, with the x-value slightly larger.

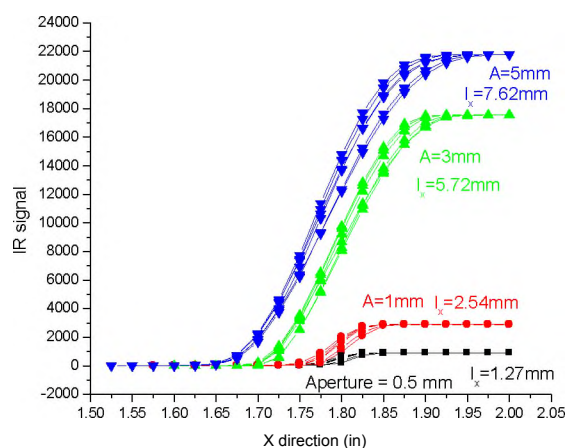


Figure A.5. IR beam width on the X-direction at indicated aperture size.

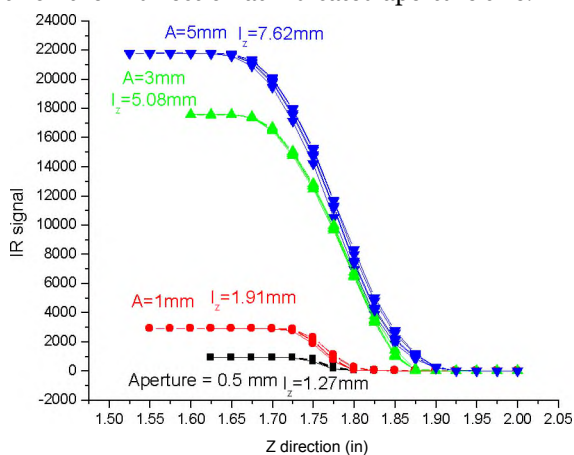


Figure A.6. IR beam width on the Z-direction at indicated aperture size.

The center position of the IR beam can be adjusted by tuning the two optical mirrors in front of the cell. The other two optical mirrors located after the cell in the IR path need to be adjusted accordingly to collect the maximum IR signal. When using the IR alone,

the Z-direction location of the IR beam is not very important as long as all of the IR beam can exit the cell via the KBr window. This is because the sample can be moved into the IR beam by the Z-direction manipulator. However, when using in conjunction with the UV source, it is crucial to make sure the UV beam and the IR beam are at the same height, for *in situ* UV-IR measurements. A similar set of measurements to locate the Z-direction location of the IR beam was made and the result is reported in Figure A.7. The UV optical cable was installed according to this measurement as well as the sample position reported in the last section.

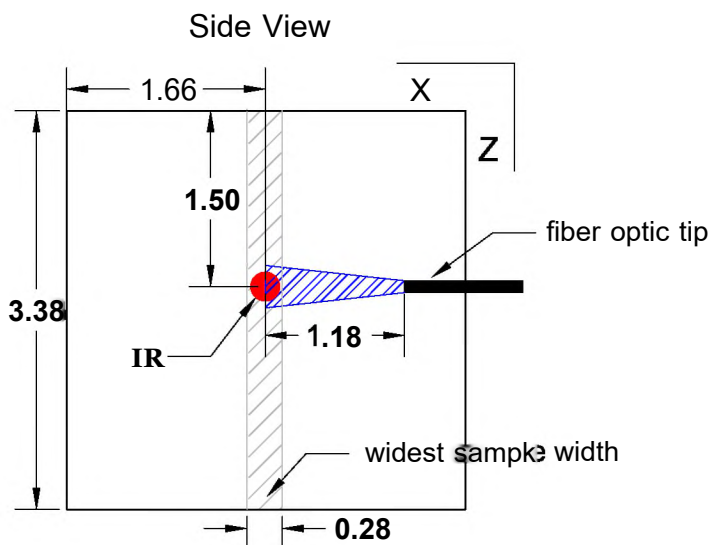


Figure A.7. Side view of the cell with sample position, IR beam position, and UV fiber optic tip position labeled (dimensions in inches).

A.3. Calibration and Installation of the Ultraviolet Fiber Optics (Notebook #9, pages 142-152; Notebook #10, pages 1-8, 24-25, 33)

a. Calibration of the UV Lamp and the Fiber Optics

The UV source in use is a Hg arc lamp. The UV light generated is then directed to the sample inside the vacuum cell through fiber optics. The fiber optics comes in 6 parts. In the connecting sequence, they are: UV source to fiber optics focus head, air part of the

fiber optics cable, air part fiber optics to CF flange connector, fiber optics CF flange, vacuum part fiber optics to CF flange connector, and the vacuum part fiber optics cable.

The output intensity of the fiber optics decays while the output spot size increases, as the target distance increases. One of the goals of the calibration is to decide the optimum distance between the fiber optics output and the sample, where the output spot size is large enough to cover the entire sample (7 mm, 0.28 in). The other goals of the calibration are to test the stability of the UV lamp, to test the loss of intensity at the air to vacuum connection, and to test the dependence of the cable outlet intensity on the target distance.

A thermopile with a 2 mm x 2 mm detector area was used for the calibration. The absolute intensities measured were not used for the position calibration purpose, but the thermopile was calibrated to 23.2 V/W with linear upper limit of 0.1 W/cm². In the calibration setup, the thermopile was fixed on the bench top, and the optical cable is attached to the manipulator stage shown in Figure A.3. The manipulator stage provided accurate distance movement for the output power decay study, and accurate lateral movement for output spot size measurements.

Figure A.8 shows the output spot size as a function of the distance between the outlet and the target. In this study, the cable outlet is moved laterally in the same plane that is located at a fixed distance away from the thermopile detector. The plots are trapezoids because the left and right legs are formed when the UV beam enters and leaves the active detector area, while the shorter base is formed when the UV beam covers the entire detecting area, generating higher and constant measured intensity. The outlet spot size is revealed as the length of the longer base of the trapezoid. The optimum distance between the outlet and the sample is 3 cm, where a ~9 mm (0.36 in) output is observed.

This spot size is big enough to cover the entire 7 mm-diameter maximum sample, with some space for mis-alignment.

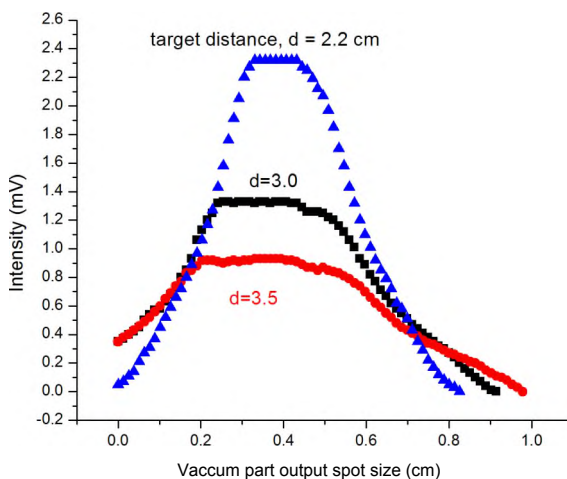


Figure A.8. Fiber optic vacuum part cable output spot size measured at indicated target distance.

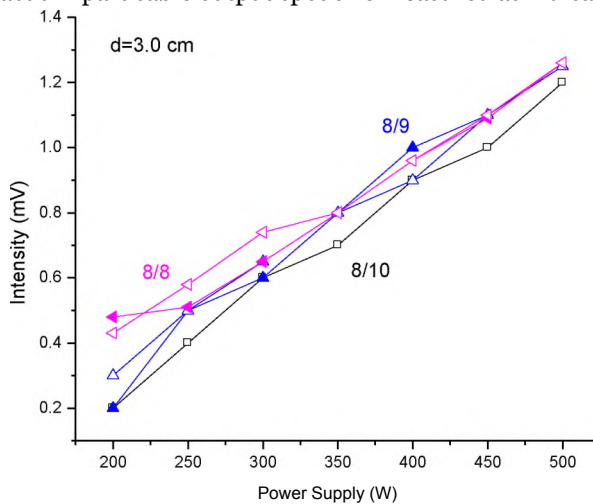


Figure A.9. UV lamp stability test.

The UV lamp power supply provides 150-500 W of power. The UV lamp intensity can be controlled accurately by tuning the power supply output. Figure A. 9 shows the vacuum part cable output intensity at 3 cm distance as a function of power supply output,

over 3 days of testing. The measurements were made after the lamp had warmed up at 500 W power for 30 min.

The UV output intensity decrease as target distance increases was measured at the air part cable outlet and the vacuum part cable outlet, as shown in Figure A. 10. This study shows that there is a loss of the power at the CF flange connectors.

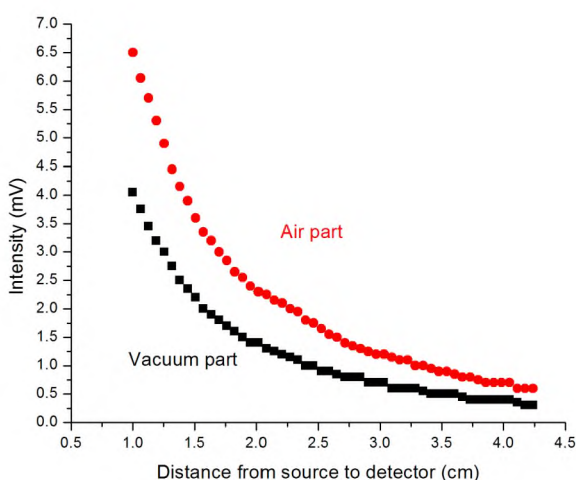


Figure A.10. Plots of the outlet intensity decay as a function of increasing target distance from the end of separate parts of the fiber optics cables. Both the air cable output and the vacuum cable output are reported.

b. Installation of the Fiber Optics.

As shown in Figure A.10, the UV output intensity decays roughly exponentially with increasing distance to the target. In addition, the UV output spot is only slightly bigger than the sample. As a result, it is very important to fix the tip of the vacuum part of the fiber optics cable at the correct position.

The vacuum part of the fiber optic cable is 14.5 in long. The cable has some flexibility, but it cannot be bent at a sharp angle or it will damage the fiber inside. In order to keep the fiber optic cable straight, the length of the IR cell was extended by 4 additional CF flange extension tubes with lengths of 2.5 in, 5 in, 5 in, and 2.625 in (total 15.125 in). A

special clamp was designed to hold the tip of the cable at the exact position, 3 cm away from the cross where the sample and the IR beam meets, as shown in Figure A.7. The clamp was slotted to avoid virtual leaks. A front view scheme of the clamp is given in Figure A.11.

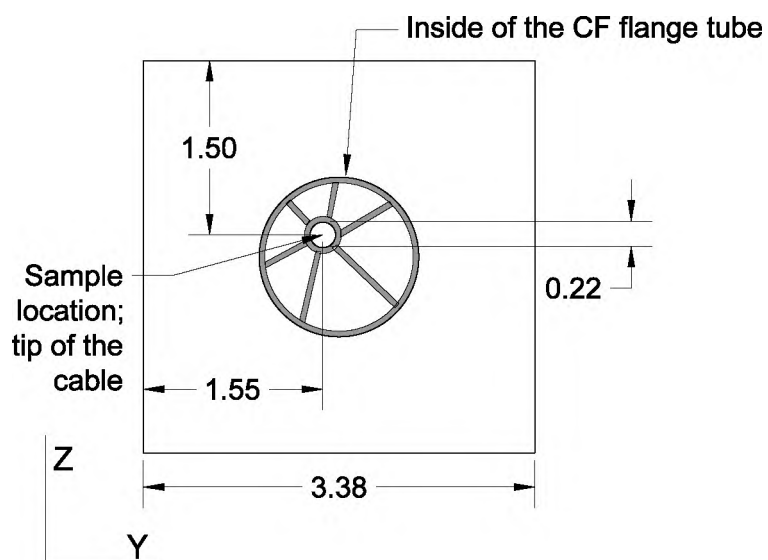


Figure A.11. A front view scheme of the fiber optic clamp.

Appendix B

Maintenance of the Parker Purging Gas Generator.

The Parker Balston® FT-IR purging gas generator (Model 75-52) filters out the H_2O (-73 F dewpoint) and CO_2 (<1ppm) components from the compressed air provided by the department, to produce IR silent purging gas for the FTIR spectrometer. It consists of four main parts (Figure B.i) that need maintenance from time to time: 1) pre-filter, 2) logic box, 3) twin-filter towers, and 4) humidity indicator.

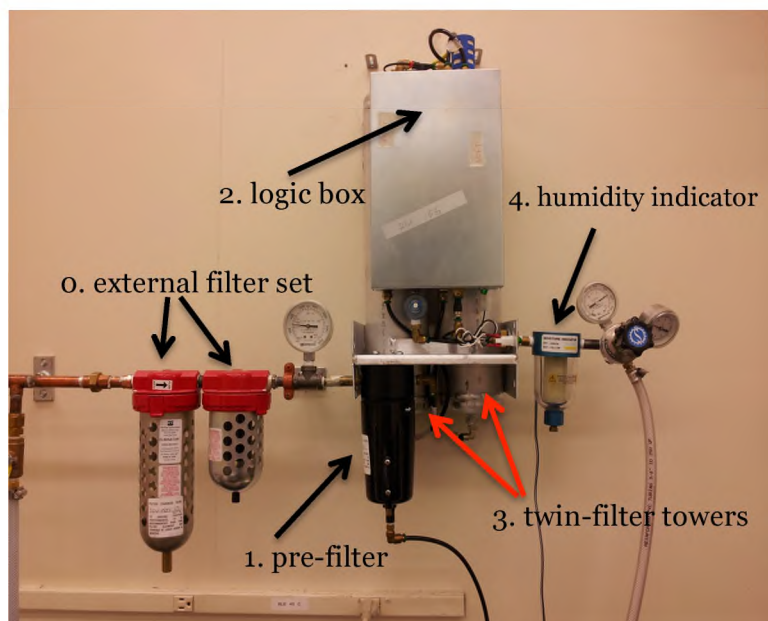


Figure B.i. The purging gas generator system with extra external filters installed.

The generator operates at room temperature with an inlet air pressure of 60-125 psi. The sorbent material inside the twin-filter towers (3) removes a moderate amount of moisture from incoming air. However, an excessive amount of water or oil damages the filtration material irreversibly. The pre-filter (1) prevents some of the oil and liquid water

from entering the towers by adsorptive filtration. The excess liquid oil and water caught by the pre-filter accumulates at the bottom of the airtight container and exits when the stopper floats up. The pre-filter will get saturated and gradually lose its filtration ability. The manufacturer suggests changing the pre-filter annually.

It has been noticed that the compressed air entering the gas generator sometimes carries a large amount of water and oil that cannot be completely removed by the pre-filter. An additional set of external filters (o) is installed in front of the pre-filter, as shown in Figure B.1. These external filters are purchased from Reading Technologies (800-521-9200, www.driair.com) and the filters inside need to be replaced every 6 months. The part numbers for the external filter replacement elements are: 23-P4 and 23-P14.

It is very important to have good pre-filter to protect the gas generator. However, if the twin-filter towers get damaged, indicated by IR observation, replacements can be purchased from Parker (part number B05-0020). Figure B.2 shows an example of the gas phase CO₂ level as a function of time, when one of the twin towers is damaged.

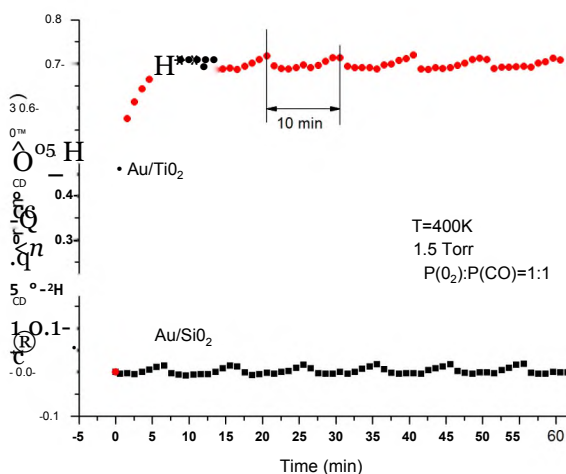


Figure B.2. Plots of integrated absorbance of CO₂, in purged IR pathway and in IR cell, as a function of time.

The twin towers work alternatively, controlled by the logic box (3). The inlet air is directed to one tower at a time—the working tower, while the other tower is idling. The outlet H₂O- and CO₂- free air from the working tower is divided to two parts, one used to purge and clean the idling tower, the other one directed to the outlet of the generator. Each tower works for about 4 min and 54 s. The switch is activated by the electronics in the logic box (3). A loud outgassing sound can be heard when the switch occurs, as the working tower loses air and the idling tower picks up the pressurized air. One can monitor the switching noise to diagnose if the logic box is working properly. The outgassing sound should happen every $4'54'' \pm 2''$. The cycle interval shown in Figure B.2 is ~10 min, indicating that only one tower is damaged. The logic box can also be purchased from Parker.

When switching to new twin-filter towers, the generator should run 24 h with the outlet to the IR spectrometer closed, in order to activate/clean the filtration materials inside the towers. This can also be performed periodically to regenerate the generator.

Part 4 of the gas generator is a humidity indicator. When the generator is working properly, the indicator should be green. If the outlet air contains a large amount of water, the indicator will be yellow. However, the humidity indicator is not as sensitive as the IR spectrometer. One would notice the unusual CO₂ and H₂O noise level before the humidity indicator turns yellow. To change the humidity indicator, simply unscrew the nut at the bottom.

The annual maintenance kit (part number MK7552) sold by Parker contains a pre-filter and a humidity indicator. It is very important to keep monitoring the status of the pre-filter (1) and the external filters (o). They should be replaced more often than in the standard interval when compressed air quality is poor, and less often when compressed air quality is good.

Appendix C

Gas Line Volume Calibration.*

^Contents from this chapter are located on Notebook #6, pages 36-43.

When dosing gas reactants to the IR cell, sometimes mixtures of two or more gases with fixed ratios need to be made in the gas line. Such operations are performed by mixing together known amount of different gases trapped in separate portions of the gas line. The gas amount in each portion is calculated from the pressure of the gas and the volume of the part of the gas line filled with that gas, following the Ideal Gas Law.

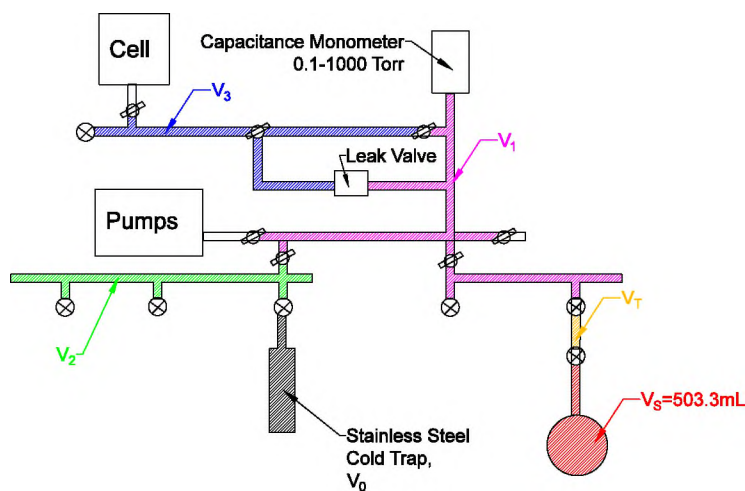


Figure C.1. Scheme of the gas line and the sectioning of the volume calibration.

A gas line volume calibration was carried out in order to fulfill the needs of mixing gases. A diagram of the gas line and the calibration sectioning is shown in Figure C.1. A glass bulb (standard) with known volume (V_s , 503.3 mL) is attached to the gas line. A 6" long stainless steel cold trap (with a double male connector) noted as V_0 was also calibrated. The volume between the glass bulb and the gas line, noted as V_T , was also

calibrated. This small volume is the connection between a female (on the gas line) and a male VCR. It can change slightly from connection to connection, depending on how the male VCR is welded to the next connection (possibly a valve). The rest of the gas line was divided into 3 sections, noted as V_1 , V_2 , and V_3 . The final result of the calibrated volumes of each labeled section is given in Table C.1.

The volume calibration is done using room temperature air, following Boyle's law: $P_i V_i = P_f V_f$. Room temperature air is a good and free substitute/model for other gases under dosing conditions. Air from an initial section (V_i) with a known pressure (P_i) is expanded to a larger final section (V_f) to obtain a new equilibrium pressure (P_f). As shown in Figure C.1, there is only one gauge on the gas line for pressure reading, which is a 0.1-1000 Torr capacitance monometer. As a result to the position of the pressure gauge, V_i need to be included in all pressure measurements in order to have a pressure reading.

Table C.1. Gas Line Sections Volume

Section	V_o	V_1	V_2	V_3	V_T
Volume (mL)	57.7	99.7	40.6	51.0	2.6

The closed IR cell with the UV fiber optics extension and without the QMS portion is ~ 2.5 L (note that the cell volume changes with the sample z-position). Following is a sample calculation of how to produce 20 Torr of 1:100 ratio O₂:H₂ mixture in the gas line section V_1+V_2 , where O₂ is connected to the V_2 portion of the gas line while H₂ is connected to the V_1 part of the gas line.

$$\frac{P(O_2) \times V_2}{P(H_2) \times V_1} = \frac{1}{100}$$

$$20 \text{ Torr} \times (V_1 + V_2) = P(O_2) \times V_2 + P(H_2) \times V_1$$

Solving the two equations together yields $P(\text{O}_2)=0.7$ Torr and $P(\text{H}_2)=27.9$ Torr. (Keep in mind that the pressure gauge reads to the 0.1 Torr.) Since the pressure gauge is connected to V_1 , trapping H_2 in V_1 should be the last step. In other words, one should fill (V_1+V_2) with 0.7 Torr of O_2 first. Then trap the 0.7 Torr of O_2 in V_2 and evacuate V_1 for H_2 trapping. After 27.9 Torr of H_2 is trapped in V_1 , open the valve between V_1 and V_2 to let O_2 and H_2 mix. The pressure gauge should read close to 20 Torr after all operations.

Appendix D

List of Publications.

1. I. X. Green, W. Tang, M. Neurock, J. T. Yates, Jr., “*Watching the Special Au-Ti₄⁺ Dual Perimeter Site at Work for Oxidation Reactions*”, in preparation for **Accounts of Chemical Research**.
2. I. X. Green, W. Tang, M. McEntee, M. Neurock, J. T. Yates, Jr., “*Making Acetic Acid from Ethylene on a Au/TO Catalyst*”, in preparation for **The Journal of Physical Chemistry Letters**.
3. I. X. Green, W. Tang, M. Neurock, J. T. Yates, Jr., “*Mechanism of the Partial Oxidation of Acetic Acid by O₂ at the Dual Perimeter Sites of a Au/TO Catalyst*”, in preparation for **The Journal of Physical Chemistry C**.
4. I. X. Green, W. Tang, M. Neurock, J. T. Yates, Jr., “*Localized Deep Oxidation of Acetic Acid at the Dual Perimeter Sites of the Au/TO Catalyst - Formation of Gold Ketenylidene*”, **Journal of the American Chemical Society**, Accepted (2012).
5. I. X. Green, W. Tang, M. McEntee, M. Neurock, J. T. Yates, Jr., “*Inhibition at Perimeter Sites of Au/TiO₂ Oxidation Catalyst by Reactant Oxygen*”, **Journal of the American Chemical Society**, ASAP (2012).
6. I. X. Green, W. Tang, M. Neurock, J. T. Yates, Jr., “*Spectroscopic Observation of Dual Catalytic Sites During Oxidation of CO on a Au/TO Catalyst*”, **Science**, 333, 736 (2011).
7. I. X. Green, W. Tang, M. Neurock, J. T. Yates, Jr., “*Low-Temperature Catalytic H₂ Oxidation over Au Nanoparticle/TO Dual Perimeter Sites*”, **Angewandte Chemie International Edition**, 50, 10186 (2011).
8. I. X. Green, C. Buda, Z. Zhang, M. Neurock, J. T. Yates, Jr., “*IR Spectroscopic Measurement of Diffusion Kinetics of Chemisorbed Pyridine through TiO₂ Particles*”, **The Journal of Physical Chemistry C**, 114, 16649 (2010).
9. I. X. Green, J. T. Yates, Jr., “*Vibrational Spectroscopic Observation of Weakly Bound Adsorbed Molecular Oxygen on Powdered Titanium Dioxide*”, **The Journal of Physical Chemistry C**, 114, 11924 (2010).
10. X. Wang, S. Kim, C. Buda, M. Neurock, O. B. Koper, J. T. Yates, Jr., “*Direct Spectroscopic Observation of The Role of Humidity in Surface Diffusion through an*

Ionic Adsorbent Powder. The Behavior of Adsorbed Pyridine on Nanocrystalline MgO", **The Journal of Physical Chemistry C**, 113, 2228 (2009).

11. S. Kim, X. Wang, C. Buda, M. Neurock, O. B. Koper, J. T. Yates, Jr., "IR Spectroscopic Measurement of Diffusion Kinetics of Chemisorbed Pyridine through Nanocrystalline MgO Particles. The Involvement of Surface Defect Sites in Slow Diffusion", **The Journal of Physical Chemistry C**, 113, 2219 (2009).